Integrated Research on Redox-type Chemical Heat Storage Systems Targeting Medium-high Temperature Ranges
（中高温域をターゲットとしたレドックス型化学蓄熱システムに関する一貫研究）

Department of Chemical Systems Engineering,

Graduate School of Engineering,

Nagoya University

CHEN Xiaoyu

January 2025

Contents

Chapter 1. General Introduction

1.1 Path to Carbon Neutrality: Renewable energy and storage

The 2016 Paris Agreement marked critical moment in the global climate action, with 195 countries committing to a long-term temperature control goal: limiting the rise in global surface temperature to well below 2 ℃ above the pre-industrial levels (1760–1840). To achieve this ambitious target, the greenhouse gas emissions must be significantly reduced, with a 50% cut required by 2030 [1]. To respond to this urgent need, Carbon Neutrality (CN) has emerged as a critical strategy for governments to address global climate change and facilitate energy structure transformation. The International Renewable Energy Agency (IRENA) has outlined a comprehensive "Global energy transformation: a roadmap to 2050", highlighting several major challenges in achieving CN [2]:

1. The share of modern renewable energy would need to rise from 10% of total final energy consumption today to two-thirds in 2050.
2. The share of renewable energy in power generation would rise from 25% today to 86% in 2050. About 60% of total generation in 2050 would be accounted for by variable renewables, such as solar and wind.

Renewable energy plays a key role in the long journey towards CN, helping to reduce the demand for fossil fuels by providing cleaner sources of energy. However, the widespread capture of renewable energy faces significant challenges. The generation of renewable energy primarily relies on naturally occurring factors such as river flows, solar, and wind, making these sources inherently unstable and intermittent. In order to achieve the widespread utilization of renewable energy, various energy storage technologies play an important role in the intermittent and instable nature of renewable energy and the spital and temporal mismatch issues between energy supply and demand.

Currently, the energy storage technologies can be classified into various type based on

their working mechanism (Figure 1-1) [3], such as electrical (capacitor, supercapacitor), electrochemical (lithium battery, redox flow battery), thermal (sensible, latent, chemical), chemical (biomass, hydrogen, power-to-gas (SNG)), and mechanical energy storage (compressed-air, pumped hydroelectric, flywheels).

Different energy storage technologies have distinct advantages and disadvantages based on their working mechanism. The selection of an appropriate energy storage technology generally depends on specific energy storage requirements and the constraints of the real-world environment.

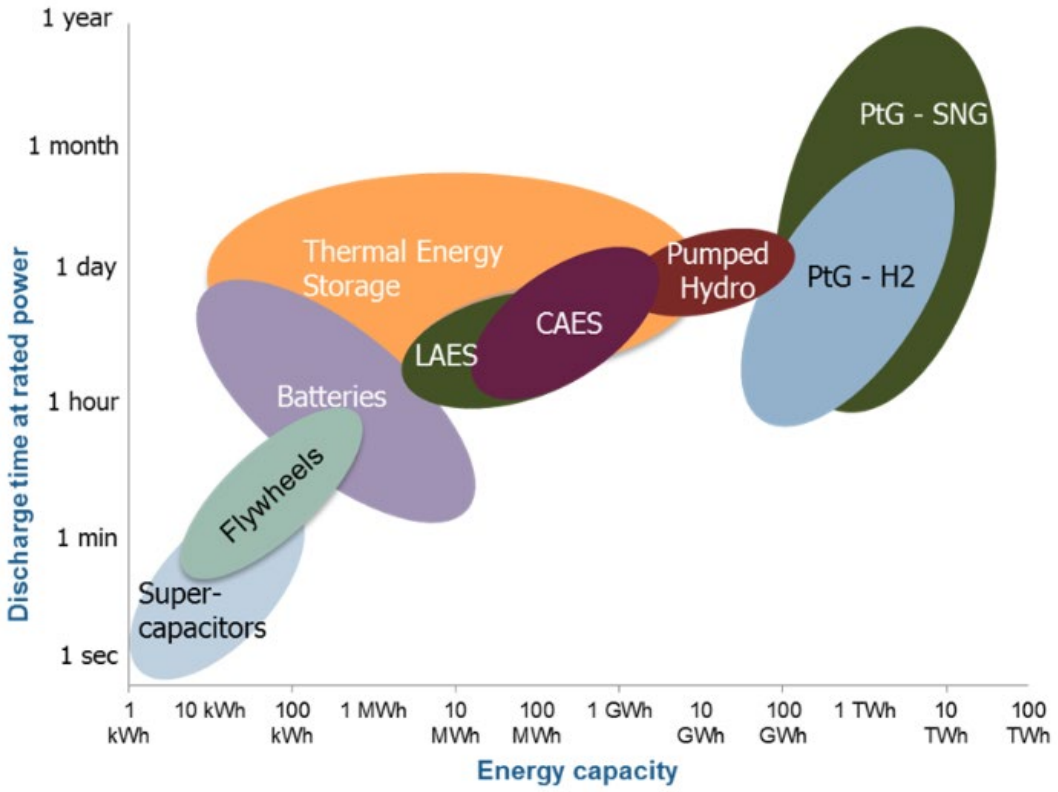

Figure 1-1 Mapping energy storage technologies according to their characteristics (Liquid Air Energy Storage, LAES; Compressed Air Energy Storage, CAES; PtG, Power-to-Gas)

1.2 Thermal energy storage

Thermal energy (heat) is one of the most critical and indispensable forms of energy for human society. According to the report of International Energy Agency (IEA), heat accounted for almost half of total final energy consumption and 38% of energy related CO_2 emissions in 2022 [4]. However, there are significant differences between thermal energy and electrical energy, such as the fact that the qualities of thermal energy are strongly influenced by its temperature and that it cannot be transported as easily as electrical energy.

In recent decades, thermal energy storage (TES) technology has emerged as a solution to address the challenges of temperature mismatches, spatial distance discrepancies, and temporal disparities in thermal energy utilization. TES occupies a central position among various energy storage technologies in terms of energy storage density and duration (Figure 1-1), making it well-suited for large-scale deployments. It is worth noting that, compared to other large-scale energy storage technologies, such as power-to-gas, TES stands out for its safety and cost-effectiveness. Furthermore, unlike pumped-storage hydroelectricity, which is currently gaining considerable attention, TES is not constrained by geographical limitations.

As TES technologies have advanced, their applications have expanded beyond industrial and building purposes. Now, TES is being deployed in power generation plants equipped with large-scale energy storage systems, such as concentrated solar power (CSP) plants and Carnot batteries [5,6].

TES is generally classified into sensible, latent, and chemical heat storage technologies, which are different in their working mechanisms (Figure 1-2) [7]. Sensible heat storage (SHS) technologies store heat by temperature changes via storage medium, which can be either a liquid (oil, water, etc.), solid (sand, stone, etc.), or a mixed phase. Latent heat storage (LHS) is based on the phase change of heat storage materials, the most common case is solid-liquid transitions (but also solid-solid transitions). Chemical heat storage

(CHS) is based on reversible chemical reactions. Energy charging and discharging steps are conducted by an endothermic (heat storage) and exothermic reaction (heat release).

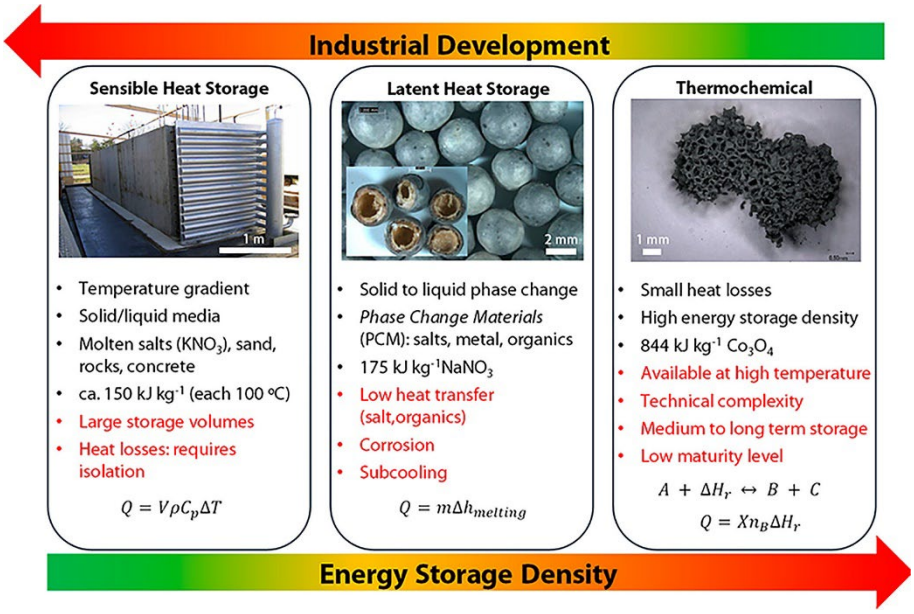

Figure 1-2 Comparison of sensible, latent, and chemical heat storage technologies

Exergy efficiency (η_{ex}) allows analyzing the thermal performance of the TES systems, and it is defined as following:

$$\eta_{ex} = \frac{Q_{out}}{Q_{in}} \cdot \frac{\left(1 - \frac{T_c}{T_{out}}\right)}{\left(1 - \frac{T_c}{T_{in}}\right)} \qquad (1-1)$$

where Q_{out} and Q_{in} are the heat that systems released and stored, respectively. T_{out} and T_{in} are the heat discharge/charge temperatures. T_c is the minimum working temperature of the TES systems. Therefore, the exergy efficiency of TES mainly depends on the ratio of heat that system released/stored and actual working temperature.

To date, SHS technologies have reached the stage of commercial implementation, making them the most mature among TES technologies. However, the other two, LHS

and CHS, are less developed, with CHS being the least advanced. Although recent studies have highlighted the promising advantages of CHS, these technologies remain largely confined to laboratory-scale research. The following subsections will provide a brief introduction to each technology.

1.2.1 Sensible heat storage (SHS)

Sensible heat storage (SHS) is based on the temperature changes in the storage medium, which can be a liquid or solid, and the sensible heat (Q, [J/g]) can be calculated by following equation:

$$Q = V\rho C_p \Delta T \qquad (1-2)$$

where V is the volume, ρ is the density, C_p is the specific heat capacity, and ΔT is the temperature change.

Most common SHS materials are water, oils (mineral, synthetic, silicone, etc.) and molten salts (solar salt ($NaNO_3$-KNO_3), commercial Hitec ($NaNO_3$-$NaNO_2$-KNO_3)) [8]. Molten salts mixtures allow heat to be stored at higher temperature than water or oils, therefore, they were investigated for CSP purposes first. However, they present shortcomings related with minimum working temperature, which results in salt freezing and corrosion [9].

For high-temperature heat storage purposes (600-1200 °C), Al_2O_3 ceramic sphere is commonly used in industrial regenerative burner systems because of their low cost. However, Al_2O_3 typically has a low heat storage density (~150 kJ/kg per 100 °C) due to its low specific heat capacity. Recent research in SHS technologies has focused on enhancing rapid heat storage and releasing capabilities through composition modification. Zhou et al. developed an advanced composite heat storage material combining Al_2O_3 with Fe-Co-Mn-Al spinel [10]. Using a medium entropy (contains three or more elements),

they improved the infrared absorptivity of Al_2O_3 from 0.2 to 0.8 in the temperature range of 600-1200 °C in optimal doping ratios. By preparing this composite into hollow spheres, they further enhance heat storage and release speed. Compared to conventional systems, this approach increased heat storage power by 24.6%, and the heat storage density of the packed-bed reactor by 16.7%.

Similarly, Liao et al. innovatively developed a rice husk composite heat storage material (mainly composed of SiC and Al_2O_3) [11]. This material exhibited a radiative absorptivity of 0.96 in the 600-1200 °C range, surpassing both SiC (0.85) and Al_2O_3 (0.25) ceramic spheres, thus achieving even more rapid heat storage and release performance. However, it should be noted that the lower heat storage density of SHS materials leads to increased heat storage reactor volumes and potentially larger heat losses in the mid- to long-term heat storage scenarios.

1.2.2 Latent heat storage (LHS)

Latent heat storage (LHS) makes use of the heat involved in phase changes, mainly solid-liquid phase transitions. The latent heat storage capacity can be calculated by the equation below:

$$Q = m\Delta h_m \qquad (1-3)$$

where m is the mass of storage material, Δh_m ([J/g]) is the latent heat related to the phase change.

Materials used for LHS are known as phase change materials (PCMs), which attracted many researchers. The common PCMs are metals (Zn, Al), metal alloys (Mg-Zn), salts (alkali nitrates, hydroxides, or chlorides), or salt mixtures (KNO_3-KCl); their working temperatures cover a broad range from 250 ℃ to 800 ℃ [8]. Organic compounds also have been proposed for thermal energy storage, but their low melting temperature restrict

them to low- and low-medium temperature applications [12]. Generally, metals exhibit better thermal properties than salts, but salts are more cost-effective. The heat storage densities of PCMs are varying from 74 kJ/kg of KNO_3-KCl (95.5 : 4.5), 498 kJ/kg of Al-Si alloy (88 : 12), and 530 kJ/kg of $LiNaCO_3$-C (90 : 10) [8]. Some hydroxides or chlorides are corrosive; hence, they require special containers for storage which may cause higher costs.

Because PCMs are usually suffered from low thermal conductivities (~ 1W/(m·K)) and supercooling, some researchers focus on the techniques to enhance the heat transfer performance by incorporating structure that enlarge the surface area (such as fins, cylindrical tubes, plates, and rods) [13].

Currently, the research trend in PCMs primarily focuses on widening the working temperature range, improving thermal conductivity, and increasing heat storage density. However, a specialized area of PCMs research addresses the challenges of changes in volume, physical property and leakage issues that occur during the phase change process after heat storage. From a more philosophical perspective, this research area aims to utilize PCMs as “solid powders”.

In 2015, Nomura et al. innovatively proposed Microencapsulation Phase Change Materials (MEPCMs) for high-temperature heat storage purposes [14]. Their team encapsulated Al-Si alloy PCM particles with α-Al_2O_3, demonstrating good durability in cycling performance tests. They suggest that MEPCMs could be applied in various endothermic and exothermic reactions to control the reaction rates. Additionally, they proposed that MEPCMs could be combined with porous or honeycomb ceramics to create monolithic reactors with high heat storage density with thermostatic function. Subsequently, Nomura’s team expanded their research by preparing a series of MEPCMs using different alloys as cores [15–22]. This approach allowed them to create MEPCMs suitable for various working temperature and heat storage scenarios. To validate the properties of the MEPCMs, they conducted a demonstration experiment using packed-

bed reactor with MEPCMs pellets [23]. This comprehensive approach demonstrated the versatility and practical feasibility of their products across different thermal management requirements, such as waste heat recovery in the steel industry or battery thermal management in electric vehicles.

A growing number of researchers have shifted their focus from solid-liquid PCMs (S-L PCMs) to a unique category of solid-solid PCMs (S-S PCMs) [24]. These S-S PCMs are emerging as a promising alternative to S-L PCMs, offering several advantages: processability at solid state, negligible volume change during phase transitions, non-polluting characteristics, and long cycle lifetime. These properties make S-S PCMs particularly promising for applications in lithium-ion battery thermal management, solar thermal storage, building energy-saving, and other thermal energy storage research fields.

Currently, S-S PCMs are primarily classified into three categories: organic, inorganic, and hybrid. Despite their potential, these materials face significant challenges that hinder their practical application, such as relative low operating temperatures (~100 °C), low heat storage density (~100 kJ/kg).

1.2.3 Chemical heat storage (CHS)

Chemical heat storage (CHS) or thermochemical energy storage (TCES) is based on storing energy of chemical bond using reversible chemical reactions (Equation 1-4).

$$A + \Delta H_r \Leftrightarrow B + C \qquad (1-4)$$

In this process, a reactant A , undergoes decomposition into products B and C through an endothermic reaction, representing the energy charging step of CHS [25]. Typically, products B and C are stored separately to prevent a reverse reaction. During the energy discharging step, B recombines with C, releasing heat through an exothermic reaction. For one mol of the reaction described in Equation 1-4, the amount of stored heat can be

determined using the following equation:

$$Q = X\Delta H_r \qquad (1-5)$$

where X is the conversion ratio of reaction, and ΔH_r is the molar reaction enthalpy.

Compared to SHS and LHS, CHS offers several advantages, such as higher energy storage densities and minimal energy losses during long-term heat storage when product B and C are stored separately. Additionally, its broader operating temperature range (100 ℃–1000 ℃) provides engineers with the flexibility to select the most appropriate reaction for specific applications.

CHS reaction systems based on gas-solid reactions can be broadly classified according to the types of solid and gaseous reactants involved (Figure 1-3). These include metal sulfides (H_2O), metal hydrides (H_2), metal carbonates (CO_2), metal hydroxides (H_2O), and metal oxides (O_2). Among these, the metal oxide system is commonly referred to as the redox-type CHS system.

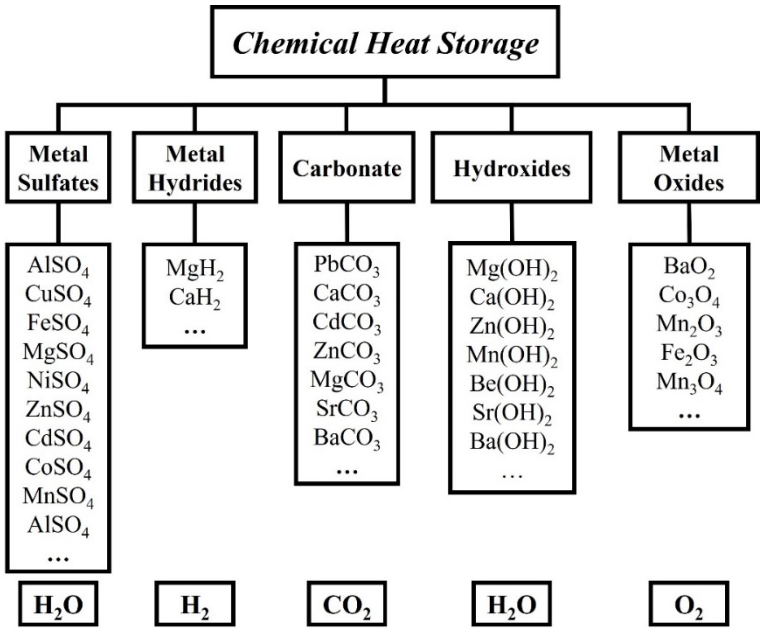

Figure 1-3 Classification of CHS systems

It is worth noting that, although some reactions fall within the aforementioned reaction systems, they may not be suitable for CHS applications for various reasons.

Here, we propose several criteria for screening suitable reaction systems for CHS applications:

A. Good reaction reversibility in both directions, without side reactions
B. High reaction enthalpy to maximize energy storage density
C. High durability to ensure stability during long-term heat storage periods
D. Rapid reaction rates and a reaction mechanism that is as simple as possible
E. Low raw material costs to facilitate cost-effective large-scale deployment

1.3 Concept of medium-high temperature redox-type CHS

1.3.1 Application of redox-type CHS in CSP systems

As discussed in the previous section, the international emphasis on Carbon Neutrality has driven the development of various energy storage technologies to enhance the efficient storage and utilization of renewable energy. Among these, thermal energy storage (TES) technology stands out for its wide application in renewable energy storage, offering the advantages of high energy storage density and long storage duration. These features are critical in mitigating the intermittency issues inherent to renewable energy sources.

Concentrated Solar Power (CSP) plant is a particularly promising renewable energy technology where thermal energy storage plays an important role. Unlike photovoltaic (PV) systems, CSP generates electricity by focusing sunlight with reflectors (e.g., parabolic trough, heliostats) (Figure 1-4a [26]) onto a collector. This collector converts sunlight into high-temperature thermal energy, which then powers a steam turbine or other heat engines to generate electricity (Figure 1-4b [27]). Thermal energy storage is a core component of CSP systems, ensuring stable power generation by storing excess heat. This

technology also enables continuous power generation at night, effectively addressing the intermittent issue of solar power. In recent years, researchers have explored coupling CSP's thermal energy storage component with other renewable energy systems, such as PV and wind power, to achieve energy sources complementarity [28,29].

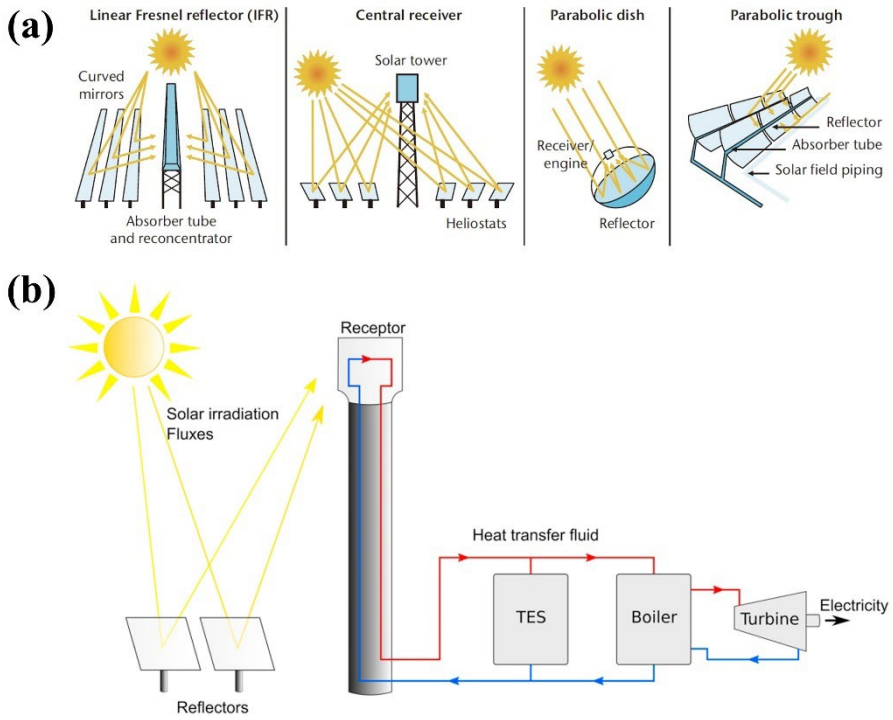

Figure 1-4 (a) Main reflector technology for CSP; (b) CSP plant with a TES system

In the previous Section 1.2, three types of TES technology were introduced: sensible (SHS), latent (LHS) and chemical heat storage (CHS). Currently, most commercial CSP systems utilize molten salt as the heat storage medium. This choice is driven by molten salt (typically a mixture of sodium nitrate and potassium nitrate) advantages, including high heat storage density (high specific heat capacity) and cost-effective. However, this technology also faces several significant technical challenges:

- **High-temperature decomposition:** Molten salts decompose at temperatures above 600°C, limiting the maximum operating temperature of CSP systems and

thereby reducing their overall power generation efficiency (Equation 1-1).

- **Solidification at low temperatures**: Molten salts tend to solidify at lower temperatures, which can cause pipeline blockages and system downtime.
- **Equipment corrosion**: At high temperatures, molten salts are highly corrosive to storage tanks, pipelines, and heat exchangers, significantly increasing system maintenance costs.

To further advance CSP technology, the development of new TES technologies that can operate stably at higher temperatures is essential. It will help the current limitations of molten salt and improve the overall efficiency and reliability of CSP systems. In recent years, LHS technologies utilizing metals or metal alloys have been proposed as new heat storage solutions for next-generation CSP systems [30]. However, LHS technologies based on microencapsulated phase change materials still face significant technical challenges including high costs, low heat transfer efficiency, leakage, and severe subcooling problem after encapsulation.

To overcome these challenges, researchers have introduced reversible reduction-oxidation reaction of metal oxides for TES purposes in CSP systems, also known as redox-type CHS technology [31–34]. This innovative approach offers potential for addressing the limitations of existing SHS and LHS technologies while enhancing the efficiency and reliability of CSP systems.

Redox-type CHS technology is based on the redox reactions of metal oxides (Figure 1-5). During the heat storage process (charging), the metal oxide in oxidized state (MO_{ox}) undergoes reduction, transitioning to its reduced state (MO_{re}) while releasing oxygen from its lattice and absorbing heat from environment. During the heat release process (discharging), the reduced state reacts with oxygen again to release the stored heat. The most representative reaction for redox-type CHS technology is the redox reaction based on cobalt oxides:

$$Co_3O_4 + \Delta H_r \rightleftharpoons 3CoO + 1/2O_2 \qquad (1-6)$$

Theoretically, redox-type CHS does not require a storage tank for gas products, as oxygen can be absorbed from or released into the atmosphere. In this case, air serves as both the reactant and the heat transfer fluid, offering significant advantages in terms of better energy utilization efficiency, reduced reactor volume and improved economic feasibility.

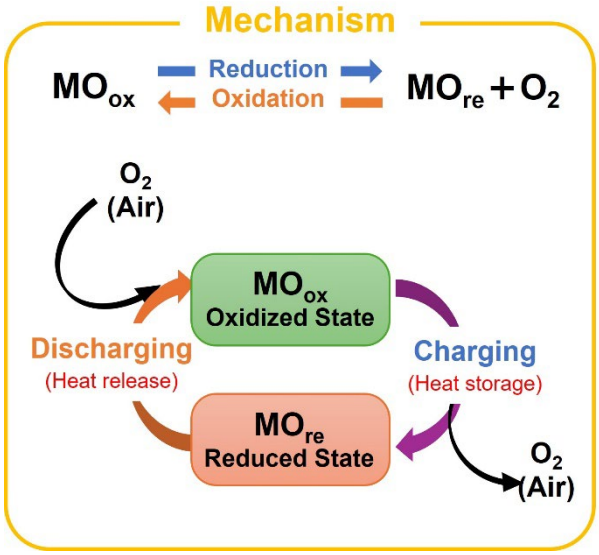

Figure 1-5 Mechanism of redox-type CHS technology

1.3.2 Application of redox-type CHS in heat recovery for Japan's heavy industry

When focusing on the research background in Japan, it becomes clear that, due to the geographical constraints, no demonstrative CSP projects have been established inside the country. However, this does not imply that redox-type CHS technology lacks applications prospects in Japan.

In Japan, as a major industrial country, energy recovery in the industrial sector is one

of the most important ways for it to achieve its goal of Carbon Neutrality. We can know from Figure 1-6 that the heavy industry in Japan emits at least 32 PJ (>500 ℃) of exhaust gas per year [35].

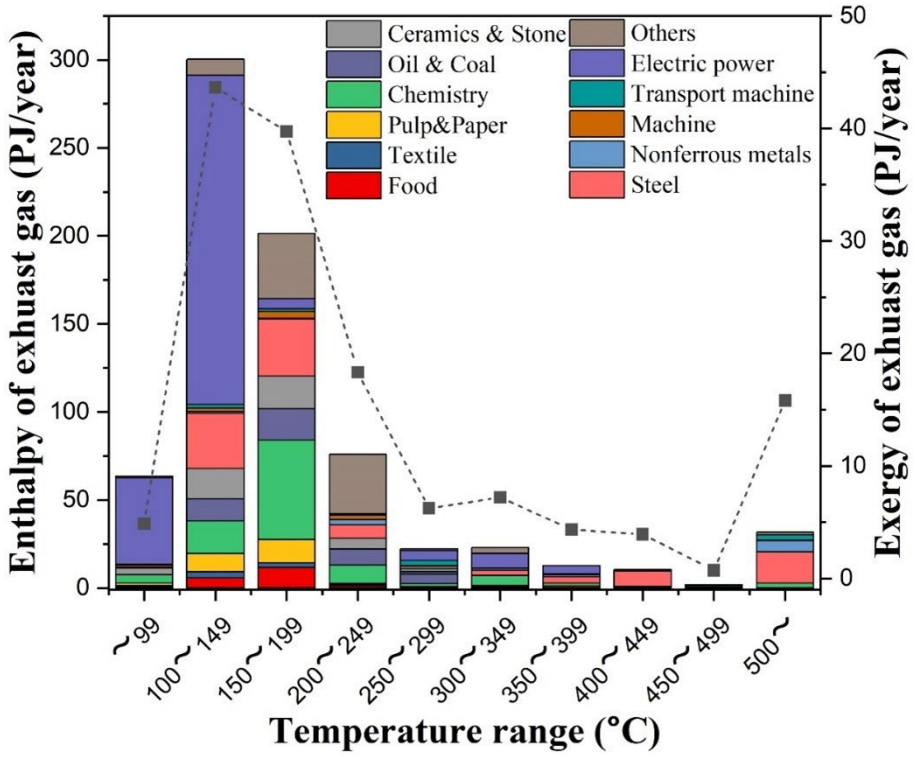

Figure 1-6 Estimation of enthalpy and exergy of exhaust gas by industrial category and temperature range (Japan, 2019)

In the temperature range of 100–200 °C, waste heat can typically be efficiently recovered and recycled through hot water or steam heat exchange . However, heat recovery becomes significantly more challenging when waste heat temperatures exceed 500 °C. This difficulty arises from two primary technical constraints:

1. **Insulation Challenges:** The performance of insulation materials deteriorates markedly at high temperatures, resulting in substantial heat loss. As temperature increases, maintaining effective thermal barriers becomes progressively more complex.

2. **Heat Transfer Fluid Limitations:** Conventional heat transfer fluids like water or oil become unsuitable at extreme temperatures due to potential evaporation and risk of thermal decomposition

Consequently, in industries such as steel and non-ferrous metals processing, medium- and high-temperature waste heat (typically above 500 °C) is frequently released directly into the atmosphere without meaningful recovery.

We believe that the redox-type CHS technology offers a unique advantage for heat recovery of heavy industry. The most favorable feature of redox-type CHS technology is its ability to allow the heat storage material to come into direct contact with medium-high temperature industrial waste heat, enabling efficient heat exchange and recovery. When the stored heat needs to be released, fresh air is all that required to drive the oxidation reaction, releasing the stored heat. In this process, the air serves as both reactant and heat transfer fluid, facilitating efficient energy exchange and significantly enhancing the overall efficiency of the system. Furthermore, since the oxygen concentration of industrial waste heat is typically lower than that of the atmosphere (0.21 atm), this property effectively reduces the maximum working temperature of the system. It also reduces the additional costs associated with insulation requirements, thereby improving the system's economic feasibility and operational simplicity.

However, research on redox-type CHS technology is still in its early stages, with significant challenges remaining. Currently, there is a notable lack of new redox-type CHS materials that exhibit high reactivity, high heat storage density, and low raw material costs. Moreover, much of the existing research has focused primarily on the heat storage materials themselves, without systematically addressing several critical aspects, including comprehensive evaluation of reaction kinetics, molding and module design of heat storage materials, reactor design and experimental validation, and optimization of overall redox-type CHS system.

From the next section, we will review the latest research progress in the design of heat

storage materials and reactors for redox-type CHS technology. Additionally, we will discuss the key bottlenecks currently faced by this field and propose a potential research direction.

1.4 Research progress in redox-type CHS materials

As we introduced above, redox-type CHS relies on the reduction-oxidation reactions of metal oxides (Equation 1-7).

$$MO_{ox}(s) + \Delta H_r \Leftrightarrow MO_{re}(s) + O_2(g) \qquad (1-7)$$

In the early stages of research, the thermodynamics, kinetics, and reversibility of the BaO_2/BaO [36], and CuO/Cu_2O [37] redox couples were initially investigated. Subsequently, additional redox couples were analyzed by the American company General Atomics [38]. However, many of these redox couples were recognized unsuitable for CHS applications due to several limitations, including extremely low working temperatures (e.g., Cr_5O_{12}, Li_2O_2, MgO_2), extremely high working temperatures (V_2O_5), toxicity (e.g., U_2O_3, PbO_2), lack of redox reversibility (e.g., Sb_2O_5, MnO_2), and high cost (e.g., PtO_2, Rh_2O_3).

As a result, the redox couples BaO_2/BaO, CuO/Cu_2O, Co_3O_4/CoO, Fe_2O_3/Fe_3O_4, and Mn_2O_3/Mn_3O_4 have emerged as the most promising candidate in the redox-type CHS field. Currently, research on redox-type CHS materials is mainly based on these types of typical redox reaction, where crystal structure modulation (e.g., transformation to spinel, perovskite, and brownmillerite structures) is achieved by elemental doping. This approach aims at optimizing key performance parameters of materials, such as reaction temperature, reaction rate, and heat storage density.

In the following subsections, the progress made in the development of materials based

on these redox couples will be discussed, highlighting their advancements and potential for CHS applications.

1.4.1 BaO_2/BaO and Ba-based redox couples

In 1977, Ervin firstly investigated the redox transition between BaO_2 and BaO for CHS applications [39]. This redox couple exhibits a unique behavior that the Ba^+ cation does not involve in the valence change. Instead, the electron transfer occurs in the anion site, transforming from peroxide (O_2^{2-}) to oxide (O^{2-}). Experimental results demonstrated that BaO_2/BaO is an interesting candidate with moderate heat storage density (474 kJ/kg), elemental abundance (Ba is the 14th most abundant element in the Earth's crust), and moderate working temperature (charging at about 800 ℃, and discharging at 600–700 ℃).

However, there are also challenges associated with this redox system. The reduced state, BaO, readily reacts with atmospheric CO_2 and H_2O, leading to potential material degradation issues [40]. Moreover, a study by Fahim's research group investigated the reversibility of 20 charge/discharge cycles of BaO_2/BaO [36]. Their results revealed a loss of cyclability, identified by progressive conversion decay with each cycle. Full conversion for redox was achieved only during the initial cycle. This issue was attributed to the formation of a BaO_2 layer during the oxidation of BaO, which likely hinders further reaction.

Doping with Sr and Mg has shown potential for enhancing heat storage properties of BaO_2/BaO redox system. Chen et al. [41,42] reported a single-phase, three-element alkaline-earth oxide, (BaSrMg)O, which demonstrated promising characteristics for chemisorption and oxygen separation applications. This material exhibited rapid oxygen adsorption (oxidation) and desorption (reduction) and higher adsorption capacity which significantly exceeding that of plain BaO_2/BaO, suggesting a greater weight change during the redox reaction and, consequently, a higher heat storage density. However, the material was found to be easy to form (BaSrMg)CO_3 in the presence of CO_2 in air. This

side-reaction leads to gradual deactivation of the material during cycling, posing a challenge for its long-term stability when air is used as the working fluid.

Perovskite and double-perovskite type material based on Ba are also potential candidates for redox-type CHS applications. Mueller et al. [43,44] synthesized and studied $Ba_{0.5}Sr_{0.5}Co_{0.8}Fe_{0.2}O_{3-\delta}$, a type of perovskite material, providing a detailed analysis of the effects of temperature and oxygen partial pressure on the oxygen non-stoichiometric reactions from a materials science perspective. Motohashi et al. [45,46] developed a double perovskite structure, $BaYMn_2O_{5+\delta}$, as oxygen storage material and explored its potential applications in areas such as oxygen separation and flame-free combustion. This material demonstrated good reactivity and moderate reaction temperature, indicating potential for practical application. However, the heat storage density based on its non-stoichiometric reaction remains unclear. Further research is necessary to evaluate its practical performance and validity in CHS applications.

1.4.2 CuO/Cu_2O and Cu-based redox couples

CuO/Cu_2O was first introduced as a candidate for CHS applications in the early 1980s. While it has not been extensively studied as other redox systems, it offers a high heat storage density (811 kJ/kg), making it an attractive option for CHS research. However, this redox couple faces several significant challenges that limit its practical application.

One major issue is the high operating temperature required for the transition from CuO to Cu_2O, which occurs at approximately 1120 ℃ under atmosphere. Additionally, the narrow working temperature range, defined by the melting point of Cu_2O at 1232 ℃, poses constraints [38], [47]. The small temperature window implies that the reactor must maintain extremely homogeneous temperature profiles to avoid localized hot spots and temperature gradient, which could lead to the melting of Cu_2O.

Studies have investigated the cyclability and kinetics of the CuO/Cu_2O redox couple. Chadda et al. [37] assessed its durability over 20 redox cycles and found it to exhibit high

stability. They also analyzed the reaction kinetics, reporting an activation energy of 332 kJ/mol for the reduction of CuO and 85 kJ/mol for the oxidation of Cu_2O.

Efforts to lower the reduction temperature include the use of an inert atmosphere or vacuum environment, which can effectively decrease the temperature requirements. However, these approaches introduce additional energy consumption, which must be considered when evaluating the overall efficiency of the CHS system. Another strategy involves element doping to adjust the working temperature. For example, Block et al. [47] explored Cu-based solid solutions, including Cu-Co, Cu-Cr, and Cu-Fe. Although doping successfully reduced the working temperature, the resulting materials exhibited lower heat storage densities due to the contributions of the additional elements, reducing their appeal.

In addition, some studies have been conducted to improve the heat storage and release performance during sintering by directly optimizing the transferability of lattice oxygen. Liu et al. developed a Cu-Ce heterogeneous interface by Ce doping through the concept of lattice matching. Their study demonstrated that this material retained 98% to 100% of its initial cycling performance even after 600 cycles, a remarkable improvement compared to pure CuO, which maintained only about 40% of its initial performance under the same conditions. These findings suggest excellent potential for the Cu-Ce oxides in advancing CHS applications, particularly in systems requiring high cycling stability.

While CuO/Cu_2O and Cu-based redox couples show potential for CHS applications due to their high heat storage density and low cost, the challenges of its relatively high working temperature and sintering issues must be addressed before it can be widely applied in CHS systems.

1.4.3 Co_3O_4/CoO

With a high heat storage density of 884 kJ/kg and an appropriate working temperature of 900 °C, Co_3O_4/CoO redox couple are highly attractive candidate for CHS applications.

However, the Co_3O_4/CoO has two significant drawbacks. First, the cost of cobalt oxides is substantially higher than that of other material for CHS purposes, with cobalt priced at $58.5 per kilogram compared to $2.06 per kilogram for manganese [48]. Additionally, cobalt ore reserves are geographically concentrated in a few countries, with the Democratic Republic of Congo, China, and Finland being the main exporters. Which raises concerns about supply chain stability and resource availability. Second, cobalt oxides are highly toxic, and there is evidence suggesting their carcinogenicity [49].

To date, most researchers have focused on assessing the heat storage density, reaction kinetics, and reversibility of Co_3O_4/CoO. While the oxidation rate of CoO is significantly faster than that of many other redox couples, it remains the slowest step in the cycle. Notably, the isothermal oxidation of CoO at 860 ℃ can take up 2 h for complete [50]. This prolonged reaction time highlights a key limitation in the kinetics of the Co_3O_4/CoO, despite its overall favorable properties for chemical heat storage.

Agrafiots et al. [50] synthesized Zu, Cu, Mg, Ni-doped Co_3O_4 via solids-state method. Thermogravimetric redox experiments on these doped Co oxides revealed that none of the materials demonstrated significant improvements compared to the plain Co_3O_4/CoO redox system. Similarly, Carrillo et al. [31] evaluated Mn-doped Co oxides, but the results showed that the Mn-doped presented slower reaction rates and lower heat storage density. André et al. [51] revisited Co-Fe mixed oxides, finding that the addition of 5% Fe improved performance. However, further increases in Fe content raised the reduction temperature, as predicted by Co-Fe-O phase diagrams. Tamayo et al. [52] studied redox reactions of Cu-Co spinels, with a detailed analysis of surface cationic distribution via XPS measurement. They claimed that the presence of Cu^+ on tetrahedral positions favored the oxygen release during the reduction step.

Additionally, some studies have shown that small amount of Ni [53,54] and Mg [55,56] doping can form a solid solution within Co_3O_4, effectively lowering the reaction temperature of Co_3O_4/CoO redox couple without altering its crystal structure. For

instance, $Co_{2.8}Mg_{0.2}O_4$ exhibited a reduction onset temperature of 775.6 ℃, which is significantly lower than ~900 ℃ of Co_3O_4.

The performance of Co_3O_4/CoO can also be enhanced through shaping and morphological modifications. Agrafiots et al. [57] investigated the behavior of porous ceramic structure (foams and honeycombs), made from Al_2O_3, ZrO_2, SiC, cordierite, which were coated with Co_3O_4. These structures are advantageous for heat exchange due to their high surface area and porosity. The redox behavior of Co_3O_4-coated ceramic foams and honeycombs were evaluated using thermogravimetric analysis over multiple cycles. Among these, Co_3O_4-coated cordierite foam exhibited a stable reversibility behavior over 100 charge/discharge cycles, demonstrating its potential for long-term CSP applications. More recently, Liu et al. [58] prepared Co_3O_4/CoO with a cubic micro-nanostructure and they found that morphology of commercial Co_3O_4/CoO sintered completely while that of the cubic oxide retains the approximate shape of a cube. Furthermore, the thermal hysteresis was reduced by cubic micro-nanostructure modification.

1.4.4 Fe_2O_3/Fe_3O_4

Fe_2O_3/Fe_3O_4 redox couple is among the lease studied systems in redox-type CHS, primarily due to the extremely high temperatures (~1400 ℃) required for reduction of Fe_2O_3. Experimental studies have shown that this redox couple has a heat storage density of 600 kJ/kg [48].

Efforts to lower the reduction temperature through element doping, such as with Co, Cu, or Mn, have been proven effective. However, this approach often comes with the drawback of reduced heat storage density [48]. Among the doped systems, Fe_2O_3/Fe_3O_4 with 33% Cu-doping exhibited a faster reduction and oxidation rate which occurring at temperature around 1040 ℃ with reaction enthalpy of 330 kJ/kg.

It is also worth mentioning that Fe oxides have been extensively studied for

thermochemical hydrogen production (thermochemical water splitting) over the past few decades, with significant contributions from research group such as those led by Weimer [59], [60] and Kodama [61]. These studies underline the versatility of Fe oxides, not only as heat storage materials but also for hydrogen generation, expanding their potential applications in energy systems.

1.4.5 Mn_2O_3/Mn_3O_4 and Mn-based redox couples

Due to the multivalent properties of manganese and the abundance of manganese ores (12th most abundant element in the Earth's crust), Mn oxides have emerged as promising candidates for redox-type CHS applications. The manganese oxide transitions, from low to high temperatures, include MnO_2, Mn_2O_3, Mn_3O_4, and MnO.

The low-temperature transition of MnO_2/Mn_2O_3 (~500 ℃) has been experimentally confirmed to lack reversibility [62]. A research team from the Australian National University (ANU) has proposed the Mn_2O_3/MnO redox cycle for CHS purposes. This cycle operates at high temperatures and involves a two-step process. First, Mn_2O_3 transforms into Mn_3O_4 at approximately 950 ℃ with a heat storage density of 202 kJ/kg. Subsequently, Mn_3O_4 is reduced to MnO at an extremely high temperature of 1500 ℃, releasing a significant enthalpy change of 897 kJ/kg [63]. However, the reversibility of the MnO to Mn_3O_4 has not yet been reported in the literature.

Based on the reasons mentioned above, the most attractive redox couple in Mn-oxides is Mn_2O_3/Mn_3O_4, which exhibits more moderate working temperature and reversibility compared to other Mn-based transitions. During the phase transition from Mn_2O_3 to Mn_3O_4, manganese undergoes an oxidation state transition from +3 in the oxidized state to an average of +2.67 in the reduced state.

However, the Mn_2O_3/Mn_3O_4 redox couple has notable drawbacks. It has the lowest heat storage density among all redox couples proposed for CHS application and suffers from slow oxidation reaction rate. Material degradation due to particle sintering can also reduce

efficiency or cyclability. Additionally, the large thermal hysteresis (~200 °C) limits the operational temperature range and lowers heat storage efficiency (η_{ex}) compared to Co_3O_4/CoO, which has a smaller hysteresis (30–50 °C)

Carrillo et al. [64] studied the impact of initial particle size on the cyclability of Mn_2O_3/Mn_3O_4. They synthesized Mn_2O_3 with different initial particle sizes by adjusting the Mn precursor concentration during the precipitation using ammonia. Their findings showed that Mn oxides with low initial particle size (<88 nm) and high surface area experienced a complete loss of cyclability after just two redox cycles. This failure was attributed to a high degree of sintering.

Several cationic dopants have been proposed for chemical modification of Mn_2O_3/Mn_3O_4 to improve their performance. However, the additions of Co and Al were found to hinder rather than enhance the re-oxidation of Mn_3O_4 [48], [31]. On the other hand, Cu-doping has shown promising results, allowing the reduction temperature to be lowered to 915 °C with 3-5% or 10% Cu incorporation [48].

Fe-doping has proven to be one of the most effective methods to improve the performance of Mn_2O_3/Mn_3O_4. Carrillo et al. [65] evaluated Fe-doping at levels ranging from 1 to 40 mol%, finding that Fe-doped Mn oxides exhibited faster oxidation rates. This improvement led to more stable cycle stability, narrower thermal hysteresis, and larger heat storage density. Further research by Carrillo's research group identified the optimal performance for a 20% Fe-doped Mn oxide synthesized via a modified Pechini method. This material showed a slightly higher reduction temperature (995 °C) compared to pure Mn oxides, but it also demonstrated narrower hysteresis (ΔT = 113 °C), higher heat storage density, and improved cyclability of 75 cycles [66].

Additionally, the redox kinetics of $(Mn_{0.8}Fe_{0.2})_2O_3$/$(Mn_{0.8}Fe_{0.2})_3O_4$ couple were studied using TGA isothermal experiments, revealing that both reduction and oxidation reactions followed a nucleation and growth kinetic mechanism [66].

Recently, Wokon et al. [67] conducted a detailed thermodynamic and kinetic analysis

of $(Mn_{0.75}Fe_{0.25})_2O_3/(Mn_{0.75}Fe_{0.25})_3O_4$ redox couple using both thermobalance and a fixed-bed reactor. They reported the highest heat storage density for Fe-doped Mn oxides at 271 kJ/kg, along with remarkably stable redox reversibility over 100 cycles.

A novel redox couple based on Li-Mn spinels has been proposed by Varsano et al. [32], demonstrating an experimental heat storage density of approximately 200 kJ/kg. The reduction of Li-Mn spinels occurred at 970 ℃, while oxidation reaction began at 886 ℃, resulting in a narrow thermal hysteresis gap. However, considering the high cost of lithium, Li-Mn spinels may not be suitable for large-scale applications despite their promising performance characteristics.

In summary, Fe-doped Mn_2O_3/Mn_3O_4 stands out as one of the most promising redox couples for CHS applications. This is attributed to the abundance of the raw materials, their nontoxicity, low cost, moderate heat storage density, fast redox kinetics, and excellent cyclability.

1.4.6 Short summary of progress in redox-type CHS materials and bottlenecks

In the above sections, we discussed the prospects of BaO_2/BaO, CuO/Cu_2O, Co_3O_4/CoO, Fe_2O_3/Fe_3O_4, and Mn_2O_3/Mn_3O_4 redox couple as potential materials for CHS applications, along with the progress made in these material's research. To further analyze the characteristics of these materials, their operating temperatures and theoretical heat storage densities are plotted in Figure 1-7. From the figure, it can be observed that the reaction temperatures of most of the current potential redox couple (highlighted with blue color) are close to 1000 ℃. In addition, BaO_2/BaO was excluded from the analysis due to its reactivity with CO_2 in air, which makes it unsuitable for practical applications.

While higher operating temperatures improve energy utilization efficiency, they also introduce challenges in practical heat storage applications, including increased equipment design complexity and costs. Lower operating temperatures, on the other hand, can suit a broader range of application scenarios and reduce overall system costs.

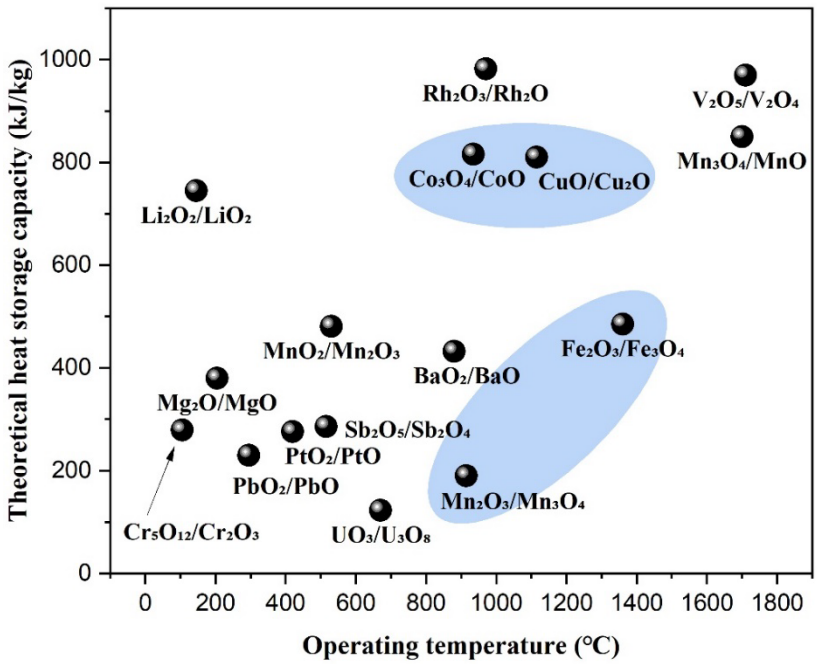

Figure 1-7 Operating temperature and theoretical heat storage capacity of common single-metal-oxides for CHS system

Despite significant research into redox-type CHS materials development, there has been relatively little focus on the development of materials that can operate effectively at lower temperatures.

As described in Section 1.4.3, there is research demonstrating that the doping small amounts of Mg and Ni into Co_3O_4/CoO redox system can effectively reduce the reaction temperature. However, the high cost of cobalt has significantly hindered the widespread adoption of this technology. Consequently, the development of a low-cost redox-type CHS material capable of stable operation at lower temperatures has become an urgent challenge for advancing the practical applications of redox-type CHS technology.

1.5 Research progress in redox-type CHS reactors

Over the past few decades, various reactor designs have been developed to accommodate different heat storage material shapes since redox-type CHS technology

was proposed for medium-high temperature heat storage. Among these designs, the packed-bed reactor is one of the most common, using granular heat storage materials as the core component [67–70].

In an early study of this technology, Wokon et al. [67] conducted laboratory-scale validation using a packed-bed reactor filled with granular manganese-iron oxides. The experimental results demonstrated the feasibility of this redox-based heat storage concept, highlighting several advantages: direct heat transfer between the heat storage material and heat transfer fluid, and the operational flexibility of an open system. These characteristics make this technology highly promising for practical applications.

However, the study also revealed a significant challenge: severe sintering occurred between the granular heat storage material after just 17 cycles (Figure 1-8). This issue poses a serious challenge to the long-term operational stability of the whole system. This issue not only reduced the heat storage material's performance but also caused high-pressure-drop problems inside the reactor because most fluid flow paths are blocked.

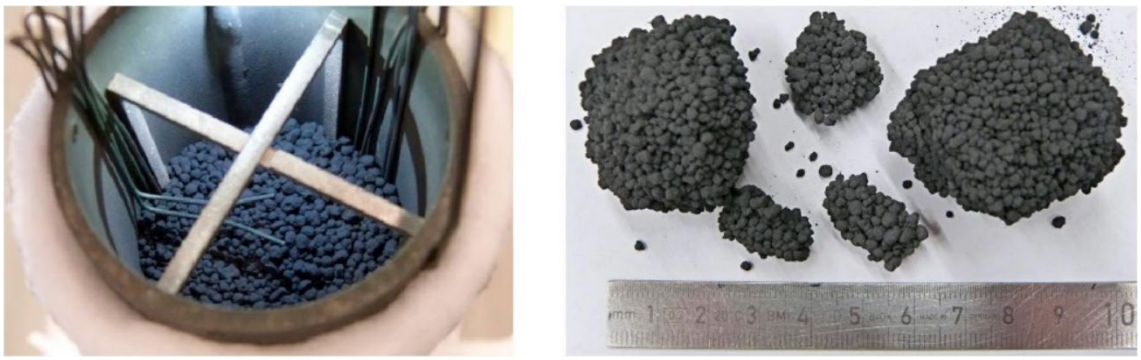

Figure 1-8 (left) View of manganese-iron oxide granulate in the reaction chamber prior to cycling; (right) Agglomerated heat storage material after 17 redox cycles in air

Sintering is a common issue not only in packed-bed reactors using manganese-iron oxide granulate but also in other types of materials. Gigantino et al. [69] addressed this problem by synthesizing porous copper-oxide-based granulate with yttria-stabilized-

zirconia (YSZ) as a sintering inhibitor. Their study verified the heat storage and release performance of the YSZ-added granulate, showing that YSZ effectively enhanced sintering resistance to some extent. However, even with the addition of YSZ, significant sintering of the heat storage material granulate was observed after 30 cycles.

Although some researchers have proposed the use of granular flow reactor and tubular falling bed reactors with flowing granulate to minimize particle sintering [70,71], the high design and manufacturing costs of these reactors limit their feasibility. As a result, this study will focus on the design and optimization of fixed-bed reactors, which offer a more cost-effective and practical solution for redox-type CHS systems.

For fixed-bed reactors, porous foam structures and honeycomb structures with regular channels show great promise. Typically, heat storage material is coated to the surface of the porous foam or honeycomb structure. However, this approach has a significant drawback: the limited coating capacity of the heat storage material results in a low heat storage density. An alternative approach involves directly preparing the porous form or honeycomb structure from the heat storage material itself. This design has the potential to significantly enhance the heat storage density. However, a major challenge lies in maintaining the mechanical strength of these structures while ensuring high reactivity during the heat storage and release processes.

1.6 Main contents and targets in this study

In this study, we propose integrated research on redox-type chemical heat storage system targeting medium-high temperature ranges (500–1000 °C) (Figure 1-9). The initial focus was on developing a redox-type chemical heat storage material capable of operating in this temperature range. Based on this material, heat storage modules and reactor systems were designed to enable rapid heat storage and release, addressing the diverse needs of industrial and residential application in this temperature range.

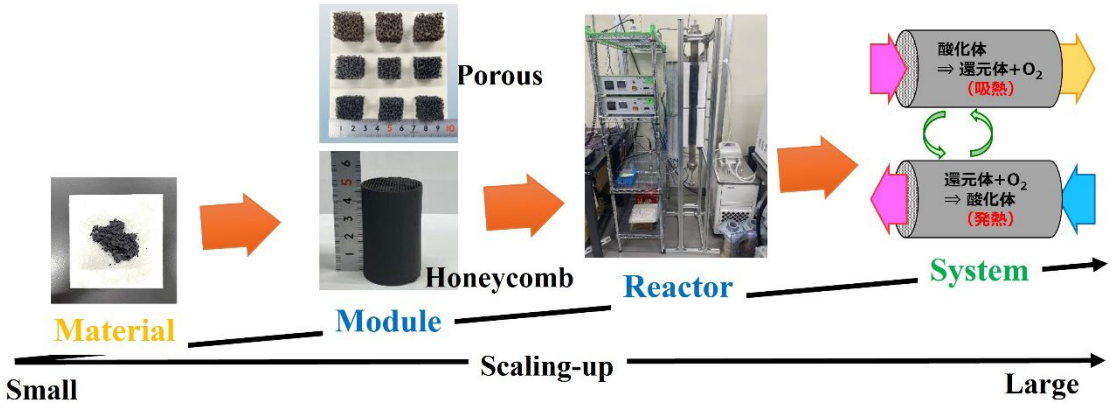

Figure 1-9 Integrated research on redox-type chemical heat storage system

In the following Chapter 2, we investigated the potential of Sr-based perovskite/brownmillerite for achieving rapid heat storage and release in the medium-high temperature range. Their reactivity, heat storage density, and durability are comprehensively evaluated.

In Chapter 3, we shifted our focus to Cu-based spinel/delafossite for heat storage applications. Our findings indicate that $CuMn_2O_4/CuMnO_2$ exhibit moderate heat storage density, good reactivity, and excellent durability. Notably, the reduced state ($CuMnO_2$) can also undergo re-oxidation below 500 °C, releasing the stored heat.

In Chapter 4, we explored the effect of Cr-doping at the B-site of $CuMn_2O_4/CuMnO_2$ on material's properties, such as reaction temperature, reaction rate, and heat storage density.

In Chapters 5 and 6, kinetic studies were conducted for plain and Cr-doped $CuMn_2O_4/CuMnO_2$, respectively, to establish their corresponding reaction kinetic models.

In Chapter 7, we used machine learning approaches integrated with DFT calculations to systematically evaluate the effects of nearly all elements from the periodic table at the A- and B-sites of $CuMn_2O_4/CuMnO_2$. This method effectively identifies potential dopants that could further reduce the reaction temperature of the material.

In Chapter 8 and 9, we developed two types of heat storage modules based on $CuMn_2O_4/CuMnO_2$: porous foam structure and honeycomb structure module. Their practical application potential is evaluated through experimental testing. Furthermore, we designed a tubular furnace reactor for honeycomb structure heat storage module, demonstrating its capability for efficient heat storage and release in the medium-high temperature range.

In Chapter 10, I highlighted the concept of data circulation and its broad applicability to chemistry-related fields. This chapter also reflects my contributions to the Graduate Program for Real-world Data Circulation Leaders.

Finally, in Chapter 11, we summarized the research findings and discussed the prospects of chemical heat storage technologies. Key unresolved challenges in this field were analyzed, with some recommendations for advancing technology.

Reference

[1] United Nations Framework Convention on Climate Change (UNFCCC), Paris Agreement, (2015). https://unfccc.int/sites/default/files/english_paris_agreement.pdf.

[2] International Renewable Energy Agency, Global energy transformation: a roadmap to 2050, 2019. https://www.irena.org/publications/2019/Apr/Global-energy-transformation-A-roadmap-to-2050-2019Edition.

[3] World Energy Council, World Energy Resources E-storage: Shifting from cost to value Wind and solar applications, (2016). https://www.worldenergy.org/assets/downloads/Resources-E-storage-report-2016.02.04.pdf.

[4] IEA, Renewables 2023, (2024). https://www.iea.org/reports/renewables-2023.

[5] O. Dumont, G.F. Frate, A. Pillai, S. Lecompte, M. De paepe, V. Lemort, Carnot battery technology: A state-of-the-art review, Journal of Energy Storage 32 (2020).

https://doi.org/10.1016/j.est.2020.101756.

[6] T. Liang, A. Vecchi, K. Knobloch, A. Sciacovelli, K. Engelbrecht, Y. Li, Y. Ding, Key components for Carnot Battery: Technology review, technical barriers and selection criteria, Renewable and Sustainable Energy Reviews 163 (2022) 112478. https://doi.org/10.1016/j.rser.2022.112478.

[7] A.J. Carrillo, J. González-Aguilar, M. Romero, J.M. Coronado, Solar Energy on Demand: A Review on High Temperature Thermochemical Heat Storage Systems and Materials, Chemical Reviews 119 (2019) 4777–4816. https://doi.org/10.1021/acs.chemrev.8b00315.

[8] L.A. Weinstein, J. Loomis, B. Bhatia, D.M. Bierman, E.N. Wang, G. Chen, Concentrating Solar Power, Chemical Reviews 115 (2015) 12797–12838. https://doi.org/10.1021/acs.chemrev.5b00397.

[9] M. Liu, N.H. Steven Tay, S. Bell, M. Belusko, R. Jacob, G. Will, W. Saman, F. Bruno, Review on concentrating solar power plants and new developments in high temperature thermal energy storage technologies, Renewable and Sustainable Energy Reviews 53 (2016) 1411–1432. https://doi.org/10.1016/j.rser.2015.09.026.

[10] X. Zhou, S. Liao, S. Yamashita, M. Kubota, A. Takeuchi, P. Gao, M. Liu, R. Li, C. Zhang, H. Kita, Enhanced radiation heat transfer performance of Alumina-Spinel composite sphere with hollow structure for rapidly ultra-high temperature thermal storage/release process, Chemical Engineering Journal 479 (2024) 147381. https://doi.org/10.1016/j.cej.2023.147381.

[11] S. Liao, X. Zhou, X. Chen, F. Bao, H. Zhang, S. Yamashita, H. Kita, Development of rice husk composite ceramic sphere with enhanced radiation heat transfer for rapid heat storage and release at high temperature, Ceramics International (2024) S0272884224030475. https://doi.org/10.1016/j.ceramint.2024.07.167.

[12] A. Gil, M. Medrano, I. Martorell, A. Lázaro, P. Dolado, B. Zalba, L.F. Cabeza, State of the art on high temperature thermal energy storage for power generation. Part 1-

Concepts, materials and modellization, Renewable and Sustainable Energy Reviews 14 (2010) 31–55. https://doi.org/10.1016/j.rser.2009.07.035.

[13] S. Kuravi, J. Trahan, D.Y. Goswami, M.M. Rahman, E.K. Stefanakos, Thermal energy storage technologies and systems for concentrating solar power plants, Progress in Energy and Combustion Science 39 (2013) 285–319. https://doi.org/10.1016/j.pecs.2013.02.001.

[14] T. Nomura, C. Zhu, N. Sheng, G. Saito, T. Akiyama, Microencapsulation of Metal-based Phase Change Material for High-temperature Thermal Energy Storage, Sci Rep 5 (2015) 9117. https://doi.org/10.1038/srep09117.

[15] T. Kawaguchi, J. Yoolerd, H. Sakai, Y. Shimizu, A. Kurniawan, T. Nomura, Modified preparation of Al2O3@Al microencapsulated phase change material with high durability for high-temperature thermal energy storage over 650 °C, Solar Energy Materials and Solar Cells 237 (2022) 111540. https://doi.org/10.1016/j.solmat.2021.111540.

[16] D. Ajito, A. Kurniawan, Y. Shimizu, R. Ishida, T. Kawaguchi, K. Dong, H. Sakai, T. Nomura, Functional surface modification of Al-Si@Al2O3 microencapsulated phase change material, Journal of Energy Storage 52 (2022) 104919. https://doi.org/10.1016/j.est.2022.104919.

[17] K. Dong, T. Kawaguchi, Y. Shimizu, H. Sakai, T. Nomura, Optimized Preparation of a Low-Working-Temperature Gallium Metal-Based Microencapsulated Phase Change Material, ACS Omega 7 (2022) 28313–28323. https://doi.org/10.1021/acsomega.2c02801.

[18] Y. Shimizu, T. Kawaguchi, H. Sakai, K. Dong, A. Kurniawan, T. Nomura, Al–Ni alloy-based core-shell type microencapsulated phase change material for high temperature thermal energy utilization, Solar Energy Materials and Solar Cells 246 (2022) 111874. https://doi.org/10.1016/j.solmat.2022.111874.

[19] J.C. Mba, H. Sakai, K. Dong, Y. Shimizu, M. Kondo, T. Nakamura, M. Jeem, T.

Nomura, Suppression of supercooling and phase change hysteresis of Al-25mass%Si Micro-Encapsulated Phase Change Material (MEPCM) synthesized via novel dry synthesis method, Journal of Energy Storage 94 (2024) 112066. https://doi.org/10.1016/j.est.2024.112066.

[20] T. Kawaguchi, M. Jeem, A. Kurniawan, K. Dong, M. Kondo, Y. Sato, T. Nakamura, T. Nomura, Composite phase change material based on Al alloy with durability of over 10,000 cycles for high-temperature heat utilization, Journal of Energy Storage 75 (2024) 109635. https://doi.org/10.1016/j.est.2023.109635.

[21] Y. Shimizu, S. Cho, T. Kawaguchi, K. Tanahashi, K. Dong, T. Nakamura, A. Kurniawan, M. Jeem, T. Nomura, Novel microencapsulated ternary eutectic alloy-based phase change material, Journal of Energy Storage 75 (2024) 109535. https://doi.org/10.1016/j.est.2023.109535.

[22] M. Jeem, R. Ishida, M. Kondo, Y. Shimizu, T. Kawaguchi, K. Dong, A. Kurniawan, Y. Kunisada, N. Sakaguchi, T. Nomura, Shell-Driven Localized Oxide Nanoparticles Determine the Thermal Stability of Microencapsulated Phase Change Material, ACS Appl. Mater. Interfaces 16 (2024) 3509–3519. https://doi.org/10.1021/acsami.3c17129.

[23] H. Koide, A. Kurniawan, T. Takahashi, T. Kawaguchi, H. Sakai, Y. Sato, J.Nw. Chiu, T. Nomura, Performance analysis of packed bed latent heat storage system for high-temperature thermal energy storage using pellets composed of micro-encapsulated phase change material, Energy 238 (2022) 121746. https://doi.org/10.1016/j.energy.2021.121746.

[24] M. Zhi, S. Yue, L. Zheng, B. Su, J. Fu, Q. Sun, Recent developments in solid-solid phase change materials for thermal energy storage applications, Journal of Energy Storage 89 (2024) 111570. https://doi.org/10.1016/j.est.2024.111570.

[25] L. Cabeza, Advances in Thermal Energy Storage Systems Methods and Applications 2nd Edition, Elsevier, 2020.

[26] IEA, Technology Roadmap Solar Thermal Electricity, (2015).

https://doi.org/10.1787/9789264238824-en.

[27] U. Pelay, L. Luo, Y. Fan, D. Stitou, M. Rood, Thermal energy storage systems for concentrated solar power plants, Renewable and Sustainable Energy Reviews 79 (2017) 82–100. https://doi.org/10.1016/j.rser.2017.03.139.

[28] J. Iñigo-Labairu, J. Dersch, T. Hirsch, S. Giuliano, M. Loevenich, D. Córdoba, Techno-Economic Evaluation of CSP–PV Hybrid Plants with Heat Pump in a Temperature Booster Configuration, Energies 17 (2024) 2634. https://doi.org/10.3390/en17112634.

[29] S. Liu, Y. Zhao, C. Yang, L. Ren, Research on optimal scheduling of "wind-PV-thermal-energy storage" system considering net output characteristics, in: 2024 3rd International Conference on Energy, Power and Electrical Technology (ICEPET), 2024: pp. 247–251. https://doi.org/10.1109/ICEPET61938.2024.10626248.

[30] D.S. Jayathunga, H.P. Karunathilake, M. Narayana, S. Witharana, Phase change material (PCM) candidates for latent heat thermal energy storage (LHTES) in concentrated solar power (CSP) based thermal applications - A review, Renewable and Sustainable Energy Reviews 189 (2024) 113904. https://doi.org/10.1016/j.rser.2023.113904.

[31] A.J. Carrillo, J. Moya, A. Bayón, P. Jana, V.A. De La Peña O'Shea, M. Romero, J. Gonzalez-Aguilar, D.P. Serrano, P. Pizarro, J.M. Coronado, Thermochemical energy storage at high temperature via redox cycles of Mn and Co oxides: Pure oxides versus mixed ones, Solar Energy Materials and Solar Cells 123 (2014) 47–57. https://doi.org/10.1016/j.solmat.2013.12.018.

[32] F. Varsano, C. Alvani, A. La Barbera, A. Masi, F. Padella, Lithium manganese oxides as high-temperature thermal energy storage system, Thermochimica Acta 640 (2016) 26–35. https://doi.org/10.1016/j.tca.2016.07.018.

[33] L. Imponenti, K.J. Albrecht, J.W. Wands, M.D. Sanders, G.S. Jackson, Thermochemical energy storage in strontium-doped calcium manganites for

concentrating solar power applications, Solar Energy 151 (2017) 1–13. https://doi.org/10.1016/j.solener.2017.05.010.

[34] E. Mastronardo, X. Qian, J.M. Coronado, S.M. Haile, The favourable thermodynamic properties of Fe-doped CaMnO3for thermochemical heat storage, Journal of Materials Chemistry A 8 (2020) 8503–8517. https://doi.org/10.1039/d0ta02031a.

[35] Thermal Management Materials and Technology Research Association, Survey of Exhaust Heat in the Industrial Sector, 2019.

[36] M. a Fahim, J.D. Ford, Energy storage using the BaO2/ BaO reaction cycle, The Chemical Engineering Journal 27 (1983) 21–28.

[37] D. Chadda, J.D. Ford, M.A. Fahim, Chemical energy storage by the reaction cycle CuO/Cu2O, International Journal of Energy Research 13 (1989) 63–73. https://doi.org/10.1002/er.4440130107.

[38] U.S.D. of Energy, Thermochemical Heat Storage for Concentrated Solar Power, Thermochemical System Reactor Design for Thermal Energy Storage, Industrial & Engineering Chemistry 19 (2011) 594–596.

[39] E. Guy, Solar Heat Storage Using Chemical Reactions, Journal of Solid State Chemistry 22 (1977) 51–61.

[40] C. Agrafiotis, M. Roeb, C. Sattler, Exploitation of thermochemical cycles based on solid oxide redox systems for thermochemical storage of solar heat. Part 4: Screening of oxides for use in cascaded thermochemical storage concepts, Solar Energy 139 (2016) 695–710. https://doi.org/10.1016/j.solener.2016.04.034.

[41] X. Chen, T. Jung, J. Park, W.S. Kim, Preparation of tunable (BaSrMg)O for oxygen chemisorption: Formation mechanism and characterization, Inorganic Chemistry 54 (2015) 5419–5425. https://doi.org/10.1021/acs.inorgchem.5b00454.

[42] X. Chen, T. Jung, J. Park, W.S. Kim, Preparation of single-phase three-component alkaline earth oxide of (BaSrMg)O: A high capacity and thermally stable chemisorbent

for oxygen separation, Journal of Materials Chemistry A 3 (2015) 258–265. https://doi.org/10.1039/c4ta05045b.

[43] D.N. Mueller, R.A. De Souza, T.E. Weirich, D. Roehrens, J. Mayer, M. Martin, A kinetic study of the decomposition of the cubic perovskite-type oxide BaxSr1-xCo0.8Fe0.2O 3-δ (BSCF) (x = 0.1 and 0.5), Physical Chemistry Chemical Physics 12 (2010) 10320–10328. https://doi.org/10.1039/c0cp00004c.

[44] D.N. Mueller, R.A. De Souza, H.I. Yoo, M. Martin, Phase stability and oxygen nonstoichiometry of highly oxygen-deficient perovskite-type oxides: A case study of (Ba,Sr)(Co,Fe)O 3-δ, Chemistry of Materials 24 (2012) 269–274. https://doi.org/10.1021/cm2033004.

[45] T. Motohashi, T. Ueda, Y. Masubuchi, M. Takiguchi, T. Setoyama, K. Oshima, S. Kikkawa, Remarkable oxygen intake/release capability of BaYMn2O 5+δ: Applications to oxygen storage technologies, Chemistry of Materials 22 (2010) 3192–3196. https://doi.org/10.1021/cm100290b.

[46] T. Motohashi, T. Takahashi, M. Kimura, Y. Masubuchi, S. Kikkawa, Y. Kubota, Y. Kobayashi, H. Kageyama, M. Takata, S. Kitagawa, R. Matsuda, Remarkable oxygen intake/release of BaYMn2O5+δ viewed from high-temperature crystal structure, Journal of Physical Chemistry C 119 (2015) 2356–2363. https://doi.org/10.1021/jp511648b.

[47] T. Block, M. Schmücker, Metal oxides for thermochemical energy storage: A comparison of several metal oxide systems, Solar Energy 126 (2016) 195–207. https://doi.org/10.1016/j.solener.2015.12.032.

[48] T. Block, M. Schmücker, Metal oxides for thermochemical energy storage: A comparison of several metal oxide systems, Solar Energy 126 (2016) 195–207. https://doi.org/10.1016/j.solener.2015.12.032.

[49] T. Block, N. Knoblauch, M. Schmücker, The cobalt-oxide/iron-oxide binary system for use as high temperature thermochemical energy storage material, Thermochimica Acta 577 (2014) 25–32. https://doi.org/10.1016/j.tca.2013.11.025.

[50] C. Agrafiotis, M. Roeb, M. Schmücker, C. Sattler, Exploitation of thermochemical cycles based on solid oxide redox systems for thermochemical storage of solar heat. Part 1: Testing of cobalt oxide-based powders, Solar Energy 102 (2014) 189–211. https://doi.org/10.1016/j.solener.2013.12.032.

[51] L. André, S. Abanades, L. Cassayre, High-temperature thermochemical energy storage based on redox reactions using Co-Fe and Mn-Fe mixed metal oxides, Journal of Solid State Chemistry 253 (2017) 6–14. https://doi.org/10.1016/j.jssc.2017.05.015.

[52] A. Tamayo, M.A. Rodríguez, C. Arroyo, J. Beltran-Heredia, F. Rubio, Dependence of the synthetic strategy on the thermochemical energy storage capability of CuxCo3-xO4 spinels, Journal of the European Ceramic Society 38 (2018) 1583–1591. https://doi.org/10.1016/j.jeurceramsoc.2017.10.038.

[53] Y. Portilla-Nieto, A. Zaki, K. Vidal, M. Hernaiz, E. Aranzabe, S. Doppiu, A. Faik, Development of Co3-xNixO4 materials for thermochemical energy storage at lower red-ox temperature, Solar Energy Materials and Solar Cells 230 (2021) 111194. https://doi.org/10.1016/j.solmat.2021.111194.

[54] Y. Portilla-Nieto, K. Vidal, M. Hernaiz, E. Aranzabe, S. Doppiu, E. Palomo del Barrio, Development and stabilization of Co2.4Ni0.6O4 material for long-term thermochemical energy storage, Journal of Energy Storage 52 (2022) 104876. https://doi.org/10.1016/j.est.2022.104876.

[55] L. Liu, Z. Zhou, X.E. Cao, Y. Zhou, D. Peng, Y. Liu, X. Liu, M. Xu, Screening of optimal dopants on cobalt-based ceramics for high-temperature thermochemical energy storage, Ceramics International 49 (2023) 2329–2339. https://doi.org/10.1016/j.ceramint.2022.09.201.

[56] L. Liu, Z. Zhou, Y. Zhou, D. Peng, X. Liu, M. Xu, Co2.8Mg0.2O4 as a promising thermochemical energy storage material with lower reduction onset temperature and higher energy density, Journal of Energy Storage 55 (2022) 105594. https://doi.org/10.1016/j.est.2022.105594.

[57] C. Agrafiotis, M. Roeb, M. Schmücker, C. Sattler, Exploitation of thermochemical cycles based on solid oxide redox systems for thermochemical storage of solar heat. Part 2: Redox oxide-coated porous ceramic structures as integrated thermochemical reactors/heat exchangers, Solar Energy 114 (2015) 440–458. https://doi.org/10.1016/j.solener.2014.12.036.

[58] L. Liu, Z. Zhou, C. Wang, J. Xu, H. Xia, G. Chang, X. Liu, M. Xu, Superior thermochemical energy storage performance of the Co3O4/CoO redox couple with a cubic micro-nanostructure, Journal of Energy Storage 43 (2021) 103167. https://doi.org/10.1016/j.est.2021.103167.

[59] J.R. Scheffe, A.H. McDaniel, M.D. Allendorf, A.W. Weimer, Kinetics and mechanism of solar-thermochemical H2 production by oxidation of a cobalt ferrite-zirconia composite, Energy and Environmental Science 6 (2013) 963–973. https://doi.org/10.1039/c3ee23568h.

[60] J.R. Scheffe, J. Li, A.W. Weimer, A spinel ferrite/hercynite water-splitting redox cycle, International Journal of Hydrogen Energy 35 (2010) 3333–3340. https://doi.org/10.1016/j.ijhydene.2010.01.140.

[61] T. Kodama, N. Gokon, R. Yamamoto, Thermochemical two-step water splitting by ZrO2-supported NixFe3-xO4 for solar hydrogen production, Solar Energy 82 (2008) 73–79. https://doi.org/10.1016/j.solener.2007.03.005.

[62] M.I. Zaki, M.A. Hasan, L. Pasupulety, K. Kumari, Thermochemistry of manganese oxides in reactive gas atmospheres: Probing catalytic MnOx compositions in the atmosphere of CO+O2, Thermochimica Acta 311 (1998) 97–103. https://doi.org/10.1016/s0040-6031(97)00417-6.

[63] Q. Lei, R. Bader, P. Kreider, K. Lovegrove, W. Lipiński, Thermodynamic analysis of a combined-cycle solar thermal power plant with manganese oxide-based thermochemical energy storage, E3S Web of Conferences 22 (2017). https://doi.org/10.1051/e3sconf/20172200102.

[64] A.J. Carrillo, D.P. Serrano, P. Pizarro, J.M. Coronado, Thermochemical heat storage based on the Mn2O3/Mn3O4 redox couple: Influence of the initial particle size on the morphological evolution and cyclability, Journal of Materials Chemistry A 2 (2014) 19435–19443. https://doi.org/10.1039/c4ta03409k.

[65] A.J. Carrillo, D.P. Serrano, P. Pizarro, J.M. Coronado, Improving the thermochemical energy storage performance of the Mn2O3/Mn3O4 redox couple by the incorporation of iron, ChemSusChem 8 (2015) 1947–1954. https://doi.org/10.1002/cssc.201500148.

[66] A.J. Carrillo, D.P. Serrano, P. Pizarro, J.M. Coronado, Understanding Redox Kinetics of Iron-Doped Manganese Oxides for High Temperature Thermochemical Energy Storage, Journal of Physical Chemistry C 120 (2016) 27800–27812. https://doi.org/10.1021/acs.jpcc.6b08708.

[67] M. Wokon, A. Kohzer, M. Linder, Investigations on thermochemical energy storage based on technical grade manganese-iron oxide in a lab-scale packed bed reactor, Solar Energy 153 (2017) 200–214. https://doi.org/10.1016/j.solener.2017.05.034.

[68] M. Hamidi, V.M. Wheeler, X. Gao, J. Pye, K. Catchpole, A.W. Weimer, Reduction of iron–manganese oxide particles in a lab-scale packed-bed reactor for thermochemical energy storage, Chemical Engineering Science 221 (2020) 115700. https://doi.org/10.1016/j.ces.2020.115700.

[69] M. Gigantino, S.S. Brunser, A. Steinfeld, High-temperature thermochemical heat storage via the CuO/Cu2O redox cycle: From material synthesis to packed-bed reactor engineering and cyclic operation, Energy and Fuels 34 (2020) 16772–16782. https://doi.org/10.1021/acs.energyfuels.0c02572.

[70] A.J. Schrader, G.L. Schieber, A. Ambrosini, P.G. Loutzenhiser, Experimental demonstration of a 5 kWth granular-flow reactor for solar thermochemical energy storage with aluminum-doped calcium manganite particles, Applied Thermal Engineering 173 (2020) 115257. https://doi.org/10.1016/j.applthermaleng.2020.115257.

[71] K. Randhir, M. Hayes, P. Schimmels, J. Petrasch, J. Klausner, Zero carbon solid-state rechargeable redox fuel for long duration and seasonal storage, Joule 6 (2022) 2513–2534. https://doi.org/10.1016/j.joule.2022.10.003.

Chapter 2. Sr-based perovskite/brownmillerite CHS materials

2.1 Introduction

Perovskites are mixed-metal oxides of the form of ABO_3, in which A is a large cation and B normally a transition metal cation of smaller size. Redox cycles based on perovskites are currently concentrating on several energy-related applications, such as [1], thermochemical solar fuel production [2], CO_2 reforming [3], oxygen separation [4], and chemical looping combustion [5].

The main difference between redox cycles of perovskite and stoichiometric metal oxides is that for reduction process of perovskites is accompanied by the creation of a limited amount of oxygen vacancies and it does not involve the formation of a new phase like well-defined stoichiometric metal oxides did. On the other hand, because perovskites do not show well-defined redox transition, they are beyond a certain threshold of reduction/oxidation temperature, which strongly depends on the oxygen partial pressure pO_2, exhibiting a continuous linear-like oxygen intake/release within a very wide temperature range. This also leads to a more gradual change in mass during TGA experiments when compared to the sharp transitions of stoichiometric materials.

During oxidation, such vacancies are re-occupied by oxygen through an exothermic reaction with the consequent release of heat. The non-stoichiometric value of perovskites is denoted as δ (Equation 2-1), it also presents the extent of reaction and the amount of released lattice oxygen.

$$ABO_3\ (Perovskite) + \Delta H_r \leftrightarrow ABO_{3-\delta}\ (Brownmillerite) + \frac{\delta}{2}O_2 \qquad (2-1)$$

Because the redox reaction of perovskites can be performed without suffering any crystallographic transition, this feature might directly affect the long-term stability of materials.

Babiniec et al. [6] evaluated (denoted as LSCM, M= Mn, Fe) perovskite materials as

chemical heat storage media. More than 30 different compositions were analyzed via TGA, finding that $La_{0.3}Sr_{0.7}Co_{0.9}Mn_{0.1}O_{3-\delta}$ exhibited the highest enthalpy of reaction (250 kJ/kg). Later, Babiniec's research team [7,8] further found Ti-doped $CaMnO_{3-\delta}$ possesses a superior heat storage density (390 kJ/kg for $CaTi_{0.2}Mn_{0.8}O_{3-\delta}$) if compared with their previous report of LSCM perovskites. Imponenti et al. [9] from the Colorado School of Mines analyzed the effect of A- and B-site doping of Ca-Mn oxides and found that $Ca_{0.95}Sr_{0.05}MnO_{3-\delta}$can store 554.7 kJ/kg thermal energy if reduced at 1000 ℃ and pO_2 = 10^{-4} bar. They further tested the stability of Sr-doped $CaMnO_{3-\delta}$ using a fixed-bed lab scale reactor over 1000 cycles, demonstrating the high stability of perovskite materials over prolonged cycling.

In the previous research, $SrCoO_x$ has been reported as reversible oxygen sponge at low temperature (200-300 ℃) [10], which implies the strontium perovskites may possess the ability to store heat at medium-high temperature. Zhang et al. [11] reported Ba and Sr series perovskites for thermochemical energy storage, and they claimed that oxygen monoatomic ion of perovskites released from the crystal lattice is not subjected by a single energy threshold and results in an inconspicuous DSC peak during reduction and oxidation. Although Sr-based perovskites are already reported by the literature, the detailed studies on heat storage density and cyclability test are lacking due to the limitation of their experiment apparatus.

In this chapter, the feasibility of Sr-based perovskite ($SrBO_{3-\delta}$ (B=Mn, Fe, Co, Ni, Cu)) were investigated for medium-high temperature CHS. Composition analysis, redox capacity and cyclability of each sample was investigated using XRD, TGA, and SEM. Oxidation enthalpy was investigated by a combination of tubular furnace and DSC analysis.

2.2 Experimental approach

2.2.1 Material synthesis

$SrBO_{3-\delta}$ (B=Mn, Fe, Co, Ni, Cu) perovskite was synthesized by a modified Pechini method [12]. Stoichiometric amounts of nitrate salts $Sr(NO_3)_2$ (98%, FUJIFILM Wako Pure Chemical Corpora-tion), $Mn(NO_3)_2 \cdot 6H_2O$ (98%, FUJIFILM Wako Pure Chemical Corporation), $Fe(NO_3)_3 \cdot 9H_2O$ (99%, FUJIFILM Wako Pure Chemical Corporation), $Co(NO_3)_2 \cdot 6H_2O$ (98%, FUJIFILM Wako Pure Chemical Corporation), $Ni(NO_3)_2 \cdot 6H_2O$ (98%, FUJIFILM Wako Pure Chemical Corporation), and $Cu(NO_3)_2 \cdot 3H_2O$ (98%, FUJIFILM Wako Pure Chemical Corporation) were dissolved in deionized water, then citric acid was added to the solution at a ratio of 1:2 (cation : citric acid). Ethylene glycol was introduced as a reactant with citric acid, then adjusted the pH value to around 9 with ammonia solution subsequently. The solution was dried and pre-calcined at 500 °C for 1h in air to remove all the organic components. After grounding, the powders were pelletized with a 25 mm die at 30 MPa, then the pellets were heated to 1200 °C for 5 hours in air. To preserve the brownmillerite phase (reduction state of perovskite) until XRD analysis was performed, a few samples were quenched by liquid N_2. The remaining samples were cooled at room temperature. For convenience, the quenched samples are denoted as Q-$ABO_{3-\delta}$ and the samples without quenching are denoted as NQ-$ABO_{3-\delta}$.

2.2.2 Structural characterization

The pre-calcined sample, Q-$ABO_{3-\delta}$ and NQ-$ABO_{3-\delta}$ sample were investigated using X-ray diffraction (XRD) (SmartLab, Rigaku) with Cu Kα radiation (λ = 0.15418 nm, 40 kV – 25 mA). Crystalline phases were analyzed using PDXL2 (Rigaku Data Analysis Software).

2.2.3 Redox behavior and morphologic investigation

Three temperature programs were performed for this study. For the first program, the redox behavior and mass change of the NQ-$ABO_{3-\delta}$ and Q-$ABO_{3-\delta}$ families were

evaluated. The redox behavior investigation of the NQ-$ABO_{3-\delta}$ and Q-$ABO_{3-\delta}$ families was tested using pellet fragments (~20mg) in a TGA (HITACHI STA7300). This experiment could not determine the absolute δ values of each sample but provided an appropriate standard for comparing different families.

The first program consisted of two cycles. The initial cycle aims to remove any impurity (i.e., adsorbed species on the surface of the sample) and eliminate the quenching effect [6,13,14]. The weight at 100 °C was recorded as the initial weight, and the sample was heated up to 1000 °C holding for 1 h then re-oxidized in the air while cooling to 100 °C for 90 min.

The second program functioned as a "pre-experiment" aims to obtaining an oxidation rate of the reduced perovskites at room temperature. This ensured the validity of combining a tubular furnace and DSC analysis.

The third program was set up for the cycling tests. The SEM morphology was also studied using as-prepared sample, 1 cycle and 10 cycles samples. Details on each TG program will be presented in a later section.

2.2.4 Oxidation enthalpies measurement

To measure oxidation enthalpy, NQ-$ABO_{3-\delta}$ samples were heated to 1000 °C and then cooled down to room temperature in an argon flow using tubular furnace to obtain the pure reduced $ABO_{2.5}$ brownmillerite phase. The so-called "isothermal method" was performed for the measurement of $SrCoO_{3-\delta}$ and $SrFeO_{3-\delta}$. After heating the sample to the appropriate temperature under N_2 protection, the gas was changed to air when target temperature was stable. The exothermic signal was detected using DSC apparatus (DSC-60, Shimadzu Corp.). Especially, the "non-isothermal method" was used for the oxidation enthalpy measurement of $SrMnO_{3-\delta}$.

2.3 Results and discussion

2.3.1 Synthesis mechanism and characterization of composition

The preparation schematic of the sample using Pechini method was shown in Figure 2-1. Metallic cations were initially chelated with citric acid. With the aid of polyalcohol, the corresponding metallic citrates were cross-linked to form a gel through esterification. The organic compositions were removed after pre-calcine process, and the cations were subsequently oxidized at high temperature to form a perovskite structure.

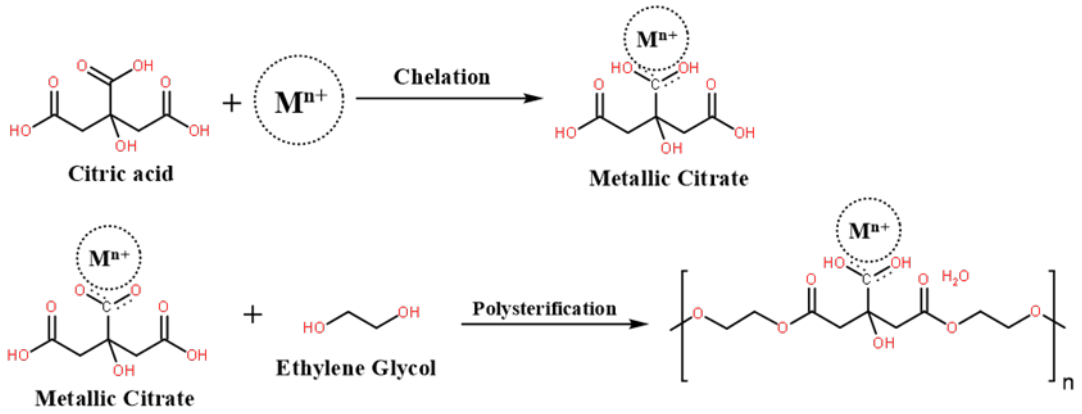

Figure 2-1 Preparation schematic using Pechini method

During the pre-experiments of this study, although $SrNiO_{3-\delta}$ and $SrCuO_{3-\delta}$ perovskite were also prepared using Pechini method, pure $SrNiO_{3-\delta}$ and $SrCuO_{3-\delta}$ perovskite were not obtained because of their instability in ambient conditions [15,16]. Therefore, only $SrCoO_{3-\delta}$, $SrFeO_{3-\delta}$ and $SrMnO_{3-\delta}$ were considered for further study.

To confirm the validity of the Pechini method, XRD analysis was performed on pre-calcined, NQ-$ABO_{3-\delta}$, and Q-$ABO_{3-\delta}$ samples. The results are summarized in Table 2-1, and the typical XRD patterns of NQ-$ABO_{3-\delta}$ and Q-$ABO_{3-\delta}$ samples are presented in Figure 2-2.

The phase composition of the unquenched samples (NQ-$SrCoO_{3-\delta}$, NQ-$SrFeO_{3-\delta}$, and NQ-$SrMnO_{3-\delta}$) was analyzed using XRD. Upon comparison with standard PDF cards, it

was found that, instead of the predicted $SrCoO_3$ phase, the NQ-$SrCoO_{3-\delta}$ sample exhibited the $Sr_6Co_5O_{15}$ phase, indicating a molar ratio of Sr to Co that deviates from 1:1. Previous studies suggest that during room-temperature cooling of $SrCoO_{3-\delta}$ prepared via the Pechini method, the material decomposes into $Sr_6Co_5O_{15}$ along with a small amount of Co_3O_4. Based on the synthesis mechanism of the pre-calcined samples, it can be inferred that during cooling at room temperature, a small amount of Co decomposed from $SrCoO_{3-\delta}$ and gradually oxidized in air. Meanwhile, the remaining $SrCoO_{3-\delta}$ transformed into the more thermodynamically stable $Sr_6Co_5O_{15}$ phase. The Sr-Co-O phase diagram also indicates that, at temperatures below 1150 K, the formation of the $SrCoO_3$ perovskite phase is not possible, even with a 1:1 molar ratio of the raw materials [17].

Conversely, $SrFeO_{3-\delta}$ maintains its phase stability from high temperature down to room temperature. However, even the unquenched sample exhibits an unsaturated phase (e.g., $SrFeO_{2.875}$), likely because the dense pelletization of the sample obstructs oxygen diffusion, preventing the inner regions from acquiring sufficient oxygen. Some researchers have suggested that oxygen vacancies may still exist in $SrFeO_3$ even at room temperature in an air atmosphere. Theoretically, achieving pure $SrFeO_3$ may require heating the sample to a temperature slightly above room temperature and maintaining it for a while under pure oxygen [18].

The metastable brownmillerite phase can be obtained using the quenching method. However, Q-$SrFeO_{3-\delta}$ also contains $SrFeO_{2.875}$, maintaining a relatively larger δ value. This suggests that although the sample was “frozen” by quenching, it will still slowly oxidize over time. Interestingly, the quenching effect has not been observed in $SrMnO_{3-\delta}$, likely due to the stronger Mn-O bond, which requires a higher temperature to release lattice oxygen. Furthermore, $SrMnO_3$ exhibits a hexagonal structure instead of the standard ABO_3 perovskite cubic structure, resulting in redox behavior, such as oxygen exchange capacity, that deviates from the other two compounds [19].

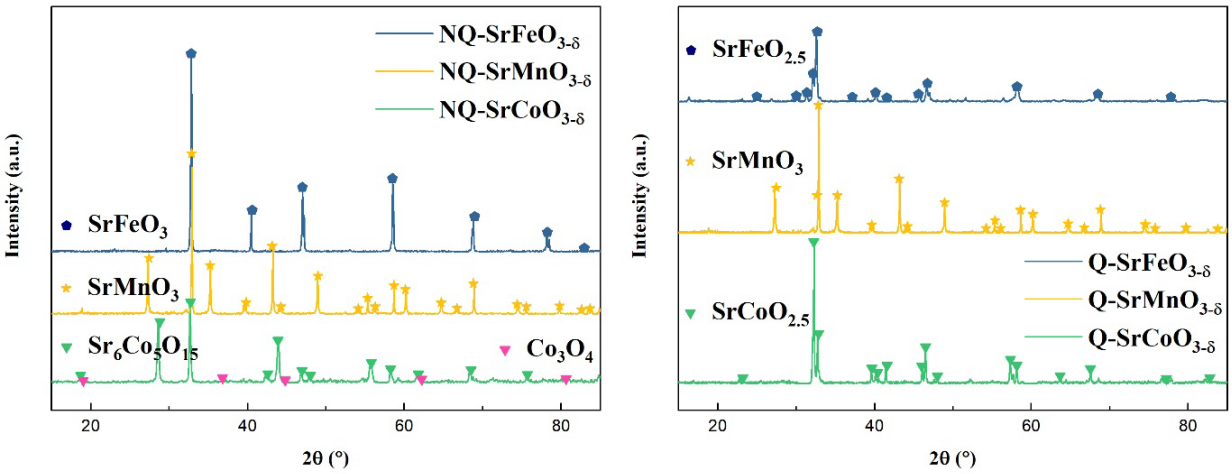

Figure 2-2 XRD patterns of NQ-ABO_3 and Q-ABO_3 samples

Table 2-1 Main phase, crystal structure and PDF-code of each sample

Sample	Main phase	Crystal Structure	PDF-#
Pre-calcined-$SrCoO_{3-\delta}$	α-Sr, γ-Sr, $Co_{2.62}O_4$	(-)	(-)
Pre-calcined-$SrFeO_{3-\delta}$	α-Sr, γ-Sr, Fe_3O_4	(-)	(-)
Pre-calcined-$SrMnO_{3-\delta}$	α-Sr, γ-Sr, Mn_2O_3	(-)	(-)
NQ-$SrCoO_{3-\delta}$	$Sr_6Co_5O_{15}$	Trigonal, *R32 (155)*	00-060-0757
NQ-$SrFeO_{3-\delta}$	$SrFeO_3$, $SrFeO_{2.75}$	Cubic, *Pm-3m (221)* Orthorhombic, *Cmmm (65)*	01-070-6802, 01-070-5777
NQ-$SrMnO_{3-\delta}$	$SrMnO_3$	Hexagonal, *P63/mmc (194)*	01-084-1612
Q-$SrCoO_{3-\delta}$	$SrCoO_{2.5}$	Orthorhombic, *Ima2 (46)*	01-078-5502
Q-$SrFeO_{3-\delta}$	$SrFeO_{2.5}$, $SrFeO_{2.875}$	Orthorhombic, *Icmm (74)* Tetragonal, *I4/mmm (139)*	01-070-0836, 00-059-0638
Q-$SrMnO_{3-\delta}$	$SrMnO_3$	Hexagonal, *P63/mmc (194)*	01-084-1612

2.3.2 Redox behavior

The redox behavior of the NQ-$ABO_{3-\delta}$ and Q-$ABO_{3-\delta}$ families was determined using TGA. Figure 2-3 presents the TGA program profile and the mass change for each sample. $SrCoO_{3-\delta}$ and $SrFeO_{3-\delta}$ exhibited very similar redox behavior when heated to 1000 °C in ambient atmosphere, whereas $SrMnO_{3-\delta}$ remained inactive under these conditions. The mass changes of unquenched $SrCoO_{3-\delta}$, $SrFeO_{3-\delta}$, and $SrMnO_{3-\delta}$ samples are 2.11%, 2.34%, and 0.34%, respectively. In contrast, the mass changes of the quenched $SrCoO_{3-\delta}$,

$SrFeO_{3-\delta}$, and $SrMnO_{3-\delta}$ samples were significantly lower, at 1.70%, 2.20%, and 0.33%, respectively. The change in δ, referred to as Δδ, can be easily calculated using Equation 2-2:

$$\Delta\delta = \frac{\Delta m \cdot MW_{ABO3}}{m_{initial} \cdot MW_O} \qquad (2-2)$$

where Δm presents the change in mass, $m_{initial}$ is the initial mass, MW_{ABO3} is the molecular weight of perovskite (δ = 0), MW_O is the molecular weight of monoatomic oxygen. The calculated Δδ values are presented in Table 2-2.

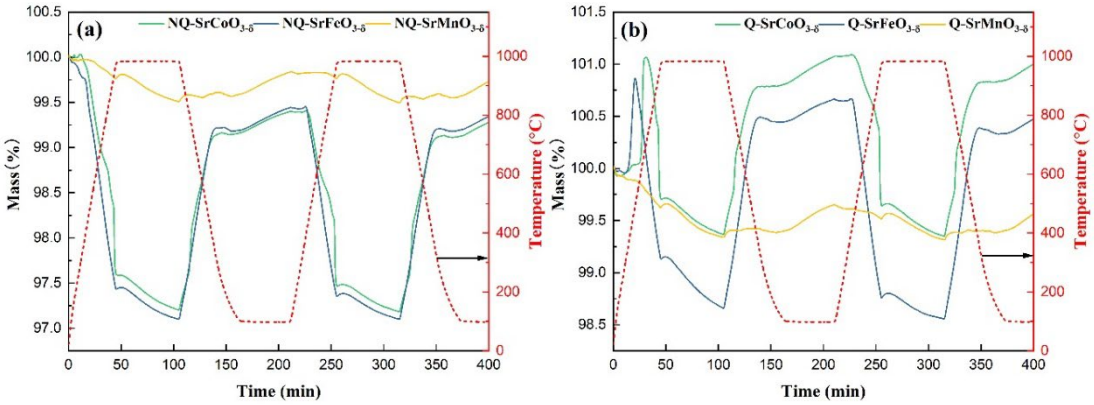

Figure 2-3 Redox behavior of (a) NQ-$ABO_{3-\delta}$ and (b) Q-$ABO_{3-\delta}$ families

Table 2-2 The value of Δδ for No-Quenched and Quenched families

Experiment Condition	$SrCoO_{3-\delta}$	$SrFeO_{3-\delta}$	$SrMnO_{3-\delta}$
No-Quench	0.266 ± 0.007	0.279 ± 0.003	0.049 ± 0.006
Quenched	0.199 ± 0.008	0.262 ± 0.007	0.048 ± 0.007

It is noteworthy that after the quenching process, the redox behavior of Q-$ABO_{3-\delta}$ was slightly worse than that of the NQ-$ABO_{3-\delta}$. This decline is primarily attributed to irreversible damage to sample during quenching, preventing the material from fully

returning to its most oxidized state, thereby narrowing the range of mass change. Notably, the Q-$ABO_{3-\delta}$ families exhibit rapid mass change behavior in the first cycle, occurring around 700 °C and 400 °C for $SrCoO_{3-\delta}$ and $SrFeO_{3-\delta}$, respectively. Through quenching, the perovskite sample can be "frozen" in a reduced state until it returns to room temperature. Upon reheating, the oxidation rate increases.

As shown in Figure 2-3 (b), when a certain temperature is reached—around 800 °C for $SrCoO_{3-\delta}$ and 500 °C for $SrFeO_{3-\delta}$—the Q-$ABO_{3-\delta}$ samples nearly recover their initial mass. However, as the temperature continues to rise, reduction behavior becomes apparent. Although the reduction reaction occurs throughout the heating process, its rate remains lower than that of oxidation until a specific temperature is reached. In contrast to the other perovskites, $SrMnO_{3-\delta}$ shows no significant quenching effect, aside from a slight variation in mass change.

In fact, the redox behaviors of $SrCoO_{3-\delta}$ and $SrFeO_{3-\delta}$ differ significantly due to their distinct properties. The mass change of $SrFeO_{3-\delta}$ resembles a linear function over the temperature range from 400 °C to 1000 °C during both reduction and oxidation. This linear behavior is maintained across multiple cycles, as confirmed by cyclability tests. In contrast, $SrCoO_{3-\delta}$ exhibits a more complex reduction behavior, which can be described as a piecewise linear function with a change in slope occurring around 900 °C. This shift in behavior is likely due to the formation of various Sr-Co-O ternary phases. Ondřej Jankovský et al. previously investigated the detailed phase composition of the Sr-Co-O system [17]. According to the Sr-Co-O phase diagram, at temperatures below 877 °C, Sr and Co can only form the quasi-one-dimensional $Sr_6Co_5O_{15}$ phase, rather than the $SrCoO_{3-\delta}$ perovskite structure [20]. These findings align perfectly with our results. From a different perspective, the occurrence of varied phase changes during the redox process poses challenges for further investigation due to the complexity of reaction kinetics.

On the other hand, even when $SrMnO_{3-\delta}$ was heated to 1000 °C, it remained in a relatively high oxidation state. In a supplementary experiment conducted by Zhang et

al.[11], despite heating $SrMnO_{3-\delta}$ perovskite to 1150 °C in an Ar atmosphere—effectively reducing it under extremely low oxygen partial pressure—it exhibited a mass change of less than 2%. This suggests that $SrMnO_{3-\delta}$ may have a high reduction enthalpy, with the estimated value reported by other researchers [21,22]. However, for heat storage applications at medium to high temperatures, the strict operating conditions present significant challenges.

2.3.3 Oxidation enthalpies measurement

To confirm that the oxidation rate of the reduced sample under ambient conditions was slow enough for DSC measurement, a preliminary experiment was conducted, with the results shown in Figure 2-4.

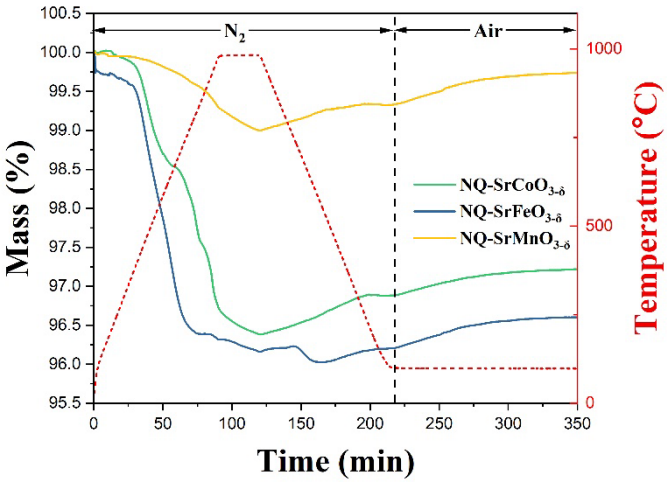

Figure 2-4 Re-Oxidation behavior of reduced NQ-ABO_3 at 100 °C in air atmosphere

The NQ-$ABO_{3-\delta}$ family was heated to 1000 °C in N_2 atmosphere to obtain reduced samples. Subsequently, the gas was switched to synthetic air while maintaining the temperature at 100 °C to determine the oxidation rate under normal conditions. The $\Delta\delta$ values in N_2 and air are listed in Table 2-3. To evaluate the thermochemical heat storage density per unit volume, the density of each sample was measured using the helium pycnometer method, yielding results of 5.70 g/cm³ for $SrCoO_{3-\delta}$, 5.79 g/cm³ for $SrFeO_{3-}$

$_{\delta}$, and 6.82 g/cm³ for $SrMnO_{3-\delta}$.

Table 2-3 The δ changes of each sample during the experiment performed in Figure 2-4

Experiment Condition	NQ-$SrCoO_{3-\delta}$	NQ-$SrFeO_{3-\delta}$	NQ-$SrMnO_{3-\delta}$
Reduction in N_2	0.439	0.459	0.119
Oxidation in air at 100 °C	0.041	0.048	0.049

According to the calculation results from Figure 2-4, $SrCoO_{3-\delta}$ and $SrFeO_{3-\delta}$ were almost fully reduced to the $ABO_{2.5}$ brownmillerite phase. The changes in δ for both $SrCoO_{3-\delta}$ and $SrFeO_{3-\delta}$ were negligible when the gas was switched to air. Oxidized samples were heat-treated in a tubular furnace to obtain reduced samples. The reduced samples were then heated to the appropriate temperature under N_2 protection, after which the gas was switched to air, and the exothermic peak was monitored using DSC. This technique is referred to as the isothermal oxidation method. Typical DSC results are presented in Figure 2-5.

An appropriate oxidation temperature is crucial for each reduced sample, given the sensitivity of perovskite materials to both temperature and oxygen partial pressure. An excessively high oxidation temperature can lead to incomplete oxidation, as high temperatures may also promote the reduction reaction. Conversely, if the temperature is too low, the oxidation reaction may proceed too slowly to generate a visible peak. Therefore, the oxidation temperatures for $SrCoO_{3-\delta}$ and $SrFeO_{3-\delta}$ were set at 450 °C and 400 °C (program temperature), respectively.

Among the DSC results, only $SrFeO_{3-\delta}$ exhibited a well-defined exothermic peak, while $SrCoO_{3-\delta}$ displayed a semi-peak or vaulted peak. Interestingly, the DSC curve of $SrCoO_{3-\delta}$ shows two distinct baselines before and after the reaction, indicating a change in its specific heat capacity. This can be attributed to the formation of $Sr_6Co_5O_{15}$, as discussed previously. Despite the similarity in the redox behavior of $SrCoO_{3-\delta}$ and $SrFeO_{3-\delta}$, the

oxidation enthalpy of $SrCoO_{3-\delta}$ is 47.6 ± 5.7 kJ/kg-$ABO_{3-\delta}$ (270.5 ± 32.3 kJ/L-$ABO_{3-\delta}$), which is slightly lower than that of $SrFeO_{3-\delta}$ at 81.7 ± 3.4 kJ/kg-$ABO_{3-\delta}$ (473.5 ± 20.0 kJ/L-$ABO_{3-\delta}$). It is also worth noting that the exothermic peak measured by DSC is usually smaller than the actual value due to inevitable heat loss.

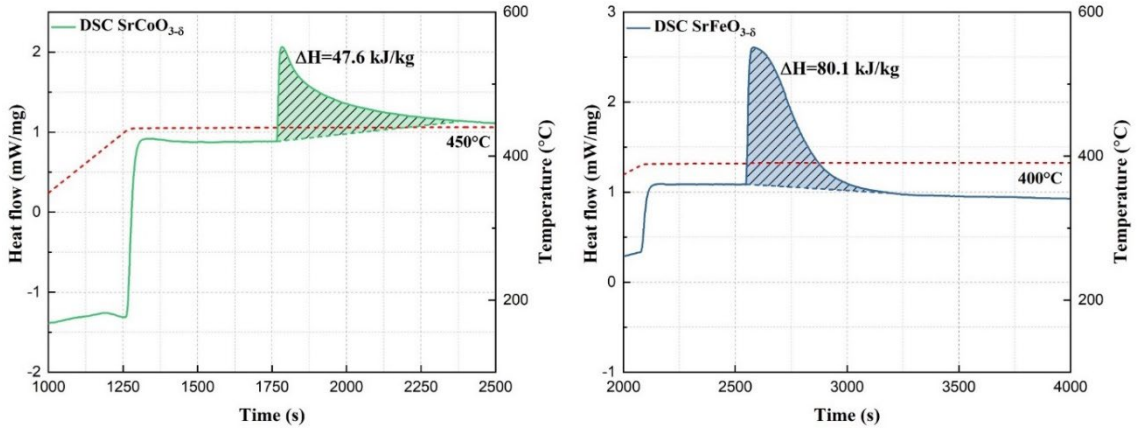

Figure 2-5 DSC curve for reduced $SrCoO_{3-\delta}$ and $SrFeO_{3-\delta}$ under isothermal oxidation

On the other hand, $SrMnO_{3-\delta}$ demonstrates a significant oxygen affinity. Even when the reduced $SrMnO_{3-\delta}$ was heated to 500 °C in a N_2 atmosphere (extremely low oxygen partial pressure), it re-oxidized within 30 minutes. As shown in Figure 2-6, the reduced $SrMnO_{3-\delta}$ exhibits similar oxidation behavior in both N_2 and air. For this reason, a non-isothermal oxidation method was adopted. The reduced $SrMnO_{3-\delta}$ was heated at a constant rate of 10 °C/min in air. After integrating the exothermic peak, the oxidation enthalpy was determined to be 25.6 ± 5.8 kJ/kg-$ABO_{3-\delta}$ (230.3 ± 39.4 kJ/L-$ABO_{3-\delta}$). A typical pattern is presented in Figure 2-7.

Since $SrMnO_{3-\delta}$ was found to achieve only a small $\Delta\delta$ (as shown in Figure 2-6, where $\Delta\delta$ reached only 0.1), even under high temperature and low pO_2 conditions, its oxidation enthalpy was not satisfactory. However, it exhibits unusual stability, suggesting that $SrMnO_{3-\delta}$ may possess the highest oxidation enthalpy among all Sr-based perovskites, provided that its $\Delta\delta$ is sufficiently large. Unfortunately, because the relationship between

Δδ and enthalpy is not always linear, predicting the complete oxidation value using the DSC method from a single data point remains challenging.

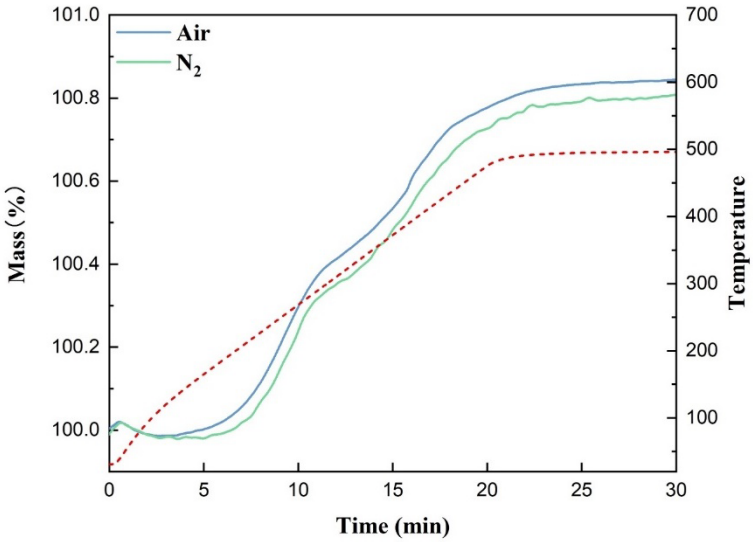

Figure 2-6 Oxidation behavior of reduced $SrMnO_{3-\delta}$ in air/N_2 during heating

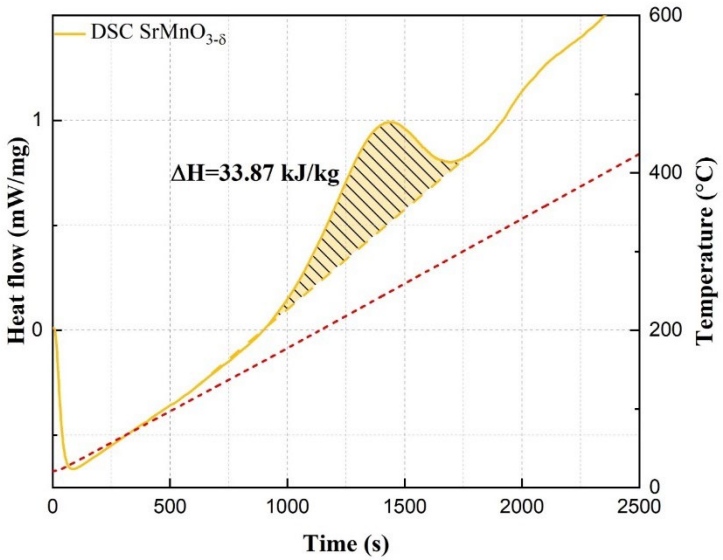

Figure 2-7 DSC curve for reduced $SrMnO_{3-\delta}$ with non-isothermal oxidation method

Vieten et al. [21] estimated the reaction enthalpy of $SrMnO_{3-\delta}$ (373 ± 55 kJ/mol-O_2) using the Van't Hoff approach, but this method involves significant measurement

uncertainties due to the small mass changes detected. It is important to note that the unit used (kJ/mol-O_2) refers to the amount of heat released when the perovskite reacts with one mol of oxygen. In 2001, Rørmark et al. [22] measured the oxidation enthalpy of $SrMnO_{3-\delta}$ to be 293 ± 10 kJ/mol-O_2 and 73.3 ± 0.5 kJ/mol-Mn (~384.65 kJ/kg). Additionally, DFT-based studies reported the reaction enthalpy to be 340 kJ/mol-O_2 [23–25]. From these studies, $SrMnO_{3-\delta}$ is confirmed to possess a large reaction enthalpy, as expected from the design principles. However, its high stability in the 500–1000 °C range presents practical challenges. In conclusion, only $SrFeO_{3-\delta}$ was found to be suitable for operation under medium to high-temperature conditions.

2.3.4 Cyclability test

$SrFeO_{3-\delta}$ was selected for further cyclability testing over 10 redox cycles, as shown in Figure 2-8. Except for the first cycle, which did not achieve a satisfactory depth of reduction, the remaining cycles demonstrated excellent cyclability in air. The large mass loss observed during the first cycle can be attributed to the desorption of water vapor or other adsorbed species. From this perspective, $SrFeO_{3-\delta}$ was able to return to a relatively high oxidation state, with its mass very close to the original initial mass, when the temperature was cooled to 100 °C.

As shown in Figure 2-9 (a-b), some $SrFeO_{3-\delta}$ particles agglomerated, forming relatively large particles over 20 μm in size. These agglomerated particles exhibit a terraced and exfoliated structure. In the magnified view, the terraced structure is distinct, with small holes (approximately 1 μm) visible on the particle surfaces. Point defects in crystal growth may play a significant role in determining surface morphology. For example, these defects could accelerate the oxygen exchange rate by increasing the surface area.

However, after two cycles, only a small portion of the terraced structure remains, and the point defects are no longer detectable, as seen in Figure 2-9 (c-d). The results after 10 cycles, shown in Figure 2-9 (e-f), indicate that $SrFeO_{3-\delta}$ experiences severe sintering, with

the terraced structure no longer present. Although some holes remain visible, they are likely due to incomplete sintering rather than point defects. Surprisingly, despite the significant sintering, the redox behavior of $SrFeO_{3-\delta}$ remains adequate.

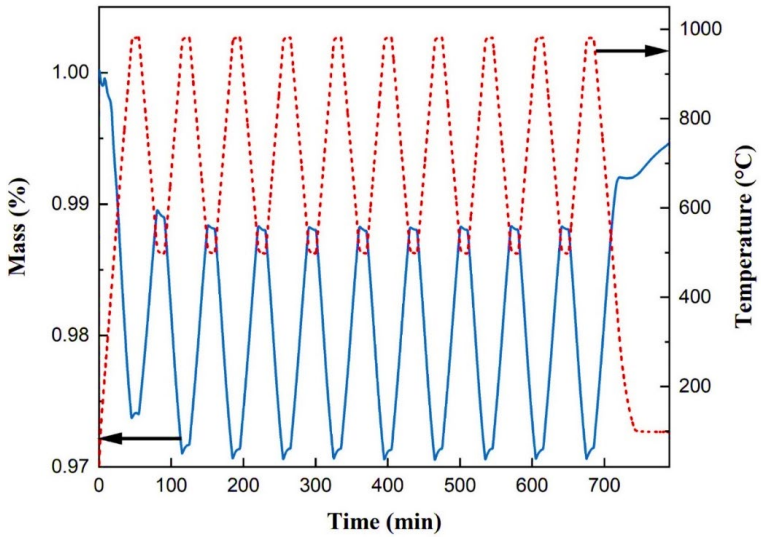

Figure 2-8 10-cycles cyclability experiment of $SrFeO_{3-\delta}$

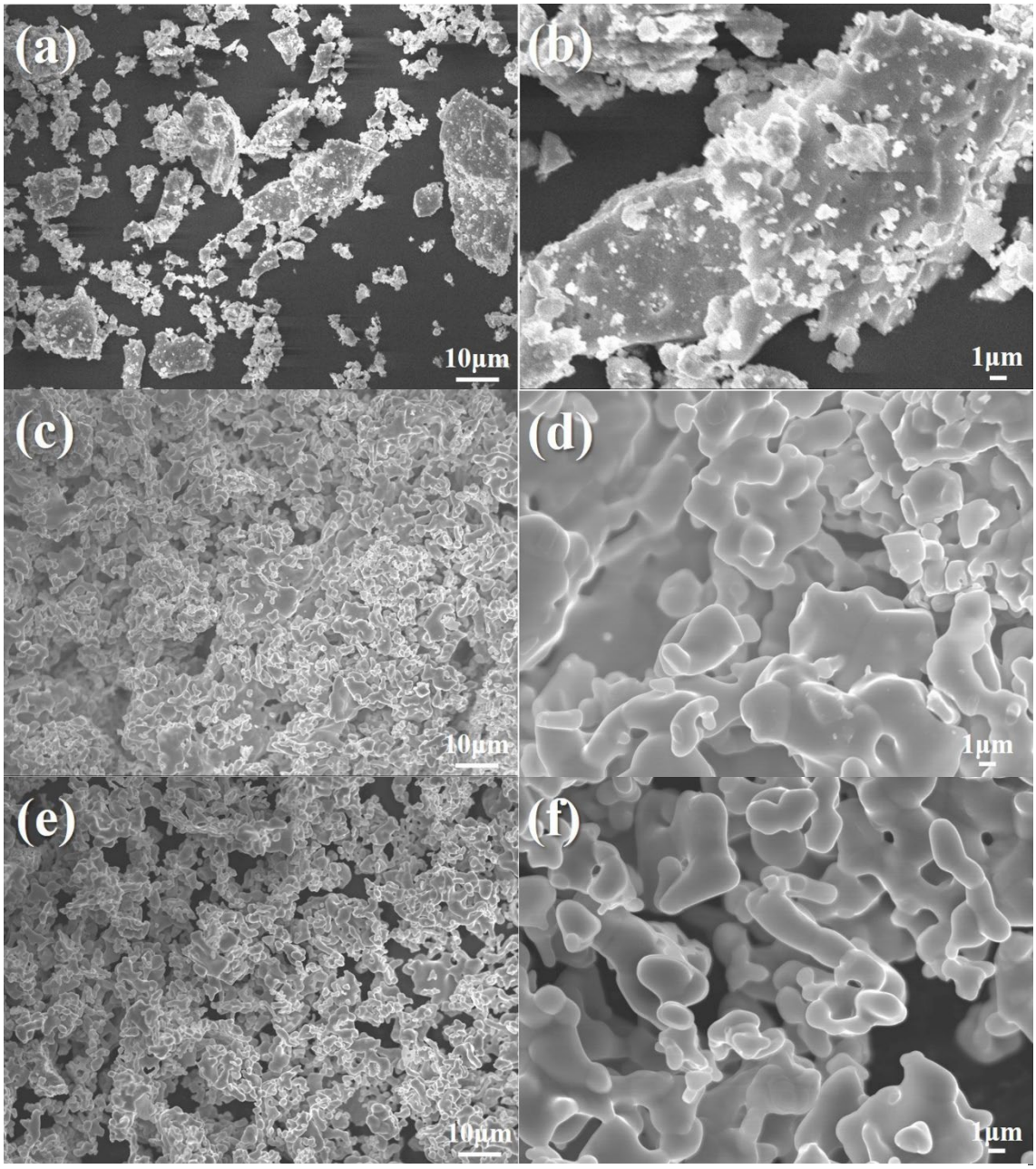

Figure 2-9 SEM images of $SrFeO_{3-\delta}$: (a-b) for as-prepared sample, (c-d) for 2-cycled sample and (e-f) for 10-cycled sample

2.4 Conclusions

In this chapter, Sr-based transition metal perovskites were prepared for chemical heat storage at medium to high temperatures. Due to the instability of $SrCuO_{3-\delta}$ and $SrNiO_{3-\delta}$, only $SrCoO_{3-\delta}$, $SrFeO_{3-\delta}$, and $SrMnO_{3-\delta}$ were successfully synthesized using the modified Pechini method. "Frozen" samples were obtained through quenching to investigate their crystal structure. The structure of $SrMnO_{3-\delta}$ deviates from the ideal cubic perovskite structure, exhibiting diminished redox capacity at 1000 °C, even in an N_2 atmosphere. However, several studies have reported that $SrMnO_{3-\delta}$ may have the highest reaction enthalpy (300–400 kJ/mol-O_2) among the three candidates, attributed to stronger Mn–O bonds and its non-cubic structure.

Although $SrCoO_{3-\delta}$ has a redox capacity similar to that of $SrFeO_{3-\delta}$, its phase transitions, according to the Sr-Co-O phase diagram, are unfavorable for chemical heat storage systems. $SrCoO_{3-\delta}$, $SrFeO_{3-\delta}$, and $SrMnO_{3-\delta}$ were heated to 1000 °C to obtain their reduced phases. After DSC measurements, the oxidation enthalpies of each sample were determined to be 47.6 ± 5.7 kJ/kg-$ABO_{3-\delta}$ (270.5 ± 32.3 kJ/L-$ABO_{3-\delta}$), 81.7 ± 3.4 kJ/kg-$ABO_{3-\delta}$ (473.5 ± 20.0 kJ/L-$ABO_{3-\delta}$), and 25.6 ± 5.8 kJ/kg-$ABO_{3-\delta}$ (230.3 ± 39.4 kJ/L-$ABO_{3-\delta}$), respectively. Theoretically, if all samples achieve the same $\Delta\delta$, the oxidation enthalpy is expected to increase with the metallicity of the element. This trend may be associated with differences in the strength of M–O bonds. $SrNiO_{3-\delta}$ and $SrCuO_{3-\delta}$ are not considered viable for this purpose, as their M–O bonds are too weak to form stable structures.

Since $SrFeO_{3-\delta}$ exhibited excellent redox capacity, additional cyclability tests were conducted, and its morphology was examined using SEM. The results demonstrated good cyclability over 10 cycles, even after sintering.

In conclusion, $SrFeO_{3-\delta}$ meets the requirements for operation under moderate oxygen partial pressure and within the medium to high-temperature range, exhibiting exceptional cyclability. However, its limited heat storage density makes it difficult for further practical

applications.

Reference

[1] R. Wang, M. Mujahid, Y. Duan, Z. Wang, J. Xue, Y. Yang, A Review of Perovskites Solar Cell Stability, Adv Funct Materials 29 (2019) 1808843. https://doi.org/10.1002/adfm.201808843.

[2] M. Kubicek, A.H. Bork, J.L.M. Rupp, Perovskite oxides – a review on a versatile material class for solar-to-fuel conversion processes, J. Mater. Chem. A 5 (2017) 11983–12000. https://doi.org/10.1039/C7TA00987A.

[3] Z. Bian, Z. Wang, B. Jiang, P. Hongmanorom, W. Zhong, S. Kawi, A review on perovskite catalysts for reforming of methane to hydrogen production, Renewable and Sustainable Energy Reviews 134 (2020) 110291. https://doi.org/10.1016/j.rser.2020.110291.

[4] J. Sunarso, S.S. Hashim, N. Zhu, W. Zhou, Perovskite oxides applications in high temperature oxygen separation, solid oxide fuel cell and membrane reactor: A review, Progress in Energy and Combustion Science 61 (2017) 57–77. https://doi.org/10.1016/j.pecs.2017.03.003.

[5] T. Dawa, B. Sajjadi, Exploring the potential of perovskite structures for chemical looping technology: A state-of-the-art review, Fuel Processing Technology 253 (2024) 108022. https://doi.org/10.1016/j.fuproc.2023.108022.

[6] S.M. Babiniec, E.N. Coker, J.E. Miller, A. Ambrosini, Investigation of LaxSr1-xCoyM1-yO3-δ (M=Mn, Fe) perovskite materials as thermochemical energy storage media, Solar Energy 118 (2015) 451–459. https://doi.org/10.1016/j.solener.2015.05.040.

[7] S.M. Babiniec, Doped calcium manganites for advanced high- temperature thermochemical energy storage, INTERNATIONAL JOURNAL OF ENERGY RESEARCH 40 (2016) 280–284. https://doi.org/10.1002/er.

[8] S.M. Babiniec, E.N. Coker, J.E. Miller, A. Ambrosini, Doped calcium manganites for advanced high-temperature thermochemical energy storage, International Journal of Energy Research 40 (2016) 280–284. https://doi.org/10.1002/er.3467.

[9] L. Imponenti, K.J. Albrecht, J.W. Wands, M.D. Sanders, G.S. Jackson, Thermochemical energy storage in strontium-doped calcium manganites for concentrating solar power applications, Solar Energy 151 (2017) 1–13. https://doi.org/10.1016/j.solener.2017.05.010.

[10] Q. Lu, S. Huberman, H. Zhang, Q. Song, J. Wang, G. Vardar, A. Hunt, I. Waluyo, G. Chen, B. Yildiz, Bi-directional tuning of thermal transport in SrCoOx with electrochemically induced phase transitions, Nature Materials 19 (2020) 655–662. https://doi.org/10.1038/s41563-020-0612-0.

[11] Z. Zhang, L. Andre, S. Abanades, Experimental assessment of oxygen exchange capacity and thermochemical redox cycle behavior of Ba and Sr series perovskites for solar energy storage, Solar Energy 134 (2016) 494–502. https://doi.org/10.1016/j.solener.2016.05.031.

[12] Maggio P Pechini, Method of preparing lead and alkaline earth titanates and niobates and coating method using the same to form a capacitor, n.d. https://patents.google.com/patent/US3330697A/en.

[13] A. Ambrosini, E.N. Coker, M.A. Rodriguez, S. Livers, L.R. Evans, J.E. Miller, E.B. Stechel, Synthesis and characterization of ferrite materials for thermochemical CO2 splitting using concentrated solar energy, ACS Symposium Series 1056 (2010) 1–13. https://doi.org/10.1021/bk-2010-1056.ch001.

[14] E. Ksepko, Perovskite-type Sr(Mn1-xNix)O3 materials and their chemical-looping oxygen transfer properties, International Journal of Hydrogen Energy 39 (2014) 8126–8137. https://doi.org/10.1016/j.ijhydene.2014.03.093.

[15] M. Zinkevich, Constitution of the Sr-Ni-O system, Journal of Solid State Chemistry 178 (2005) 2818–2824. https://doi.org/10.1016/j.jssc.2005.06.035.

[16] C.B. Aicock, B. Li, Thermodynamic Study of the Cu-Sr-O System, 1990.

[17] O. Jankovský, D. Sedmidubský, J. Vítek, P. Šimek, Z. Sofer, Phase diagram of the Sr-Co-O system, Journal of the European Ceramic Society 35 (2015) 935–940. https://doi.org/10.1016/j.jeurceramsoc.2014.09.040.

[18] E. Heifets, E.A. Kotomin, A.A. Bagaturyants, J. Maier, Thermodynamic stability of non-stoichiometric $SrFeO_{3-\delta}$: a hybrid DFT study, Phys. Chem. Chem. Phys. 21 (2019) 3918–3931. https://doi.org/10.1039/C8CP07117A.

[19] M.T. Curnan, J.R. Kitchin, Effects of concentration, crystal structure, magnetism, and electronic structure method on first-principles oxygen vacancy formation energy trends in perovskites, Journal of Physical Chemistry C 118 (2014) 28776–28790. https://doi.org/10.1021/jp507957n.

[20] A.S. Botana, P.M. Botta, C. De La Calle, A. Piñeiro, V. Pardo, D. Baldomir, J.A. Alonso, Non-one-dimensional behavior in charge-ordered structurally quasi-one-dimensional Sr6Co5O15, Physical Review B - Condensed Matter and Materials Physics 83 (2011) 1–8. https://doi.org/10.1103/PhysRevB.83.184420.

[21] J. Vieten, B. Bulfin, M. Senholdt, M. Roeb, C. Sattler, M. Schmücker, Redox thermodynamics and phase composition in the system SrFeO3 − δ — SrMnO3 − δ, Solid State Ionics 308 (2017) 149–155. https://doi.org/10.1016/j.ssi.2017.06.014.

[22] L. Rørmark, A.B. Mørch, K. Wiik, S. Stølen, T. Grande, Enthalpies of oxidation of CaMnO3-δ, Ca2MnO4-δ and SrMnO3-δ - Deduced redox properties, Chemistry of Materials 13 (2001) 4005–4013. https://doi.org/10.1021/cm011050l.

[23] A. Jain, G. Hautier, S.P. Ong, C.J. Moore, C.C. Fischer, K.A. Persson, G. Ceder, Formation enthalpies by mixing GGA and GGA + U calculations, Phys. Rev. B 84 (2011) 045115. https://doi.org/10.1103/PhysRevB.84.045115.

[24] A. Jain, G. Hautier, C.J. Moore, S. Ping Ong, C.C. Fischer, T. Mueller, K.A. Persson, G. Ceder, A high-throughput infrastructure for density functional theory calculations, Computational Materials Science 50 (2011) 2295–2310.

https://doi.org/10.1016/j.commatsci.2011.02.023.

[25] A. Jain, S.P. Ong, G. Hautier, W. Chen, W.D. Richards, S. Dacek, S. Cholia, D. Gunter, D. Skinner, G. Ceder, K.A. Persson, Commentary: The Materials Project: A materials genome approach to accelerating materials innovation, APL Materials 1 (2013) 011002. https://doi.org/10.1063/1.4812323.

Chapter 3. Cu-based spinel/delafossite CHS materials

3.1 Introduction

Although Sr-based perovskite/brownmillerite meets some requirements for medium-high temperature redox-type CHS applications. Its limited heat storage density, resulting from their non-stoichiometric reaction properties, prompted a shift in our research focus back to stoichiometric reactions.

In 2009, Kato et al. [1] investigated the oxygen storage capacity of delafossite $CuMO_2$ (M = Al, Fe, Mn, Ga). They reported that the oxygen storage capacities of $CuMnO_2$ and $CuFeO_2$ were significantly higher than those of $CuAlO_2$, $CuGaO_2$, and CeO_2-based materials, with oxygen storage behavior occurring at relatively low temperatures (300–600 °C). Later, Kato's group explored Cu-based rare earth delafossites, $CuLaO_2$ and $CuYO_2$, as new oxygen storage materials [2], demonstrating capacities far superior to conventional CeO_2-based materials commonly used as promoters in automobile catalysts. Recently, Huang et al. [3] reported enhanced oxygen diffusion and storage capacity in monoclinic crednerite $CuMnO_2$ at lower temperatures through surface modification with CeO_2.

Based on previous research, Cu-based delafossite materials exhibit the unique ability to re-oxidize at relatively low temperatures, meeting a part of requirements for medium-high temperature CHS application. Furthermore, their distinct phase transitions may result in a higher reaction enthalpy, and thus greater heat storage density, compared to Sr-based perovskites. However, the goals of oxygen storage and heat storage research differ: the former emphasizes the oxidation process, while the latter prioritizes reaction reversibility, heat storage density, and durability. Additionally, more specific information is needed to confirm the feasibility of Cu-based spinel/delafossite systems for medium-high temperature CHS, particularly regarding their heat storage density and long-term durability.

Cu-based spinel/delafossite systems with Mn and Fe as secondary cations were synthesized using a modified Pechini method to explore potential materials for medium-

high temperature (500–1000 °C) CHS systems. The physicochemical properties were analyzed using XRD and SEM, while redox behavior and cyclability were studied through TGA, phase diagrams, and SEM. The oxidation enthalpy of each delafossite sample was measured using DSC.

3.2 Experimental approach

3.2.1 Material synthesis

Oxidized state CuM_2O_4 (M = Mn, Fe) spinel and reduced state $CuMO_2$ (M = Mn, Fe) delafossite were synthesized using a modified Pechini method [50]. Stoichiometric metal nitrate salts (1:1) were dissolved in deionized water, followed by the addition of citric acid (CA) at a 1:2 molar ratio (metal cation). Ethylene glycol was added as a reactant for polyesterification, and the pH of the solution was adjusted to 9 using ammonia. The solution was stirred at 120 °C for 4 hours, then dried in a vacuum oven for 24 hours. The resulting gel was pre-calcined at 500 °C for 1 hour. After grinding, the powder was heated at 960–1000 °C for 12 hours under different gas atmospheres. The specific synthesis conditions are summarized in Table 3-1. For convenience, samples heated in an oxidizing atmosphere are referred to as O-CuM (M = Mn, Fe), and those heated in a reducing atmosphere as R-CuM.

Table 3-1 Synthesis condition for each sample

M	Temperature (°C)	Atmosphere	Abb.
Mn	960	Air	O-CuMn
Mn	960	Ar	R-CuMn
Fe	1000	Air	O-CuFe
Fe	1000	Ar	R-CuFe

3.2.2 Crystal structural and morphological characterization

The structures of the pre-calcined, O-CuM, and R-CuM samples were analyzed using X-ray diffraction (XRD) (SmartLab, Rigaku Corp.). The crystalline phases of each

sample were identified with PDXL2 (Rigaku Data Analysis Software). The particle morphologies of the as-prepared O-CuM and R-CuM samples were investigated by scanning electron microscopy (SEM) (JSM-7500F, JEOL Ltd.).

3.2.3 Redox behavior investigation

The redox capacity of the oxidized-state samples was investigated using thermogravimetric analysis (TGA) (STA7300, HITACHI High-Tech Science Corp.). Two different temperature programs were applied. The first program involved heating and cooling from 500 °C to 1000–1065 °C at a rate of 20 °C/min under synthetic air flow. The second program followed a similar procedure but involved heating to 900–950 °C in N_2 flow, followed by re-oxidation at 600–650 °C in air. This program aimed to evaluate the reduction depth and the medium-temperature re-oxidation ability of each sample.

3.2.4 Oxidation enthalpies measurement

The reduced-state (R-CuM) samples were selected for oxidation enthalpy measurements using differential scanning calorimetry (DSC) (DSC-60, Shimadzu Corp.). An isothermal oxidation method was employed in this study. After heating the samples to the target temperature under N_2 protection, the gas was switched to synthetic air once the temperature stabilized. The resulting exothermic peak was monitored by the DSC and analyzed using TA-60WS software (Shimadzu Corp.).

3.2.5 Cyclability test

A 20-cycle program was designed for the cyclability test, consisting of continuous heating and cooling steps from 500 °C to 1000 °C in synthetic air. However, the holding time for each cycle was decreased to 10 minutes. The SEM morphology of samples after 10 and 20 cycles was examined to assess their durability. Additionally, XRD crystallite size analysis of the as-prepared and 20-cycle samples was conducted to further elucidate the redox mechanism.

3.3 Results and discussion

3.3.1 Materials characterization

The pre-calcined and as-prepared samples were characterized using XRD to investigate the preparation mechanism and determine the crystal structure. A summary of the results is provided in Table 3-2.

Table 3-2 Main phase, crystal structure and PDF-code of each sample

Sample	Main phase	Crystal Structure	PDF-#
Pre-CuMn	$Cu_{1.5}Mn_{1.5}O_4$	Cubic, F (0)	00-035-1172
	CuO	Monoclinic, Cc (9)	01-080-1916
O-CuMn	$CuMn_2O_4$	Cubic, Fd-3m (227)	01-074-1919
	CuO	Monoclinic, C2/c (15)	01-080-1268
R-CuMn	$CuMnO_2$	Monoclinic, C2/m (12)	00-050-0860
	$Cu(Cu_{0.04}Mn_{0.96})O_2$	Monoclinic, C2/m (12)	01-083-0034
Pre-CuFe	$Cu_{0.75}Fe_{2.25}O_4$	Cubic, Fd-3m (227)	01-073-2316
	CuO	Monoclinic, Cc (9)	01-080-1916
O-CuFe	$CuFe_2O_4$	Tetragonal, I41/amd (141)	01-072-1174
	CuO	Monoclinic, C2/c (15)	01-080-1268
R-CuFe	$CuFeO_2$	Trigonal, R-3m (166)	01-070-6670

The Pechini method has been widely used for synthesizing mixed metal oxides due to its versatility and precise component control. In this method, metallic cations are dispersed within a polymer framework formed by the polyesterification of citric acid and ethylene glycol. During the pre-calcination process, the organic framework is removed. As shown in Table 3-2, the primary phase of the pre-calcined sample indicates the initial formation of simple CuO and unsaturated phases. With further heating, Cu-based spinel

gradually develops. The detailed formation mechanism aligns with those reported in our previous research [4].

The typical XRD patterns of O-CuM and R-CuM are presented in Figure 3-1. According to the XRD results, none of the Cu-based spinels exhibited a pure phase; instead, they showed a mixture of the corresponding spinel and CuO, likely due to the equimolar amounts of metal nitrates used during synthesis. Interestingly, only R-CuFe displayed a pure $CuFeO_2$ phase (PDF-01-070-6670). In contrast, R-CuMn exhibited two distinct phases: $CuMnO_2$ (PDF-00-050-0860) and $Cu(Cu_{0.04}Mn_{0.96})O_2$ (PDF-01-083-0034).

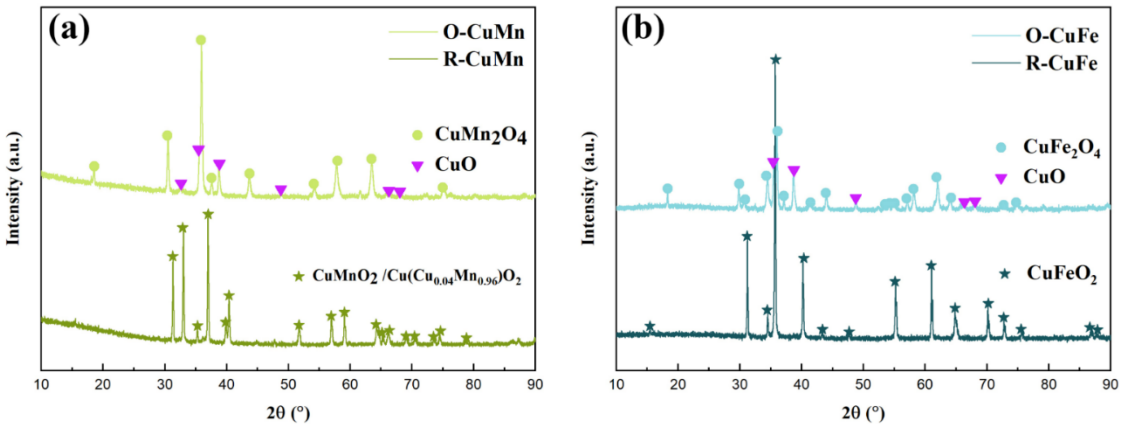

Figure 3-1 XRD patterns of (a) O-CuM; (b) R-CuM

The SEM images of the as-prepared O-CuMn and R-CuMn samples are shown in Figure 3-2, while those of O-CuFe and R-CuFe are presented in Figure 3-3. The low-magnification image of O-CuMn (Figure 3-2a) reveals that the particles agglomerated into large blocks, with small debris visible due to grinding prior to SEM observation. In contrast, R-CuMn (Figure 3-2c) exhibited well-distributed particles with sizes ranging from 2 to 3 μm. Notably, the particles of O-CuMn also appear as irregular strips, similar to those of O-CuFe (Figure 3-3a), but more aggregated. A prominent terrace-like structure is visible in the high-magnification images of both O-CuMn and R-CuMn (Figure 3-2b,

Figure 3-2d).

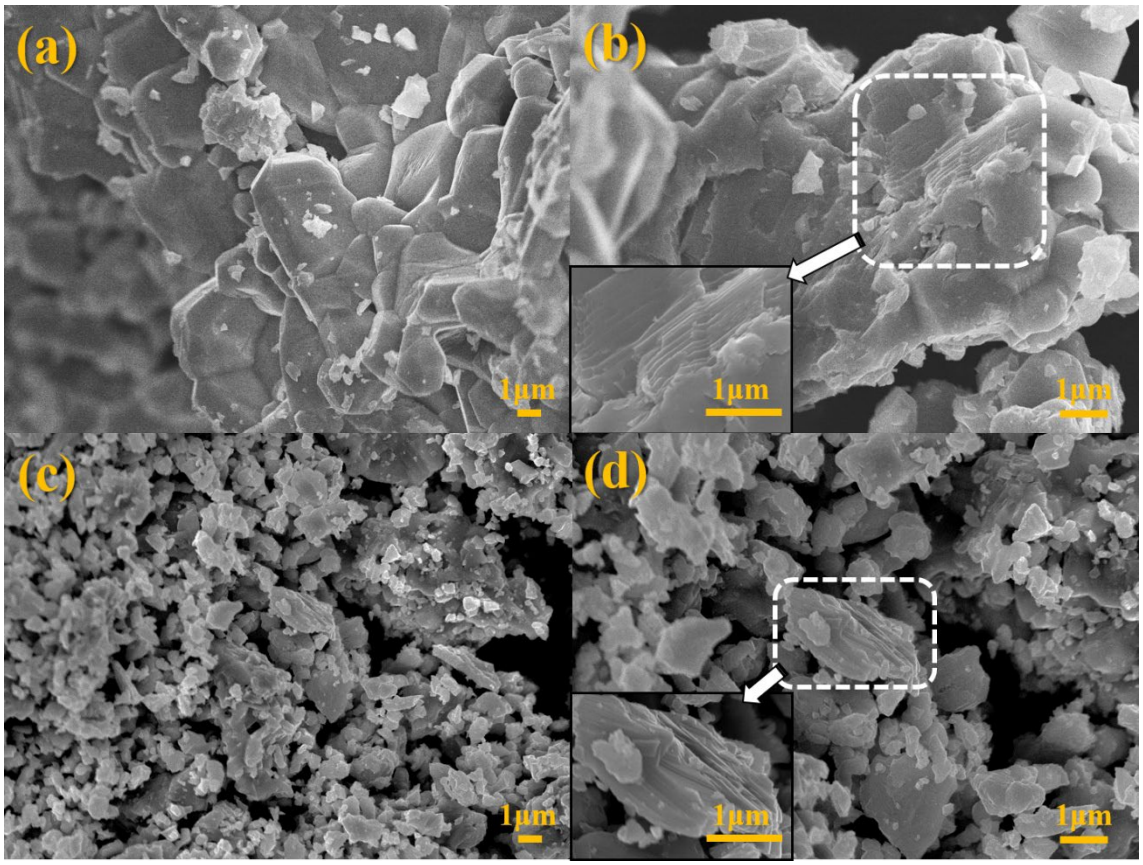

Figure 3-2 SEM images of the as-prepared samples: (a-b) O-CuMn; (c-d) R-CuMn.

Kato et al. [1] and Huang et al. [3] described delafossite-type oxides, such as $CuFeO_2$, $CuMnO_2$, $CuLaO_2$, and $CuYO_2$, as having a layered structure composed of edge-sharing MO_6 octahedra, with two-coordinated Cu+ cations occupying interlayer sites. However, their studies did not include morphological investigations of these delafossite-type materials. However, it is still reasonable to deduce that O-CuMn ($CuMn_2O_4$) also possesses a similar layered structure, sufficiently regular to be visible. Interestingly, R-CuFe exhibited a flaky structure with visible holes at low magnification (Figure 3-3c). However, the terrace-like structure—representing the edge-sharing MO_6 octahedral layers—was barely discernible, even at high magnification in O-CuFe and R-CuFe

(Figure 3-3b, Figure 3-3d), with the layers measuring less than 1 μm in length.

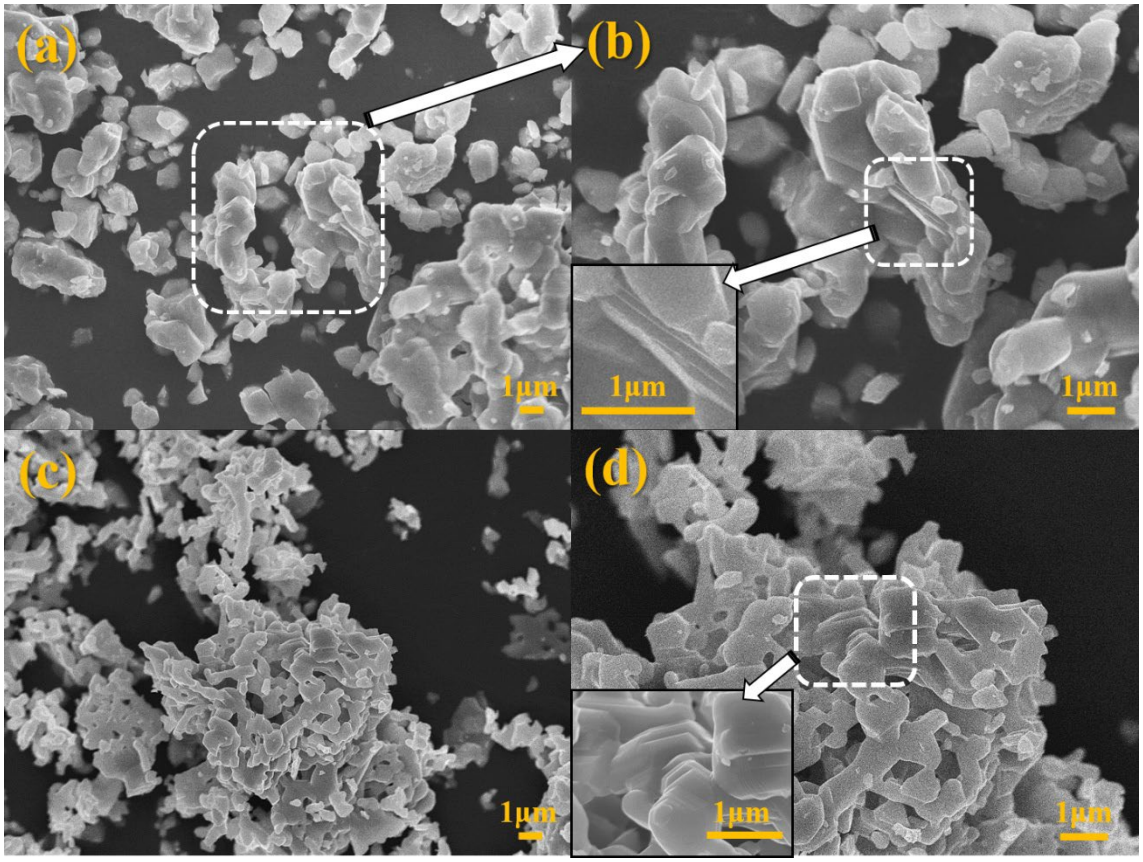

Figure 3-3 SEM images of as-prepared samples: (a-b) for O-CuFe; (c-d) for R-CuFe

3.3.2 Redox behavior

The redox behavior of O-CuMn is shown in Figure 3-4a. O-CuMn exhibited approximately a 4% mass change when heated to 1000 °C. In the second cycle, the mass changed rapidly at 980 °C ($T_{onset\text{-}red}$), differing from the smoother behavior observed in the first cycle. During the oxidation process, the reaction occurred at 900 °C ($T_{onset\text{-}ox}$) with a much stronger DTA signal peak than the reduction process.

According to the Cu-Mn-O phase diagram shown in Figure 3-4b, a mixed phase of spinel and CuO is observed when x(Cu)=0.5 at temperatures below 900 °C. This observation is consistent with the XRD results in Figure 3-1a, which indicate the presence

of a small amount of CuO. As the temperature increases, the system transitions to a mixed phase of spinel and delafossite, corresponding to the 4% mass change observed in Figure 3-4a. Driessens et al. [5] classified delafossite ($Cu_yMn_{1-y}O_2$, $0.54 < y < 0.6$, hexagonal) and crednerite ($Cu_yMn_{1-y}O_2$, $0.5 < y < 0.53$, monoclinic) as two distinct phases. Based on the Cu-Mn-O phase diagram, crednerite is considered the more reduced phase compared to delafossite. However, it is challenging to convert the spinel structure $CuMn_2O_4$ to the pure crednerite structure $CuMnO_2$ under normal air conditions at temperatures below 1000 °C.

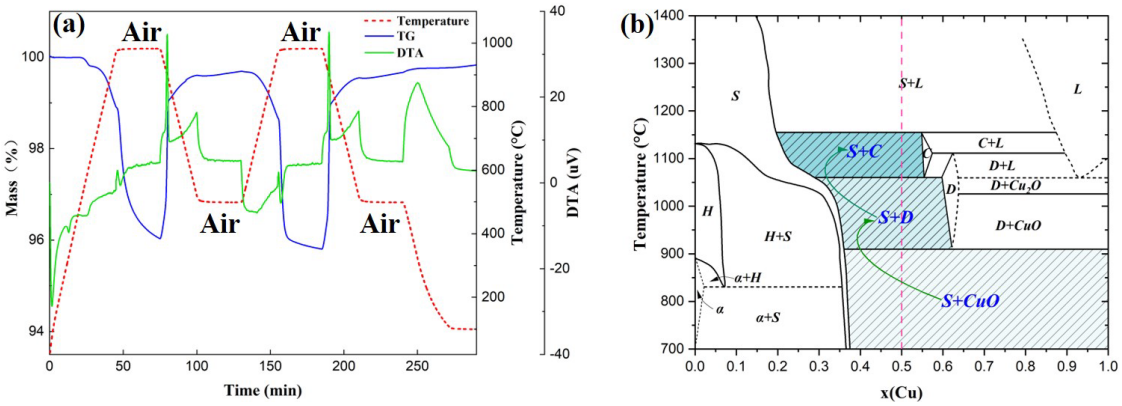

Figure 3-4 O-CuMn: (a) redox in air from 500 °C to 1000 °C; (b) Cu-Mn-O phase diagram (pO_2 = 0.21 atm), replotted from Driessens et al. (H = hausmannite, S = spinel, C = crednerite, D = delafossite, α = α-Mn_2O_3)

The redox behavior of O-CuFe (Figure 3-5a) was similar to that of O-CuMn but required higher temperatures for both reduction (1030 °C) and oxidation (950 °C), with a 5% change in mass. In contrast to O-CuMn, the endothermic peak accompanying the reduction of O-CuFe was clearly detectable. According to the Cu-Fe-O phase diagram (Figure 3-5b), replotted from Khvan et al. [6], the CuO + spinel mixed phase converts to a spinel + $CuFeO_2$ mixed phase at 925 °C. As with R-CuMn, the spinel peaks were not observed in the XRD pattern of R-CuFe, likely due to their small quantity. However,

previous studies reported this phase conversion at 1004 °C [7] and 1015 °C [8], closely aligning with our results.

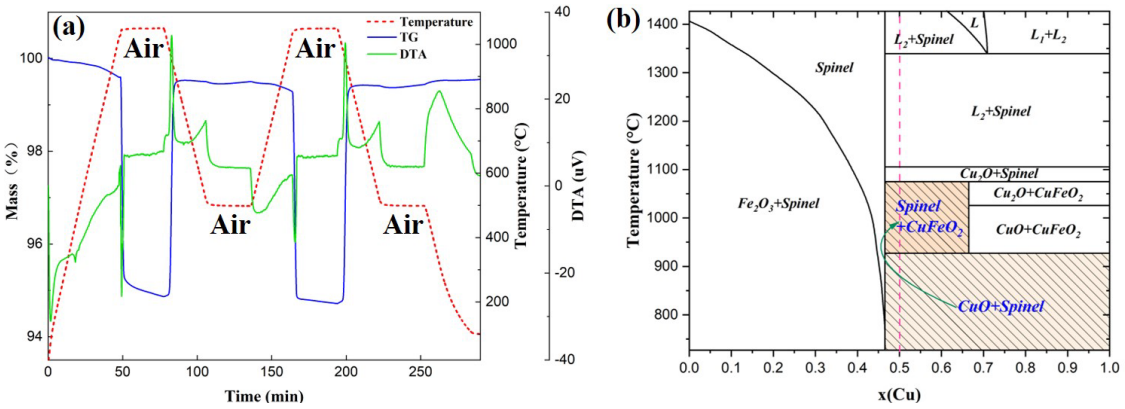

Figure 3-5 O-CuFe: (a) redox in air from 500 °C to 1065 °C; (b) Cu-Fe-O phase diagram (pO_2 = 0.21 atm), replotted from Khvan et al.

In our pre-experiment, we explored the re-oxidation ability of each sample within the medium temperature range. O-CuM was first reduced under N_2 flow, followed by isothermal oxidation at temperatures between 400 and 700 °C. After comparing their conversion rates and re-oxidation reaction times, a typical result of 600 °C is presented in Figure 3-6. As shown in the figures, O-CuMn underwent a deeper reduction, with approximately a 6% mass change at the lower temperature of 850 °C. Additionally, during isothermal oxidation at 600 °C, a much milder exothermic peak was observed. Meanwhile, O-CuFe exhibited a similar reduction depth under N_2 as compared to the behavior under air, suggesting that only one phase transition occurred during the reduction process (Figure 3-6b).

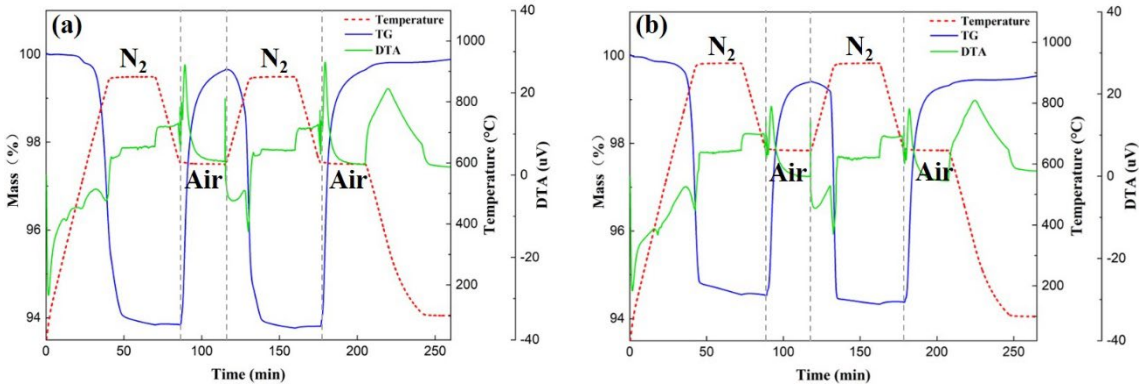

Figure 3-6 (a) O-CuMn: heated to 900 °C in N_2, followed by re-oxidation at 600 °C in air; (b) O-CuFe: heated to 950 °C, followed by re-oxidation at 650 °C in air.

As shown in Figures 3-4a and Figure 3-5a, O-CuMn and O-CuFe exhibited hysteresis (80 °C for both) between the reduction onset temperature and the oxidation onset temperature, similar to other well-known redox couples. For example, the hysteresis temperature is 30 °C for Co_3O_4/CoO and 200 °C for Mn_2O_3/Mn_3O_4 [9]. However, as indicated in Figure 3-6, the reduced O-CuMn and O-CuFe also demonstrated the ability to re-oxidize at temperatures significantly lower than their oxidation onset temperatures. This behavior can be explained by differences in the activation energy of oxidation. From a structural perspective, the presence of MO_6 octahedra may also facilitate this behavior.

A similar phenomenon has been reported in perovskites (general formula ABO_3), which also contain MO_6 octahedra. Specifically, the lattice oxygen in perovskites is released in a non-stoichiometric manner during heating, forming the $ABO_{3-\delta}$ phase. Zhang et al. [10] evaluated Ba- and Sr-based perovskites for solar energy storage, reporting that $SrCoO_3$, $SrFeO_3$, and $BaCoO_3$ reduced between 500 °C and 1000 °C and re-oxidized at 600 °C. Additionally, Jeen et al. [11] demonstrated that epitaxial stabilization could lower the redox temperature of $SrCoO_{3-\delta}$ to 200–300 °C. They also showed that the phase transition between $SrCoO_{3-\delta}$ (perovskite) and $SrCoO_{2.5}$ (brownmillerite) could occur within a remarkably short time (<1 min). It is important to note that although perovskites share a similar structure with spinels and delafossites, perovskites exhibit point-sharing MO_6

octahedra, whereas spinels and delafossites feature edge-sharing structures.

3.3.3 Reaction mechanism of $CuMn_2O_4$/$CuMnO_2$ under different oxygen partial pressures

Based on the results we observed in Section 3.3.2 and some related literatures [1,2,5,12–15], we believe that the reaction equations for $CuMn_2O_4$/$CuMnO_2$ redox couple vary slightly under different oxygen partial pressure conditions.

The reaction equation of Equation 3-1 was first introduced by Kato et al., who investigated $CuMO_2$ (M = Al, Fe, Mn, Ga, La, Y) as oxygen storage material.

$$2CuMnO_2(s) + \frac{1}{2}O_2(g) \rightleftharpoons CuMn_2O_4(s) + CuO(s) \qquad (3-1)$$

For $CuMnO_2$, a weight gain of approximately 6 wt% was observed during re-oxidation in air. André et al. [15] also reported a weight loss of approximately 6 wt% when the Cu-Mn oxide (x(Cu) = 0.5 (mol/mol)) underwent reduction in Ar. Although the experiments used different criteria for the initial weight (at oxidized or reduced state), both showed a consistent weight change of approximately 6 wt%, which aligns with the results we observed. However, we found that the theoretical maximum weight change should be 5.05 wt% (using the oxidized state as the reference) or 5.32 wt% (using the reduced state as the reference) when we applied Equation 3-1. This discrepancy suggests that the actual reaction mechanism may be more complicated than predicted. Although Huang et al. [3] explored more detailed reaction mechanisms in their subsequent work, they did not provide an in-depth discussion of this discrepancy.

In 1967, Driessens et al. reported the tetragonal phase of $Cu_xMn_{3-x}O_{4+\gamma}$ ($\gamma \approx 0.05$) while studying Cu-Mn-O phase diagram, describing it as a slight deformation of the cubic phase of $Cu_xMn_{3-x}O_4$ [5]. This excess oxygen may be the primary reason for the observed weight change exceeding the theoretical value predicted by the reaction equation.

Similarly, Hlongwa et al. [13] and Fan et al. [16] reported that the reversible decomposition reaction of $CuMn_2O_4$ in air can be described by the following equation:

$$CuMn_2O_4(s) \rightleftharpoons CuMnO_2(s) + \frac{1}{3}Mn_3O_4(s) + \frac{1}{3}O_2(g) \qquad (3-2)$$

By comparing Equation 3-1 and Equation 3-2, we find that the 1 mol of $CuMn_2O_4$ decomposes into 2 mol of $CuMnO_2$ and more 1/6 mol O_2 released under inert gas conditions. This suggests that the reduced state samples obtained in inert atmosphere may exhibit larger reduction depth. Since we prepared the samples using nitrate with a molar ratio of Cu : Mn was 1 : 1, the composition in the fully oxidized state should be a mixture of $CuMn_2O_4$ and CuO with the molar ratio of 1 : 1. Consequently, we rewrote Equation 3-2 to Equation 3-3, which corresponds to the oxidized state sample used in our experiments.

$$CuMn_2O_4(s) + CuO(s) \rightleftharpoons CuMnO_2(s) + \frac{1}{3}Mn_3O_4(s) + CuO(s) + \frac{1}{3}O_2(g) \quad (3-3)$$

Interestingly, we observed in our experiments that the weight change (approximately 4 wt%) was still larger than the theoretical weight change (3.48 wt%) calculated from the reaction equation in Equation 3-3. Moreover, during the TGA experiment at 1000 ℃, we observed a slow, continuous weight change, indicating that additional reactions may be occurring at high temperatures (Figure 3-4). On closer observation, it is possible that Mn_3O_4 continues to react with residual CuO to form more $CuMnO_2$, releasing additional oxygen (Equation 3-4). However, due to the limitation of chemical equilibrium in an air atmosphere, Equation 3-4 does not proceed fully, resulting in a smaller weight change than would be expected under an inert atmosphere.

$$\frac{1}{3}Mn_3O_4(s) + CuO(s) \rightleftharpoons CuMnO_2(s) + \frac{1}{6}O_2(g) \qquad (3-4)$$

3.3.4 Oxidation enthalpies measurement

R-CuMn and R-CuFe were selected for oxidation enthalpy measurements. The isothermal oxidation method was used during the oxidation enthalpy measurements. The sample was heated to the target temperature under N_2 flow. Once the temperature and DSC signal stabilized, the gas was then switched to air, resulting in a significant exothermic peak detected by the DSC apparatus. The oxidation enthalpies of R-CuMn and R-CuFe were 258.32 ± 15.31 kJ/kg-$CuMO_2$ (1402.68 ± 83.13 kJ/L-$CuMO_2$) and 190.35 ± 4.81 kJ/kg-$CuMO_2$ (1048.83 ± 26.50 kJ/L-$CuMO_2$), respectively (Figure 3-7).

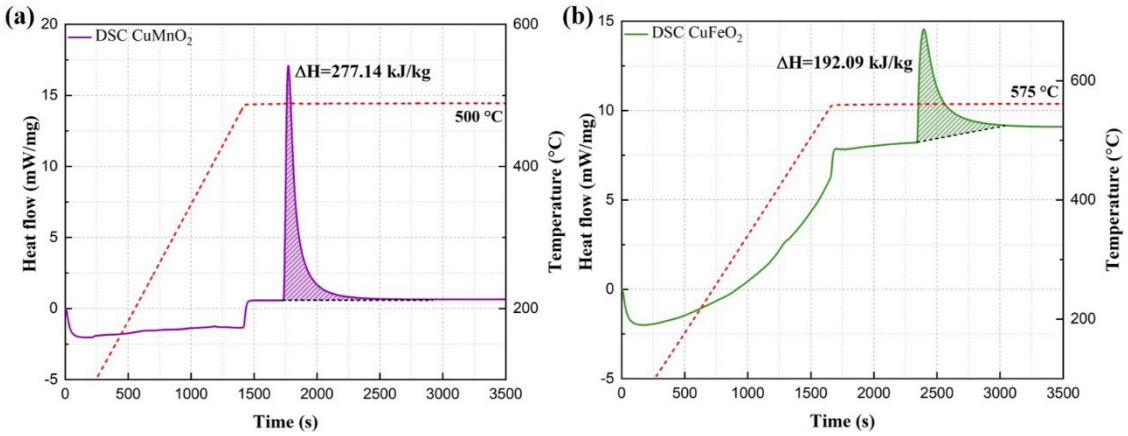

Figure 3-7 DSC curve of (a) R-CuMn and (b) R-CuFe with isothermal oxidation method

Notably, the oxidation enthalpy of $CuMnO_2$ reported here is significantly higher than previously reported values (145 kJ/kg [13,15]) . This difference is likely due to R-CuMn being in a deeper and purer reduced state than those obtained through TG reduction over several hours. Furthermore, the oxidation enthalpies of these Cu-based redox couples are several times higher than those of Sr-based perovskites (81.7 ± 3.4 kJ/kg-$ABO_{2.5}$ or 473.5 ± 20.0 kJ/L-$ABO_{2.5}$) reported in Chapter 2. In addition, a smooth baseline is observed in

Figure 3-7a, indicating that the specific heat capacities of the reactant and product were nearly identical. In contrast, R-CuFe exhibited a rugged baseline (Figure 3-7b), making it challenging to calculate precise values.

3.3.5 Cyclability test

Due to its favorable redox behavior in the range of 500–1000 °C and relatively higher oxidation enthalpy, O-CuMn was selected for further cyclability testing. A 20-cycle program was designed for the study, as shown in Figure 3-8a. In the first cycle, O-CuMn did not achieve the desired reduction depth, with only a 3.2% mass change. Interestingly, as the number of cycles increased, the reduction depth gradually improved. After 13 cycles, the mass change stabilized at approximately 4%. This suggests that O-CuMn undergoes a run-in period to reach optimal redox behavior under the shortened 10-minute holding time at high temperature.

Compared with the as-prepared O-CuMn (Figure 3-2b), the samples after 10 and 20 cycles (Figure 3-8b, c) exhibited a melting or collapse of the terrace-like structure. To better understand the redox mechanism, crystallite size analysis was performed using data extracted from XRD (Figure 3-9). The as-prepared sample had a crystallite size of 27 nm, which increased to 34 nm after 20 cycles. Notably, the XRD pattern of the 20-cycle sample shifted slightly to a lower angle (<1°), indicating an increase in interplanar spacing according to Bragg's law.

The small crystallite size and tight interplanar spacing may hinder the release of lattice oxygen, resulting in a macroscopically smaller oxygen exchange capacity. As the crystals grow and form larger structures over repeated cycles, the more ordered crystal lattice may facilitate faster binding of oxygen atoms to available sites, thereby accelerating the oxygen exchange rate within a short time.

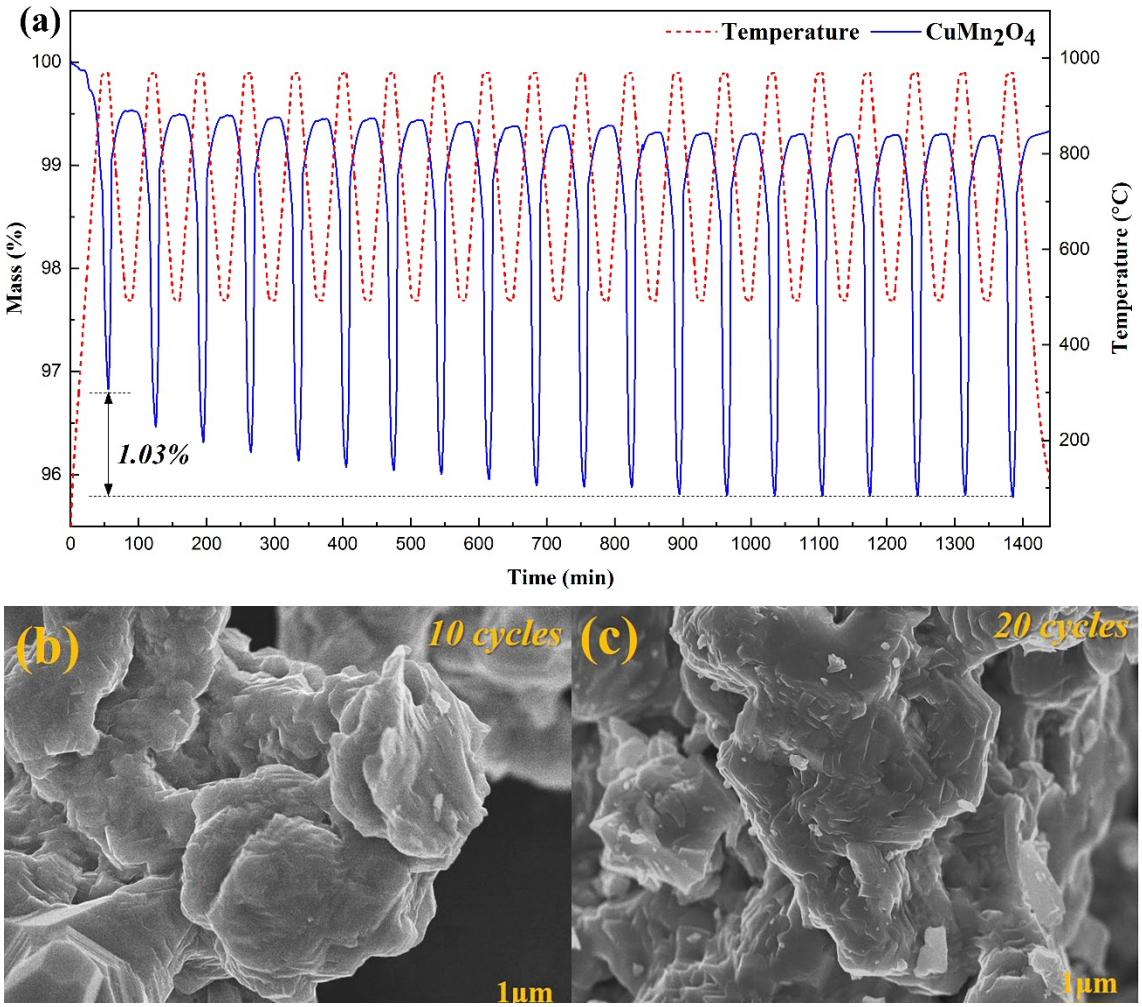

Figure 3-8 (a) Cyclability test of O-CuMn under synthetic air; (b) SEM image of the 10 cycles $CuMn_2O_4$; (c) SEM image of the 20 cycles $CuMn_2O_4$

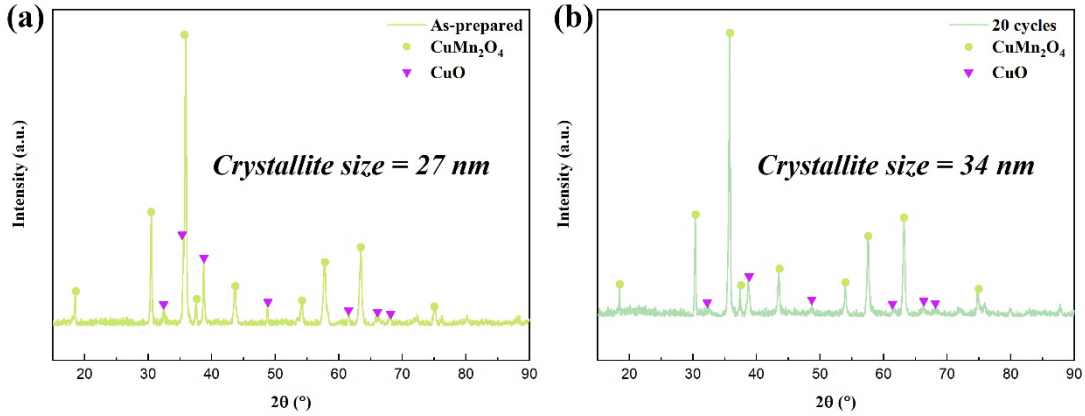

Figure 3-9 XRD patterns of (a) as-prepared and (b) 20 cycles O-CuMn

3.4 Conclusions

In this chapter, we investigated Cu-based spinel/delafossite systems with Mn and Fe as secondary cations to assess the feasibility of a redox-type chemical heat storage (CHS) system for medium to high-temperature applications. The Pechini method was selected for sample preparation due to its high component controllability. The physicochemical properties of the samples were characterized using XRD and SEM.

XRD results revealed that O-CuMn and O-CuFe exhibited CuM_2O_4 + CuO mixed phases, indicating that the input ratio of raw materials significantly influences phase formation. Notably, R-CuFe presented a pure $CuFeO_2$ delafossite phase, consistent with the Cu-Fe-O phase diagram. In contrast, R-CuMn exhibited a mixed phase of $CuMnO_2$ and $Cu(Cu_{0.04}Mn_{0.96})O_2$, making it challenging to determine the proportions of each phase.

SEM analysis of O-CuM and R-CuM revealed terrace-like structures, possibly related to the presence of edge-sharing MO_6 octahedral layers. O-CuMn demonstrated favorable redox behavior within the 500–1000 °C range, while O-CuFe required a higher reduction onset temperature (1030 °C). Despite having lower re-oxidation temperatures than their oxidation onset temperatures, both O-CuMn and O-CuFe were able to re-oxidize at 600 °C and 650 °C under air, respectively. The MO_6 octahedral structure may facilitate this re-oxidation behavior.

Reaction mechanism of $CuMn_2O_4/CuMnO_2$ under different oxygen partial pressures was investigated. The results indicate that, at the same temperature, a greater depth of reduction occurs in an inert gas atmosphere compared to air. Interestingly, regardless of the gas used for the reduction, the observed mass change is consistently larger than the value predicted by the chemical reaction equation, suggesting that the reaction mechanism of $CuMn_2O_4/CuMnO_2$ is more complex than expected.

Heat storage density measurements using DSC revealed oxidation enthalpies of 258.32 ± 15.31 kJ/kg-$CuMO_2$ (1402.68 ± 83.13 kJ/L-$CuMO_2$) for R-CuMn and 190.35 ± 4.81 kJ/kg-$CuMO_2$ (1048.83 ± 26.50 kJ/L-$CuMO_2$) for R-CuFe. In the 20-cycle cyclability

study of O-CuMn, the reduction depth gradually increased over repeated cycles, accompanied by the melting of the terrace-like structure. After a run-in period of 13 cycles, the mass change stabilized at approximately 4%.

Through this research, the $CuMn_2O_4/CuMnO_2$ emerged as a promising candidate for CHS applications. However, challenges related to undefined kinetics and relatively high reduction temperatures will be discussed in the following chapters.

Reference

[1] S. Kato, R. Fujimaki, M. Ogasawara, T. Wakabayashi, Y. Nakahara, S. Nakata, Oxygen storage capacity of CuMO2 (M = Al, Fe, Mn, Ga) with a delafossite-type structure, Applied Catalysis B: Environmental 89 (2009) 183–188. https://doi.org/10.1016/j.apcatb.2008.11.033.

[2] S. Kato, H. Sato, M. Ogasawara, T. Wakabayashi, Y. Nakahara, S. Nakata, Oxygen storage capacity of delafossite-type CuLnO 2 (Ln = La, Y) and their stability under oxidative/reductive atomosphere, Solid State Sciences 14 (2012) 177–181. https://doi.org/10.1016/j.solidstatesciences.2011.11.021.

[3] X. Huang, C. Ni, G. Zhao, J.T.S. Irvine, Oxygen storage capacity and thermal stability of the CuMnO2-CeO2 composite system, Journal of Materials Chemistry A 3 (2015) 12958–12964. https://doi.org/10.1039/c5ta01361e.

[4] X. Chen, M. Kubota, S. Yamashita, H. Kita, Investigation of Sr-based perovskites for redox-type thermochemical energy storage media at medium-high temperature, Journal of Energy Storage 38 (2021) 102501. https://doi.org/10.1016/j.est.2021.102501.

[5] F.C.M. Driessens, Phase Equilibria in the System Cu-Mn-O, Zeitschrift Für Anorganische Und Allgemeine Chemie 351 (1967) 48–62. https://doi.org/10.1023/A:1010113711219.

[6] A.V. Khvan, O.B. Fabrichnaya, G. Savinykh, R. Adam, H.J. Seifert, Thermodynamic assessment of the Cu-Fe-O system, Journal of Phase Equilibria and Diffusion 32 (2011) 498–511. https://doi.org/10.1007/s11669-011-9951-5.

[7] S.C. Schaefer, G.L. Hundley, F.E. Block, R.A. McCune, R.V. Mrazek, Phase equilibria and X-ray diffraction investigation of the system Cu-Fe-O, Metallurgical Transactions 1 (1970) 2557–2563. https://doi.org/10.1007/BF03038384.

[8] K.T. Jacob, K. Fitzner, C.B. Alcock, Activities in the spinel solid solution, phase equilibria and thermodynamic properties of ternary phases in the system Cu-Fe-O, Metallurgical Transactions B 8 (1977) 451–460. https://doi.org/10.1007/BF02696932.

[9] H.B. Dizaji, H. Hosseini, A review of material screening in pure and mixed-metal oxide thermochemical energy storage (TCES) systems for concentrated solar power (CSP) applications, Renewable and Sustainable Energy Reviews 98 (2018) 9–26. https://doi.org/10.1016/j.rser.2018.09.004.

[10] Z. Zhang, L. Andre, S. Abanades, Experimental assessment of oxygen exchange capacity and thermochemical redox cycle behavior of Ba and Sr series perovskites for solar energy storage, Solar Energy 134 (2016) 494–502. https://doi.org/10.1016/j.solener.2016.05.031.

[11] H. Jeen, W.S. Choi, M.D. Biegalski, C.M. Folkman, I.C. Tung, D.D. Fong, J.W. Freeland, D. Shin, H. Ohta, M.F. Chisholm, H.N. Lee, Reversible redox reactions in an epitaxially stabilized SrCoO x oxygen sponge, Nature Materials 12 (2013) 1057–1063. https://doi.org/10.1038/nmat3736.

[12] S. Kato, R. Kawashima, M. Ogasawara, Oxygen storage–release behavior of delafossite-type CuC1−xMxO2 (M = Fe, Ga), Journal of Materials Science 50 (2015) 2876–2883. https://doi.org/10.1007/s10853-015-8850-2.

[13] N.W. Hlongwa, D. Sastre, E. Iwuoha, A.J. Carrillo, C. Ikpo, D.P. Serrano, P. Pizarro, J.M. Coronado, Exploring the thermochemical heat storage capacity of AMn2O4 (A = Li or Cu) spinels, Solid State Ionics 320 (2018) 316–324.

https://doi.org/10.1016/j.ssi.2018.03.019.

[14] B.E. Martin, A. Petric, Electrical properties of copper–manganese spinel solutions and their cation valence and cation distribution, Journal of Physics and Chemistry of Solids 68 (2007) 2262–2270. https://doi.org/10.1016/j.jpcs.2007.06.019.

[15] L. André, S. Abanades, L. Cassayre, Experimental Investigation of Co-Cu, Mn-Co, and Mn-Cu Redox Materials Applied to Solar Thermochemical Energy Storage, ACS Applied Energy Materials 1 (2018) 3385–3395. https://doi.org/10.1021/acsaem.8b00554.

[16] J. Fan, Y. Zhang, Y. Yang, J. Hao, Y. Wang, A. Qian, Performance of thermochemical energy storage for spinel CuMn2O4 material, Journal of Energy Storage 41 (2021) 102881. https://doi.org/10.1016/j.est.2021.102881.

Chapter 4. Cr-doping effect on $CuMn_2O_4/CuMnO_2$ redox couple

4.1 Introduction

In Chapter 3, $CuMn_2O_4/CuMnO_2$ was identified as a promising candidate for CHS application due to its favorable properties. However, its relatively high reduction temperature poses a challenge for practical applications, necessitating further research to lower the operating temperature.

Recently, Portilla-Nieto et al. [1] from CIC energiGUNE reported the effects of Ni-doping on Co_3O_4, a well-known material in the CHS field. They found that $Co_{2.4}Ni_{0.6}O_4$ exhibited the lowest reduction temperature (735–800 °C) within the $Co_{3-x}Ni_xO_4$ ($0 \leq x \leq 1$) system, while maintaining relatively good reactivity. This finding suggests that the reduction/oxidation temperatures of CHS materials can potentially be minimized through element doping. However, according to the Cu-Ni-O phase diagram [2], Ni dopants may form a hard-to-decompose solid solution, $(Ni,Cu)O_{ss}$, with Cu in the $CuMn_2O_4/CuMnO_2$ redox couple, which means Ni may not be a good dopant for Cu-Mn complex oxides.

More recently, Carrillo et al. [3] explored the effect of Cr doping in the Mn_2O_3/Mn_3O_4 redox couple for CHS applications. Their results indicated that Mn_2O_3/Mn_3O_4 with 5% Cr doping exhibited improved cyclability, a faster re-oxidation rate, and reduced thermal hysteresis.

Based on the aforementioned literature, Cr-doping appears to be an effective approach to accelerate reaction rates and potentially regulate the operating temperature of the $CuMn_2O_4/CuMnO_2$ redox couple discussed in Chapter 3. Therefore, in this chapter, the effect of Cr-doping on the $CuMn_2O_4/CuMnO_2$ redox couple was investigated to develop novel medium-high temperature (500–1000 °C) CHS materials with improved performance.

The study of Cr doping in this chapter consists of two parts. **Part A** explores the effects across the entire doping concentration range (0–1.0), aiming to comprehensively analyze the trends of Cr doping on the reaction mechanism and heat storage properties of the $CuMn_2O_4/CuMnO_2$ system. **Part B** focuses on the specific doping levels that

demonstrated unique properties in **Part A**, providing an in-depth discussion of their effects on the microscopic structure to better understand and explain the observed macroscopic phenomena.

4.2 Part A-Experimental approach

4.2.1 Material synthesis

For spinel-type $CuMn_2O_4$, which follows the general formula AB_2O_4, Cr doping can be introduced at either the A or B site. In this study, we primarily focused on doping at the B site. Cr-doped $CuMn_2O_4$ (oxidation state, denoted as O-$CuCr_xMn_{1-x}$) and Cr-doped $CuMnO_2$ (reduction state, denoted as R-$CuCr_xMn_{1-x}$) were synthesized using a modified Pechini method as we introduced in the previous chapter.

Mixtures of $Cu(NO_3)_2 \cdot 3H_2O$, $Cr(NO_3)_2 \cdot 9H_2O$, and $Mn(NO_3)_2 \cdot 6H_2O$ in molar ratios of $1 : x : (1 - x)$ were dissolved in deionized water ($x = 0, 0.1, 0.3, 0.5, 0.7, 0.9, 1.0$). Citric acid and ethylene glycol were added as reactants for the polyesterification reaction. The solution was evaporated at 120 °C for 4 hours and dried in a vacuum oven for 1 day. After pre-calcination at 500 °C for 1 hour, the resulting powder was heated at 1000 °C for 12 hours (in air for O-$CuCr_xMn_{1-x}$; in Ar for R-$CuCr_xMn_{1-x}$).

4.2.2 Structural characterization

The structure and phase composition of the as-prepared O-$CuCr_xMn_{1-x}$ and R-$CuCr_xMn_{1-x}$ samples were investigated using XRD (SmartLab, Rigaku Corp.). The phase composition of each sample was analyzed with PDXL2 (Rigaku Data Analysis Software).

4.2.3 Redox and re-oxidation behavior investigation

The redox behavior of the O-$CuCr_xMn_{1-x}$ sample was investigated using TGA (STA7300, HITACHI High-Tech Science Corp.). The TGA temperature program included heating and cooling steps from room temperature to 1000 °C at a rate of 20 °C/min under a synthetic air flow of 200 mL/min.

R-$CuCr_xMn_{1-x}$ sample was heated from room temperature to 1000 ℃ at a rate of 20 ℃/min in synthetic air flow (200 ml/min). The heating process of each R-$CuCr_xMn_{1-x}$ sample was extracted for re-oxidation behavior investigation.

4.2.4 Oxidation enthalpies measurement

The R-$CuCr_xMn_{1-x}$ sample was selected for oxidation enthalpy measurement using DSC (DSC-60, Shimadzu Corp.) via the isothermal oxidation method. The sample was heated to the target temperature under N_2 protection, and once the temperature stabilized, the gas atmosphere was switched to synthetic air. With the introduction of oxygen, the oxidation reaction occurred, releasing heat rapidly. The exothermic peak was simultaneously monitored by the DSC.

4.2.5 Cyclability test

O-$CuCr_xMn_{1-x}$ (x = 0, 0.1, 0.3) was selected for a 20-cycle heating and cooling cyclability test within the temperature range of 500–1000 °C.

4.3 Part A-Results and discussion

4.3.1 Material Characterization

The XRD patterns of O-$CuCr_xMn_{1-x}$ and R-$CuCr_xMn_{1-x}$ (x = 0, 0.1, 0.3, 0.5, 0.7, 0.9, 1.0) in the 2θ range of 15°–90° are shown in Figure 4-1. As seen in Figure 4-1a, no significant differences are observed in the XRD patterns of O-$CuCr_xMn_{1-x}$ for x = 0, 0.1, 0.3, and 0.5. A comparison with the standard ICDD PDF cards for $CuMn_2O_4$ (01-074-1919) and $CuCr_2O_4$ (01-077-4323) indicates that both materials adopt a cubic crystal structure. Furthermore, the lattice constants and peak positions of these materials are so similar that Cr peaks are indistinguishable in the XRD patterns of O-$CuCr_xMn_{1-x}$ (x = 0, 0.1, 0.3, 0.5).

Interestingly, although O-$CuCr_{0.9}Mn_{0.1}$ and O-CuCr were prepared in air (pO_2 = 0.21 atm), an oxidizing atmosphere, they exhibited the same XRD patterns as their reduced

counterparts, R-$CuCr_{0.9}Mn_{0.1}$ and R-CuCr. This result suggests that during the heating process of Cr-rich samples (x > 0.7), the precursor initially converts to spinel-type $Cu(Cr_xMn_{1-x})_2O_4$, which subsequently transforms into delafossite at higher temperatures. However, Cr-rich samples (x > 0.7) lack the ability to re-oxidize into the spinel phase when the oxygen partial pressure is maintained at 0.21 atm.

Additionally, the appearance of $CuCrO_2$ characteristic peaks at 2θ = 31.3°, 36.3°, 40.8°, 55.7°, 61.6°, and 62.3° in the XRD pattern of O-$CuCr_{0.7}Mn_{0.3}$ indicates that the O-$CuCr_xMn_{1-x}$ system does not form an ideal solid solution. Instead, it forms a mixed phase of spinel and delafossite when x ≥ 0.7.

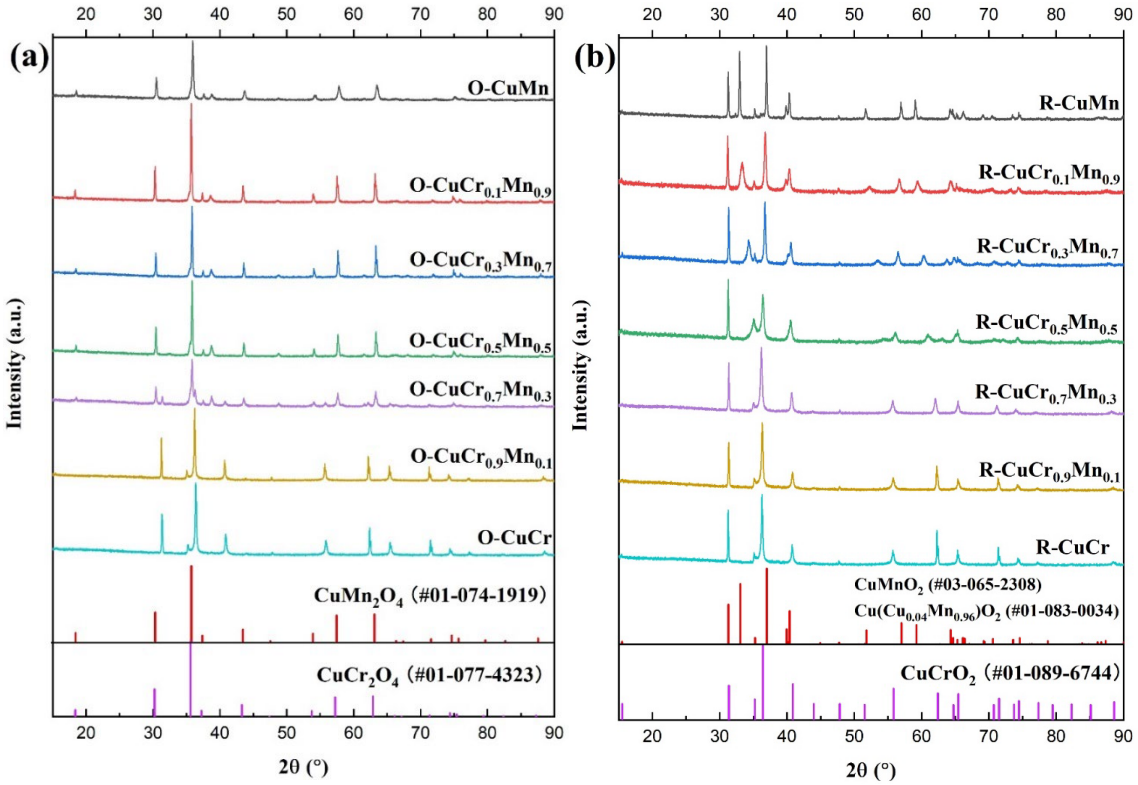

Figure 4-1 XRD patterns of each sample, (a): O-$CuCr_xMn_{1-x}$; (b): R-$CuCr_xMn_{1-x}$

R-CuMn exhibited two similar phases, $CuMnO_2$ (03-065-2308) and $Cu(Cu_{0.04}Mn_{0.96})O_2$ (01-083-0034), consistent with our findings in Chapter 3. Huang et

al. [5] reported that during the heating process of spinel-type $CuMn_2O_4$, the material easily converts to $Cu_{1+y}Mn_{1-y}O_2$. However, in this study, the influence of secondary phases can be considered negligible.

The delafossite-type $CuMnO_2$ and $CuCrO_2$ possess unique characteristic peaks. For instance, $CuCrO_2$ displays distinct peaks at 2θ = 55.7°, 62.3°, 65.3°, 71.4°, and 74.3°, which are absent in $CuMnO_2$. Notably, some characteristic peaks of $CuMnO_2$ exhibit shifting and broadening as the Cr content increases, indicating corresponding changes in its crystal structure.

4.3.2 Redox behavior

The redox behavior of each sample is shown in Figure 4-2. As illustrated in Figure 4-2a, when the Cr-doping level is between 0 and 0.5, a larger mass change was observed during the redox experiment as the Cr content increased. In contrast, O-$CuCr_{0.9}Mn_{0.1}$ and O-CuCr did not exhibit any redox capacity during the heating and cooling process, aligning with the XRD results indicating that these samples were already in their reduced state.

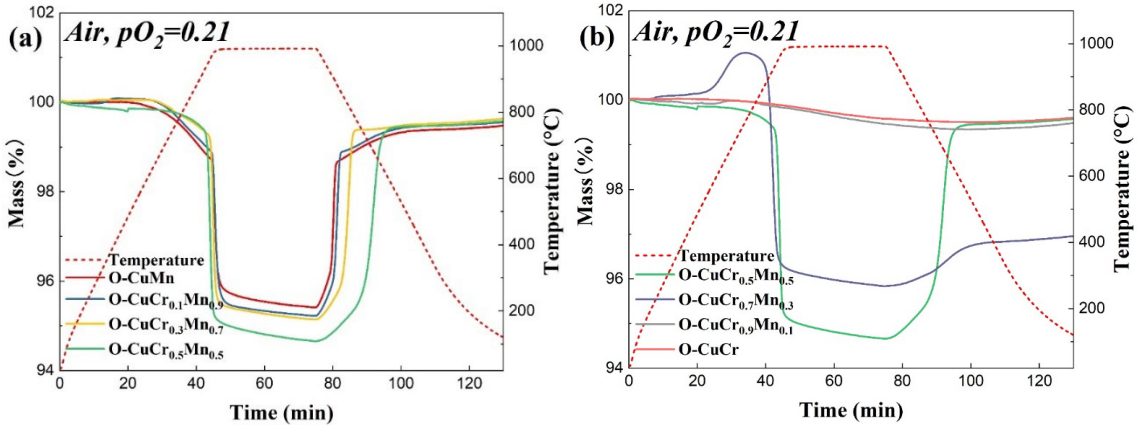

Figure 4-2 Redox behaviors of O-$CuCr_xMn_{1-x}$, (a): x = 0-0.5; (a): x = 0.5-1

O-$CuCr_{0.7}Mn_{0.3}$ demonstrated re-oxidation behavior within the temperature range of 550–750 °C, suggesting the presence of its reduced state. However, once O-$CuCr_{0.7}Mn_{0.3}$

was fully reduced, it became difficult to re-oxidize within a short time.

On the other hand, we observed that when the temperature was below approximately 900 °C, each material exhibited varying degrees of oxygen non-stoichiometric behavior, similar to what has been reported in other spinel-type materials [6,7]. However, this behavior cannot be attributed to the phase transition between spinel and delafossite. As the Cr content increased, the mass change associated with non-stoichiometry decreased.

We believe that the heat storage capacity of Cu-Mn oxide CHS materials is primarily driven by the phase transition between spinel and delafossite. Therefore, reducing the contribution of non-stoichiometric mass change would be more favorable for enhancing heat storage performance.

The mass change, reduction starting temperature, and oxidation ending temperature of each redox-active sample are summarized in Table 4-1. Notably, the reduction starting temperatures of Cr-doped materials were slightly lower than that of pure $CuMn_2O_4$. This observation aligns with the Cu-Cr-O (Figure 4-3) [8] and Cu-Mn-O phase diagrams presented in Chapter 3, which indicate that $CuMn_2O_4$ requires a higher reduction temperature (920 °C) compared to $CuCr_2O_4$ (782 °C). However, the oxidation ending temperatures exhibited greater variability as the Cr content increased, resulting in larger temperature hysteresis.

Table 4-1 Properties summary of redox-active samples

Sample	Mass Change (%)	Reduction Starting Temp. (°C)	Oxidation Ending Temp. (°C)
O-CuMn	4.57	969	883
O-$CuCr_{0.1}Mn_{0.9}$	4.78	966	859
O-$CuCr_{0.3}Mn_{0.7}$	4.86	956	784
O-$CuCr_{0.5}Mn_{0.5}$	5.34	934	611

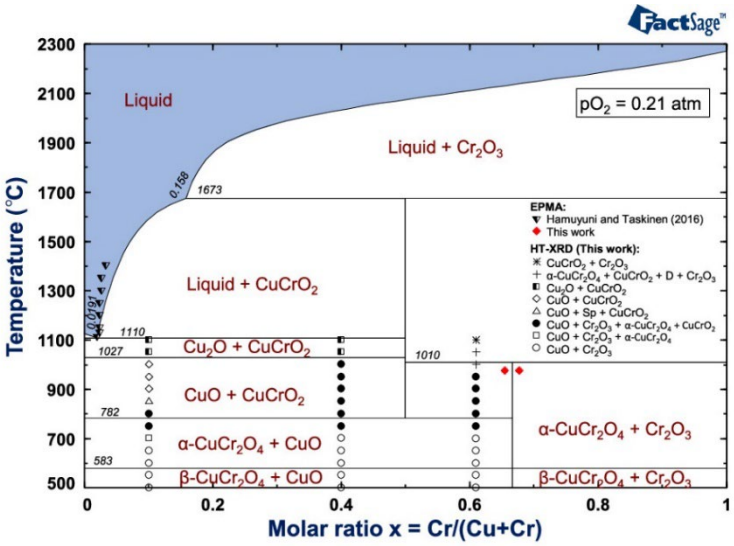

Figure 4-3 Phase diagram of Cu-Cr-O (pO_2=0.21 atm)

4.3.3 Re-oxidation behavior

The re-oxidation behavior of R-$CuCr_xMn_{1-x}$ is shown in Figure 4-4. R-$CuCr_{0.9}Mn_{0.1}$ and R-CuCr did not exhibit any re-oxidation capacity during the non-isothermal heating process with a ramp rate of 20 °C/min. The most noteworthy aspect of Figure 4-4 is that the Cr-doped samples ($x \leq 0.7$) demonstrated faster reaction rates than R-CuMn, as the slope of each curve reflects the reaction rate under a fixed heating ramp. Additionally, the re-oxidation reaction of R-$CuCr_{0.1}Mn_{0.9}$ occurred at a lower temperature (305 °C) compared to R-CuMn (337 °C). However, R-$CuCr_{0.5}Mn_{0.5}$ and R-$CuCr_{0.7}Mn_{0.3}$ required higher temperatures for their re-oxidation reactions, despite exhibiting faster reaction rates than R-CuMn.

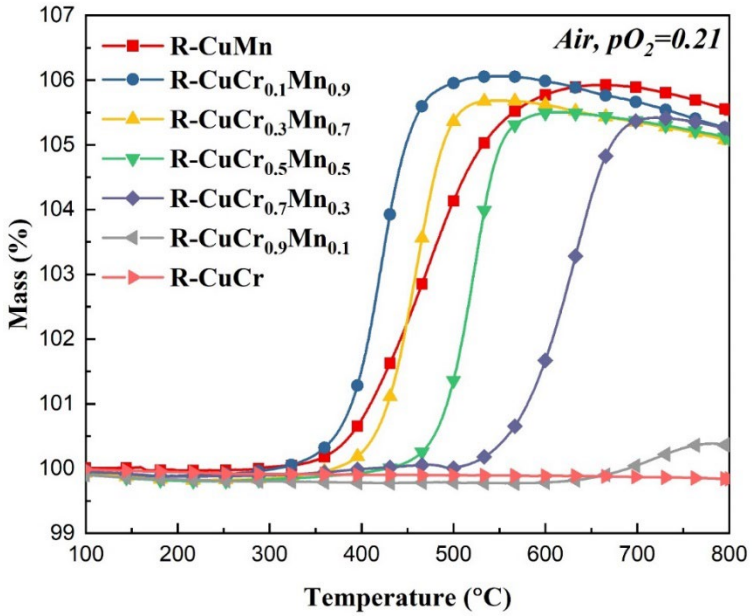

Figure 4-4 Re-oxidation behaviors of R-$CuCr_xMn_{1-x}$

4.3.4 Reaction mechanism of Cr-doped $CuMn_2O_4/CuMnO_2$

In Chapter 3, we discussed how the reaction equation of the $CuMn_2O_4/CuMnO_2$ system may vary under different oxygen partial pressures. The doping of Cr may also influence the reaction mechanism, as evidenced by the significantly larger mass changes observed in Cr-doped samples compared to the undoped ones (Figure 4-2).

We previously explained that the reduction of the oxidized sample should ideally yield a pure delafossite-type phase. However, reduction in an air atmosphere is insufficient, resulting in the presence of the Mn_3O_4 phase. We hypothesize that Mn_3O_4 could continue to react with unreacted CuO to generate additional delafossite phases. However, due to certain limitations (e.g., temperature), the reaction cannot proceed to completion. Similarly, we propose that the Cr-doped samples exhibit the same phenomenon. The reaction equation for the redox process in air can be expressed as follows:

$$Cu(Cr_xMn_{1-x})_2O_4(s) + CuO(s) \rightleftharpoons CuCr_xMn_{1-x}O_2(s) + \frac{1}{3}(Cr_xMn_{1-x})_3O_4(s) + CuO(s) + \frac{1}{3}O_2(g) \quad (4-1)$$

$$\frac{1}{3}(Cr_xMn_{1-x})_3O_4(s) + CuO(s) \rightleftharpoons CuCr_xMn_{1-x}O_2(s) + \frac{1}{6}O_2(g) \quad (4-2)$$

From Figure 4-2, we also observe that when the Cr doping level is below 0.5, the forward progression of Equation 4-2 appears to be more favorable, as indicated by the larger mass changes.

When the samples are reduced in an inert gas, the chemical reaction equation can be expressed as follows:

$$Cu(Cr_xMn_{1-x})_2O_4(s) + CuO(s) \rightleftharpoons 2\,CuCr_xMn_{1-x}O_2(s) + \frac{1}{2}O_2(g) \quad (4-3)$$

Equation 4-3 can be considered a combination of Equation 4-1 and Equation 4-2, driving the reaction in Equation 4-2 forward due to the lower oxygen partial pressure in the inert gas. As shown in Figure 4-4, the mass increment of each sample (~6 wt%) is nearly identical, indicating that their oxidation reactions can be described by the reverse of Equation 4-3.

4.3.5 Oxidation enthalpies

The redox-active samples R-$CuCr_xMn_{1-x}$ (x = 0, 0.1, 0.3, 0.5) were selected for oxidation enthalpy measurement using the isothermal oxidation method. A typical DSC curve of R-CuMn is shown in Figure 4-5a, where a sharp exothermic peak, corresponding to the oxidation reaction, is observed. Figure 4-5b presents the oxidation enthalpies of each sample: 236.11 ± 5.40 kJ/kg (1.30 ± 0.03 MJ/L) for R-CuMn, 293.67 ± 1.25 kJ/kg (1.62 ± 0.01 MJ/L) for R-$CuCr_{0.1}Mn_{0.9}$, 305.61 ± 16.45 kJ/kg (1.68 ± 0.09 MJ/L) for R-$CuCr_{0.3}Mn_{0.7}$, and 292.59 ± 7.00 kJ/kg (1.61 ± 0.04 MJ/L) for R-$CuCr_{0.5}Mn_{0.5}$. It is worth

noting that the heat storage densities present here are calculated based on the reduced state.

As the Cr content increases, the heat storage density initially increases but subsequently decreases, suggesting that a small amount of Cr improves the material's heat storage density. However, when the Cr content exceeds a certain threshold (x > 0.3), the non-redox behavior associated with $CuCrO_2$ becomes dominant, reducing the material's heat storage density and even hindering its re-oxidation behavior.

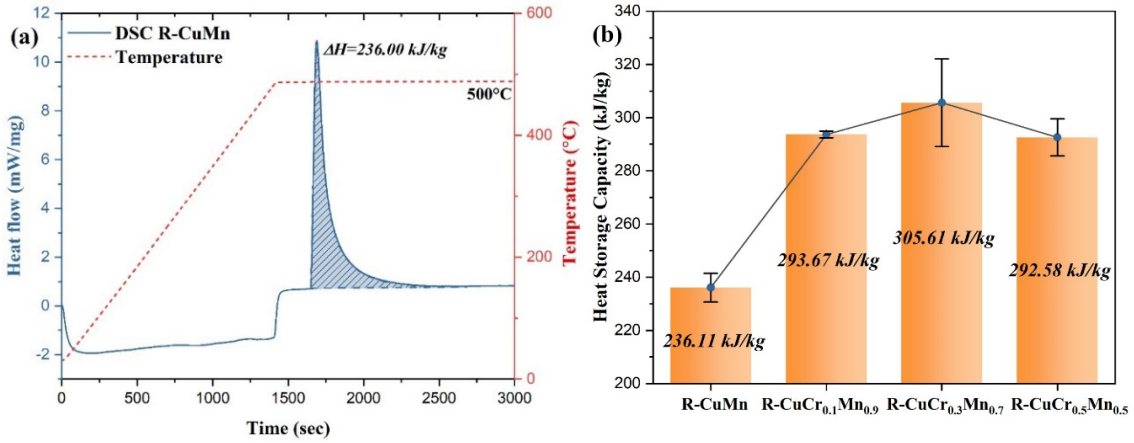

Figure 4-5 (a) A typical DSC curve of R-CuMn (re-oxidation in air, pO_2 =0.21 atm); (b) Oxidation enthalpies of R-$CuCr_xMn_{1-x}$ (x = 0, 0.1, 0.3, 0.5)

4.3.6 Cyclability test

Due to the favorable redox behavior and higher heat storage density, O-$CuCr_{0.1}Mn_{0.9}$ and O-$CuCr_{0.3}Mn_{0.7}$ were selected for a 20-cycle cyclability test within the temperature range of 500–1000 °C. For comparison, the cyclability of O-CuMn was also evaluated using the same TGA heating/cooling program, with a typical TGA profile for O-CuMn shown in Figure 4-6a.

The mass changes (Δm) of each sample over the 500–1000 °C range are summarized in Figure 4-6b. Both O-CuMn and O-$CuCr_{0.1}Mn_{0.9}$ exhibited stable mass changes

throughout the 20-cycle test, while O-$CuCr_{0.3}Mn_{0.7}$ showed more fluctuant behavior. It is noteworthy that the Cr-doped samples exhibited larger mass changes compared to the undoped sample, consistent with the redox results shown in Figure 4-6b, which was also discussed in Section 4.3.4.

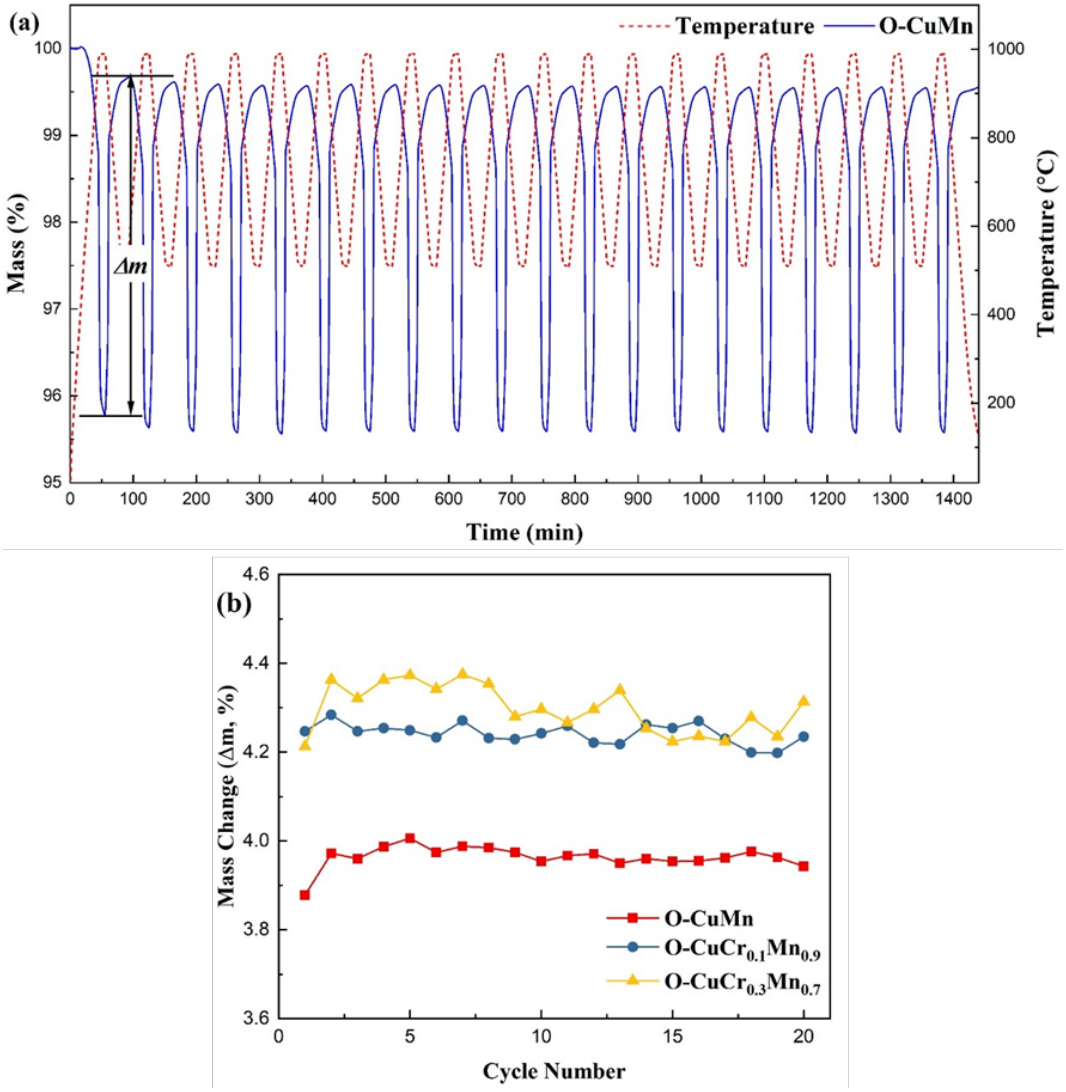

Figure 4-6 (a) A typical 20 cycles TGA program of O-CuMn in synthetic air (500-1000 ℃), holding time for 10 mins; (b) Summary of mass changes of each sample during 20 cycles test

4.4 Part B-Experimental approach

4.4.1 Rietveld refinement analysis by XRD

To investigate the effect of small amounts of Cr doping on the crystal parameters of base material (such as lattice constants and angles, unit cell volumes, and atomic positions), the Rietveld refinement analysis was performed.

For the analysis, the precise diffraction data of R-$CuCr_xMn_{1-x}$ (x = 0, 0.1, 0.3) was collected by XRD (Smartlab, Rigaku Corp.) in the experimental condition of 2θ range of 10 – 120°, scan speed of 2°/min, and scan step of 0.02°, with Cu Kα radiation (λ = 0.15418 nm, 40 kV – 25 mA). The crystalline phase of each sample was also determined using PDXL2 (Rigaku Data Analysis Software). After the initial phase analysis, the obtained XRD diffraction patterns were analyzed by Rietveld method using GSAS-II software package [4].

4.4.2 Morphology analysis by SEM-EDS

For the morphology analysis of each sample and elemental ratios of Cu, Cr and Mn in the system, the R-$CuCr_xMn_{1-x}$ (x = 0, 0.1, 0.3) was observed as a representative for either reduced state or oxidized state using SEM (JSM-7500F, JEOL) equipped with EDS (JEOL).

4.4.3 Elemental valence analysis by XPS

The elemental valence investigation of R-$CuCr_xMn_{1-x}$ (x = 0, 0.1, 0.3) was performed using XPS (ESCALAB250Xi, Thermo-Fisher Scientific) with Mg/Al X-ray source. All the XPS measurements were performed inside the analysis chamber under an average base vacuum of 1.0×10^{-8} – 10^{-10} mBar. After comparing the experimental C1s signal with standard value of 284.8 eV, no binding energy calibration was performed because the small specimen charging phenomenon was not observed.

4.5 Results and discussion of Part B

4.5.1 In-depth investigation R-CuCr$_x$Mn$_{1-x}$ (x = 0, 0.1, 0.3) based on crystal structure

From the results of re-oxidation behavior (Figure 4-4) and oxidation enthalpies (Figure 4-5), we observe that a small amount of Cr doping yields interesting effects. Specifically, R-CuCr$_{0.1}$Mn$_{0.9}$ exhibits a lower re-oxidation temperature than R-CuMn, while R-CuCr$_{0.3}$Mn$_{0.7}$ shows the highest heat storage density. However, further increases in Cr doping led to a deterioration in reactivity and a decline in heat storage density. In this section, we aim to explain the effect of small amounts of Cr doping based on investigations into crystal structure, morphology, and chemical valence.

The XRD patterns of R-CuCr$_x$Mn$_{1-x}$ are shown in Figure 4-7a. As discussed in the previous section, the reduced state of $CuMn_2O_4$ can exhibit two similar phases: $CuMnO_2$ (#03-065-2308) and $Cu_{1.04}Mn_{0.96}O_2$ (#01-083-0034). Some researchers have reported that in pure crednerite $CuMnO_2$, Cu typically exhibits a valence of +1, while Mn has a valence of +3. However, when the elemental ratio of Cu to Mn deviates from the ideal 1:1 ratio, the average valence of the Cu element may shift to a higher value.

From Figure 4-7a, noticeable peak shifts can be observed at 31° (002), 33° (200), and 37° ($\bar{1}$11), suggesting that certain cell parameters are changed by Cr doping. We further employed Rietveld refinement to obtain more accurate parameters, with the results presented in Figures 4-7b,c,d and Table 4-2.

Although minor fluctuations exist between the fitted curve and the actual pattern in the 30–40° range (Figures 4-7b,c,d), the overall errors (Rwp ≤ 10; GOF (Goodness of Fit) ≤ 2) are small enough to be considered reliable. As shown in Table 4-2, a small amount of Cr doping does not change the space group of the Cu-Mn oxide system.

With increasing Cr content, the parameters *b*, *c*, and *β* show an increasing trend, while *a* exhibits a more pronounced decrease. This reduction in *a* leads to a smaller overall cell volume in the Cr-doped materials (92.18 Å^3 for R-CuMn, 91.44 Å^3 for R-CuCr$_{0.1}$Mn$_{0.9}$,

and 90.16 Å^3 for R-CuCr$_{0.3}$Mn$_{0.7}$). Furthermore, Cr doping alters the bond distances between elements, such as the formation of shorter Cu-O and Mn-Mn bonds along the *a* -axis, which may account for the observed changes in cell volume.

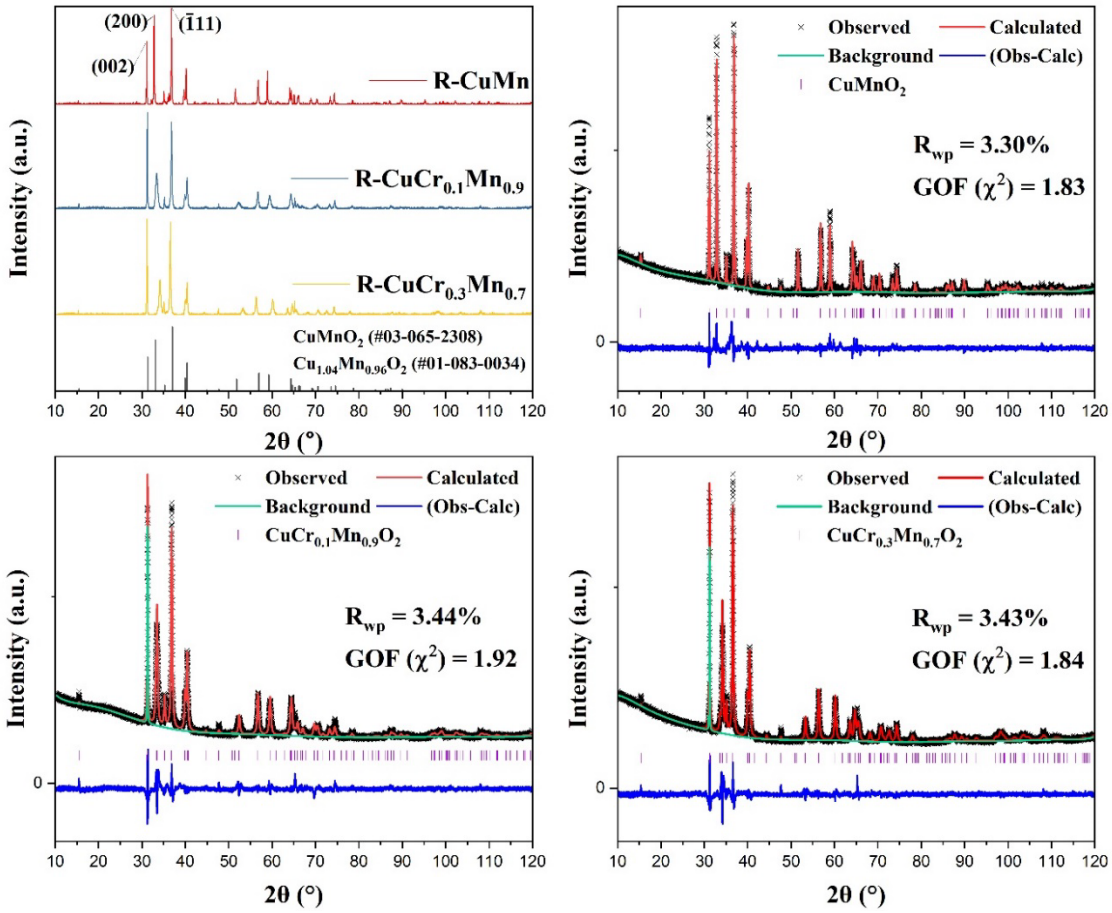

Figure 4-7 (a)XRD patterns of R-CuCr$_x$Mn$_{1-x}$ (x = 0, 0.1, 0.3); (b) Rietveld refinement for R-CuMn; (c) Rietveld refinement for R-CuCr$_{0.1}$Mn$_{0.9}$; (d) Rietveld refinement for R-CuCr$_{0.3}$Mn$_{0.7}$

It is worth noting that the MO_6 octahedra of R-CuCr$_{0.1}$Mn$_{0.9}$ exhibit the most similar Mn-O' (apical) and Mn-O'' (equatorial) bond lengths, indicating that R-CuCr$_{0.1}$Mn$_{0.9}$ has a lower degree of Jahn-Teller distortion (as reflected by the Mn-O' (apical) / Mn-O'' (equatorial) ratio) [9]. In non-linear molecular systems, it is common for the system to

reduce its symmetry and energy through geometric distortion to enhance stability, a phenomenon known as Jahn-Teller distortion [10]. Therefore, the lower Jahn-Teller distortion in R-$CuCr_{0.1}Mn_{0.9}$ places it in a more energetically unstable state.

The reduced phase, which typically forms only at high temperatures, is retained during the cooling process under an Ar atmosphere (extremely low oxygen partial pressure), leaving the material with higher exergy. However, the exergy, or energy preserved through phase transition, can be released by heating or other forms of stimulation (such as microwave irradiation and mechanical friction). This structural instability may result in the easier re-oxidation behavior observed for R-$CuCr_{0.1}Mn_{0.9}$ in previous Section 4.3.3 ($T_{re\text{-}ox}$ of 305 °C for R-$CuCr_{0.1}Mn_{0.9}$ vs. 337 °C for R-CuMn).

Interestingly, oxygen atoms enter the crystal structure along the *a*- and *b*-axis directions during the re-oxidation process (Figure 4-8). However, the shorter Cu-O bond distances and reduced cell volume caused by Cr doping may hinder the re-oxidation process. This hindrance can be seen as competing with the "catalytic effect" associated with the structural instability described above.

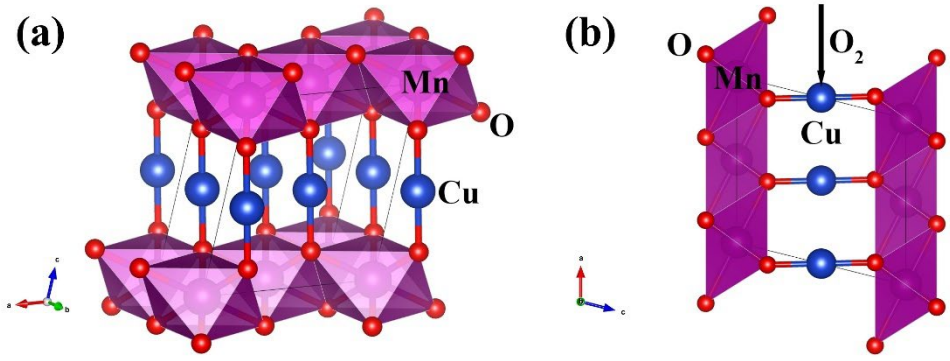

Figure 4-8 Cell model of $CuMnO_2$ (PDF card: #03-065-2308)

Table 4-2 Cell parameters summarization of R-$CuCr_xMn_{1-x}$ (x = 0, 0.1, 0.3)

Sample/parameters	**R-$CuMnO_2$**	**R-$CuCr_{0.1}Mn_{0.9}$**	**R-$CuCr_{0.3}Mn_{0.7}$**
Space group	*C2/m*	*C2/m*	*C2/m*
Cell parameters			
a (Å)	5.5937	5.5249	5.4153
b (Å)	2.8830	2.8971	2.9179
c (Å)	5.8906	5.9033	5.9161
α (Å)	90	90	90
β (Å)	103.9920	104.5950	105.3360
γ (Å)	90	90	90
Cell volume ($Å^3$)	92.1770	91.4380	90.1550
Occupancy			
Cu	1	1	1
Cr	0	0.1	0.3
Mn	1	0.9	0.7
Bond distances			
Mn-O' (apical)	2.2971 × 2	2.1078 × 2	2.1341 × 2
Mn-O'' (equatorial)	1.9294 × 4	2.0698 × 4	2.0428 × 2
Mn-Mn (Å)	3.1485 × 4	3.1191 × 4	3.0757 × 4
	2.8830 × 2	2.8971 × 2	2.9179 × 4
Cu-O (Å)	1.8174 × 2	1.7578 × 2	1.7373 × 2
R_{wp} (%)	3.298	3.436	3.428
GOF (χ^2) (%)	1.83	1.92	1.84

4.5.2 In-depth investigation R-CuCr$_x$Mn$_{1-x}$ (x = 0, 0.1, 0.3) based on morphology

The morphologies of the as-prepared R-CuCr$_x$Mn$_{1-x}$ samples are shown in Figure 4-9. R-CuMn exhibits the typical spinel/delafossite-type bulk-shaped particles with some degree of agglomeration, consistent with our previous observations in Chapter 3. Generally, samples with Cr addition display a smaller particle size distribution, with R-CuCr$_{0.3}$Mn$_{0.7}$ exhibiting the smallest particle size, approximately 2 µm. Because all samples underwent the same grinding process (10 minutes), the effect of grinding time can be considered negligible. These findings suggest that Cr addition significantly influences both the morphology and particle size of the samples.

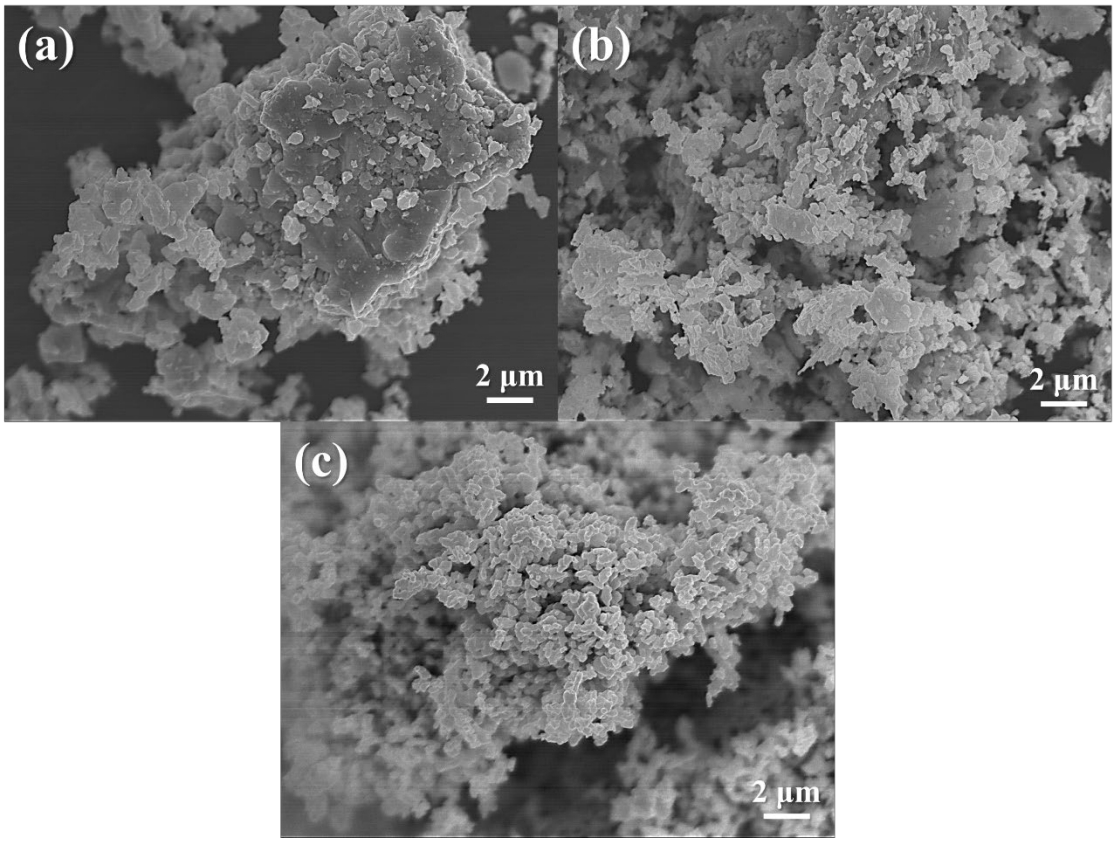

Figure 4-9 SEM morphology of (a): R-CuMn; (b): R-CuCr$_{0.1}$Mn$_{0.9}$; (c): R-CuCr$_{0.3}$Mn$_{0.7}$

In general, particles consist of grains (or crystallites) with varying sizes and orientations. As noted earlier, the cell volume of the reduced-state material decreases with

increasing Cr doping, which may also limit the particle size. Additionally, small amounts of Cr dopants—acting as impurities—can lower the energy required for particle formation at nucleation sites, a common phenomenon in heterogeneous nucleation [11].

According to the EDS elemental mapping (Figure 4-10a,b,c), the distribution of Cr is uniform, enabling nucleation to occur simultaneously at multiple locations, which contributes to the reduced particle size. Furthermore, SEM-EDS elemental ratio analysis (Figure 4-10d) confirmed that the target product was synthesized precisely using the modified Pechini method.

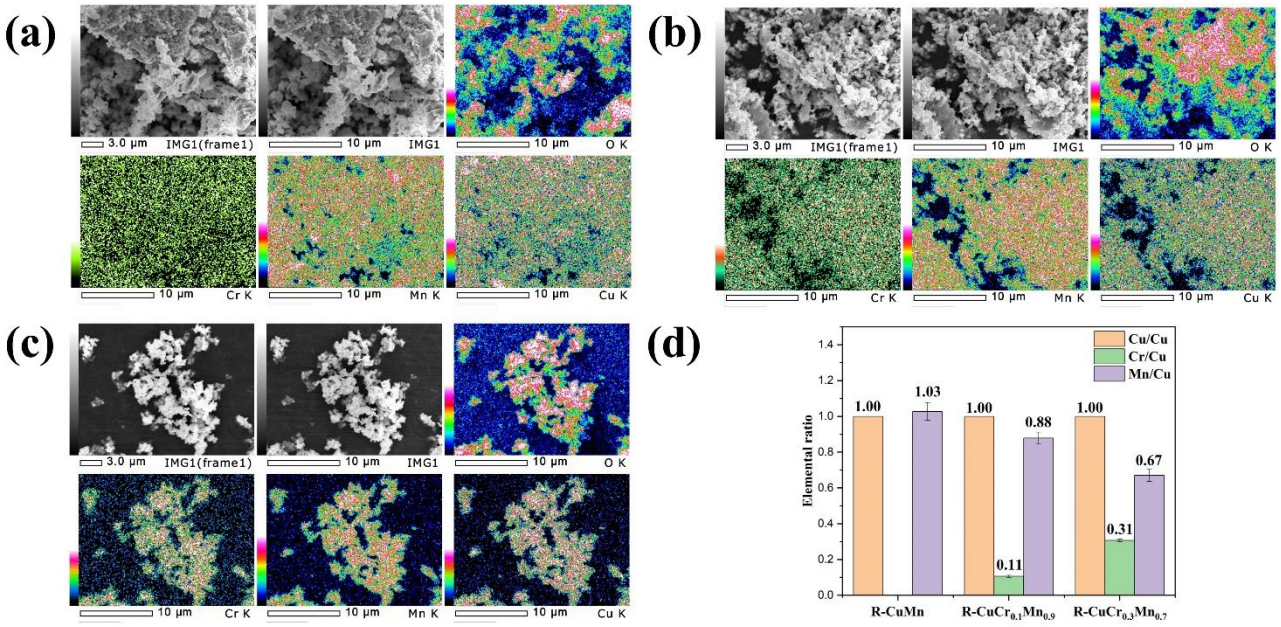

Figure 4-10 EDS elemental mappings of (a): R-CuMn; (b): R-CuCr$_{0.1}$Mn$_{0.9}$; (c): R-CuCr$_{0.3}$Mn$_{0.7}$; elemental ratio analysis of R-CuCr$_x$Mn$_{1-x}$ (x = 0, 0.1, 0.3)

4.5.3 In-depth investigation R-CuCr$_x$Mn$_{1-x}$ (x = 0, 0.1, 0.3) based chemical valence

The XPS spectra of the Cu element for each reduced-state sample are shown in Figure 4-11. Overall, Cu exists not only in the form of Cu(I) but also partially as Cu(II). This phenomenon could be attributed to two factors: (a) During the preparation of the reduced-

state sample, the temperature was limited to below 1000 °C, preventing the complete reduction of Cu(II) in the spinel phase to Cu(I) in the delafossite phase.(b) Since the reduced-state sample is in a high-entropy state, surface oxidation may occur even at room temperature. In Chapter 2, we observed that the reduced state could undergo partial oxidation within a very short time, even at room temperature. Additionally, XPS can only probe a depth of 5–10 nm from the surface, which explains why Cu(II)-containing phases were not detected in the XRD patterns of the reduced-state sample.

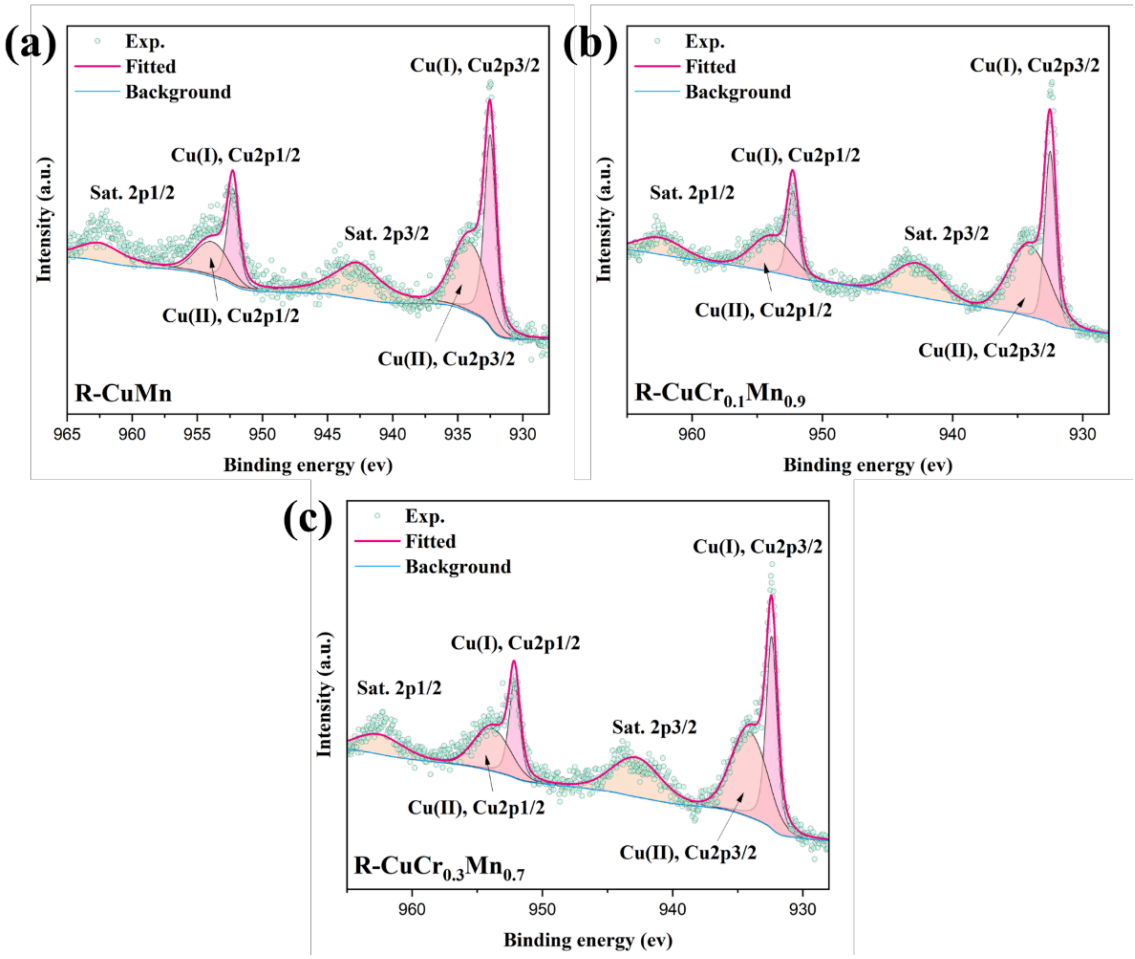

Figure 4-11 XPS spectra of Cu for (a): R-CuMn; (b): R-$CuCr_{0.1}Mn_{0.9}$; (c): R-$CuCr_{0.3}Mn_{0.7}$

Although the XPS experiments cannot capture the elemental state of the entire sample,

they still provide valuable reference information. In the binding energy range of 936–966 eV, the 2p orbital of Cu splits into a major peak for 2p3/2 (932.5 eV for Cu(I) and 934.1 eV for Cu(II)) and a minor peak for 2p1/2 (952.3 eV for Cu(I) and 953.9 eV for Cu(II)) (Figure 4-11). Additionally, two broad peaks are observed at approximately 942.7 eV and 963.0 eV, which are attributed to the satellite peaks of Cu(II), as the satellite peak of Cu(I) at 945 eV is too weak to detect.

With increasing Cr content, no peak shifts were observed in the Cu XPS spectra. However, a variation in the ratio of the 2p3/2 peaks of Cu(I) to Cu(II) was found (Figure 4-12), leading to a change in the average surface chemical valence of Cu: 1.51 for R-CuMn, 1.48 for R-$CuCr_{0.1}Mn_{0.9}$, and 1.55 for R-$CuCr_{0.3}Mn_{0.7}$. The surface valence of Cu initially decreases and then increases with higher Cr doping levels. Since all samples were kept under identical conditions, we can reasonably infer that this trend is likely consistent throughout the bulk of the samples.

During the oxidation of the reduced-state sample, the B-site elements in the spinel structure (AB_2O_4) theoretically do not participate in the valence change. This suggests that the chemical reaction and electron transfer primarily involve Cu at the A-site and oxygen ($4Cu^{+} \rightarrow 4Cu^{2+}$; $O^{2} \rightarrow 2O^{2-}$). As the Cu valence approaches the ideal Cu(I) state found in delafossite-type samples, Cu has more electrons to donate, facilitating electron transfer to oxygen and driving the reaction. This hypothesis aligns with our previous findings, where R-$CuCr_{0.1}Mn_{0.9}$ exhibited a lower re-oxidation temperature.

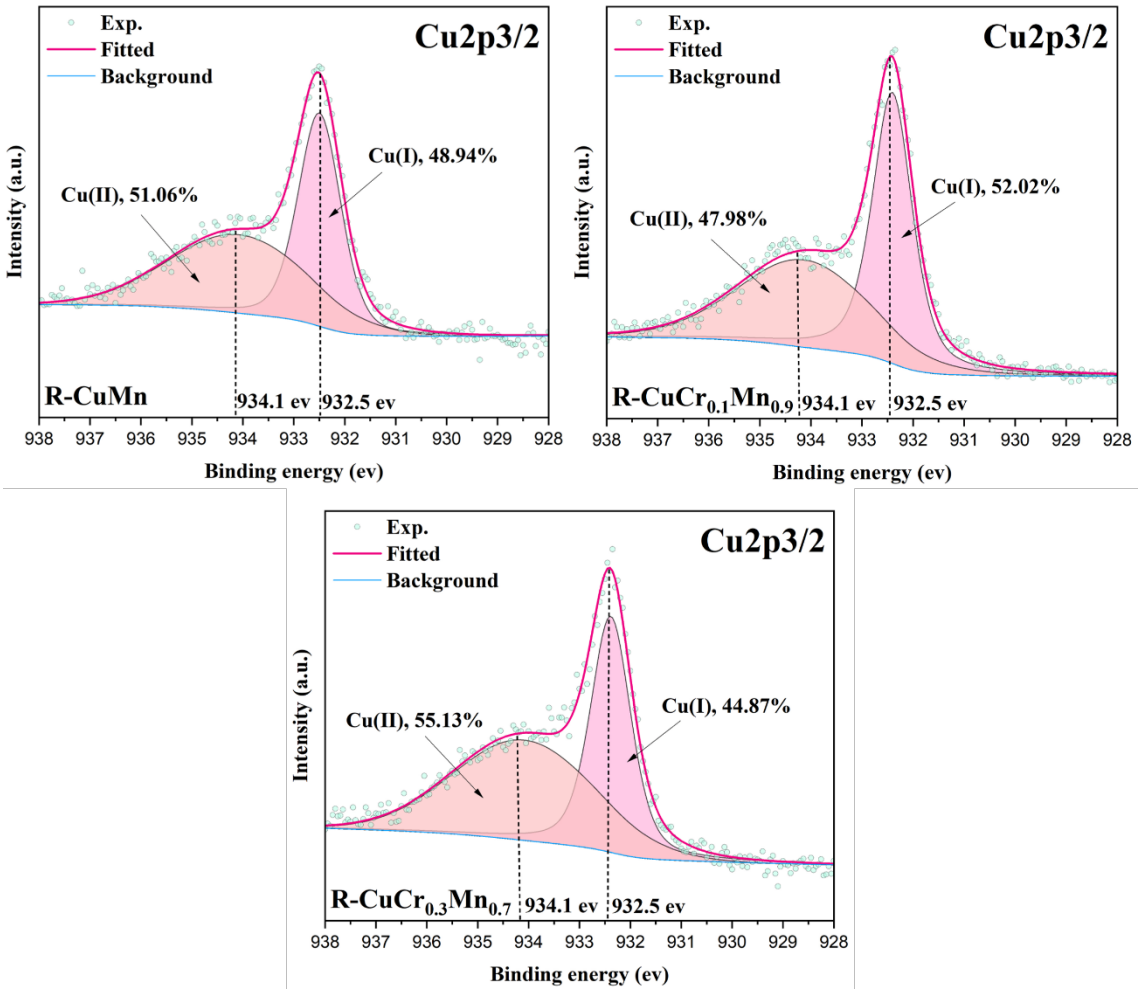

Figure 4-12 XPS chemical state analysis of Cu2p3/2 for R-$CuCr_xMn_{1-x}$ (x = 0, 0.1, 0.3)

The Cr and Mn may also act as redox-active species, therefore, their XPS spectra are also investigated and shown in Figure 4-13. Similar to the Cu spectra, the 2p orbital of Cr (Figure S5a) splits into a major 2p3/2 peak (576.0 eV for Cr(III)) and a minor 2p1/2 peak (585.3 eV for Cr(III), ΔE = 9.3 eV). The 2p orbital of Mn (Figure S5c) splits into a major 2p3/2 peak (641.4 eV for Mn(II, III) and 641.8 eV for Mn(IV)) and a minor 2p1/2 peak (652.6 eV for Mn(II, III) and 653.0 eV for Mn(IV), ΔE = 11.2 eV). As Cr doping increases, the Cr 2p peaks become more pronounced, while the Mn 2p peaks correspondingly decrease.

Notably, the Cr spectra exhibit a strong peak near 570 eV, which is not attributed to Cr but rather to the LMM Auger peak of Cu (Figure 4-13b). After marking the peak positions, we observed that R-CuCr$_{0.1}$Mn$_{0.9}$ exhibits the highest binding energy at 570.05 eV, compared to 569.96 eV for R-CuMn and 569.80 eV for R-CuCr$_{0.3}$Mn$_{0.7}$.

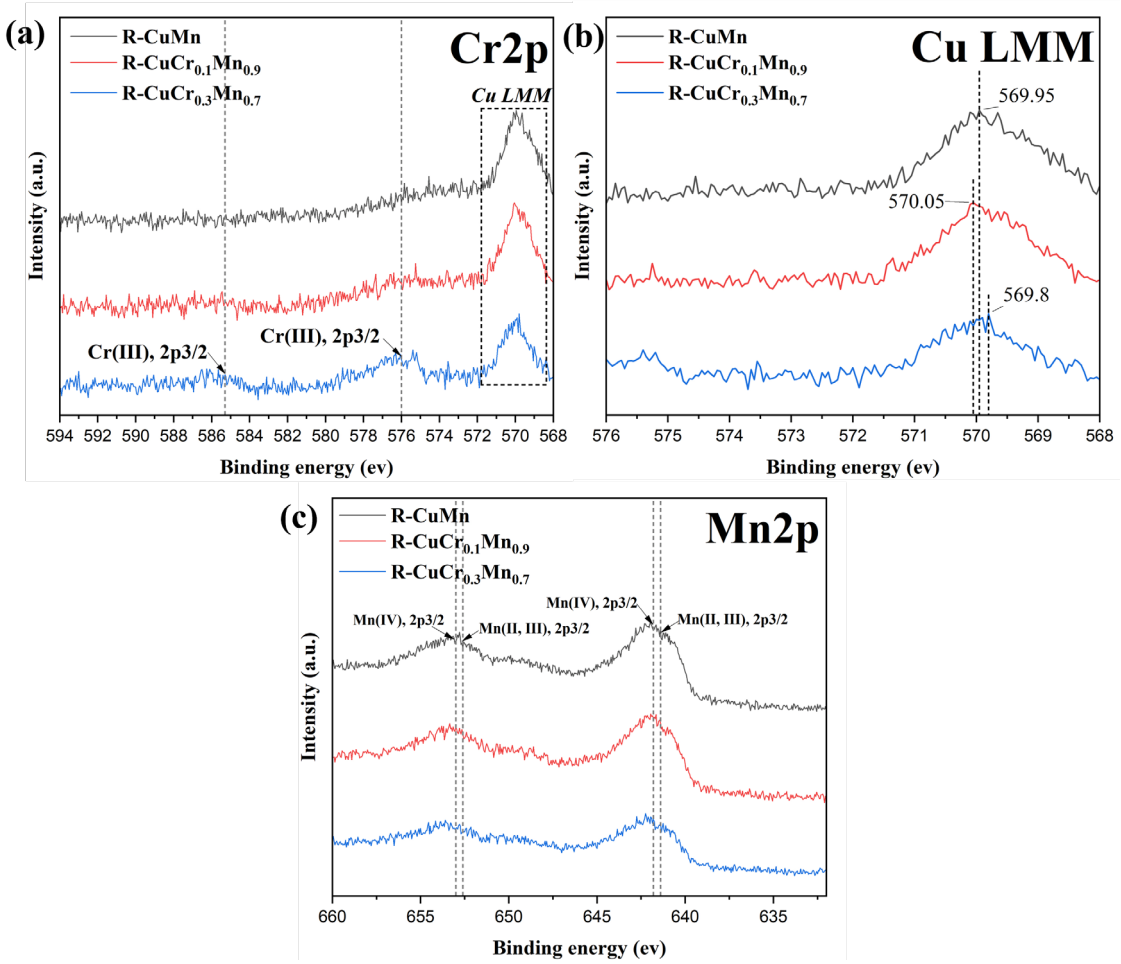

Figure 4-13 XPS spectra of R-CuCr$_x$Mn$_{1-x}$ (x=0, 0.1, 0.3) for Cr2p, Cu LMM, and Mn2p

According to the literature [12], the LMM Auger peak of Cu$_2$O (Cu(I)) has a higher binding energy than that of CuO (Cu(II)), indirectly supporting our previous hypothesis that Cu in R-CuCr$_{0.1}$Mn$_{0.9}$ exists in a lower valence state. The Mn 2p orbital can split into peaks corresponding to three oxidation states (II, III, and IV), but it is difficult to determine the average valence because Mn(II) and Mn(III) share the same 2p3/2 binding

energy at 641.4 eV. Although the ΔE of the Mn 3s orbital could provide a more precise determination of the valence, it lies beyond the scope of this work.

Based on the redox chemical equations of spinel and delafossite phases, we assume that Cr doping induces changes in the chemical valence of Cu, while Cr and Mn remain at a constant valence state of +3.

4.6 Conclusions

In this chapter, we developed Cr-doped $CuMn_2O_4/CuMnO_2$ for use in medium-high temperature (500–1000 °C) CHS systems. The study of Cr doping is divided into two parts.

Part A explores the effects across the entire doping concentration range (0–1.0). The Pechini method was employed for the synthesis of all samples due to its precise component controllability, and structural characterization was performed using XRD. Most samples were successfully synthesized using the Pechini method. In the redox experiments, Cr-doped samples exhibited lower reduction temperatures and reduced oxygen non-stoichiometric properties. R-$CuCr_{0.1}Mn_{0.9}$ and R-$CuCr_{0.3}Mn_{0.7}$ demonstrated faster reaction rates than R-CuMn, with R-$CuCr_{0.1}Mn_{0.9}$ showing a lower re-oxidation temperature than R-CuMn. Speculative chemical reaction equations suggest that Cr doping facilitates reduction and promotes greater oxygen release, leading to a deeper reduced state. DSC enthalpy measurements revealed that an appropriate amount of Cr improves heat storage density, with R-$CuCr_{0.3}Mn_{0.7}$ exhibiting the highest heat storage density at 305.61 ± 16.45 kJ/kg (1.68 ± 0.09 MJ/L). Furthermore, Cr doping did not impair cyclic stability.

Part B focuses on the specific doping levels (0, 0.1, and 0.3) identified as having unique properties in **Part A**. Through Rietveld refinement and XPS analysis, R-$CuCr_{0.1}Mn_{0.9}$ exhibited structural instability, reflected by the smallest Jahn-Teller

distortion degree and a lower average chemical valence of Cu. These factors provide a reasonable hypothesis to explain why R-$CuCr_{0.1}Mn_{0.9}$ re-oxidizes more easily than both R-CuMn and R-$CuCr_{0.3}Mn_{0.7}$, as observed in **Part A**.

In conclusion, this study demonstrates that Cr doping influences the reaction temperature, re-oxidation behavior, and heat storage density of $CuMn_2O_4$/$CuMnO_2$. This approach offers a promising pathway for developing new materials in the medium-high temperature CHS field.

Reference

[1] Y. Portilla-Nieto, A. Zaki, K. Vidal, M. Hernaiz, E. Aranzabe, S. Doppiu, A. Faik, Development of Co3-xNixO4 materials for thermochemical energy storage at lower red-ox temperature, Solar Energy Materials and Solar Cells 230 (2021) 111194. https://doi.org/10.1016/j.solmat.2021.111194.

[2] H. Eric, M. Timuçin, Equilibrium relations in the system nickel oxide-copper oxide, Metallurgical Transactions B 10 (1979) 561–563. https://doi.org/10.1007/BF02662558.

[3] A.J. Carrillo, P. Pizarro, J.M. Coronado, Assessing Cr incorporation in Mn2O3/Mn3O4 redox materials for thermochemical heat storage applications, Journal of Energy Storage 33 (2021) 102028. https://doi.org/10.1016/j.est.2020.102028.

[4] B.H. Toby, R.B. Von Dreele, GSAS-II: The genesis of a modern open-source all purpose crystallography software package, Journal of Applied Crystallography 46 (2013) 544–549. https://doi.org/10.1107/S0021889813003531.

[5] X. Huang, C. Ni, G. Zhao, J.T.S. Irvine, Oxygen storage capacity and thermal stability of the CuMnO2-CeO2 composite system, Journal of Materials Chemistry A 3 (2015) 12958–12964. https://doi.org/10.1039/c5ta01361e.

[6] P.N. Lisboa-Filho, M. Bahout, P. Barahona, C. Moure, O. Peña, Oxygen stoichiometry effects in spinel-type NiMn2O 4-δ samples, Journal of Physics and Chemistry of Solids 66 (2005) 1206–1212. https://doi.org/10.1016/j.jpcs.2005.03.001.

[7] O.A. Bulavchenko, O.S. Venediktova, T.N. Afonasenko, P.G. Tsyrul'Nikov, A.A. Saraev, V.V. Kaichev, S.V. Tsybulya, Nonstoichiometric oxygen in Mn-Ga-O spinels: Reduction features of the oxides and their catalytic activity, RSC Advances 8 (2018) 11598–11607. https://doi.org/10.1039/c7ra11557a.

[8] P. Chartrand, A. Barnab, L. Cassayre, Thermodynamic and Structural Properties of CuCrO 2 and CuCr 2 O 4 : Experimental Investigation and Phase Equilibria Modeling of the Cu − Cr − O System, (2021). https://doi.org/10.1021/acs.jpcc.1c04179.

[9] K.K. Shukla, P. Shahi, S. Gopal, A. Kumar, A.K. Ghosh, R. Singh, N. Sharma, A. Das, A.K. Sinha, A.G. Joshi, A.K. Nigam, S. Chatterjee, Magnetic and optical properties of Fe doped crednerite CuMnO2, RSC Advances 5 (2015) 83504–83511. https://doi.org/10.1039/c5ra13305j.

[10] H.A. Jahn and E. Teller, Stability of Polyatomic Molecules in Degenerate Electronic States II—Spin Degeneracy, Proc. R. Soc. London 161 (1937) 220–235.

[11] G. Wypych, ed., 1 - INTRODUCTION, in: Handbook of Nucleating Agents, ChemTec Publishing, 2016: pp. 1–3. https://doi.org/10.1016/B978-1-895198-93-5.50003-4.

[12] V. Krylova, M. Andruleviçius, Optical, XPS and XRD studies of semiconducting copper sulfide layers on a polyamide film, International Journal of Photoenergy 2009 (2009). https://doi.org/10.1155/2009/304308.

Chapter 5. Kinetic study of $CuMn_2O_4/CuMnO_2$ redox couple

5.1 Introduction

To understand the redox reaction mechanisms of materials and predict key performance parameters, such as heat output and heat absorption power, conducting reaction kinetic studies is essential. Kinetic analysis allows for the determination of activation energy and other critical parameters involved in the reaction process. These insights provide a theoretical foundation for optimizing material properties and designing efficient and reliable heat storage systems.

Reaction kinetics are often studied using thermogravimetric analysis (TGA), but they can also be investigated with other techniques, such as differential scanning calorimetry (DSC), powder X-ray diffraction (XRD), and nuclear magnetic resonance (NMR). The kinetic study of chemical heat storage systems plays a crucial role in system simulation and design. The solid-state kinetic models are employed to describe the behavior of redox-type chemical heat storage systems. The rate of a solid-state reaction can generally be expressed as:

$$\frac{d\alpha}{dt} = A \cdot Exp(-E_a/RT) \cdot f(\alpha) \qquad (5-1)$$

where A is the pre-exponential factor, E_a is the activation energy, T is the absolute temperature, R is the gas constant, $f(\alpha)$ is the reaction model, and α is the conversion ratio. In gravimetric experiments, α is defined as:

$$\alpha = \frac{m_0 - m_t}{m_0 - m_f} \qquad (5-2)$$

where m_0 is initial weight, m_t is the weight at time t, and m_f is final weight.

Kinetic analysis, whether isothermal or non-isothermal, can be performed using either model-fitting or model-free (iso-conversional) methods. The use of iso-conversional

methods has become increasingly popular because they allow for the calculation of activation energy (E_a) without requiring prior knowledge of the reaction model. Kinetic parameters ($f(\alpha)$, A, E_a) can be obtained from isothermal kinetic data using the Equation 5-1. Alternatively, Equation 5-1 can be rewritten into a non-isothermal way to obtain the kinetic parameters ($f(\alpha)$, A, E_a) either. The non-isothermal rate expression describing reaction rate as a function of temperature at a constant heating rate by the following equation:

$$\frac{d\alpha}{dT} = \frac{d\alpha}{dt}\frac{dt}{dT} \qquad (5-3)$$

where $d\alpha/dT$ is the non-isothermal reaction rate, $d\alpha/dt$ is the isothermal reaction rate, and dT/dt is the heating rate, viz., the β.

Then we can obtain the non-isothermal rate law by substituting Equation 5-1 into Equation 5-3:

$$\frac{d\alpha}{dT} = \frac{A}{\beta} \cdot Exp(-E_a/RT) \cdot f(\alpha) \qquad (5-4)$$

Separating variables and integrating Equation 5-1 and Equation 5-4 respectively:

$$g(\alpha) = A \cdot Exp(-E_a/RT) \cdot t \qquad (5-5)$$

and

$$g(\alpha) = \frac{A}{\beta}\int_0^T Exp(-E_a/RT) \cdot dT \qquad (5-6)$$

where $g(\alpha)$ is the integral reaction model which is defined by:

$$g(\alpha) = \int_0^{\alpha} \frac{d\alpha}{f(\alpha)} \qquad (5-7)$$

A reaction model is a theoretical, mathematical description of the phenomena observed experimentally. Many solid-state kinetic models have been proposed based on specific mechanistic assumptions, while others are more empirical, offering little mechanistic insight. Models are generally classified based on the graphical shape of their isothermal curves (α vs. t, or dα/dt vs. α) or their underlying mechanistic assumptions. Based on curve shapes, kinetic models can be categorized as acceleratory, deceleratory, linear, or sigmoidal. However, under non-isothermal conditions, α vs. temperature plots are less distinctive than their isothermal counterparts in terms of curve shape. Based on mechanistic assumptions, models are classified into nucleation, geometrical contraction, diffusion, and reaction-order models, which can be found in Table 5-1.

Table 5-1 Different reaction models for solid-state reaction

Reaction model	Code	$f(\alpha)$	$g(\alpha)$
Nucleation models			
Power law	P4	$4\alpha^{3/4}$	$\alpha^{1/4}$
Power law	P3	$3\alpha^{2/3}$	$\alpha^{1/3}$
Power law	P2	$2\alpha^{1/2}$	$\alpha^{1/2}$
Power law	P2/3	$\frac{2}{3}\alpha^{-1/2}$	$\alpha^{3/2}$
Avrami-Erofeev	A4	$4(1-a)[-\ln(1-a)]^{3/4}$	$[-\ln(1-\alpha)]^{1/4}$
Avrami-Erofeev	A3	$3(1-a)[-\ln(1-a)]^{2/3}$	$[-\ln(1-\alpha)]^{1/3}$
Avrami-Erofeev	A2	$2(1-a)[-\ln(1-a)]^{1/2}$	$[-\ln(1-\alpha)]^{1/2}$
Geometrical contraction models			

Contracting sphere	R3	$3(1-\alpha)^{2/3}$	$1-(1-\alpha)^{1/3}$
Contracting cylinder	R2	$2(1-\alpha)^{1/2}$	$1-(1-\alpha)^{1/2}$
Diffusion models			
Three-dimensional diffusion	D3	$\frac{3(1-\alpha)^{2/3}}{2[1-(1-\alpha)^{1/3}]}$	$[1-(1-\alpha)^{1/3}]^2$
Two-dimensional diffusion	D2	$\frac{1}{[-\ln(1-\alpha)]}$	$(1-\alpha)\ln(1-\alpha)+\alpha$
One-dimensional diffusion	D1	$\frac{1}{2\alpha}$	α^2
Reaction-order models			
Mampel (first order)	F1	$1-\alpha$	$-\ln(1-\alpha)$

In this chapter, we conducted a redox kinetic study of $CuMn_2O_4/CuMnO_2$, which was developed in Chapter 3. The reduction kinetic study of $CuMn_2O_4$ was investigated using only the non-isothermal method, whereas the oxidation kinetics of $CuMnO_2$ were studied using both non-isothermal and isothermal methods to provide a comprehensive analysis.

5.2 Reduction kinetic study of $CuMn_2O_4$

5.2.1 Non-isothermal reduction kinetics of $CuMn_2O_4$

In this study, reduction kinetic analysis was performed only using the non-isothermal method. Although isothermal reduction kinetic analysis is theoretically feasible, it requires a pure oxygen environment to prevent sample reduction until the target temperature is reached, which poses certain experimental risks. Additionally, pure oxygen conditions are not relevant for practical applications.

In the reduction kinetic analysis of $CuMn_2O_4$, kinetic triplet parameters (A, E_a, $f(\alpha)$) were evaluated using non-isothermal methods. The sample was heated from room temperature to 1000°C at different heating ramps (β = 5, 10, 15, and 20 °C/min, $\beta = dT/dt$) under synthetic N_2 atmosphere (200 mL/min). The activation energy E_a can be computed

directly without the previous knowledge of reaction model $f(\alpha)$ when non-isothermal method was used. Once E_a is determined, reaction model $f(\alpha)$ can be determined by using $g(\alpha)/g(0.5)$ master plots of different existing reaction models. In the last, pre-exponential factor A can be generated easily using its internal relationship with the other two parameters.

Gas-solid reactions can be described by an Arrhenius-type law (Equation 5-8).

$$r = \frac{d\alpha}{dt} = Aexp\left(\frac{-E_a}{RT}\right) f(\alpha) \qquad (5-8)$$

where α is the conversion ratio, A is the pre-exponential factor, E_a is the activation energy, R is the gas constant, and $f(\alpha)$ is the reaction model.

The reduction activation energy (E_a) of $CuMn_2O_4$ was calculated using the non-isothermal method. Based on TGA data of a reaction involving mass loss, the conversion ratio α is obtained from Equation 5-2.

Figure 5-1 shows the α-time and α-temperature plots for the reduction reaction of $CuMn_2O_4$ in an N_2 atmosphere. From these plots, the re-oxidation activation energy E_a can be determined using the Friedman method (Equation 5-9) [1], as recommended by ICTAC [2].

$$\ln\left(\beta \frac{\mathrm{d}\alpha}{\mathrm{d}T}\right) = \ln[Af(\alpha)] - \frac{E_a}{RT} \qquad (5-9)$$

where β is the heating ramp, A is the pre-exponential factor, $f(\alpha)$ is the reaction model, E_a is the activation energy, and R is the gas constant.

The Friedman method allows determining E_a without prior knowledge of $f(\alpha)$ because a plot of the left term of Equation 5-9 vs. $1/T$ yields E_a from the slope of fitted curve. An Arrhenius plot of E_a for $CuMn_2O_4$ at $\alpha = 0.5$, is shown in Figure 5-2.

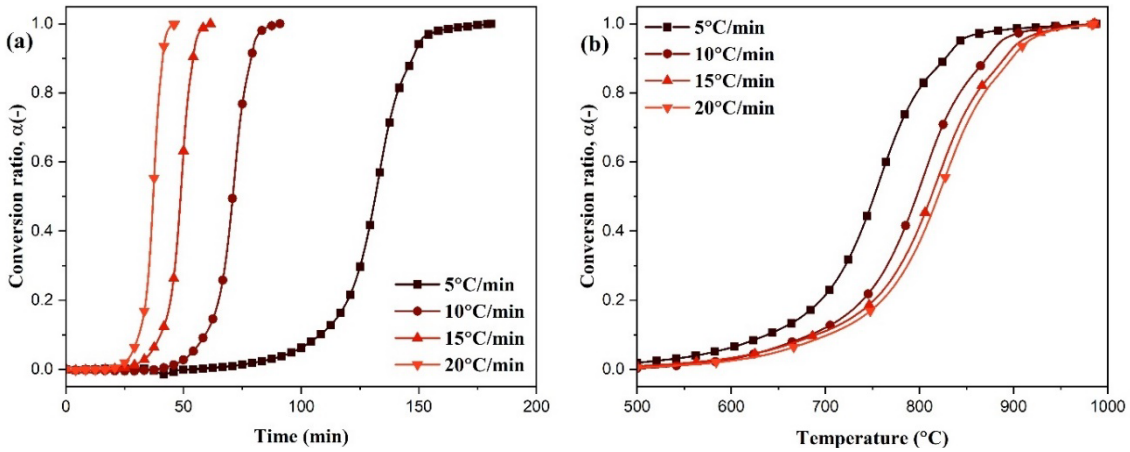

Figure 5-1 (a) α-time plots and (b) α-temperature plots for the reduction of $CuMn_2O_4$ under N_2

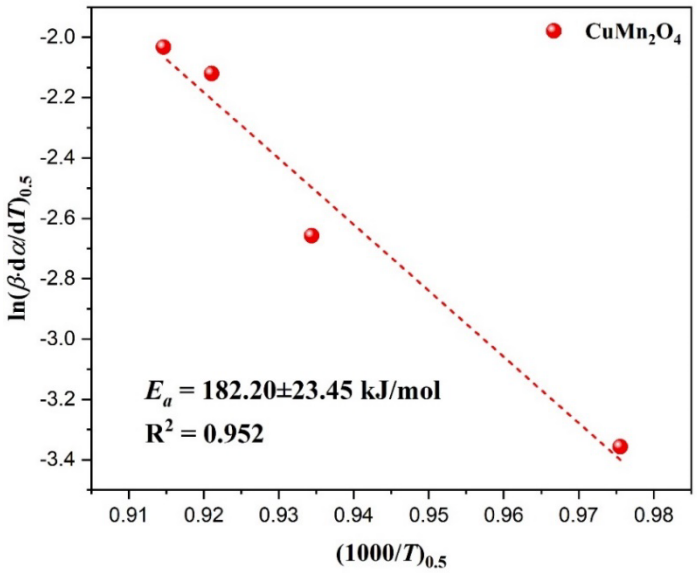

Figure 5-2 An Arrhenius plot of E_a for the reduction of $CuMn_2O_4$ under N_2

Once the activation energy E_a is determined, the reaction model and mechanism can be investigated by using the $g(\alpha)/g(0.5)$ master plots. Equation 5-10 applies under non-isothermal conditions. By introducing the average value of E_a which is computed from Friedman method, it is possible to plot experimental data extracted from TGA results (the left term of Equation 5-10) in theoretical $g(\alpha)/g(0.5)$ master plots (the right term of Equation 5-10).

$$\frac{\theta}{\theta_{0.5}} = \frac{g(\alpha)}{g(\alpha)_{0.5}} \qquad (5-10)$$

where θ is the generalized time and $g(\alpha)$ is the integral form of kinetic rate equation. The subscript of 0.5 indicates that these terms are evaluated when α = 0.5. By comparing the experimental data with theoretical master plot, the best-fitting model is selected.

The master plots for the reduction of $CuMn_2O_4$ at different heating rates are shown in Figure 5-3, identifying reaction model F1 as the model for the reduction of $CuMn_2O_4$.

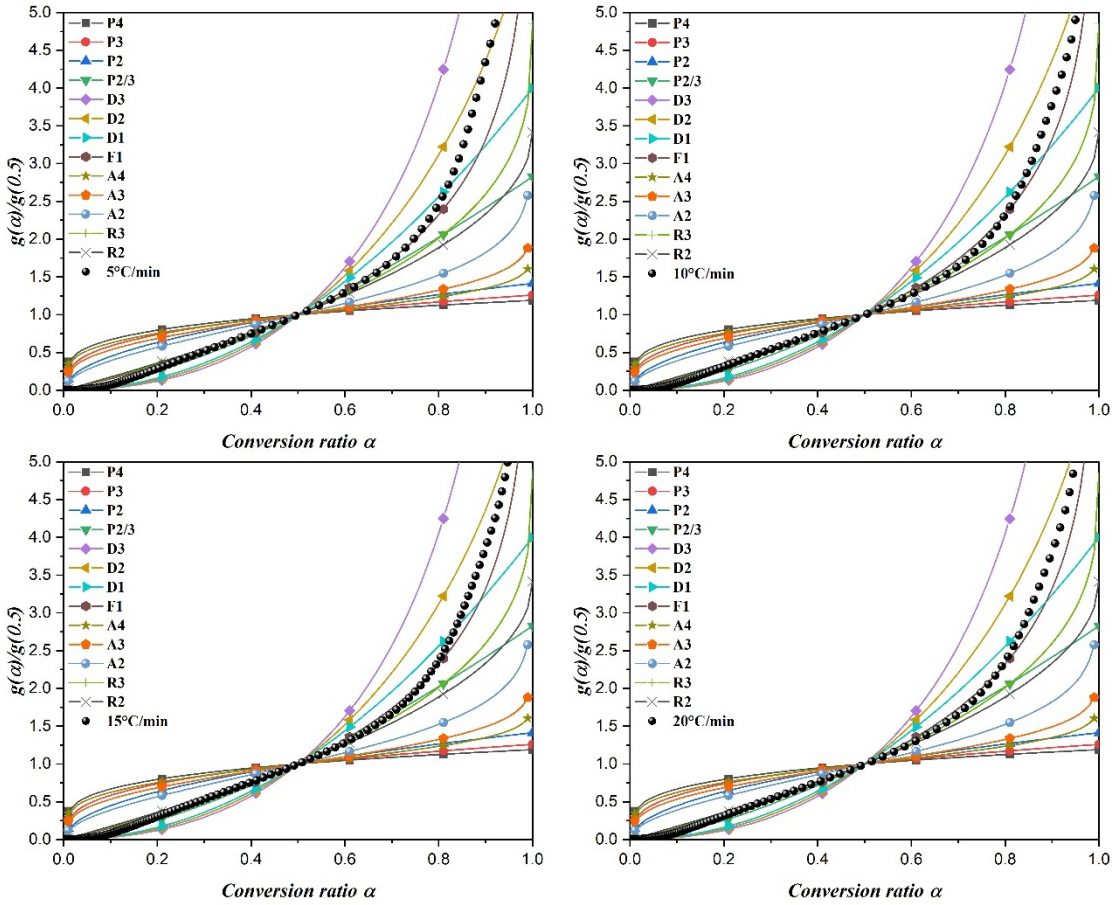

Figure 5-3 $g(\alpha)/g(0.5)$ master plots of reduction of $CuMn_2O_4$ with different heating ramps (5, 10, 15, and 20 °C/min); based on the fitting results, reaction model F1 was identified

The pre-exponential factor A can be derived from E_a and $f(\alpha)$ using the intercept of Equation 5-9. Due to the different heating ramps, A may vary in a certain range even for the same sample. Therefore, the average value of A was used for general description. The complete kinetic equation of the reduction of $CuMn_2O_4$ in N_2 atmosphere is shown below:

$$r = \frac{d\alpha}{dt} = (1.29 \pm 0.12) \times 10^8\ min^{-1} \cdot \left(\frac{-182.20 \pm 23.45\ \frac{kJ}{mol}}{RT} \right) \cdot (1-\alpha) \quad (5-11)$$

To verify the accuracy of our kinetic model, a series of predictions were performed based on the model (Figure 5-4). The kinetic model of $CuMn_2O_4$ showed good agreement with the experimental data, except for a slight deviation at lower conversion ratios (α<0.3).

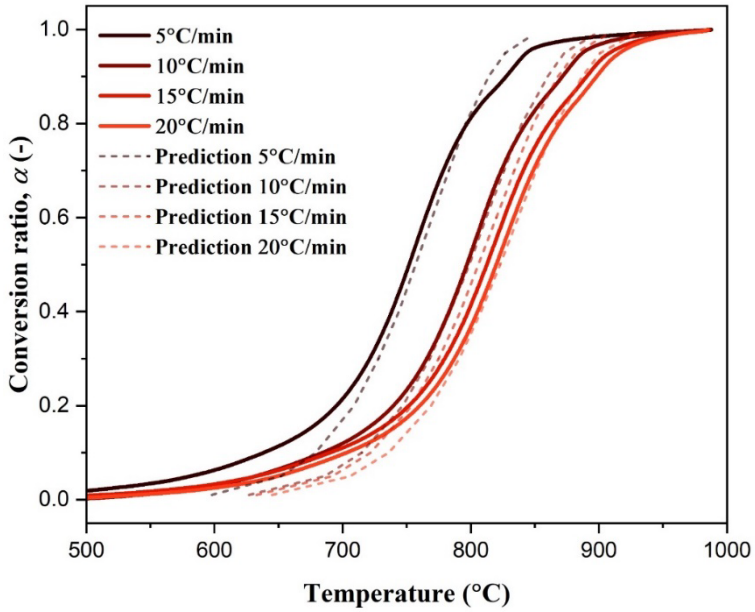

Figure 5-4 Kinetic prediction of the reduction of $CuMn_2O_4$ under N_2

5.3 Oxidation kinetic study of $CuMnO_2$

5.3.1 Non-isothermal oxidation kinetics of $CuMnO_2$

In the non-isothermal oxidation kinetic analysis of $CuMnO_2$, the sample was heated

from room temperature to 1000°C at different heating rates (β = 5, 10, 15, and 20 °C/min, $\beta = dT/dt$) under synthetic air atmosphere (200 mL/min). The activation energy E_a, reaction model $f(\alpha)$, and the pre-exponential factor A were computed following the calculation step outlined in Chapter 5.2.1.

Figure 5-5 shows the α-time *and* α-Temperature plots of the oxidation reaction of $CuMnO_2$ in air atmosphere, and the activation energy E_a that calculated by Friedman method (Figure 5-6) is 137.93 ± 16.74 kJ/mol.

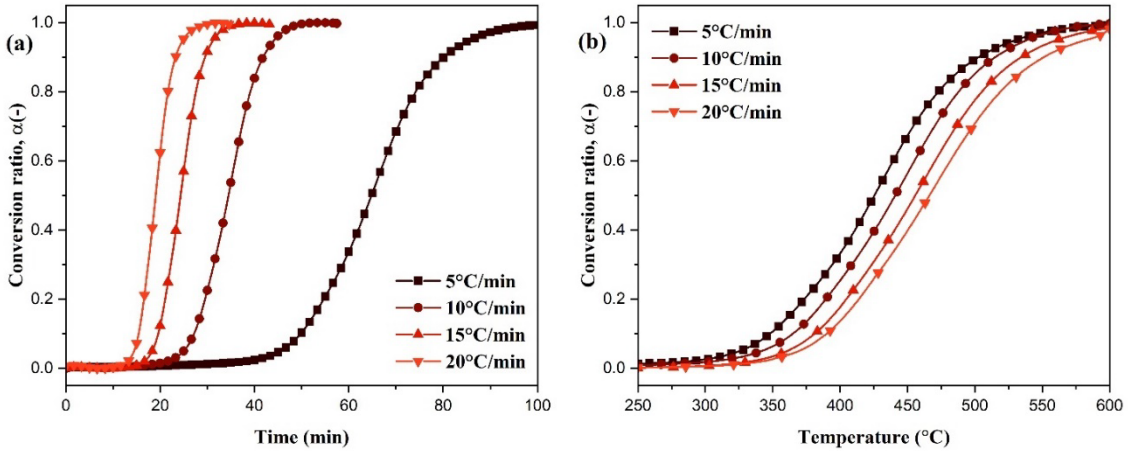

Figure 5-5 (a) α-time plots and (b) α-temperature plots for the oxidation of $CuMnO_2$ under air

The master plots for the oxidation of $CuMnO_2$ at different heating rates are shown in Figure 5-7, identifying reaction model D3 as the model for the oxidation of $CuMnO_2$.

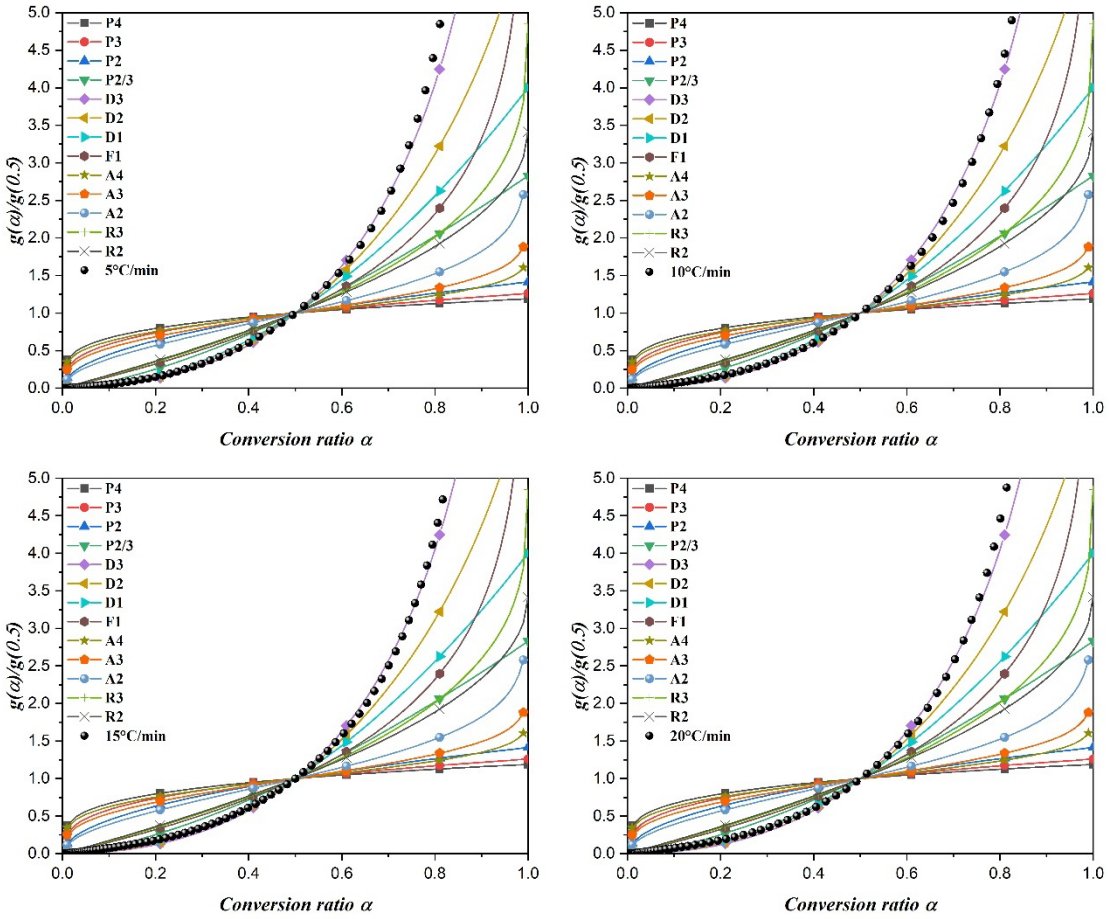

Figure 5-7 $g(\alpha)/g(0.5)$ master plots of oxidation of $CuMnO_2$ with different heating rates (5, 10, 15, and 20 °C/min); based on the fitting results, reaction model D3 was determined

The average pre-exponential factor A which calculated from Equation 5-9 is 1.70×10^{8} min^{-1}. The complete kinetic equation of the oxidation of $CuMnO_2$ in air atmosphere is shown below:

$$r = \frac{d\alpha}{dt} = (1.70 \pm 0.14) \times 10^8\ min^{-1} \cdot \left(\frac{-137.93 \pm 16.74\ \frac{kJ}{mol}}{RT} \right) \cdot \frac{3/2(1-\alpha)^{2/3}}{[1-(1-\alpha)^{1/3}]} \quad (5-12)$$

To verify the accuracy of our kinetic model, a series of predictions were performed based on the model (Figure 5-8). The kinetic model of $CuMnO_2$ showed good agreement with the experimental data across the entire conversion ratio range.

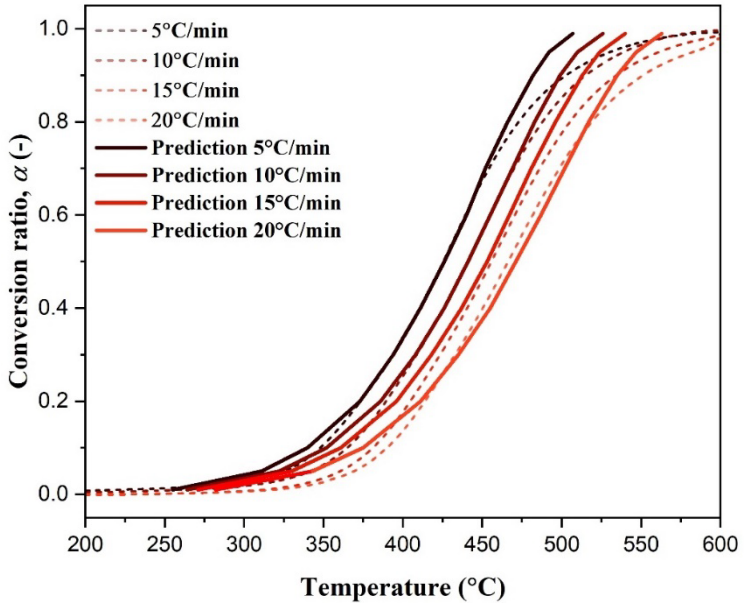

Figure 5-8 Kinetic prediction of the oxidation of $CuMnO_2$ under air

5.3.2 Isothermal oxidation kinetics of $CuMnO_2$

In isothermal oxidation kinetics experiment of $CuMnO_2$, the sample was heated from room temperature to an appropriate temperature (400-550°C) under N_2 protection (200 mL/min). Once the temperature stabilized, the atmosphere was changed into synthetic air (200 mL/min) for oxidation reaction. Figure 5-9 depicts the α-time plots of oxidation reaction of $CuMnO_2$ at different temperatures. From this plot, the reaction model can be determined through master plots method by using the equation below:

$$\frac{g(\alpha)}{g(0.5)} = \frac{t}{t_{0.5}} \qquad (5-13)$$

where $g(\alpha)$ is the integral forms of reaction model, t is the time, $g(0.5)$ is the integral forms of reaction model at $\alpha = 0.5$, and $t_{0.5}$ is the time at $\alpha = 0.5$.

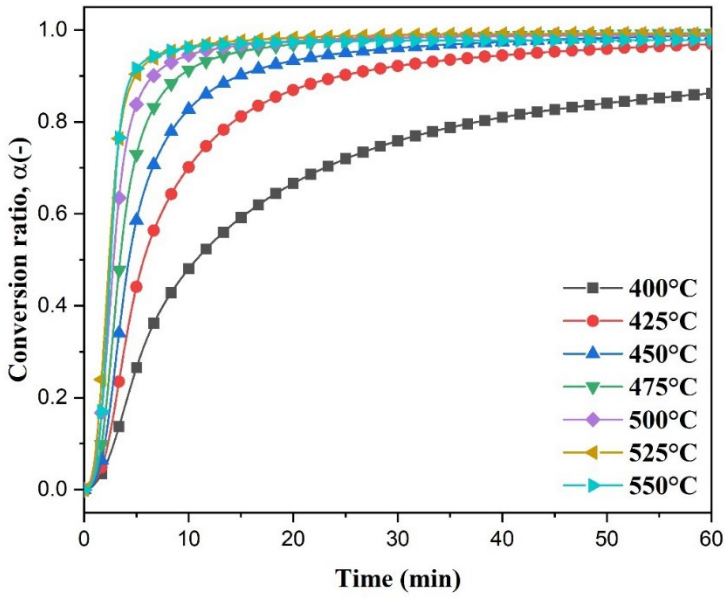

Figure 5-9 α-time plots for the oxidation of $CuMnO_2$ under air

Due to the insufficient conversion ratio at 400–450°C, only 475–550°C range was selected for further investigation. The master plots of the isothermal oxidation experiment of $CuMnO_2$ are shown in Figure 5-10, identifying reaction model A2 as the model for the isothermal oxidation of $CuMnO_2$.

Once reaction model is determined, the activation energy E_a can be calculated using the equation below:

$$\ln\left(\frac{\frac{d\alpha}{dt}}{f(\alpha)}\right)_{0.5} = \ln(A) - \frac{E_a}{RT} \qquad (5-14)$$

Plotting the left term of Equation 5-14 vs. $1/T$ yields the E_a from the slope of fitted curve which is shown in Figure 5-11.

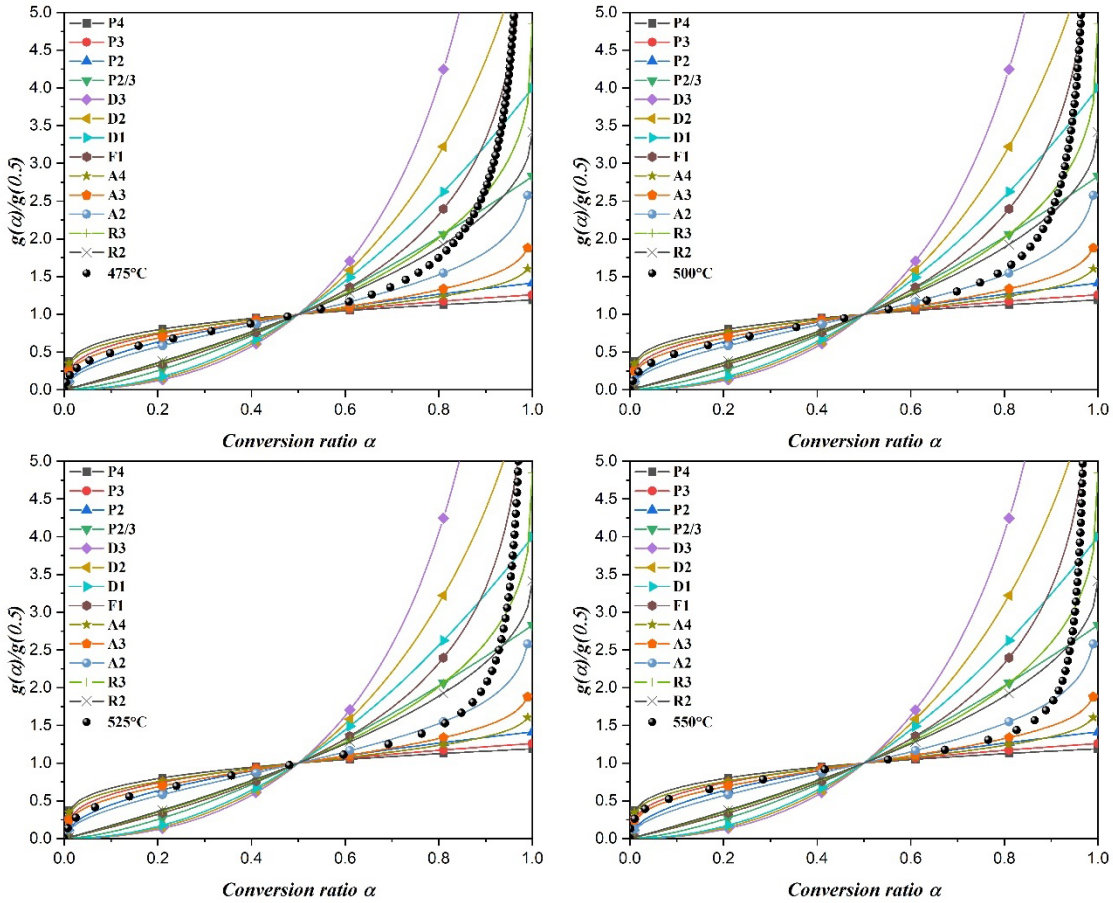

Figure 5-10 $g(\alpha)/g(0.5)$ master plots of the isothermal oxidation of $CuMnO_2$ at different temperatures (475, 500, 525, and 550°C); based on the fitting results, reaction model A2 was determined

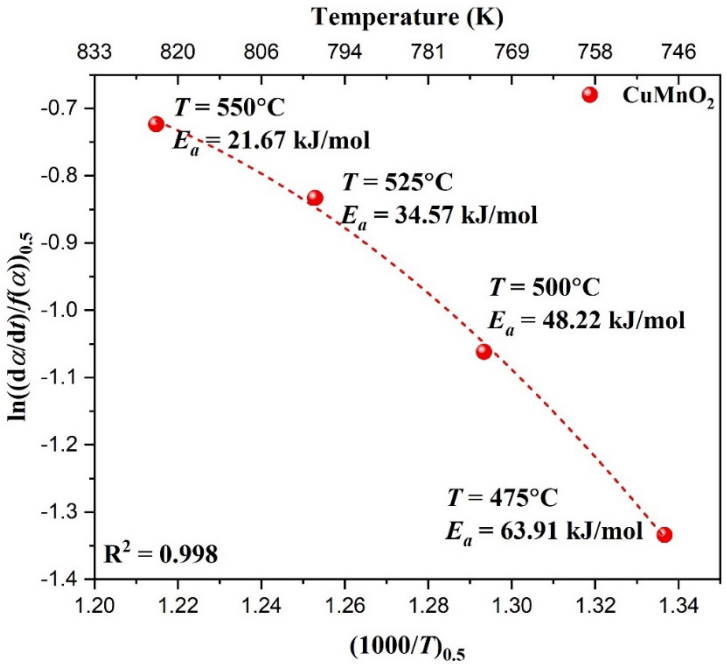

Figure 5-11 An Arrhenius plot of E_a for the isothermal oxidation of $CuMnO_2$ under air

From Figure 5-11, the curve does not exhibit linear behavior with changes in temperature, indicating that the value of E_a strongly depends on the temperature in the isothermal oxidation experiments.

Similarly, the pre-exponential factor A can be calculated from E_a and $f(a)$ using the intercept of Equation 5-14. However, it should be noted that because of the strong temperature dependence of E_a, the average value of A is not applicable here. The value of E_a, A and $f(a)$ at each temperature are summarized in Table 5-2.

To verify the accuracy of the isothermal oxidation kinetic model of $CuMnO_2$, a series of predictions were performed based on the model (Figure 5-12). The kinetic models showed good agreement with the experiment. However, because the experimental data does not fit perfectly in master plots, the prediction results exhibited a worse performance when conversion ratio a was greater than 0.8.

Table 5-2 Kinetic triplets (E_a, A, $f(a)$) of isothermal oxidation of $CuMnO_2$ under air

Temperature (°C)	E_a (kJ/mol)	A (min^{-1})	$f(a)$ = A2
475	63.01	6602.41	$2(1-a)[-\ln(1-a)]^{1/2}$
500	48.22	626.22	$2(1-a)[-\ln(1-a)]^{1/2}$
525	34.57	79.60	$2(1-a)[-\ln(1-a)]^{1/2}$
550	21.67	11.52	$2(1-a)[-\ln(1-a)]^{1/2}$

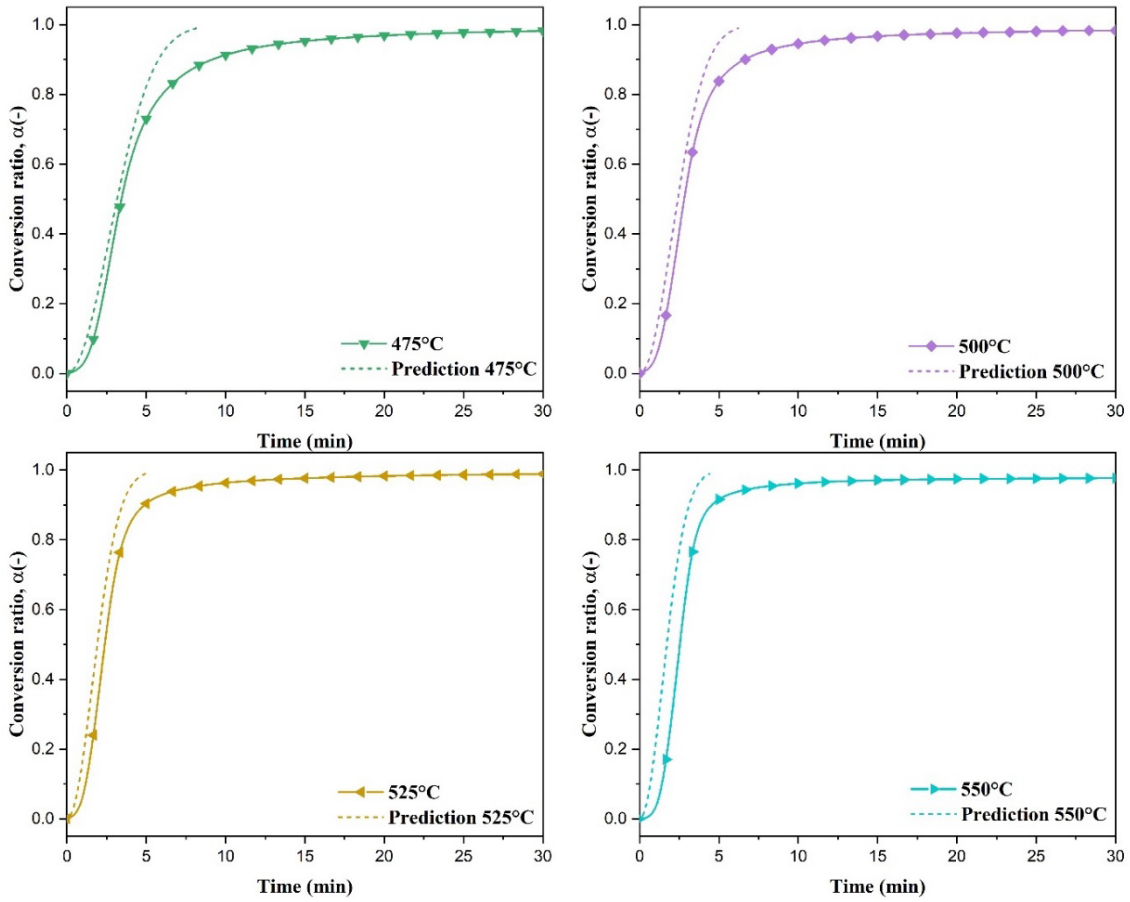

Figure 5-12 Kinetic prediction of the isothermal oxidation of $CuMnO_2$ under air

5.4 Conclusions

In this chapter, kinetic analysis of $CuMn_2O_4/CuMnO_2$ redox couple was conducted using both non-isothermal and isothermal methods. The kinetic triplet parameters (A, E_a,

$f(\alpha)$) obtained by each method are summarized in Table 5-3.

Table 5-3 Summary of redox kinetic parameters for $CuMn_2O_4/CuMnO_2$

Reaction direction	**Method**	**Temperature (℃)**	***A* (min^{-1})**	***E*$_a$ (kJ/mol)**	***f*(*α*)**
Reduction	Non-isothermal	(-)	(1.29±0.12) ×10^8	182.20±23.45	F1
Oxidation	Non-isothermal	(-)	(1.70±0.14) ×10^8	137.93±16.74	D3
	Isothermal	475	6602.41	63.01	A2
		500	626.22	48.22	A2
		525	79.60	34.57	A2
		550	11.52	21.67	A2

The model-based predictions for both the reduction and oxidation kinetic models showed good agreement with the experimental results, providing a reliable theoretical basis for future reactor design and simulation.

Reference

[1] H.L. Friedman, Kinetics of thermal degradation of char-forming plastics from thermogravimetry. Application to a phenolic plastic, Journal of Polymer Science Part C: Polymer Symposia 6 (1967) 183–195. https://doi.org/10.1002/polc.5070060121.

[2] S. Vyazovkin, A.K. Burnham, J.M. Criado, L.A. Pérez-Maqueda, C. Popescu, N. Sbirrazzuoli, ICTAC Kinetics Committee recommendations for performing kinetic computations on thermal analysis data, Thermochimica Acta 520 (2011) 1–19. https://doi.org/10.1016/j.tca.2011.03.034.

Chapter 6. Oxidation kinetic study of Cr-doped $CuMn_2O_4/CuMnO_2$ redox couple

6.1 Introduction

In the latter part of Chapter 4 we discuss in detail the effect of Cr doping on the crystalline structure, morphology, and chemical valence of $CuMn_2O_4/CuMnO_2$. And we observed that a small amount of Cr doping seems to further reduce the reaction temperature and accelerate the reaction rate in the reoxidation behavior. In this chapter we will quantitatively discuss the effect of Cr doping on the oxidation reaction rate of $CuCr_xMn_{1-x}O_2$ (R-$CuCr_xMn_{1-x}$, x = 0, 0.1, 0.3) to understand the oxidation reaction mechanism of Cr-doped $CuMn_2O_4/CuMnO_2$ and predict key performance parameters of heat output power.

6.2 Non-isothermal oxidation kinetics of Cr-doped $CuMnO_2$

The oxidation kinetic study was conducted using a non-isothermal method which was introduced in Section 5.3.1, and the re-oxidation behavior of R-$CuCr_xMn_{1-x}$ (x = 0, 0.1, 0.3) is shown in Figure 4-4, Chapter 4. An Arrhenius plot of E_a for each sample at $\alpha = 0.5$, is shown in Figure 6-1.

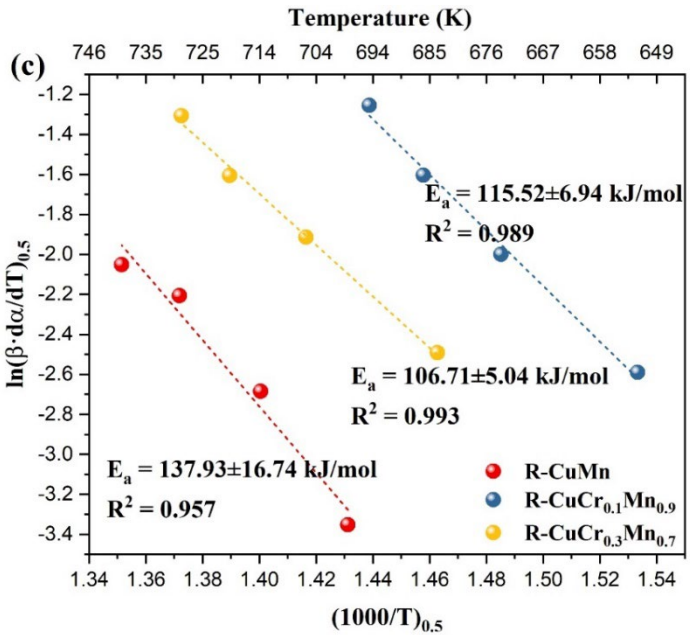

Figure 6-1 An Arrhenius plot of E_a for R-$CuCr_xMn_{1-x}$ (x = 0, 0.1, 0.3)

R-CuCr$_{0.1}$Mn$_{0.9}$ and R-CuCr$_{0.3}$Mn$_{0.7}$ exhibited lower re-oxidation E_a (115.52 ± 6.94 kJ/mol and 106.71 ± 5.04 kJ/mol) than R-CuMn (137.93 ± 16.74 kJ/mol). These results imply that Cr element may help reduce the activation energy of re-oxidation reaction, thereby accelerating the activation energy of re-oxidation reaction, as observed in Figure 4-4.

Once the activation energy E_a is determined, the model and mechanism of reaction can be investigated by using the $g(\alpha)/g(0.5)$ master plots. Since the master plots of R-CuMn are already discussed in Chapter 5, only the master plots for R-CuCr$_{0.1}$Mn$_{0.9}$ and R-CuCr$_{0.3}$Mn$_{0.7}$ are presented here (Figure 6-2 and Figure 6-3).

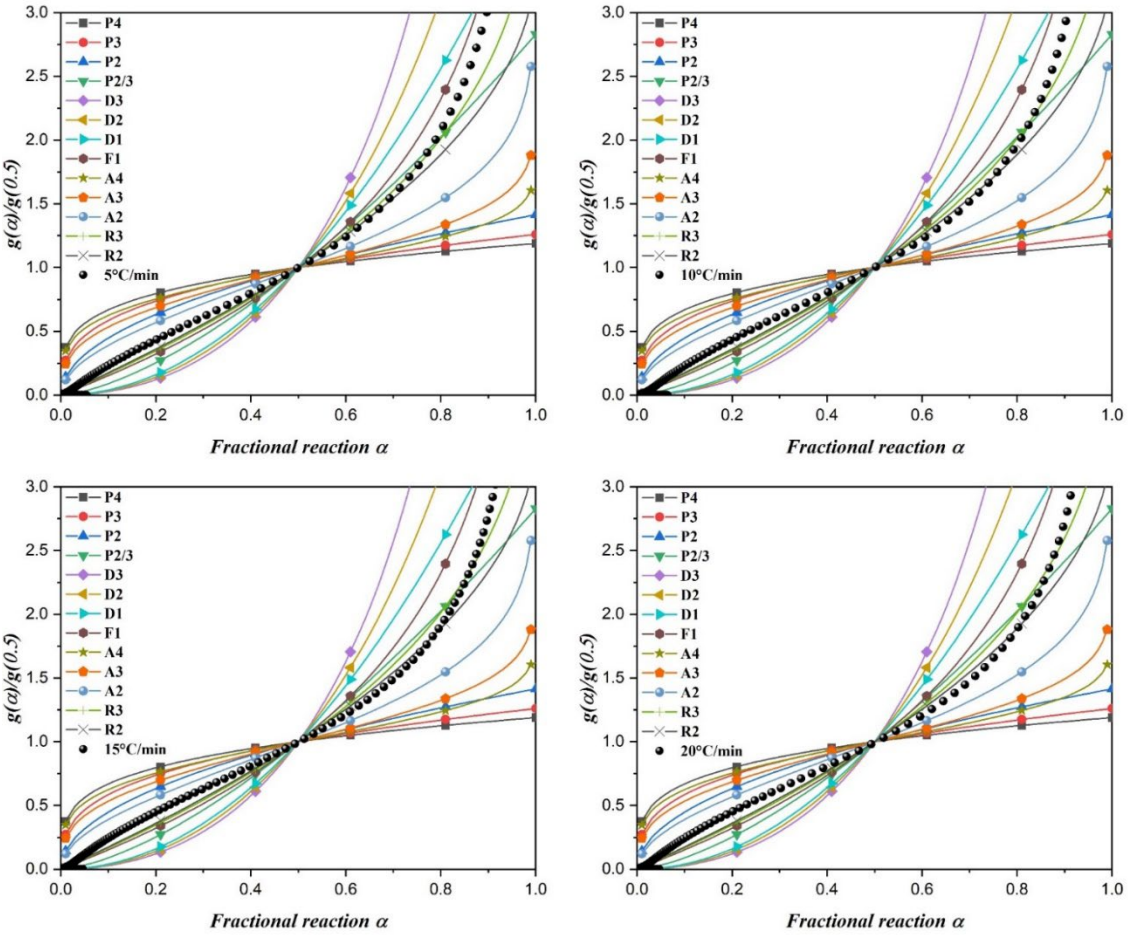

Figure 6-2 $g(\alpha)/g(0.5)$ master plots of R-CuCr$_{0.1}$Mn$_{0.9}$ with different heating rates (5, 10, 15, and 20 °C/min); based on the fitting results, reaction model R3 was determined

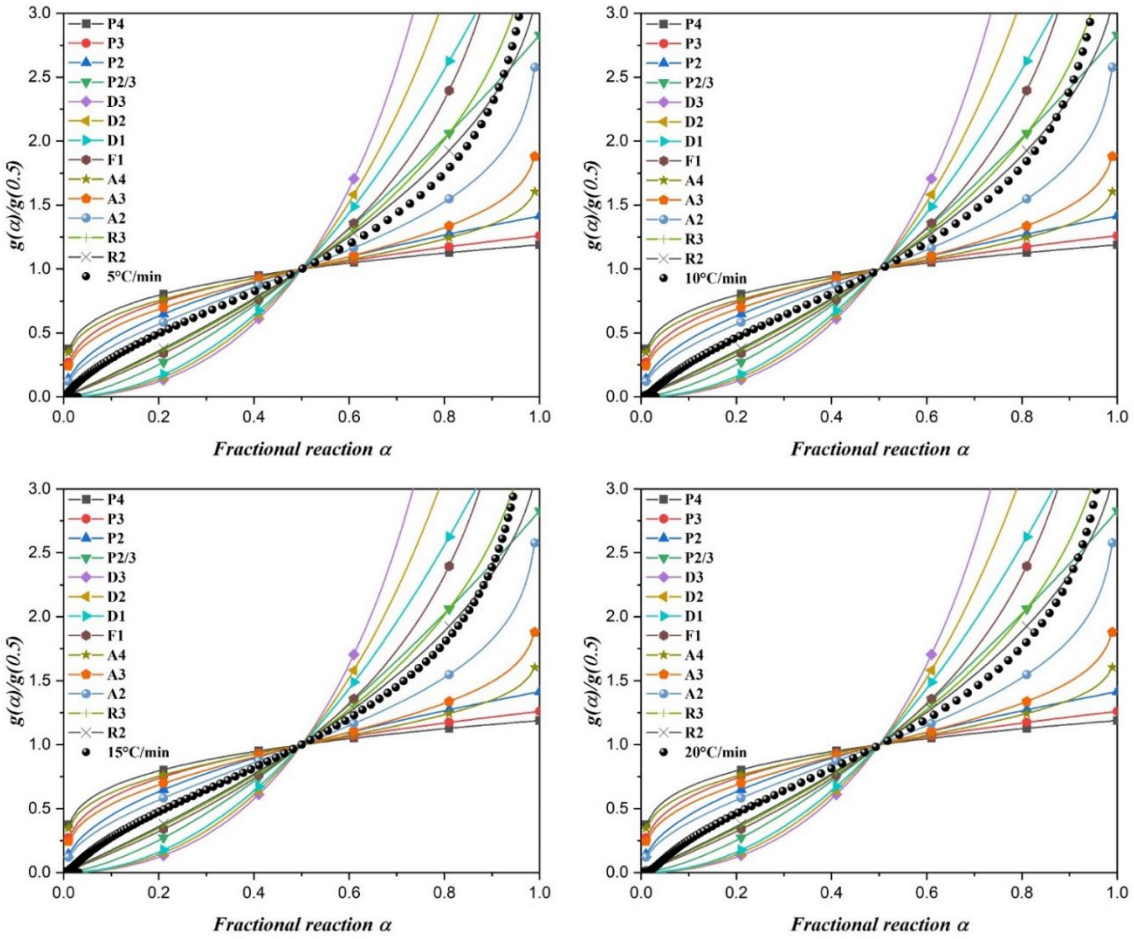

Figure 6-3 $g(\alpha)/g(0.5)$ master plots of R-$CuCr_{0.3}Mn_{0.7}$ with different heating rates (5, 10, 15, and 20 °C/min); based on the fitting results, reaction model R2 was determined

Master plot results also supported this hypothesis, although the curves of R-$CuCr_{0.1}Mn_{0.9}$ and R-$CuCr_{0.3}Mn_{0.7}$ deviated slightly from the thermotical model depending on the conversion ratio. After careful consideration, the three-dimensional diffusion (D3) model was assigned to R-CuMn, contracting sphere (R3) model for R-$CuCr_{0.1}Mn_{0.9}$, and contracting cylinder (R2) model for R-$CuCr_{0.3}Mn_{0.7}$.

The pre-exponential factor A can be generated from E_a and $f(\alpha)$ using the intercept of Equation 6-1, which is first introduced in Chapter 5 (Equation 5-9).

$$\ln\left(\beta\frac{\mathrm{d}\alpha}{\mathrm{d}T}\right)=\ln[Af(\alpha)]-\frac{E_a}{RT} \qquad (6-1)$$

Owing to different heating rates, A may vary in a certain range even for the same sample. Therefore, the average value of A was used for general description. The kinetic triplet parameters (A, E_a, $f(\alpha)$) of R-CuCr$_x$Mn$_{1-x}$ (x = 0, 0.1, 0.3) are summarized in Table 6-1.

Table 6-1 Kinetic triplet of R-CuCr$_x$Mn$_{1-x}$ (x = 0, 0.1, 0.3)

Sample	A (min^{-1})	E_a (kJ·mol^{-1})	Reaction model	$f(\alpha)$
R-CuMn	1.70×10^{8}	137.93	D3	$\frac{3(1-\alpha)^{2/3}}{2(1-(1-\alpha)^{1/3})}$
R-CuCr$_{0.1}$Mn$_{0.9}$	6.90×10^{7}	115.52	R3	$3(1-\alpha)^{2/3}$
R-CuCr$_{0.3}$Mn$_{0.7}$	8.26×10^{6}	106.71	R2	$2(1-\alpha)^{1/2}$

To verify the accuracy of our kinetic model, a series of predictions were performed based on the model (Figure 6-4).

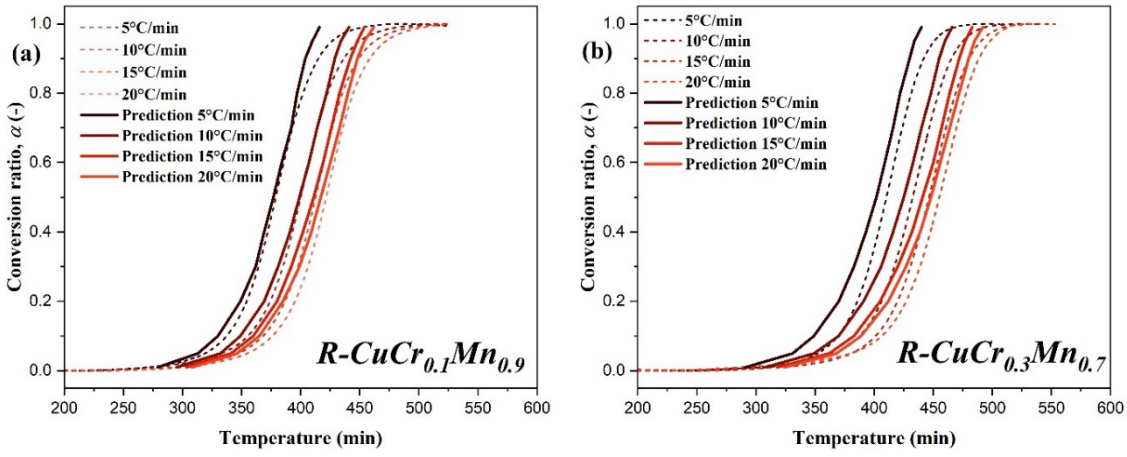

Figure 6-4 (a) Kinetic prediction of R-CuCr$_{0.1}$Mn$_{0.9}$; (b) Kinetic prediction of R-CuCr$_{0.1}$Mn$_{0.9}$

Since the kinetic predictions of R-CuMn are already provided in Chapter 5, only the predictions for R-$CuCr_{0.1}Mn_{0.9}$ and R-$CuCr_{0.3}Mn_{0.7}$ are shown here. The kinetic models for R-$CuCr_{0.1}Mn_{0.9}$ and R-$CuCr_{0.3}Mn_{0.7}$ provide good predictions, deviating only slightly from the experimental results, as their curves did not align perfectly with the theoretical reaction model in the master plots (Figure 6-2 and Figure 6-3). This also suggests that the selection of the reaction model in the previous step significantly affects the accuracy of the kinetic predictions.

6.3 Isothermal oxidation kinetics of Cr-doped $CuMnO_2$

To distinguish from equations that do not account for the oxygen pressure dependence term discussed in Chapter 5, the gas-solid reaction is re-defined as follows:

$$r = \frac{d\alpha}{dt} = k(T)f(\alpha) = A'exp\left(-\frac{E'}{RT}\right)f(\alpha) \qquad (6-2)$$

where $k(T)$ is the reaction rate constant, $f(\alpha)$ is the reaction model, A' is the pre-exponential factor and E' is the activation energy without the consideration of pressure term $h(P)$, and R is the gas constant (8.314 $J \cdot K^{-1} \cdot mol^{-1}$).

In this section, the pressure term is also considered as an important factor in the kinetic equation, therefore the Equation 6-2 can be rewritten into:

$$r = \frac{d\alpha}{dt} = k(T)f(\alpha)h(P) = Aexp\left(-\frac{E}{RT}\right)f(\alpha)(pO_2 - pO_{2,eq})^N \qquad (6-3)$$

where A is the pre-exponential factor, E is the activation energy with the consideration of pressure term $h(P)$, and $pO_{2,eq}$ is the equilibrium oxygen partial pressure. There are various expression forms for $h(P)$ were provided in the literature [1], however, we chose a simple form of pO_2-$pO_{2,eq}$ (representing the driving force of oxidation reaction) with a

modified parameter *N*. The detailed selection strategy can be find in the supplementary document of our publication [2].

6.3.1 Determination of oxygen pressure dependence term h(*P*)

To determine the pressure term h(*P*), the $pO_{2,\,eq}$ at any given temperature must be obtained in advance. Therefore, a *P*-*T* diagram for $Cu(Cr_xMn_{1-x})_2O_4/CuCr_xMn_{1-x}O_2$ (x = 0, 0.1, 0.3) (Figure 6-5) was established through a sophisticated experiment using TGA. Further detailed information can also be find in our publication [2]. Furthermore, the expression for $pO_{2,\,eq}$ can be described in the form of $a\cdot\exp(b\times1000/T)$, and the value of parameters *a* and *b* are summarized in Table 6-2.

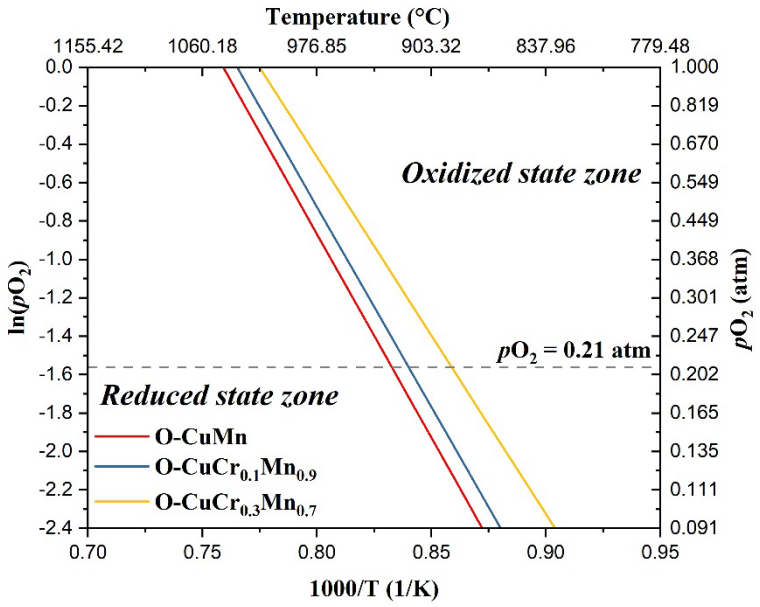

Figure 6-5 *P*-*T* diagram of $Cu(Cr_xMn_{1-x})_2O_4/CuCr_xMn_{1-x}O_2$

Table 6-2 Parameters *a* and *b* of $pO_{2,\,eq}$ for $Cu(Cr_xMn_{1-x})_2O_4/CuCr_xMn_{1-x}O_2$

Sample	*a*	*b*
O-CuMn	9.6×10^6	-21.1832
$O\text{-}CuCr_{0.1}Mn_{0.9}$	8.4×10^6	-20.8360
$O\text{-}CuCr_{0.3}Mn_{0.7}$	1.8×10^6	-18.5923

6.3.2 Isothermal oxidation kinetic modelling of Cr-doped $CuMnO_2$

The sample was heated from room temperature to 475 °C, 500 °C, 525 °C, and 550 °C under nitrogen flow (200 mL/min). When the change in mass was stable, the gas was shifted to oxidizing atmosphere (pO_2 = 0.105, 0.21, 0.5 atm) for oxidation last for 120 mins. The isothermal oxidation behavior of R-$CuCr_xMn_{1-x}$ is shown in Figure 6-6. From the figure, the isothermal oxidation of R-CuMn conducted at 475 °C did not reach a satisfactory conversion ratio (> 0.9) with 30 mins. Therefore, experiments of 500 °C were used for comparison.

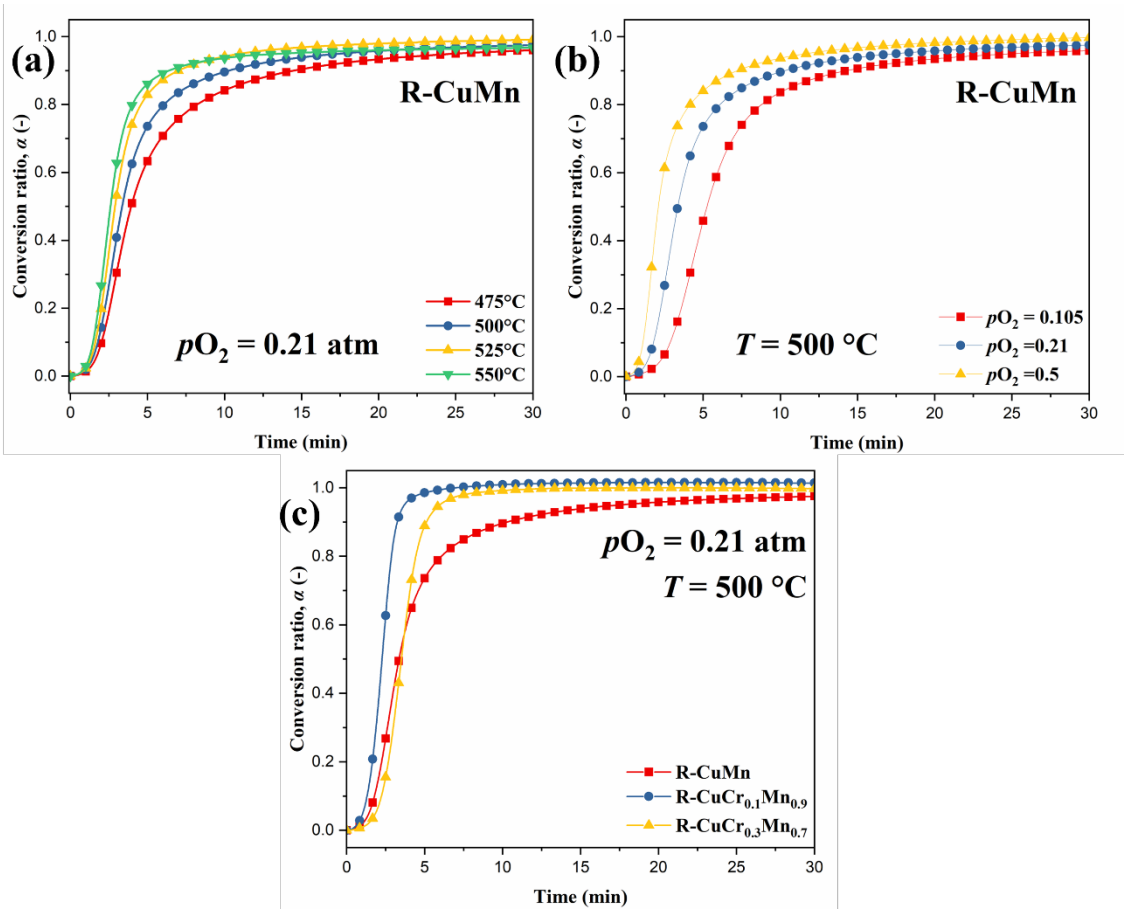

Figure 6-6 Conversion ratio, α vs time for (a): R-CuMn, pO_2 = 0.21 atm at different temperatures; (b): R-CuMn, 500 °C at different pO_2; (c): R-$CuCr_xMn_{1-x}$ at pO_2 = 0.21atm, T = 500 °C

Combining the results shown in Figure 6-6a and Figure 6-6b, either higher reaction temperature or larger oxygen partial pressure can accelerate the reaction which is consistent with the theory of gas-solid reaction kinetics. It is interesting to note that, the reaction rate of R-CuMn was faster than R-$CuCr_{0.3}Mn_{0.7}$ in the early state of reaction (Figure 6-6c), however, the reaction rate of R-$CuCr_{0.3}Mn_{0.7}$ surpassed that of R-CuMn and exhibited a higher conversion ratio within 30 mins. These observations will be discussed later in the analysis of reaction starting temperature and reaction activation energy.

In the isothermal method, the reaction model $f(\alpha)$ is the first parameter to be determined. In general, there are two types of master plots that can be used as the reference plot, $g(\alpha)/g(0.5)$ and $f(\alpha)/f(0.5)$ master plot which are based on integral and differential forms, respectively. Furthermore $g(\alpha)/g(0.5)$ and $f(\alpha)/f(0.5)$ are correlated with experimental data as follows:

$$\frac{g(\alpha)}{g(0.5)} = \frac{t}{t_{0.5}} \qquad (6-4)$$

and

$$\frac{f(\alpha)}{f(0.5)} = \frac{d\alpha/dt}{(d\alpha/dt)_{0.5}} \qquad (6-5)$$

The experimental data is plotted and compared with a series of existing models to determine the best-matching-model. As shown in Figure 6-7a and Figure 6-7b, although reaction model A2 was identified for R-CuMn in Chapter 5, significant deviations appear when the conversion ratio exceeds 0.5. Therefore, the SB model was used to fit the data in order to obtain a better result. The mathematical expression of the SB model is shown below:

$$f(\alpha) = \alpha^m \cdot (1-\alpha)^n \cdot (-\ln(1-\alpha))^p \qquad (6-6)$$

where m, n, and p are fitting parameters.

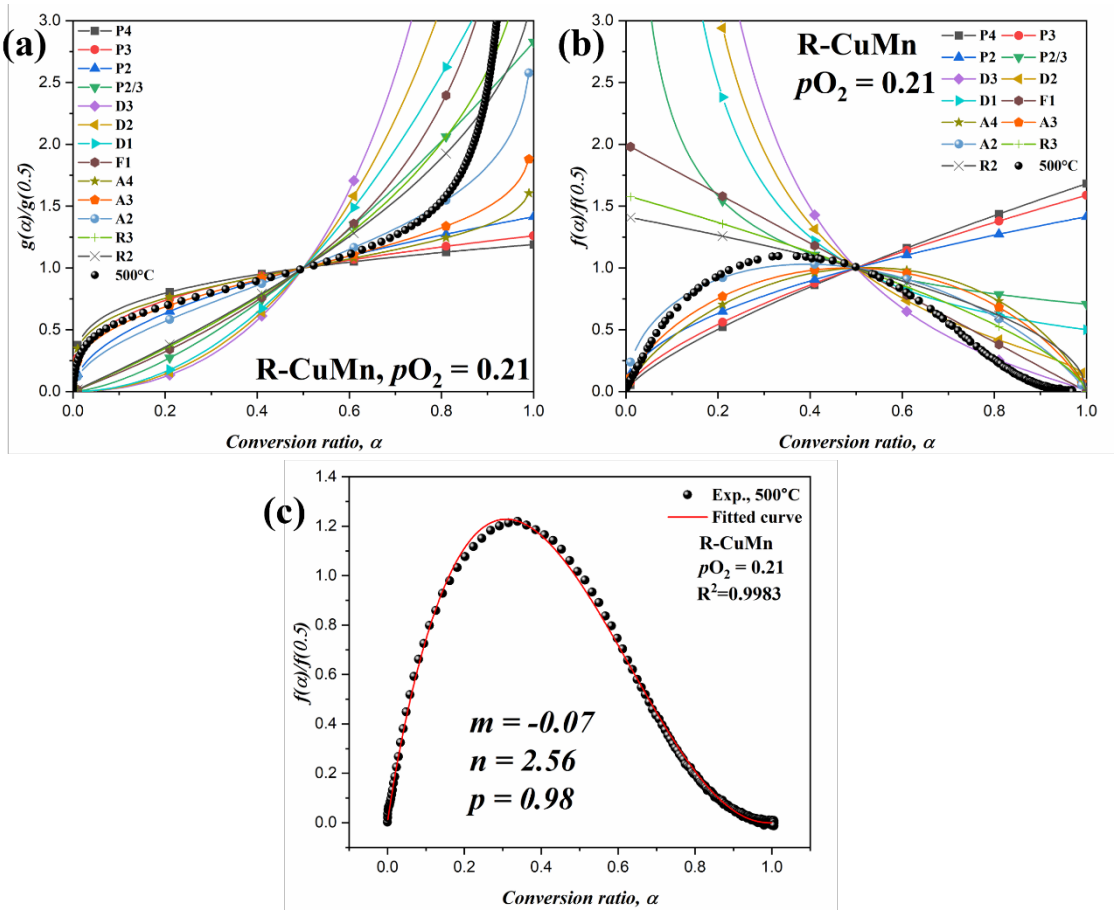

Figure 6-7 (a): $g(\alpha)/g(0.5)$ master plot for R-CuMn, 500 °C; (b): $f(\alpha)/f(0.5)$ master plot for R-CuMn, 500 °C; (c): SB mode fitting for R-CuMn, 500 °C

Figure 6-7c shows a typical SB model fitting for R-CuMn at $pO_2 = 0.21$ and $T = 500$ °C. By fitting the data at each temperature (475 – 550 °C) and oxygen partial pressure (0.105 – 0.5 atm), the average value of m = -0.04, n = 2.55, and p = 0.98 were used to describe the reaction model $f(\alpha)$ of R-CuMn. The representative $g(\alpha)/g(0.5)$ master plot (pO_2 = 0.21, T = 500 °C) for R-$CuCr_{0.1}Mn_{0.9}$ and R-$CuCr_{0.3}Mn_{0.7}$ are shown in Figure 6-8. Although the experimental data deviated from the known models when the conversion ratio was larger than 0.85, the A4 model could generally be used to describe the reaction

model $f(\alpha)$ for R-$CuCr_{0.1}Mn_{0.9}$ and R-$CuCr_{0.3}Mn_{0.7}$.

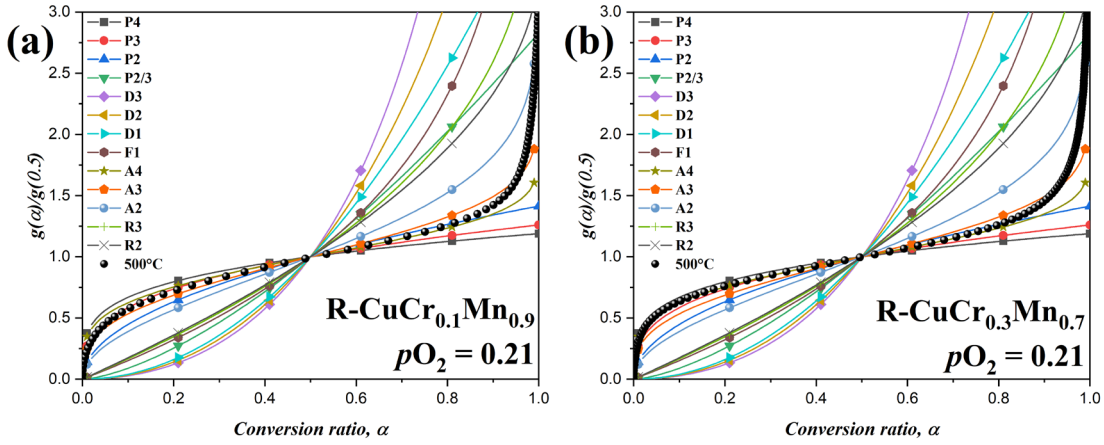

Figure 6-8 A typical $g(\alpha)/g(0.5)$ master plot for (a): R-$CuCr_{0.1}Mn_{0.9}$ at pO_2 = 0.21 atm; (b): R-$CuCr0_{.3}Mn_{0.7}$ at pO_2 = 0.21 atm

Once the reaction model $f(\alpha)$ of each sample was determined, the activation energy *E'* and pre-exponential factor *A'* that without consideration of *h(P)* can be calculated using Equation 6-7, which is obtained by taking the logarithm of Equation 6-2. The subscript represents the value was taken at a conversion ratio of 0.5.

$$\ln\left(\frac{d\alpha}{dt}\right)_{0.5} = \ln\left(A' f(\alpha)\right)_{0.5} - \left(\frac{E'}{RT}\right)_{0.5} \qquad (6-7)$$

Similarly, the following equation can be obtained by taking the logarithm of Equation 6-3.

$$\ln\left(\frac{d\alpha}{dt}\right)_{0.5} = \ln\left(A f(\alpha)\right)_{0.5} - \left(\frac{E}{RT}\right)_{0.5} - N \cdot \ln(pO_2 - pO_{2,eq}) \qquad (6-8)$$

By comparing Equation 6-7 and Equation 6-8, we can know the relationship between

A' and *A*, and *E'* and *E* from Equation 6-9a and its simplified form Equation 6-9b.

$$\ln\left(A'f(\alpha)\right)_{0.5} - \left(\frac{E'}{RT}\right)_{0.5} = \ln\left(Af(\alpha)\right)_{0.5} - \left(\frac{E}{RT}\right)_{0.5} - N \cdot \ln\left(pO_2 - pO_{2,eq}\right) \quad (6-9a)$$

$$\left[\ln A' - \left(\frac{E'}{RT}\right)\right]_{0.5} = \left[\ln A - \left(\frac{E}{RT}\right)\right]_{0.5} - N \cdot \ln\left(pO_2 - pO_{2,eq}\right) \quad (6-9b)$$

For a given temperature *T* (475, 500, 525, and 550 °C), one modified parameter *N* of pressure term *h(P)* can be obtained by plotting the ln(pO_2-$pO_{2,eq}$) vs the left term of Equation 6-9b because the equilibrium oxygen partial pressure $pO_{2,eq}$ can be easily determined by using the *P*-*T* diagram (Figure 6-5). The average value of *N* was used to describe the pressure term in the temperature range of 475–550 °C. Once *N* was determined, it can be re-substitute into Equation 6-9b to calculate the actual activation energy *E* and pre-exponential factor *A* that with the consideration of *h(P)*. More information can be found in our publication and the corresponding paragraphs in the supplementary document [2]. After processing all the experimental data of R-$CuCr_xMn_{1-x}$, the oxidation kinetic parameters were summarized in Table 6-3.

Table 6-3 Oxidation kinetic parameters of R-$CuCr_xMn_{1-x}$ (0, 0.1, 0.3) in the temperature range of *T* = 475–550 °C at pO_2 = 0.105–0.5 atm

Sample	***f(α)***	$\boldsymbol{pO_{2,eq}}$	***N***	***E*** (kJ/mol)	***A*** (min^{-1})
R-CuMn	$\alpha^{-0.04}\cdot(1-\alpha)^{2.55}\cdot[-\ln(1-\alpha)]^{0.98}$	$9.6\times10^6\times e^{(-21.18\times1000/T)}$	0.56	64.054±0.001	90259.127
R-$CuCr_{0.1}Mn_{0.9}$	$4\cdot(1-\alpha)\cdot[-\ln(1-\alpha)]^{3/4}$	$8.5\times10^6\times e^{(-20.84\times1000/T)}$	0.58	29.932±0.001	94.547
R-$CuCr_{0.3}Mn_{0.7}$	$4\cdot(1-\alpha)\cdot[-\ln(1-\alpha)]^{3/4}$	$1.8\times10^6\times e^{(-18.59\times1000/T)}$	0.61	58.049±0.004	5041.102

In Section 6.2, the activation energies of 137.93 ± 16.74 kJ/mol, 115.52 ± 6.94 kJ/mol,

106.71 ± 5.04 kJ/mol for R-CuMn, R-$CuCr_{0.1}Mn_{0.9}$, and R-$CuCr_{0.3}Mn_{0.7}$ are reported. These results indicated that Cr doping contributes to a reduction in activation energy. However, we found that the activation energies of three samples show different trends under the isothermal oxidation conditions. Specifically, R-$CuCr_{0.1}Mn_{0.9}$ exhibits the smallest activation energy of 29.93 kJ/mol.

The difference in trends can be explained by examining the non-isothermal oxidation results of R-$CuCr_xMn_{1-x}$ (Figure 4-4) that R-$CuCr_{0.1}Mn_{0.9}$ exhibits lowest oxidation onset temperature of 384 °C comparing with R-CuMn of 392 °C and R-$CuCr_{0.3}Mn_{0.7}$ of 418 °C. Since the re-oxidation of R-$CuCr_{0.3}Mn_{0.7}$ requires a higher temperature to occur, the activation energy of R-$CuCr_{0.3}Mn_{0.7}$ exhibits a larger value than that of R-$CuCr_{0.1}Mn_{0.9}$ at isothermal conditions.

However, under non-isothermal conditions, the temperature increases at a fixed rate (e.g., 20°C/min), allowing each sample to reach its optimal oxidation temperature. This results in a trend of decreasing activation energy as the amount of Cr increases under the non-isothermal method.

The typical kinetic predictions based on the data in Table 6-3 are shown in Figure 6-9. Overall, the kinetic models provide a good description of the oxidation behavior for each sample at different temperatures and oxygen partial pressures. However, under certain conditions, the prediction curve differs slightly from the experimental data. Specifically, at an oxygen partial pressure of pO_2=0.21 atm, the prediction curve at 500 °C best matches the experimental data, while the other curves show a slight shift (Figure 6-9a). Similarly, when the temperature is fixed at 500 °C, the prediction curve under pO_2=0.21 atm shows the best agreement with the experimental data (Figure 6-9b).

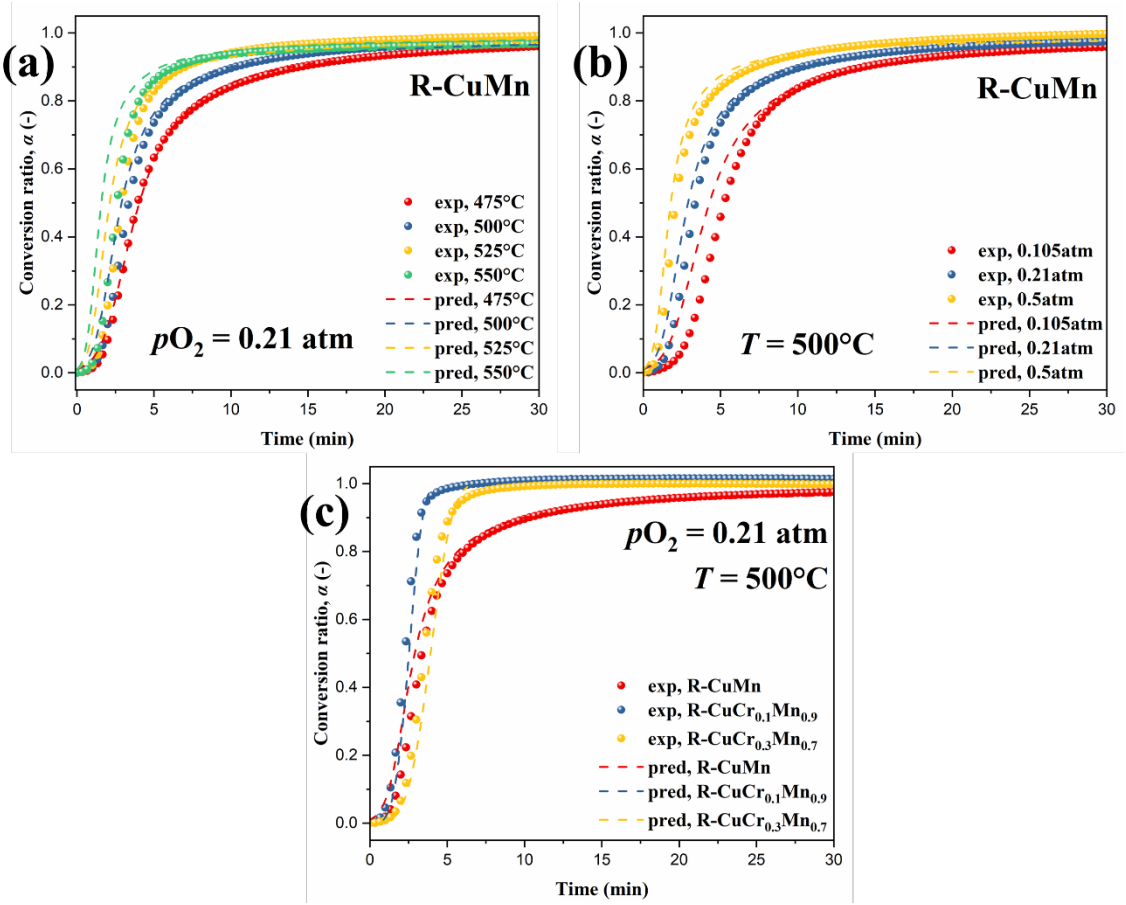

Figure 6-9 Oxidation kinetic predictions of (a): R-CuMn, pO_2 = 0.21 atm at different temperatures; (b): R-CuMn, 500 °C at different pO_2; (c): R-$CuCr_xMn_{1-x}$ (x = 0, 0.1, 0.3) at pO_2 = 0.21 atm, T = 500 °C

6.3.3 Thermal power output estimation

For practical applications, understanding the thermal power output of each material under varying conditions is essential. In Chapter 4, we reported the heat release Q (heat storage density) as 236.11 ± 5.4 kJ/kg, 293.67 ± 1.25 kJ/kg, and 305.61 ± 16.45 kJ/kg for the isothermal oxidation of R-CuMn, R-$CuCr_{0.1}Mn_{0.9}$, and R-$CuCr_{0.3}Mn_{0.7}$ at 500 °C, respectively. Assuming a constant heat release Q for each sample across different oxygen partial pressures, we can determine the thermal power output at any oxygen partial pressure by multiplying the heat release Q by the reaction rate ($d\alpha/dt$) obtained in this

study (Equation 6-10).

Furthermore, since we already know the relationship between reaction rate ($d\alpha/dt$) and time t, it is straightforward to determine the relationship between instantaneous thermal power output (P_{output}) and time t.

$$P_{output} = Q \cdot \frac{d\alpha}{dt} \qquad (6-10)$$

When T = 500 °C and pO_2 = 0.21 atm, the curve of t vs. P_{output} is shown in Figure 6-10a. The max instantaneous thermal power output ($P_{output,\ max}$) of each sample at a given oxygen partial pressure is summarized in Figure 6-10b. In general, the speed of the reaction rate at the same temperature is usually related to the concentration of the reactants. In this study, the oxidation reaction rate is only related to the oxygen concentration (partial pressure) due to R-CuCr$_x$Mn$_{1-x}$ being in a solid state. It can be observed from Figure 6-9b that the re-oxidation rate of R-CuMn increases with the increase of oxygen partial pressure.

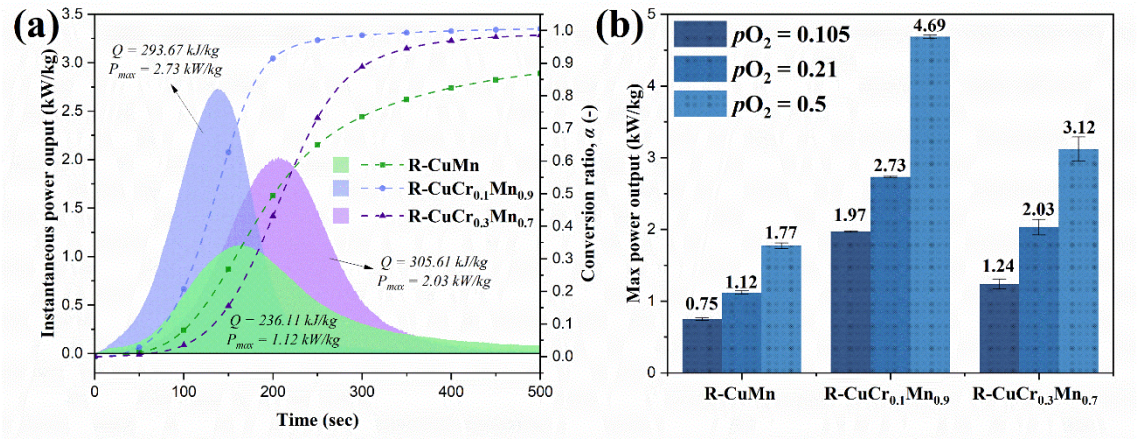

Figure 6-10 (a): Instantaneous power output of R-CuCr$_x$Mn$_{1-x}$ at pO_2 = 0.21 atm, T = 500 °C; (b): Max power output for each sample at 500 °C for various oxygen partial pressures

Since R-$CuCr_{0.1}Mn_{0.9}$ exhibited the fastest reaction rate, it reaches the $P_{output,\ max}$ in the shortest time and showed the largest $P_{output,\ max}$ among three samples at all oxygen partial pressures. From Figure 6-10b, we can see that R-$CuCr_{0.1}Mn_{0.9}$ is more affected by the oxygen atrial pressure than the other two. When the oxygen partial pressure increases from 0.21 to 0.5, the $P_{output,\ max}$ of R-$CuCr_{0.1}Mn_{0.9}$ increases by nearly 72%, while 58% for R-CuMn and 54% for R-$CuCr_{0.3}Mn_{0.7}$.

On the other hand, Figure 6-10 demonstrates that, since CHS technology relies on a chemical reaction process, its power output inherits characteristics of chemical reactions. Generally, the *α-t* plot for the redox reactions of metal oxides exhibits a sigmoidal curve, resulting in an unstable, time-dependent peak in power output. Unlike LHS technology, which can release heat at a stable temperature, the outlet temperature of the thermal energy generated by CHS may vary significantly over time, which could be disadvantageous for consumers with strict temperature requirements.

6.4 Conclusion

In this chapter, we investigated the Cr doing effect on $CuMn_2O_4/CuMnO_2$ redox couple and established the oxidation kinetic model for $CuCr_xMn_{1-x}O_2$ (R-$CuCr_xMn_{1-x}$, x = 0, 0.1, 0.3).

For non-isothermal oxidation kinetic study of R-$CuCr_xMn_{1-x}$, the sample was heated from room temperature to 1000℃ at different heating ramps. R-$CuCr_{0.1}Mn_{0.9}$ and R-$CuCr_{0.3}Mn_{0.7}$ exhibited lower re-oxidation E_a (115.52 ± 6.94 kJ/mol and 106.71 ± 5.04 kJ/mol) than R-CuMn (137.93 ± 16.74 kJ/mol) in non-isothermal conditions. The R3 model and R2 model were assigned to R-$CuCr_{0.1}Mn_{0.9}$ and R-$CuCr_{0.3}Mn_{0.7}$, respectively. The kinetic models for R-$CuCr_{0.1}Mn_{0.9}$ and R-$CuCr_{0.3}Mn_{0.7}$ provide good predictions, deviating only slightly from the experimental results.

For isothermal oxidation kinetic study of R-$CuCr_xMn_{1-x}$, a more detailed analysis was

conducted. The isothermal oxidation kinetic model of R-$CuCr_xMn_{1-x}$ was determined by TGA experiments under different oxygen partial pressures (0.105–0.5 atm) in the temperature range of 475–550 °C.

The reaction model of SB (m = -0.04, n = 2.55, p = 0.98), A4, and A4 were assigned to R-CuMn, R-$CuCr_{0.1}Mn_{0.9}$ and R-$CuCr_{0.3}Mn_{0.7}$, respectively. R-$CuCr_{0.1}Mn_{0.9}$ exhibited the smallest oxidation activation energy of 29.932 kJ/mol, compared with 64.054 kJ/mol for R-CuMn of and 58.049 kJ/mol for R-$CuCr_{0.3}Mn_{0.7}$. The pressure term $h(P)$ was taking the simple form of $(pO_2\text{-}pO_{2,eq})^N$ with a modified parameter N. The value of parameter N varies in the range of 0.56 – 0.61 owing to the addition of Cr.

The kinetic models provide a series of good descriptions of the oxidation behavior for each sample at different temperatures and oxygen partial pressures. However, the prediction curve still differs from the experimental data under certain conditions. By combining the heat release amount Q (heat storage capacity) we reported in the previous research, the thermal power output can be obtained easily. When pO_2 = 0.5 atm, R-$CuCr_{0.1}Mn_{0.9}$ showed the highest instantaneous power output of 4.69 kW/kg among all samples, and it is more affected by the oxygen partial pressure than the other two.

Finally, we point out that the power output of CHS inherits the time-dependent characteristic of the chemical reaction, which means the outlet temperature of the thermal energy generated by CHS may show a large variation over time. This issue may also cause an unfavorable problem for the consumers with strict temperature requirements.

Reference

[1] S. Vyazovkin, Kinetic effects of pressure on decomposition of solids, International Reviews in Physical Chemistry 39 (2020) 35–66. https://doi.org/10.1080/0144235X.2019.1691319.

[2] X. Chen, M. Kubota, N. Kobayashi, S. Yamashita, H. Kita, An in-depth oxidation kinetic study of CuCrxMn1-xO2 (x = 0, 0.1, 0.3) for thermochemical energy storage at medium-high temperature, Solar Energy Materials and Solar Cells 260 (2023) 112495. https://doi.org/10.1016/j.solmat.2023.112495.

Chapter 7. Machine learning-assisted DFT approach for predicting effective dopants in $CuMn_2O_4$

7.1 Introduction

In Chapter 3, we identified $CuMn_2O_4/CuMnO_2$ as a promising candidate for the redox-type chemical heat storage technology. However, the high reduction (charging) temperature of this redox couple presents many challenges for practical applications, including difficulties in insulation.

Elemental doping is a key strategy to adjust the reaction temperatures of materials. However, while most studies focus on increasing these temperatures to enhance energy efficiency, methods for lowering the reaction temperatures to reduce costs and expand applicability remain underexplored. In a preliminary attempt at elemental doping in Chapter 4, we found that a small amount of Cr added to the B-site of $CuMn_2O_4/CuMnO_2$ (AB_2O_4/ABO_2) lowers the oxidation temperature of $CuMnO_2$, along with a decrease in the reduction temperature of $CuMn_2O_4$. However, blind attempts at elemental doping are time-consuming and costly. Therefore, new approaches to efficiently identify suitable doping elements need to be developed.

In 2015, Kirklin et al. [1] released the Open Quantum Materials Database (OQMD), a high-throughput database containing nearly 300,000 density functional theory (DFT) total energy calculations of compounds from the Inorganic Crystal Structure Database (ICSD) and decorations of commonly occurring crystal structures. Notably, the OQMD is freely accessible to the public. Later, Ward et al. [2] proposed a general-purpose machine learning framework for predicting properties of inorganic materials. They subsequently packaged this framework into a toolkit called Matminer, which enables even non-experts in machine learning to easily generate features for machine learning applications using only a chemical formula [3].

Very recently, Baldassarri et al. [4] reported a high throughput computational studies and machine-learning predictions of oxygen vacancy formation energy in metal oxides. They highlighted that oxygen vacancies are common defects in metal oxide and play a crucial role in various technologies. For example, in solar thermochemical hydrogen

production, oxygen vacancies are created when metal oxides are reduced at high temperatures, and these vacancies are filled during re-oxidation by exposure to steam. Their findings inspired us to explore the connection between the reduction temperature and metal oxides and the formation of oxygen vacancies.

The formation energy of oxygen vacancies (ΔE_{vf}) can be calculated from the DFT energy difference between a compound with and without a vacancy, while appropriately accounting for the chemical potential of the removed oxygen. Therefore, the reduction temperature (i.e., the ease of reduction) of metal oxides is expected to be positively correlated with ΔE_{vf}. Although both DFT calculations can be used to estimate ΔE_{vf} the computational cost is high because these calculations require modeling supercells with vacancies, which significantly increases the complexity.

In this study, we began by calculating the ΔE_{vf} of a part of elementally doped $CuMn_2O_4$ using DFT calculations. We first generated 132 features (Feature set I) from chemical formulas using Matminer and integrated these features with the corresponding ΔE_{vf} values to create a small dataset for machine learning. Later, we also supplement 2 important features (Feature set II) constructed from the unrelaxed vacancy formation energy of binary oxides for performance improvement.

Recognizing that a small dataset may not capture the behavior of all elements, we supplemented it with a larger database of 1,000 metal oxides with various structures (e.g., perovskites) extracted from literature to enhance the model's robustness. Using this expanded dataset, we aim to predict the effect of potential doping elements on the ΔE_{vf} of $CuMn_2O_4$ and identify dopants that can effectively lower its reduction temperature.

7.2 Methodology

7.2.1 Machine learning model

Predicting ΔE_{vf} from the structure's features is a classic supervised learning task. In this chapter, a Random Forest (RF) regression model was employed. The RF model is a

machine learning algorithm designed to predict continuous numerical values by constructing multiple decision trees and averaging their predictions to produce the results (Figure 7-1).

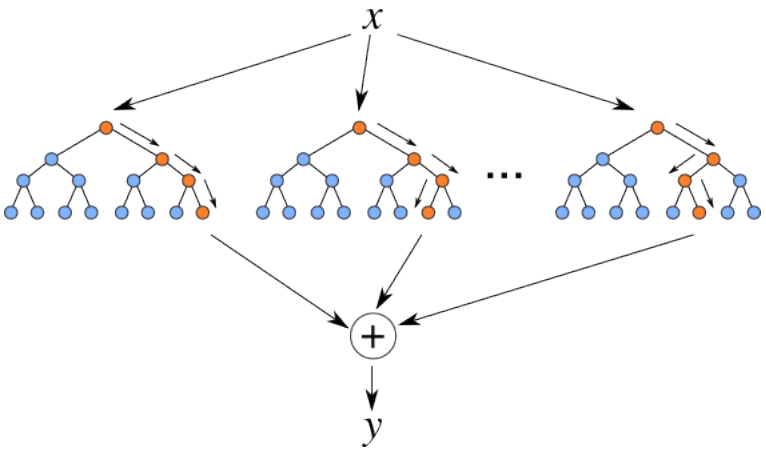

Figure 7-1 Random Forest (RF) regression model

It is worth noting that, although many neural network-based "black-box" models demonstrate excellent predictive performance, we still prioritize simplicity and therefore use RF regression models. Additionally, by analyzing feature importance from the trained RF regression model, we can identify which features play a significant role in predicting ΔE_{vf}, potentially improving the model's performance further.

The input (X) to this model consists of a set of features related to the target variable being predicted. For example, the features of each structure generated by Matminer are used as X. The output (y) is a specific numerical value; in this case, it represents each structure's ΔE_{vf}. Since this is a supervised learning approach, the model continuously adjusts its predictions to match the actual values to minimize error. Additionally, the RF regression model offers robustness and makes it easy to identify important features for further prediction.

7.2.2 Elemental doping strategies

Elemental doping can be performed at the A or B sites of $CuMn_2O_4$. Alkali metals, alkaline earth metals, transition metals, post-transition metals, and some metalloid elements from periods 2 to 4 of the periodic table are used as dopants (a total of 16 elements). Although the doping level can significantly affect ΔE_{vf} and thereby influence the reaction temperature, the primary objective of this study is to select suitable dopants. Therefore, the doping ratio was uniformly set to an elemental ratio of 0.1.

7.2.3 Feature generation

Two types of feature (*X*) sets were used for model training and prediction.

Feature set I was generated by Matminer, also known as the "Magpie feature". The Magpie features include stoichiometric attributes, elemental property statistics, electronic structure attributes, and ionic compound attributes. In total, 132 different features were generated by chemical formulae and saved in the Feature set I.

Feature set II was originated from the study of Baldassarri et al. In their study, two statistic features constructed from the unrelaxed vacancy formation energy of binary oxides were included in the feature set. The details are as follows:

(i) $min\left(\Delta E_{vf}^{MO_x}\right)$: the lowest value of $\Delta E_{vf}^{MO_x}$ among all M^{x+} cation in the structure. For example, the spinel structure $CuMn_2O_4$, where Cu^{2+} is the easiest to reduce cation. Therefore, the value of min ($\Delta E_{vf}^{MO_x}$) equals to ΔE_{vf}^{CuO}.

(ii) $\langle \Delta E_{vf}^{MO_x,NN} \rangle$: the weighted average of $\Delta E_{vf}^{MO_x}$ over all M^{x+} cation neighboring the vacancy, which is a site-specific feature. The weights are defined as a sum to 1. For a smaller $\Delta E_{vf}^{MO_x}$, the weight will be larger, in order to reflect the dominant role of smaller $\Delta E_{vf}^{MO_x}$ in determining the whole ΔE_{vf} of structure. Specifically, for each cation *i* neighboring the vacancy have $\Delta E_{vf}^{MO_{x,i}}$, its weight

is defined as:

$$w_i = \frac{u_i}{\sum_j n_j \cdot u_j} \quad (7-1)$$

$$u_i = \frac{1}{1 + \left(\Delta E_{vf}^{MO_{x,i}} - \Delta E_{vf}^{MO_{x,NN}}\right)} \quad (7-2)$$

where *j* represents all cation neighboring the vacancy including *i*, n_j is the number of cation *j* neighboring the vacancy, $\Delta E_{vf}^{MO_{x,NN}}$ is the lowest $\Delta E_{vf}^{MO_x}$ among the cations neighboring the vacancy, and the superscript *NN* represents for "nearest neighbor". For example, the spinel structure, which has two types of vacancy sites (V1's neighbors are 1 A and 3 B cations; V1's neighbors are 4 B cations). However, in the normal spinel $CuMn_2O_4$ discussed in this study, we focused only on the V1 type, since the V2 type is more often present in the inverse spinel structure. For $V1\langle\Delta E_{vf}^{MO_x,NN}\rangle$, the calculation process is as follows:

$$V1\langle\Delta E_{vf}^{MO_x,NN}\rangle = n_A \cdot w_{CuO} \cdot \Delta E_{vf}^{CuO} + n_B \cdot w_{Mn_2O_3} \cdot \Delta E_{vf}^{Mn_2O_3} \quad (7-3)$$

$$u_{CuO} = \frac{1}{1 + \left(\Delta E_{vf}^{MO_{CuO}} - \Delta E_{vf}^{MO_{x,NN}}\right)} = \frac{1}{1 + \left(\Delta E_{vf}^{MO_{CuO}} - \Delta E_{vf}^{MO_{CuO}}\right)} = 1 \quad (7-4)$$

$$u_{Mn_2O_3} = \frac{1}{1 + \left(\Delta E_{vf}^{MO_{Mn_2O_3}} - \Delta E_{vf}^{MO_{x,NN}}\right)} = \frac{1}{1 + \left(\Delta E_{vf}^{MO_{Mn_2O_3}} - \Delta E_{vf}^{MO_{CuO}}\right)} \approx 0.48 \quad (7-5)$$

$$w_{CuO} = \frac{u_{CuO}}{1 \cdot u_{CuO} + 3 \cdot u_{Mn_2O_3}} \approx 0.41 \quad (7-6)$$

$$w_{Mn_2O_3} = \frac{u_{Mn_2O_3}}{1 \cdot u_{CuO} + 3 \cdot u_{Mn_2O_3}} \approx 0.20 \quad (7-7)$$

$$V1\langle \Delta E_{vf}^{MO_x,NN} \rangle = 0.41 \cdot \Delta E_{vf}^{CuO} + 0.60 \cdot \Delta E_{vf}^{Mn_2O_3} \quad (7-8)$$

The situation is more complex for the doped $CuMn_2O_4$, as some doped elements can exhibit multiple valence states in their corresponding binary oxides (e.g., V, Cr). Therefore, a categorical approach is needed when calculating $\langle \Delta E_{vf}^{MO_x,NN} \rangle$ for the doped $CuMn_2O_4$: (a) when the valence state of the doped element matches the valence state of the original cation at the site (Cu^+/Mn^{3+} in A/B-site), the ΔE_{vf} of the binary oxide corresponding to that doped element in that valence state is used to calculate the mixed ΔE_{vf} for the site with molar ratios; (b) when there is a mismatch in valence states, the value closest to the original cation's valence state at the site is used to calculate the mixed ΔE_{vf} for the site. Once the mixed ΔE_{vf} is obtained, Equation 7-1 through Equation 7-8 can be used to recalculate the ΔE_{vf} for the doped $CuMn_2O_4$.

7.2.4 Target variable

The ΔE_{vf}, which serves as the target variable (y) in the model training, was determined by removing an oxygen atom from a supercell of the $CuMn_2O_4$ bulk structure prior to elemental doping. It can be computed as follows:

$$\Delta E_{vf} = E(Cu_nMn_{2n}O_{4n-1}) + E_o - E(Cu_nMn_{2n}O_{4n}) \quad (7-9)$$

where $E(Cu_nMn_{2n}O_{4n})$ indicates the DFT energy of a supercell (2×2×1) of $CuMn_2O_4$, $E(Cu_nMn_{2n}O_{4n-1})$ is that of a supercell of $CuMn_2O_4$ containing one oxygen vacancy, E_o is the DFT reference energy of oxygen (-4.523 eV). The supercell (2×2×1) of $CuMn_2O_4$ contains 32 Cu atoms and 64 Mn atoms; therefore, the number of atoms replaced (doped) at the A and B sites also varies. In this study, the dopant elements randomly replaced the atoms at either the A or B sites, disregarding the impact of the overall energy minimization.

All the spin-polarized DFT calculations were carried out using the Vienna Ab-initio Simulation Package (VASP) with a supercomputer platform. The generalized gradient approximation (GGA) with the Perdew-Burke-Ernzerhof (PBE) function was applied. A 2 × 2 × 1 supercell was constructed to model the system, and an energy cutoff (ENCUT) of 520 eV was applied to define the plane wave basis set. The projector-augmented wave (PAW) method was used to describe the core-valence interaction. The convergence criteria were set to EDIFF = 5.0×10^{-7} eV for the self-consistent field loop and EDIFFG = 0.01 eV/Å for the force convergence. A Monkhorst-Pack grid was employed for Brillouin zone sampling, with a K-spacing value of 0.050 to generate 1 × 1 × 2 K-point mesh.

7.2.5 Model training strategies

The small datasets constructed in Section 7.2.3 and Section 7.2.4 are referred to as Dataset A. A version of Dataset A that includes only Feature set I is called Dataset A (I), while one that includes both Feature set I and Feature set II is referred to as Dataset A (I&II). Meanwhile, data with the same structure obtained from the literature are referred to as Dataset B (I) and Dataset B (I&II).

Each dataset was randomly split into two parts: 80% (training dataset) was used for model training and the remaining 20% (test dataset) was for the model evaluation.

We first trained the RF regression model separately on each dataset (Dataset A (I),

Dataset A (I&II), Dataset B (I), and Dataset B (I&II)) to assess the contribution of Feature set II. Next, we trained the model using only Dataset B (I&II) and directly predicted Dataset A (I&II) to evaluate whether predictions could be made based solely on perovskite structure's features, without incorporating spinel structure's features. Finally, we combined Dataset A (I&II) and Dataset B (I&II) to build a generalized model for screening suitable dopant for spinel-structure $CuMn_2O_4$.

Three metrics were used to evaluate the predictive performance of the model: Mean Squared Error (MSE), Root Mean Squared Error (RMSE), and Mean Absolute Error (MAE), and their definitions are shown below:

$$MSE = \frac{\sum_{i=1}^{N}\left(y_t^i - y_p^i\right)^2}{N} \quad (7-10)$$

$$RMSE = \sqrt{MSE} \quad (7-11)$$

$$MAE = \frac{1}{N}\sum_{i=1}^{N}\left|y_t^i - y_p^i\right| \quad (7-12)$$

where y_p^i is the value predicted by model, y_t^i is the true value in dataset.

7.3 Results and discussion

7.3.1 Exploration of target variables in the dataset

To better visualize the effect of doping each element at the A and B sites of $CuMn_2O_4$, the comparison of ΔE_{vf} before and after doping is presented in Figure 7-2. From the figure, we can observe that certain transition metal elements, such as V, Fe, Co, and Ni, have a significant impact on the ΔE_{vf} of $CuMn_2O_4$, regardless of whether they are doped at the A or B sites. In contrast, elements such as Al, Sc, Ti, Cr, and Ga exhibit markedly different behaviors when doped at the B site compared to the A site.

Additionally, it is worth noting that doping elements at the A site appears to be more effective in reducing the ΔE_{vf} of $CuMn_2O_4$.

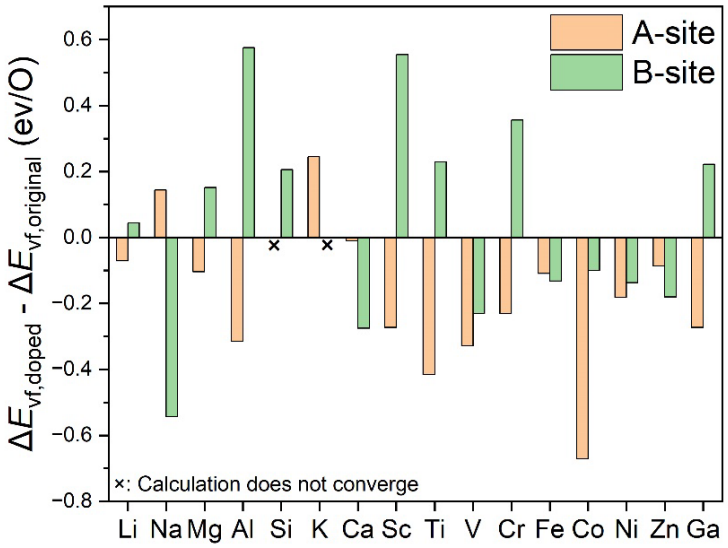

Figure 7-2 Difference in ΔE_{vf} of $CuMn_2O_4$ before and after doping

The distribution of the target variables (ΔE_{vf}) is presented in Figure 7-3. The frequency of occurrence of each value in the figure indicates that Dataset B is much larger in size than Dataset A. The kernel density estimate plot shows that the distribution of Dataset A is unimodal, whereas Dataset B displays a broader, hump-shape distribution, suggesting that it may contain various ΔE_{vf} with different structures (actually, it does contain perovskite-type and pyrochlore-type oxides). The box plot further reveals that the average value of Dataset A is around 3.6, likely due to the limited doping amount in $CuMn_2O_4$, resulting in a narrower range of ΔE_{vf} variation. By contrast, Dataset B spans a much wider range, from approximately 1.0 to 7.5. This difference in data distribution may significantly affect model training and evaluation; however, as a preliminary exploration, this chapter temporarily ignores the impact of data distribution.

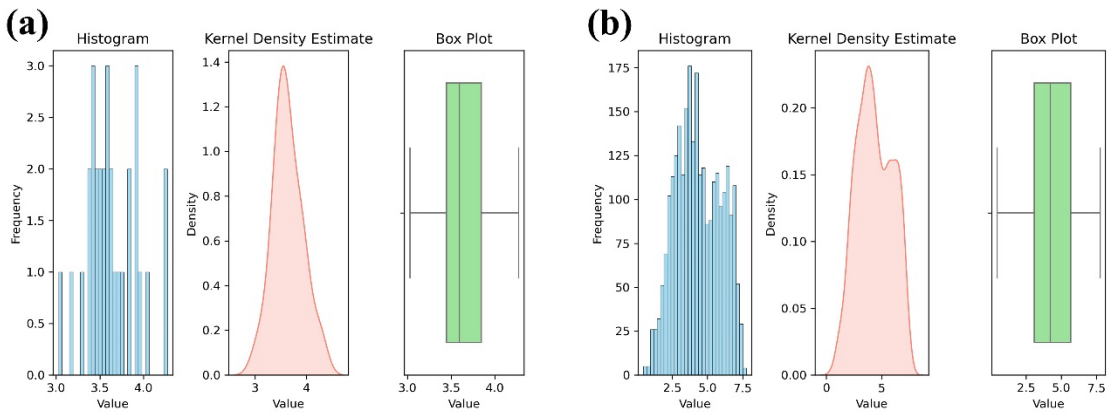

Figure 7-3 Distribution of target variable (ΔE_{vf}) in (a) **Dataset A**, and (b) **Dataset B**

7.3.2 Dataset structure

Following data integration, the structure of Dataset A is present as follows. Given the difference in features setting, the structure of Dataset A (I) and Dataset A (I&II) are shwon in Table 7-1 and Table 7-2, respectively. Accordingly, Dataset B family shares the same structure as Dataset A family.

Table 7-1 Structure of Dataset A (I)

Structure	Features			Target variable
	Feature 1	…	Feature 132	ΔE_{vf}
$CuMn_2O_4$	8		12	3.6981
$Cu_{0.9}Li_{0.1}Mn_2O_4$	3		12	3.6273
$Cu(Mn_{0.9}Li_{0.1})_2O_4$	3		12	3.7421
…	…	…	…	…

Table 7-2 Structure of Dataset A (I&II)

Structure	Features					Target variable
	Feature 1	…	Feature 132	$min(\Delta E_{vf}^{MO_x})$	$\langle \Delta E_{vf}^{MO_x,NN} \rangle$	ΔE_{vf}
$CuMn_2O_4$	8		12	2.5	3.1471	3.6981
$Cu_{0.9}Li_{0.1}Mn_2O_4$	3		12	2.97	3.3782	3.6273
$Cu(Mn_{0.9}Li_{0.1})_2O_4$	3		12	2.5	3.3022	3.7421
…	…	…	…	…	…	…

7.3.3 Effect of Feature set II on model training

The predictions were made using models trained on Dataset A (I) and Dataset A (I&II), and the results are presented in Figure 7-4. In terms of prediction accuracy, the model's performance did not improve with the including of Feature set II; on the contrary, the accuracy showed a slight decrease (MSE: 0.0540 vs. 0.0561; RMSE: 0.2323 vs. 0.2368; MAE: 0.2088 vs. 0.2152).

We then analyzed the 10 most important features used in the model training and found that the model did not effectively capture the information from these features from Feature set II (Figure7-5). This may be related to the small data sample size of Dataset A. Interestingly, however, adding Feature set II does not appear to significantly impact the top 3 important features in the model training, which remain "mean GSvolume_pa", "avg_dev GSmagmon", and "avg_dev NUnfilled". The description of each feature is presented below:

"mean GSvolume_pa": the average Goldschmidt atomic volume of each atom in a material. The Goldschmidt atomic volume estimates the space occupied by each element in a solid.

"avg_dev GSmagmon": the average deviation of the magnetic moments (magnetism) of the different elements in a material relative to the average magnetic moment.

"avg_dev NUnfilled": the average deviation in the number of unfilled electronic states of the different elements in the material.

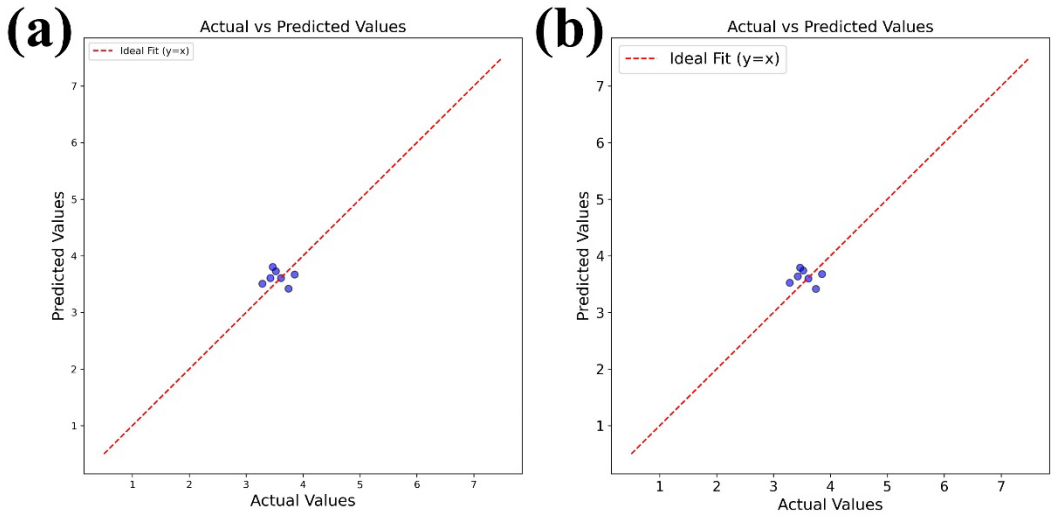

Figure 7-4 (a) Predicted results of trained RF regression model by using (a) Dataset A (I) and (b) Dataset A (I&II)

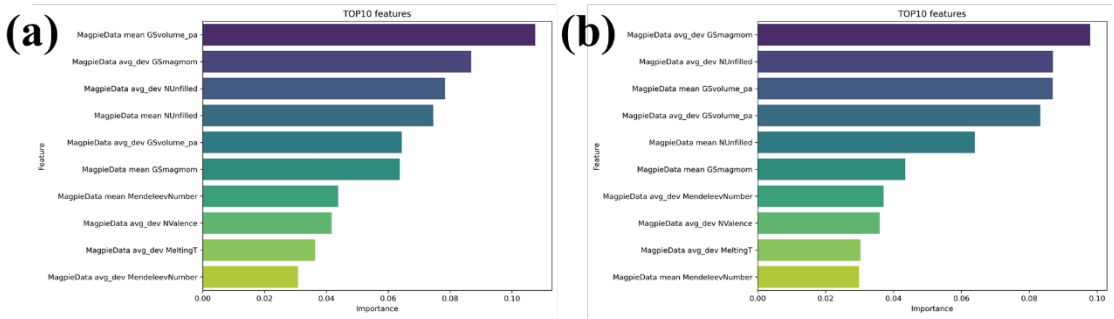

Figure 7-5 Top 10 important features of trained RF regression model by using (a) Dataset A (I) and (b) Dataset A (I&II)

Similarly, we investigated the effect of including or excluding Feature set II on Dataset B. The predictions were made using models trained on Dataset B (I) and Dataset B (I&II),

and the results are presented in Figure 7-6. Surprisingly, the figures clearly indicate that the model's performance improved significantly when Feature set II was included. Further exploration of the top 10 important features (Figure 7-7) revealed that, after adding Feature set II, features from this set accounted for approximately 90% of the total feature importance (where the sum of all feature importances equals 1). This suggests that feature $min\left(\Delta E_{vf}^{MO_x}\right)$ and $\langle \Delta E_{vf}^{MO_x,NN} \rangle$ play a crucial role in predicting the ΔE_{vf} of the material.

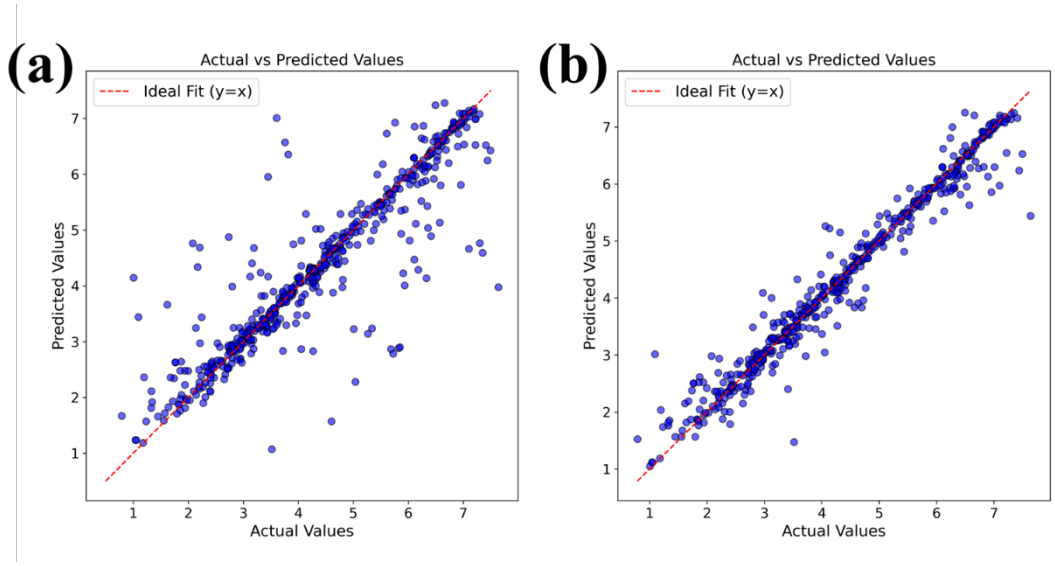

Figure 7-6 (a) Predicted results of trained RF regression model by using (a) Dataset B (I) and (b) Dataset B (I&II)

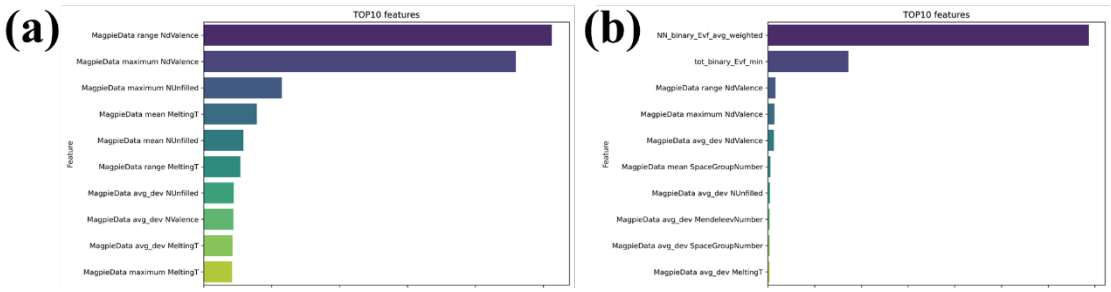

Figure 7-7 Top 10 important features of trained RF regression model by using (a) Dataset B (I) and (b) Dataset B (I&II)

It is worth noting that, in addition to the features from Feature set II, the models trained on Dataset B appear to have stronger relationships with the feature of "NdValence (Number of d-electron Valence)", which contrasts with the results of Dataset A.

7.3.4 Model training based solely on Dataset B (I&II)

To evaluate whether the model training could be conducted using only the perovskite structure feature from Dataset B, without any incorporating spinel structure features from Dataset A, we trained the model using only Dataset B (I&II) and tested on Dataset A (I&II). The predicted results and the feature importance of the trained model are presented in Figure 7-8. The figure shows that the prediction results from two parallel lines, indicating that the model does not effectively predict the spinel structures without previous learning features specific to the spinel structure (since the model prefers to predict the same value no matter what the input is).

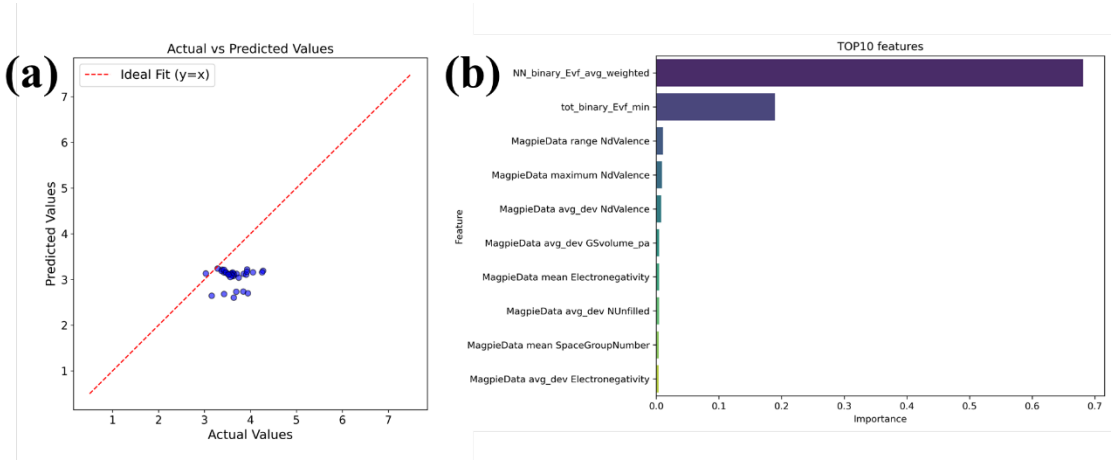

Figure 7-8 RF regression model trained on Dataset B (I&II) and tested on Dataset A (I&II): (a) Predicted results, (b) Top 10 important features

7.3.5 Model training based on combination of Dataset A (I&II) and Dataset B (I&II)

Finally, we combined Dataset A (I&II) and Dataset B (I&II) for hybrid training. Since Dataset A (I&II) was still required for testing, we used 80% of it for training and reserved the remaining 20 % for testing. The predicted results and the feature importance of the trained model are presented in Figure 7-9. The predicted results indicated that the model demonstrates good predictive performance. Notably, the Feature set II contributes over 90% to the model training, suggesting that the model has captured the potential relationship between spinel features and ΔE_{vf}, a relationship it could not capture when trained solely on Dataset A (I&II) (Figure 7-4b).

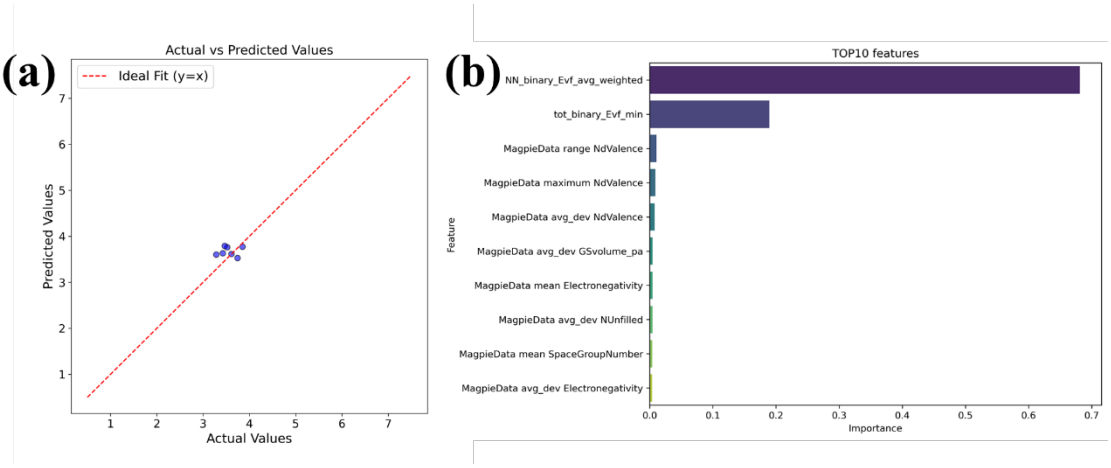

Figure 7-9 RF regression model trained on combination of Dataset A (I&II) and Dataset B (I&II): (a) Predicted results, (b) Top 10 important features

Subsequently, all predicted results using Dataset A as the test set are presented in Table 7-3. From the table, we observe that without combining Dataset B, simply including Feature set II does not enable the model to effectively capture the relationship between features and the target ΔE_{vf}. This is likely due to the small sample size of Dataset A. However, when Dataset A and Dataset B were combined, the model achieved its best predictive performance (MSE: 0.0517, RMSE: 0.2273, MAE: 0.1986), surpassing all

previous results.

Table 7-3 Comparison of predicted results based on Dataset A

Train	Test	MSE	RMSE	MAE
Dataset A (I)	Dataset A (I)	0.0540	0.2324	0.2088
Dataset A (I&II)	Dataset A (I&II)	0.0561	0.2368	0.2152
Dataset B (I&II)	Dataset A (I&II)	0.4357	0.6601	0.5822
Dataset A (I&II) + Dataset B (I&II)	Dataset A (I&II)	0.0517	0.2273	0.1986

7.3.6 New predictions based on trained model

Given the good predictive performance of the model trained on the combined Dataset A and Dataset B, we used it to explore doping effects at the A-site and B-site of $CuMn_2O_4$ for nearly all elements in the periodic table, excluding radioactive elements. The new predicted results are shown in Figure 7-10. Additionally, we have integrated the results of the new predictions and DFT calculations in Figure 7-11.

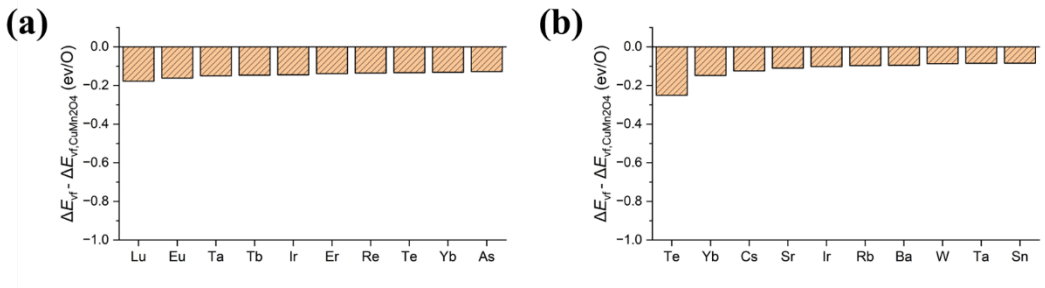

Figure 7-10 Top 10 model-predicted effective dopants for $CuMn_2O_4$ at (a) A-site and (b) B-site

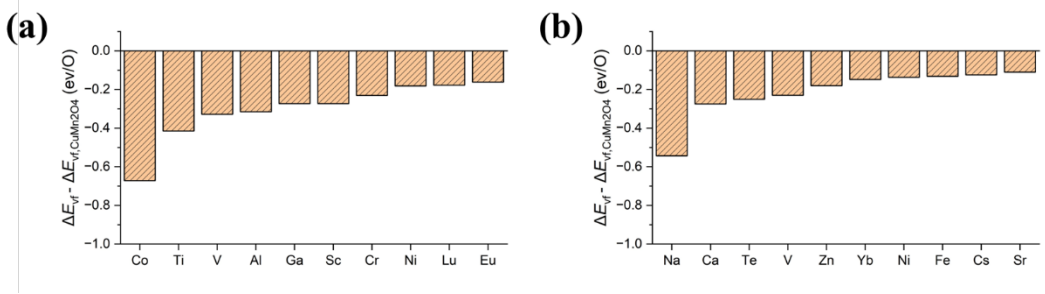

Figure 7-11 Top 10 effective dopants for $CuMn_2O_4$ at (a) A-site and (b) B-site

Overall, the doping of small amounts of transition metal elements (e.g., Co, V, Cr, Ni, etc.) at the A-site appears to significantly reduce the ΔE_{vf} of $CuMn_2O_4$. Additionally, the doping of rare earth elements also contributes to the ΔE_{vf}. From the results of B-site doping, it appears that some alkali metals and alkaline earth elements (e.g., Na, Ca, Cs, Sr, etc.) with larger ionic radii are more effective at reducing the ΔE_{vf} for $CuMn_2O_4$. Interestingly, V appears to reduce ΔE_{vf} effectively when doped at either the A or B sites. This may be significantly related to its ability to present many chemical valence states in compounds.

7.4 Conclusion

In this chapter, to identify doping elements that effectively lower the reduction temperature of $CuMn_2O_4$, we combined DFT calculations with machine learning to explore the doping effects of nearly all elements in the periodic table. We first used DFT to calculate the ΔE_{vf} of a portion of the elements after doping and then generated the corresponding features using Matminer for training the machine learning model (Random Forest Regression). Subsequently, we applied different training strategies and found that Feature set II significantly improved the model's performance. Finally, we used trained model for new predictions, which showed that doping some transition metals and rare earth elements at A-site effectively reduces the ΔE_{vf} of $CuMn_2O_4$. As B-site, some alkali

and alkaline earth metals with large ionic radii also appear to be highly effective.

This study offers a new approach for screening doping elements in future research. However, it is worth noting that the findings remain theoretical, as experimental validation has not yet been conducted. Additionally, specific strategies may be needed when combing Dataset A and Dataset B. For instance, excluding pyrochlore structure data could help simplify the model and improve its performance.

Reference

[1] S. Kirklin, J.E. Saal, B. Meredig, A. Thompson, J.W. Doak, M. Aykol, S. Rühl, C. Wolverton, The Open Quantum Materials Database (OQMD): assessing the accuracy of DFT formation energies, Npj Comput Mater 1 (2015) 15010. https://doi.org/10.1038/npjcompumats.2015.10.

[2] L. Ward, A general-purpose machine learning framework for predicting, Npj Computational Materials (2016).

[3] L. Ward, A. Dunn, A. Faghaninia, N.E.R. Zimmermann, S. Bajaj, Q. Wang, J. Montoya, J. Chen, K. Bystrom, M. Dylla, K. Chard, M. Asta, K.A. Persson, G.J. Snyder, I. Foster, A. Jain, Matminer: An open source toolkit for materials data mining, Computational Materials Science 152 (2018) 60–69. https://doi.org/10.1016/j.commatsci.2018.05.018.

[4] B. Baldassarri, J. He, A. Gopakumar, S. Griesemer, A.J.A. Salgado-Casanova, T.-C. Liu, S.B. Torrisi, C. Wolverton, Oxygen Vacancy Formation Energy in Metal Oxides: High-Throughput Computational Studies and Machine-Learning Predictions, Chem. Mater. 35 (2023) 10619–10634. https://doi.org/10.1021/acs.chemmater.3c02251.

Chapter 8. $CuMn_2O_4/CuMnO_2$-based porous foam structure heat storage module

8.1 Introduction

Developing heat storage materials with excellent properties alone is insufficient to achieve the efficient recovery and utilization of medium-high temperature heat. This goal must also involve the design of heat storage module and reactor.

Over the last decade, various module designs for the redox-type CHS systems have been proposed by researchers (Figure 8-1), including granules [1–5], honeycomb [6–10], and porous foam structures [11,12].

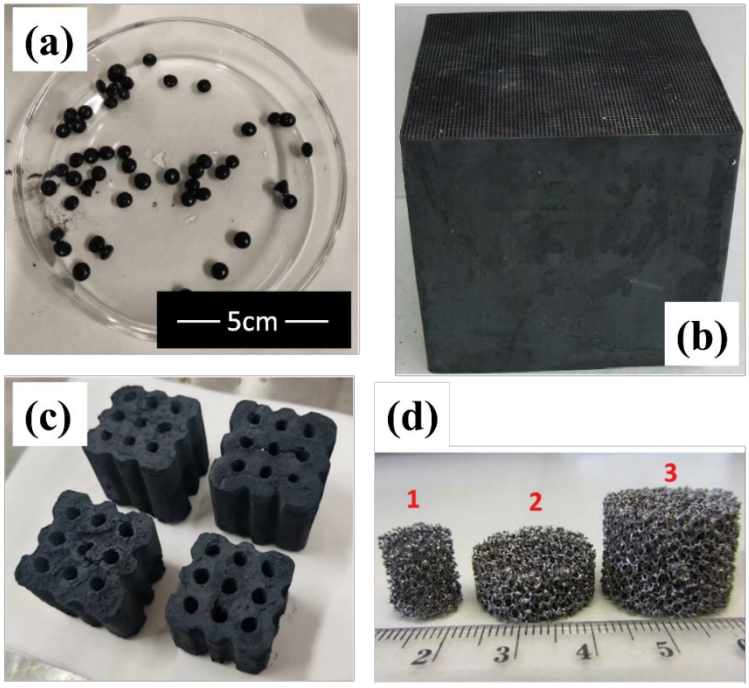

Figure 8-1 Various type of redox-type heat storage module of (a): granules; (b): material-coated honeycomb; (c): material-based honeycombs; (d): porous foams

The granules are advantageous due to their cost-effectiveness and the ability to be produced in large quantities quickly using standard granulation equipment. However, the traditional packed bed reactor using granules faces a significant pressure drop because of agglomeration after cycling, which can lead to a reduced flow rate of the heat transfer fluid at the outlet of reactor, especially in a long-size reactor. Additionally, the granules

are typically small spheres or cylinders with dense surfaces and low porosity. While this structure may benefit mechanical properties, it can hinder the diffusion rate of oxygen, a crucial reactant in redox-type CHS systems, thereby impacting on the overall performance of systems.

The honeycomb-type heat storage module offers an effective solution to the pressure drop issue encountered in the packed bed reactors. It can adapt to a very high flow rate of HTF, meeting the rapid requirements for heat storage and release. There are two sub-types of honeycomb modules: material-coated and material-based honeycomb. The former involves coating redox-type CHS materials onto the surface of common cordierite or SiC honeycomb ceramic matrices [13]. However, this approach is limited by a lower heat storage density, as the thickness of the coating layer is always not sufficient. The latter approach involves directly synthesizing honeycomb structures from redox-type CHS materials, addressing the issue of low heat storage density [10]. Nevertheless, this method requires specialized extrusion molding devices and molds, posing challenges for prototype preparation at the laboratory level.

In 2015, Agrafiotis et al. pioneered the concept of porous foam structure heat storage modules. They investigated Co_3O_4-coated and Co_3O_4-based porous modules as a part of their comprehensive study on Co_3O_4 [12]. During the experiment of Co_3O_4-based porous foam modules, they utilized foam with 30 and 45 PPI (pore per inch) to prepare the modules of approximately 0.75 cm^3 using the PU foam replica method. They claimed that the Co_3O_4-based porous module retained a good integrity and reactivity after 30 thermal cycling tests in TGA. However, the irregular shape of the as-prepared modules made it difficult to observe volume changes before and after the cycling tests. Additionally, they did not assess the specific mechanical properties of these modules.

Later, Pein et al. developed a porous cylindrical module using the perovskite-structure material $CaMnO_3$ with a maximum size of φ20 × 20 mm [11]. The redox behavior of the $CaMnO_3$-based porous module was consistent with that of the powder sample over five

TGA cycles, which might be attributed to the non-stoichiometric reaction of perovskite do not exhibit noticeable phase transitions. Subsequently, they conducted two compressive strength tests on the as-prepared modules, revealing the strength of 87.5 and 132.4 kPa. Impressively, the cylindrical integrity of the modules was well preserved after 46 cycles.

In this chapter, we synthesized a large quantity of the $CuMn_2O_4/CuMnO_2$ redox couple using the co-precipitation method. With an eye on the current research trends in TCES modules, our goal is to develop a $CuMn_2O_4/CuMnO_2$-based porous heat storage module (hereinafter referred to as porous module) with low pressure drop and high reactivity. First, we characterized the samples prepared by the co-precipitation method using conventional materials science analysis techniques. The PU foam replica method was used to prepare the $CuMn_2O_4/CuMnO_2$-based porous heat storage module. We then focused on the effect of preparation conditions (e.g., sintering temperature and holding time) on the mechanical properties (compressive strength), reactivity (redox behavior) and durability of the porous modules and selected the optimal preparation conditions based on the $CuMn_2O_4/CuMnO_2$ properties.

8.2 Experimental approach

8.2.1 Synthesis and characterization of powder raw material

For efficient larger-scale synthesis, $CuMn_2O_4$ (oxidized state of $CuMn_2O_4/CuMnO_2$ redox couple) was synthesized using a co-precipitation method (Figure 8-2) instead of the modified Pechini method we usually used in the previous research. The raw materials were corresponding metal nitrates ($Cu(NO_3)_2 \cdot 3H_2O$ (FUJIFILM Wako Pure Chemical Corp.), $Mn(NO_3)_2 \cdot 6H_2O$ (FUJIFILM Wako Pure Chemical Corp.) and precipitant (Na_2CO_3 (FUJIFILM Wako Pure Chemical Corp.)).

The metal nitrates in the molar ratio of 1 : 1 were dissolved in several beakers using

the ion-exchange water (IEW, hereinafter referred to as “water”) with the concentration of 0.5 mol/L, and the metal nitrates solution was thoroughly mixed with a powerful stirrer at 700 rpm for a few minutes, resulting in a solution with a pH value of 2.0 approximately after stirring.

For the co-precipitation reactions, a high concentration of Na_2CO_3 solution (2 mol/L) was introduced as a pH regulator and precipitant. The Na_2CO_3 solution was carefully added dropwise into the metal nitrates solution while maintaining a constant stirring rate of 1000 rpm. By the addition of Na_2CO_3 precipitant, a bright green precipitate was formed, accompanied by the generation of numerous bubbles. The addition of Na_2CO_3 should be stopped when the pH of the solution changed from acidic to weakly basic, approximately pH of 7.5. The precipitated solution was set aside for aging at room temperature for 12 hours. After the aging treatment, the solution clearly separated into two distinct layers: an upper clarified liquid layer and a lower precipitate layer. The precipitate was filtered out using vacuum filtration, and the resulting filter cake was washed three times using water. The filter cake was moved into a vacuum drying oven and dried at 100 ℃ for 12 hours. The dried filter cake was crushed and placed in a crucible and heated to 1000 ℃ using a muffle furnace under air atmosphere for 6 hours to obtain the crude sample.

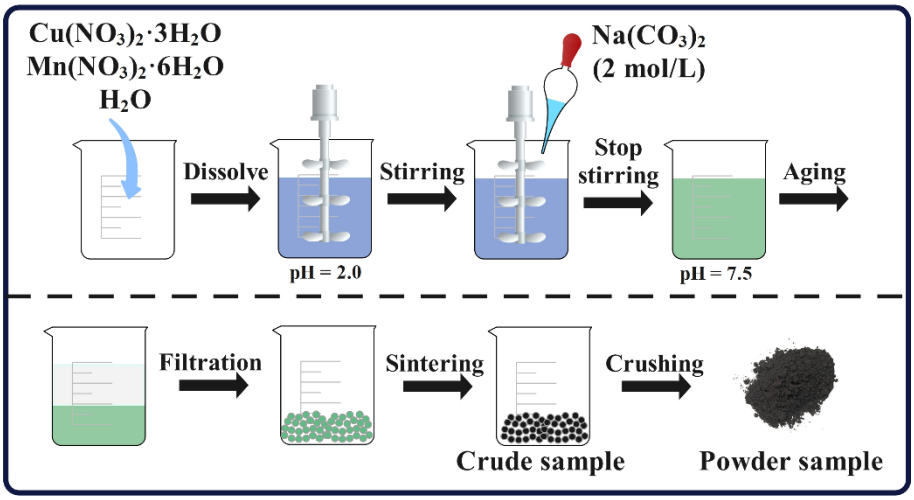

Figure 8-2 Synthesis schematic of $CuMn_2O_4$/$CuMnO_2$ using co-precipitation method.

The crude sample was crushed with a ball mill set (desktop pot mill rotating stand (PM-001, AS ONE Corp.); zirconia balls (φ 20 mm, NIKKATO Corp.); mill pot (BP-2, AS ONE Corp.)). Both the crude sample and the zirconia balls filled one-third of the pot's internal space. During the ball milling process, the rotation speed of the mill pot was maintained at 220 rpm for a duration of 12 hours. The resulting powder was sieved through a metal mesh screen (with a pore size of ≦ 75 μm). This process yielded a final powder sample weighing approximately 7.5 kg.

The powder sample was sampled randomly from different batches for physiochemical characterization. The particle size analysis was conducted using a scattering particle size distribution analyzer (LA-920, HORIBA Ltd.) with an ultrasonic dispersion within 1 minute. The phase composition of the oxidized state and reduced state powder sample synthesized by co-precipitation method was investigated using X-ray diffraction analysis (XRD) (SmartLab, Rigaku Corp.) with a scanning speed of 5 °/min in 2θ range of 15 – 90°. The phase composition of each sample was analyzed using PDXL2 (Rigaku Data Analysis Software). For morphology observations, the oxidized state sample was selected as the representative, and the elemental ratios of Cu and Mn in the system were investigated using scanning electron microscope equipped with energy dispersive spectroscopy (SEM-EDS) (JSM-7500F, JEOL Ltd.). The redox behavior of the powder sample was investigated using TGA (STA7300, HITACHI High-Tech Science Corp.).The heat storage density was measured using thermogravimetry and differential scanning calorimetry (TG-DSC) (STA 449F3, NETZSCH; TGA/DSC 3+, METTLER TOLEDO).

8.2.2 Preparation of porous modules

A series of porous modules made entirely of $CuMn_2O_4$ material was prepared using the PU foam replica method or so-called sacrificial sponge foam template method. Commercially available open-porous 20 × 20 × 20 mm^3 cubic polyurethane (PU) foam (Yuanshengxing electronic material Co.) with a cell size of 13 ± 2 PPI was used as the

template. A PU foam with a larger 13 PPI pore size was selected as the template for better understanding the wall formation process in the PU foam replica method and observing the macro-morphology changes after durability tests.

The $CuMn_2O_4$ slurry was prepared by referring to the literature on porous Al_2O_3 [14–16] and perovskite-type $CaMnO_3$ porous heat storage module [11]. The slurry was prepared with 80 wt% $CuMn_2O_4$ powder, 17 wt% water, and 3 wt% Dolapix CE 64® (Zschimmer & Schwarz Chemie GmbH, Lahnstein, Germany). The Dolapix CE 64® was employed as a dispersant and thickener. The solid component of the slurry constituted approximately 67.5 vol%, with the liquid component accounting for 32.5 vol%. The slurry exhibited a high viscosity (similar to that of mayonnaise), surpassing the maximum test range of 198 Pa·s of our laboratory's equipment during the viscosity measurement.

The PU foam was immersed in the slurry and squeezed three times to ensure complete absorption of the slurry. Subsequently, the coated foams were placed on Kimwipes® (Nippon Paper Crecia Co., Ltd.) and any excess slurry was promptly squeezed out. This step primarily aims to prevent the pores on the PU foam's surface from getting clogged with excess slurry, which could potentially reduce the performance of porous module.

After coating, the PU foams were dried at room temperature under air atmosphere for 24 hours and then transferred to a muffle furnace (ROP-003H, AS ONE Corp.) for sintering process.

The sintering temperatures should lie between the service temperature of the heat storage module and the melting point of TCES materials. In the previous chapter, we referenced the findings of Driessens et al. [17] that the melting point of Cu-Mn-O system is approximately 1150 ℃ when x(Cu) = 0.5. Considering that the material sample was prepared using the co-precipitation method, potential impurities might decrease its melting point. Therefore, we selected 1100 ℃, slightly lower than the melting point, as the maximum sintering temperature, and set 1000 ℃ as the minimum. The sintering holing time also affects the module's mechanical and heat storage performance. A short

holding time could lead to inadequate sintering, resulting in weak mechanical properties, while extended holding time might cause the module's surface to become overly dense, influencing the oxygen diffusion and the heat storage performance. Typically, the sintering holding time of porous materials that prepared by the PU foam replica method is often reported to be between 1 to 3 hours [11,14–16].

Hence, three different maximum sintering temperatures (1000 ℃, 1050 ℃, and 1100 ℃) and three holding times (1.5 hours, 3 hours, and 6 hours) were selected, and the sintering process was carried out at a heating rate of 1℃/min and a cooling rate of 2 ℃/min. Eventually, we obtained nine kinds of porous modules sintered under different conditions. The individual samples were named using a combination of sintering temperature and holding time. For example, the porous modules sintered at 1000 ℃ for 1.5 hours was labeled as "1000-1.5h".

8.2.3 Measurement of physical parameters and compressive strength of porous module

An electronic balance (GR-202, A&D Co., Ltd.) was used to measure the weight of each porous module. Apparent volume (AV, cm^3) and apparent density (AD, g/cm^3) were calculated after measuring their lengths, widths, and heights. However, there is a measurement error since the sponge templates used in this study were manually cut. For convenience, the longest side was defined as length (L), followed by the width (W), and lastly the height (H).

For true density (TD, g/cm^3) measurement, we used a high-precision gas and vapor adsorption analyzer (BELSORP MAX II, MicrotracBEL Corp.) with gas (helium) displacement method. The volume of the chamber ($V_{chamber}$) inside the instrument and the volume of the sample cell ($V_{sample\ cell}$) are known parameters before the measurement. After placing the sample in the sample cell, the sample cell and the chamber were vacuumed. The valve between the sample cell and the chamber was then closed. Subsequently, the chamber was filled with a specific amount of helium gas, and the

pressure was recorded as P_1. Upon opening the valve, the pressure was recorded as P_2 after the helium gas was allowed to enter the sample cell. The true volume of the sample can be calculated using Equation 8-1. Once we know the TD, the ratio of the AD to this true density can be used to estimate the voidage (%) for each porous module.

$$V_{sample} = V_{sample\ cell} - \frac{(P_1 - P_2) \cdot V_{chamber}}{P_2} \qquad (8-1)$$

Apparent volumetric heat storage density (AVHSD, kJ/L) was calculated by multiplying the heat storage density (kJ/kg) with the AD (g/cm^3). In this study, we used a non-isothermal method to measure the heat storage density, which differs from the isothermal method used in the previous chapters. This difference in measurement approach could influence the values of the AVHSD. Therefore, the range of AVHSD was established using the heat storage densities obtained through two methods.

A tensile and compression testing machine (SDW-2000, IMADA Co.,Ltd.) was used to test the mechanical compression strength of the nine as-prepared porous module prepared under various sintering temperatures and holding time conditions.

It is widely acknowledged that these heat storage modules must exhibit a certain level of structural strength to meet the requirements of transportation and high flow rate of heat transfer fluid without experiencing significant deformation that may affect their heat storage performance.

However, the discussion regarding the mechanical strengths of heat storage modules (such as honeycombs or granules) has yet to be quantified, possibly because they seem to exhibit a satisfactory strength visually. So far, only Bielsa et al. have made a specific discussion about this aspect, reporting a crushing strength ranging from 0.126 to 0.166 N for $Mn_{0.98}Si_{0.02}O_3$ granules [5]. However, they did not provide a specific compressive strength because of the absence of a precise definition for the granule's pressure force

area and the specialized testing equipment. For the porous module, Pein et al. tested compressive strength of $CaMnO_3$ porous ceramic foam (φ20 × 10 mm), reporting the maximum values of 132.4 kPa [11]. For comparison, the compressive strength of the Al_2O_3 porous ceramic foam developed for non-TCES purposes ranged between 1.15 and 1.30 MPa [14–16].

In our experiment, a maximum range of 500 N was chosen, and the cross-sectional area of each porous module was measured. The porous module was placed horizontally on the testing bench, and the pressure sensor was manually adjusted to ensure a snug fit against the sample before testing. The testing process involved the pressure sensor gradually approaching and pressing the porous module at a rate of 0.08 mm/s. The maximum pressure peak observed within 150 seconds was recorded as the compressive strength of each porous module.

8.2.4 Redox behavior of porous module

Due to the volume constraints within the sample cell of the TGA experimental equipment, it was not feasible to directly observe and measure the comprehensive redox behavior of the heat storage module via TGA. As a result, we indirectly investigated the overall redox behavior by using fragments of the porous module, which were obtained by gently crushing the porous module while retaining its porous structure. In this experiment, a heating/cooling TGA temperature program was used to investigate the redox behavior of the fragments obtained from each porous module. The program included heating from 100 ℃ to 1000 ℃ at a rate of 20 ℃/min under a synthetic air flow (200 mL/min). After maintaining 1000 ℃ for 30 minutes, the temperature was gradually decreased at the same rate.

Considering that the fragments originated from various sections of individual porous module, each experiment was repeated three times to ensure that the characteristics of the fragments were representative of the entire porous module.

8.2.5 Durability of porous module

A small muffle furnace (ROP-003H, AS ONE Corp.) was used to conduct a durability test directly on the porous module prepared under nine different conditions, subjecting them to 50 cycles. The porous modules were positioned horizontally on an alumina sintering plate (AS ONE Corp.). The sintering plate was then placed at the center of the muffle furnace and heated from room temperature to 1000 ℃ at a rate of 10 ℃/min and held for 60 minutes. Subsequently, the porous modules were gradually cooled down to 600 ℃ at a rate of 10 ℃/min, completing a heating-cooling cycling test (the rate of 10 ℃/min was selected due to the limitations of the muffle furnace's performance). After every five cycles, the porous modules were removed from the muffle furnace, and their shape and apparent morphology changes were recorded by photographs. Following 50 cycles, the redox behavior of the module samples was re-evaluated using TGA, utilizing the same method as described in Section 8.3.1 to obtain fragments. Additionally, SEM was employed to observe the morphological alterations on the surface of each porous module's fragments before and after 50 cycles.

8.3 Results and discussion

8.3.1 Characterization of powder material synthesized using co-precipitation method

The powder sample synthesized using the co-precipitation method (hereinafter referred to as the Co-pre sample) was tested for the particle size distribution using the scattering particle size distribution analyzer with 1-minute ultrasonic treatment. Figure 8-3 presents a representative particle size distribution, and the powder sample exhibited particle size sizes smaller than 30 μm the crushing and sieving process. The average d50 (median diameter) is 3.06 ± 0.13 μm, showing a smaller size than the pore size of the screen mesh (75 μm).

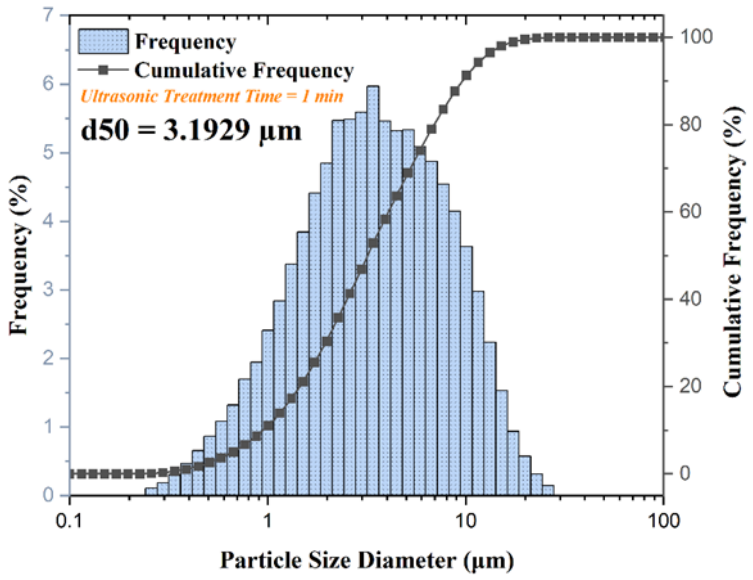

Figure 8-3 Particle size distribution of Co-pre powder sample

The XRD pattern of the oxidized and reduced states of the Co-pre powder sample are shown in Figure 8-4a and Figure 8-4b. For a convenient comparison, the corresponding XRD patterns for the Pechini powder samples are also included. As observed in Figure 8-4, the Co-pre powder sample exhibits characteristic peaks matching those of $CuMn_2O_4$ (#01-074-1919, 2θ = 30.48°, 35.95°, 57.70°, 63.43°) and $CuMnO_2$ (#03-065-2308, 2θ = 31.31°, 32.97°, 37.02°), similar to the Pechini powder sample. However, small amounts of Na-Mn oxides are also detected in the XRD patterns of the Co-pre powder samples in both the oxidized and reduced states, including Na_2MnO_7 (#78-0193, 2θ = 15.87°, 25.28°) in the oxidized state and $NaMnO_2$ (#73-0156, 2θ = 16.66°, 37.62°, 42.75°) in the reduced state. The presence of Na-Mn oxides is likely related to the use of highly concentrated (2 mol/L) Na_2CO_3 precipitant during the synthesis of the Co-pre sample. Interestingly, it appears that Mn forms compounds with Na rather than Cu, resulting in the retention of Cu and the formation of more CuO. This is also the reason why stronger characteristic peaks of CuO (#01-080-1916, 2θ = 35.52°, 38.70°, 48.70°) and Cu_2O (#01-073-6371, 2θ = 36.48°, 42.35°, 61.43°) can be observed in the XRD patterns of the Co-pre powder

samples. In addition, the Zr- or Al-oxides are not observed in the XRD pattern, suggesting that the samples remained uncontaminated throughout the ball milling process.

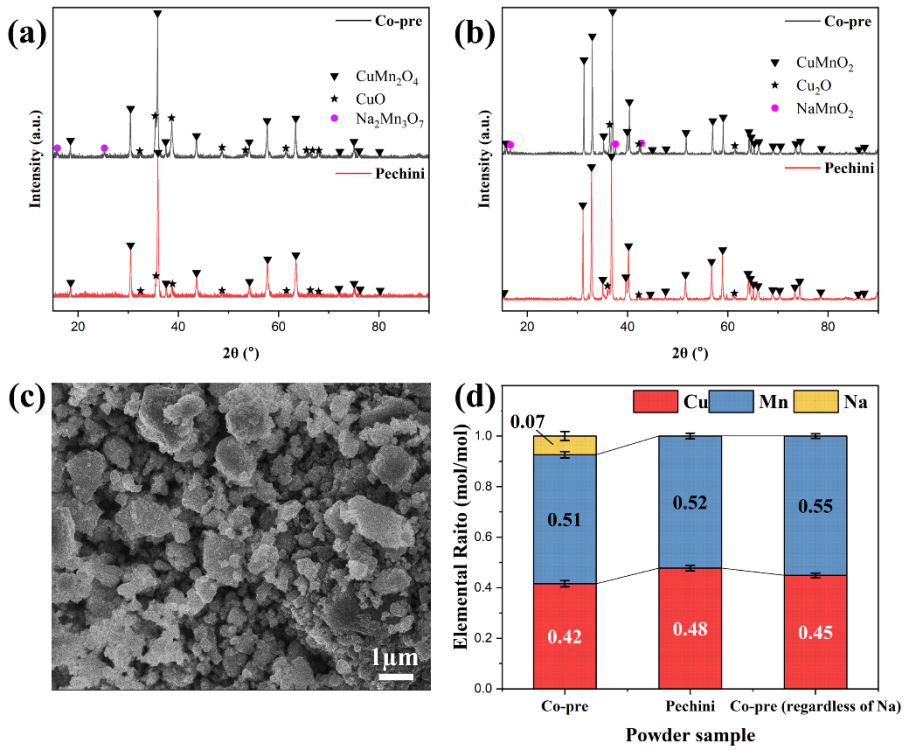

Figure 8-4 XRD patterns of the Co-pre and Pechini sample in (a): oxidized state and (b): reduced state; (c): SEM image of the Co-pre sample; (d): SEM-EDS elemental ratio analysis.

SEM was used to investigate the microscopic morphology of the Co-pre powder sample. The representative SEM image of the Co-pre powder sample (Figure 8-4c) reveals most of the particles lie between 2 to 3 μm, consistent with the results mentioned in the particle size distribution experiment described earlier. Furthermore, we conducted a metal elemental ratio analysis using EDS. As discussed in the previous XRD analysis, it was evident that the Co-pre powder sample contains a small amount of Na-Mn oxide impurities. Therefore, the elemental ratio of Na is also considered. As shown in Figure 8-4d, the ratio of Cu in both the Co-pre and Pechini powder samples consistently shows

slightly lower than that of Mn. This discrepancy may be attributed to the sensitivity of EDS to specific elements' wavelengths. Additionally, during the synthesis of the Co-pre powder sample, a highly concentrated Na_2CO_3 precipitant with strong alkalinity was used. This may have led to the formation of some soluble complexes from the former precipitated $Cu(OH)_2$ under localized strong alkaline conditions because $Cu(OH)_2$ is also dissoluble in the strong alkali [18] such as NaOH or $NH_3 \cdot H_2O$, resulting in a worse precipitation of Cu^{2+}. This could also account for why the elemental ratio of Cu in the Co-pre powder sample remains lower than that in the Pechini sample even after neglecting the Na content in the Co-pre powder sample (Figure 8-4d).

8.3.2 Redox behavior and heat storage density of powder material synthesized using co-precipitation method

The Co-pre and Pechini powder samples were tested using TGA and TG-DSC. Figure 8-5a presents the redox behavior of the Co-pre and Pechini powder samples. Both the Co-pre and Pechini powder samples exhibit two reduction steps. The first reduction is a non-stoichiometric reaction, as discussed in Chapter 4. The second reduction involves a phase transition reaction, significantly contributing to the heat storage density, specifically the phase transition of Cu-Mn oxides from spinel to delafossite structure. It is noteworthy that the Co-pre powder sample initiated its first reduction at a much lower temperature compared to the Pechini powder sample (100 ℃ vs. 500 ℃), and the former exhibits a larger weight loss during the first reduction (2.53% vs. 1.20%). Additionally, the Co-pre powder sample only returned to 98.14% of its initial weight during oxidation, while the Pechini sample could reach 99.52%. This phenomenon suggests that the first reduction of the Co-pre powder sample included a partial decomposition reaction of Na-Mn oxides, possibly explaining the presence of Na-Mn oxides in different forms in the XRD pattern of Co-pre powder sample's reduced state. Interestingly, based on the TGA results, it shows challenging for Na-Mn to re-oxidize within a short period once they decomposed completely. However, the decomposition reaction equation of Na-Mn oxides remains

unclear at present. When we exclude the effect by the decomposition of Na-Mn oxides, the Co-pre and Pechini powder samples demonstrate nearly identical redox behavior, as evidenced the maximum weight changes by using the weight gain of oxidation during cooling process (Co-pre: 4.01 ± 0.06 %; Pechini: 4.26 ± 0.05%).

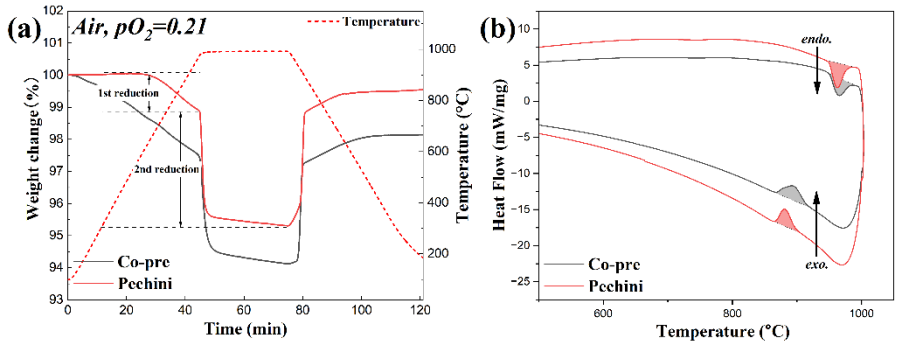

Figure 8-5 (a): Redox behavior of the Co-pre and Pechini powder sample; (b): DSC curve of the Co-pre and Pechini powder sample.

As a short summary, aside from the presence of some Na-Mn oxide impurities, there are no significant differences in phase composition, redox behavior, and heat storage density between the Co-pre and Pechini powder samples. Consequently, we chose to proceed with the Co-pre powder sample for the further preparation of the porous module.

8.3.3 Appearance, parameter, and mechanical strength of module samples

The appearance of the individual porous module prepared under different conditions is depicted in Figures 8-6a and Figure 8-6b. In these figures, these porous modules are organized in a specific pattern. The sintered porous module effectively retains the porous structure of the PU foam, and their pores remain unblocked despite the use of viscous slurry. The physical parameters of the prepared porous module are listed in Table 8-1.

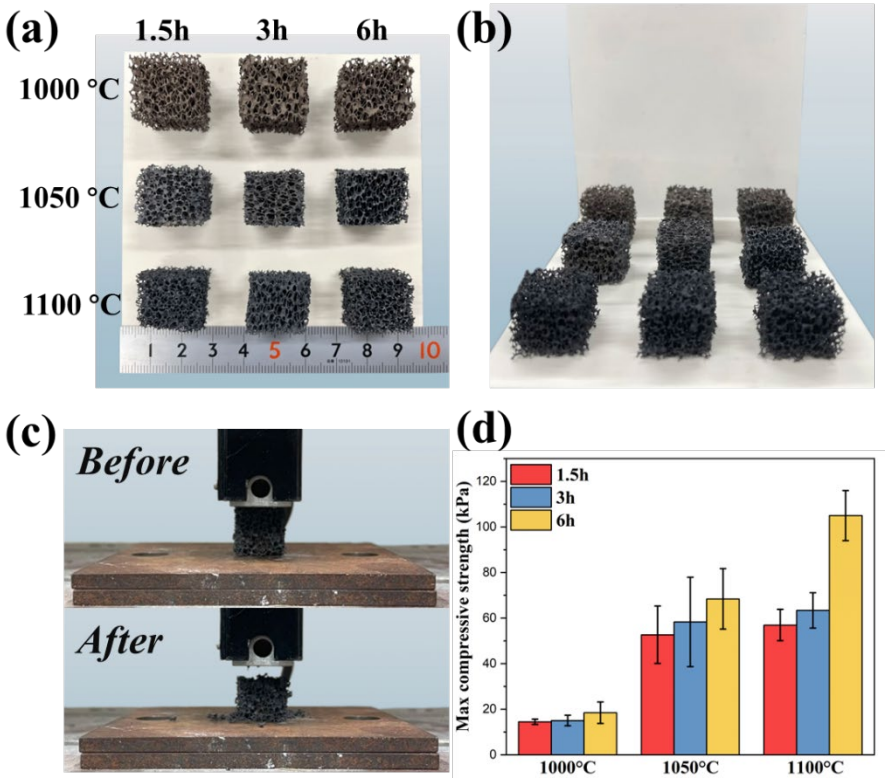

Figure 8-6 (a): Appearance of module samples (View #1); (b): Appearance of module samples (View #2); (c): Before-and-after comparison of compressive strength test for a representative 1050-3h sample; (d): Compressive strength for each module sample.

Table 8-1 Various physical parameters of prepared module samples.

Sample	Weight (g)	Length (mm)			AV (cm^3)	AD (g/cm^3)	TD (g/cm^3)	Voidage (%)	AVHSD(kJ/L)
		L	*W*	*H*					
1000-1.5h	2.32 ± 0.29	19.9 ± 0.2	18.9 ± 0.2	17.9 ± 0.2	6.71 ± 0.15	0.35 ± 0.03	3.05 ± 0.43	88.66 ± 1.94	50.09 – 81.69
1000-3h	2.51 ± 0.25	19.3 ± 0.4	18.4 ± 0.4	17.0 ± 0.0	6.01 ± 0.13	0.42 ± 0.04	3.31 ± 0.50	87.39 ± 2.27	60.42 – 98.53
1000-6h	2.57 ± 0.27	18.5 ± 0.9	17.5 ± 0.5	17.5 ± 0.9	5.65 ± 0.16	0.46 ± 0.05	3.36 ± 0.48	86.45 ± 2.42	65.91 – 107.48
1050-1.5h	2.33 ± 0.18	17.0 ± 0.0	16.4 ± 0.4	15.4 ± 0.2	4.28 ± 0.15	0.54 ± 0.03	3.23 ± 0.46	83.16 ± 2.62	78.66 – 128.29
1050-3h	2.50 ± 0.22	18.0 ± 0.0	16.8 ± 0.4	15.1 ± 0.7	4.56 ± 0.33	0.55 ± 0.04	3.61 ± 0.58	84.81 ± 1.08	79.36 – 129.43
1050-6h	2.60 ± 0.17	17.7 ± 0.5	17.0 ± 0.8	15.3 ± 1.2	4.60 ± 0.46	0.57 ± 0.02	3.88 ± 0.66	85.40 ± 2.57	82.04 – 133.79
1100-1.5h	2.41 ± 0.15	17.7 ± 0.5	16.5 ± 0.4	14.2 ± 0.5	4.13 ± 0.23	0.59 ± 0.07	4.04 ± 0.73	85.50 ± 3.10	84.89 – 138.44
1100-3h	2.58 ± 0.12	17.0 ± 0.7	16.0 ± 0.7	15.3 ± 0.4	4.15 ± 0.28	0.62 ± 0.03	4.31 ± 0.82	85.52 ± 2.86	90.29 – 147.25
1100-6h	2.59 ± 0.25	17.3 ± 0.9	15.7 ± 0.5	14.8 ± 0.2	4.03 ± 0.25	0.65 ± 0.09	4.65 ± 0.72	86.09 ± 3.35	93.60 – 152.65

It is worth noting that the porous module sintered at various temperatures show different levels of volumetric shrinkage. The porous module sintered at 1100 ℃ for 6 hours exhibits the highest AD of 0.65 ± 0.09 g/cm^3, while the porous module sintered at 1000 ℃ for 1.5 hours shows a significantly lower AD of 0.35 ± 0.03 g/cm^3. When compared to the initial volume of the PU foam temperature (20 × 20 × 20 mm^3), the sample sintered at 1000 ℃, 1050 ℃, and 1100 ℃ exhibits volumetric shrinkage ranging from 16.13 to 29.38%, 43.00 to 46.50%, and 46.00 to 50.50%, respectively. The trend in TD closely reflects that of the AD, both increasing with a higher sintering temperature. However, it should be noted that although density varied with sintering temperature and holding time, the voidage of the porous modules consistently remains within a narrow range of 83.16% to 88.60%, showing a minimal fluctuation trend. By using the heat storage densities determined through both non-isothermal and isothermal methods, it is easy to know the apparent volumetric heat storage densities of the prepared module sample. Specifically, the sample sintered at 1100 ℃ for 6 hours shows the highest heat storage density of 152.65 kJ/L.

Furthermore, the porous modules exhibit varying colors depending on the sintering temperature. The porous module prepared at 1000 ℃ display an earthy yellow color, while the 1050 ℃ and 1100 ℃ one appears dark gray. These differences in color may be closely associated with the degree of sintering, where darker colors suggest a denser surface for the porous modules.

We performed compressive strength tests on the porous modules using a tensile and compression machine. In the before-and-after comparison graph (Figure 8-6c) for a representative 1050-3h porous modules, it is evident that the sample did not collapse entirely during the 3-minute compression test. Instead, it gradually fractures along the upper and lower contact surfaces. This phenomenon is also observable in the pressure-versus-time graph (Figure 8-7): in most cases, the samples tend to break gradually rather than abruptly as the pressure gradually increased, as indicated by the absence of sudden

pressure change. Figure 8-6d shows that the compressive strength of porous modules gradually increases with rising sintering temperature. This trend can be attributed to higher temperatures facilitating the densification of the pore wall surfaces on the porous modules during the sintering process. Impressively, the 1100-6h porous modules exhibit the highest compressive strength of 105.00 ± 10.08 kPa. The impact of holding time on compressive strength is obviously evident in porous modules sintered at 1100 ℃. However, at lower sintering temperatures of 1050 ℃ or 1000 ℃, extending the holding time results in only a slight improvement in compressive strength.

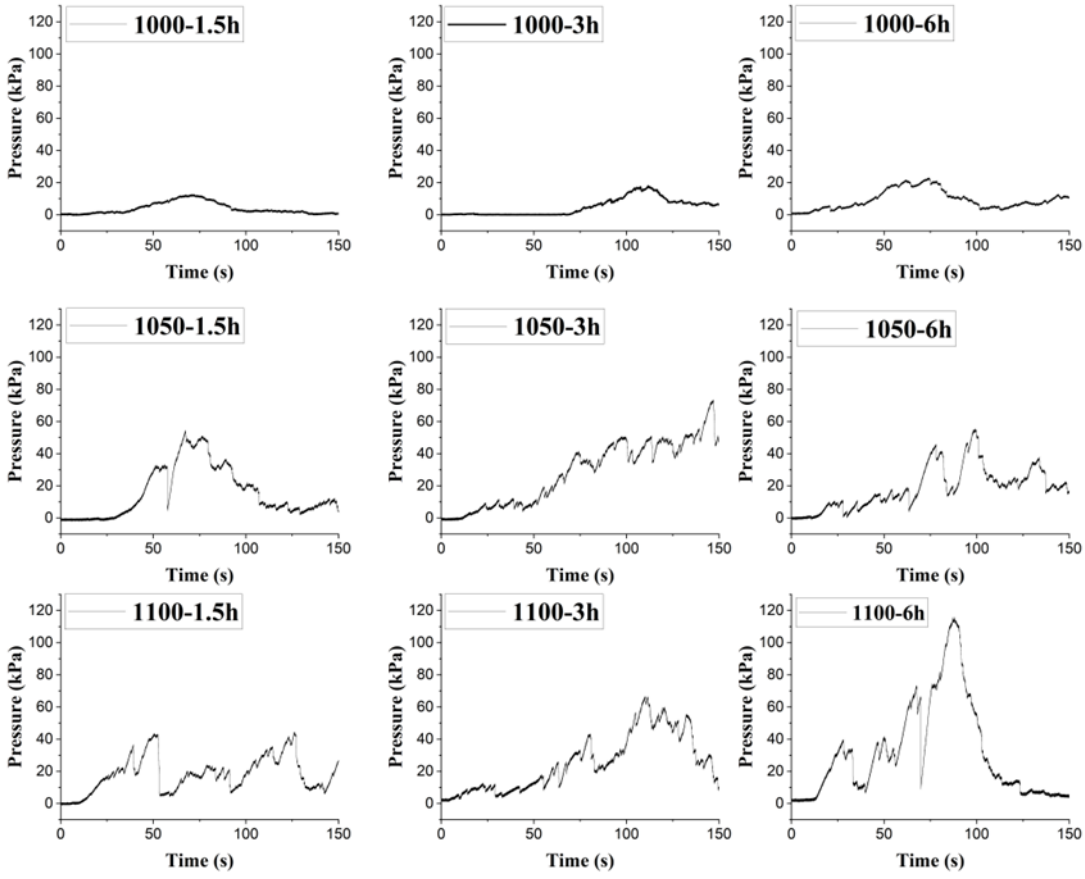

Figure 8-7 Compressive strength test for all porous modules

Figure 8-8 illustrates the sintering mechanism of the porous module sample prepared by the PU foam replica method. Initially, the PU foam template (Figure 8-8a) is immersed

in slurry and thoroughly dried, causing solid particles to adhere to the foam pore walls (Figure 8-8b). The PU foam gradually decomposes when heating in a muffle furnace, causing the adhered particles to coalesce (Figure 8-8c). With further temperature increase, these particles continue to sinter and interconnect, resulting in grain growth and a gradual reduction in voids, forming a dense pore wall surface (Figure 8-8d).

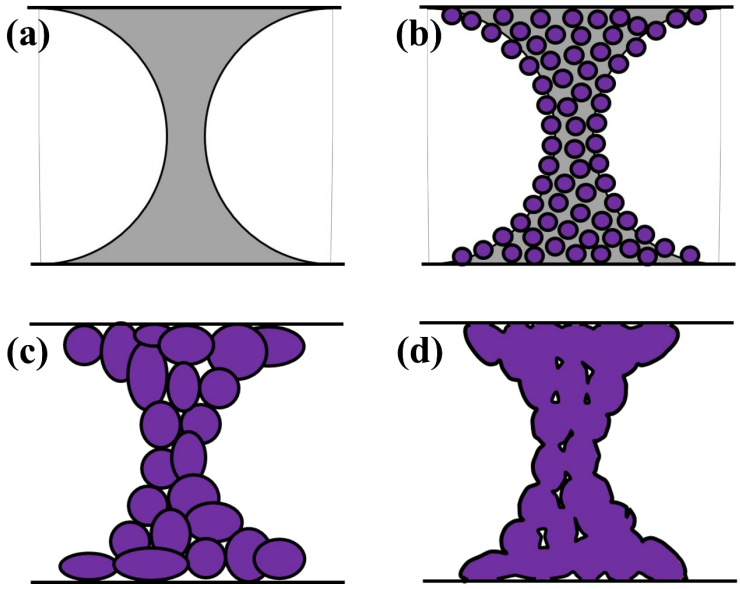

Figure 8-8 (a): PU foam pore wall (gray area) before immersed into slurry; (b): PU foam pore wall adhered by $CuMn_2O_4$/CuO particles (purple balls); (c): Decomposition of PU foam and coalescence of particles; (d): Sintering and interconnection of particles, resulting in dense pore wall surface.

8.3.4 Redox behavior of porous module

TGA was used to investigate the redox behavior of each porous module under an air atmosphere within the temperature range of 100 to 1000 °C. In Figure 8-9a, the porous modules sintered at 1000 °C with different holding times exhibits small variations in their redox behavior. Notably, the TGA tests conducted on these porous modules did not reveal an obvious decomposition of the Na-Mn oxides. The impact of holding time on the redox

behavior of the porous modules is evident in the porous modules sintered at 1050 ℃, as shown in Figure 8-9b. For example, the porous modules prepared at 1050-6h fails to achieve a satisfactory reduction depth during TGA tests when held at 1000 ℃ for 30 minutes. This phenomenon is even more observable in the 1100 ℃ one. Additionally, it is noteworthy that the 1100 ℃ one exhibits a special weight gain during the heating process in the TGA test, as shown in Figure 8-9c. This weight gain may be attributed to the fact that the cooling process of the porous module sintered at 1100 ℃ is unable to ensure complete transformation from the high-temperature-reduced state to the room-temperature-oxidized state, even with a slow cooling rate of 2°C/min. Consequently, the porous module prepared at 1100 ℃ retains a portion of the reduced state, and when the porous module is reheated, oxidation reactions occurred preferentially before reaching the phase equilibrium temperature, resulting in the observed weight gain.

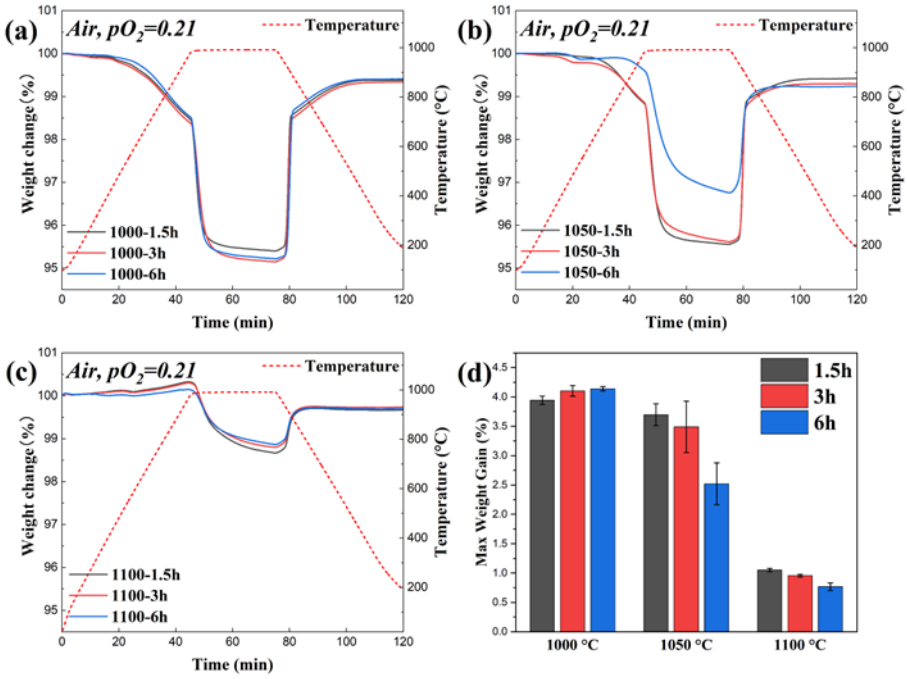

Figure 8-9 Redox behavior under an air atmosphere in 100 – 1000 ℃ for (a) 1000 ℃ porous module; (b) 1050 ℃ porous module, (c) 1100 ℃ porous module; (d): Maximum weight gain for each porous module.

To eliminate the influence of impurities on the redox behavior analysis of each sample, the weight gain during the cooling process was used as maximum weight change for relative comparison. As shown in Figure 8-9d, the 1000 °C sample exhibits a maximum weight change very close to that of the Co-pre and Pechini powder samples. However, as the sintering temperature is increased and the sintering holding time is extended, the maximum weight change decreases, indicating a degradation in the redox and thermal storage properties of the module samples.

8.3.5 Durability of porous module

The durability of each porous module was tested by 50 cycles of heating and cooling using a small muffle furnace. Photographs of the porous module after 0, 1, 5, 10, 20, 30, 40, and 50 cycles were selected for representative analysis (Figure 8-10) and their positions remained unchanged throughout the experiment. After 50 cycles, all samples retain their porous structure, but it should be noted that they also exhibit some degree of volume expansion. Accurately quantifying the volumetric expansion of the porous modules during the cycling test is a challenge because they also experienced some irregular distortion. The porous module sintered at 1000 ℃ exhibits more noticeable distortion, however, the 1100 ℃ one only exhibits a minor change. For instance, the surface of the 1000-1.5h porous module shows a tendency to concave inward after 50 cycles. This is attributed to the fact that the particles in the porous walls of the 1000 ℃ porous module are not densely packed, resulting in gradual deformation during the heating and cooling cycles. In addition, there are observable color differences among the porous modules. The 1000 ℃ porous module deepened its earthy yellow color after just one cycle and transformed to the same dark gray color as the fresh 1050 ℃ and 1100 ℃ porous module after five cycles. Interestingly, the 1050 ℃ and 1100 ℃ porous module also exhibit a slight change in color, transforming from dark gray to a brighter gray. This suggests that the surface morphology of the porous modules may have changed.

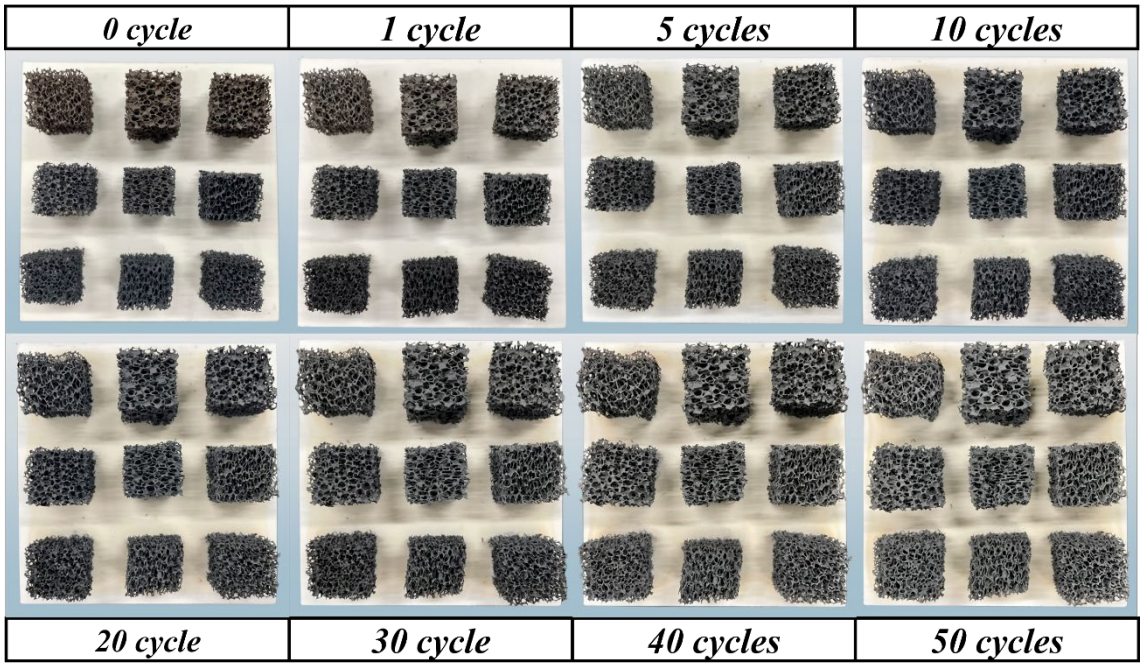

Figure 8-10 Photographs of each porous module after 0, 1, 5, 10, 20, 30, 40 and 50 cycles.

It can be roughly inferred from visual and tactile inspections that the compressive strength of the porous module has changed after 50 cycles durability test. The porous module sintered at 1000 ℃ exhibits an enhanced strength, while the 1050 ℃ and 1100 ℃ porous modules are slightly weakened. Efforts were initiated to measure the compressive strength of each porous module after 50 cycles using the same tensile and compression machine. However, the precise quantification of their compressive strength was challenging due to the irregular distortion generated by cycling tests. The distortion obstructed the porous modules from satisfying the flatness criterion for the ordinary compressive strength measurement, as the force application area could not be delineated accurately.

The redox behavior of the porous modules after 50 cycles was further investigated, and the results are shown in Figure 8-11. Surprisingly, the redox activities of each porous module exhibit a degree of recovery after cycling, which can be distinguished from an

increase in maximum weight loss and a decrease in the reduction onset temperature. The performance of the 1000 ℃ porous module exhibits no change after cycling, while the 1050 ℃ porous module shows a slight improvement. Notably, the 1100 ℃ porous module, which previously had difficulty experience redox reactions, now exhibits TGA curves similar to those of the 1000 ℃ and 1050 ℃ one.

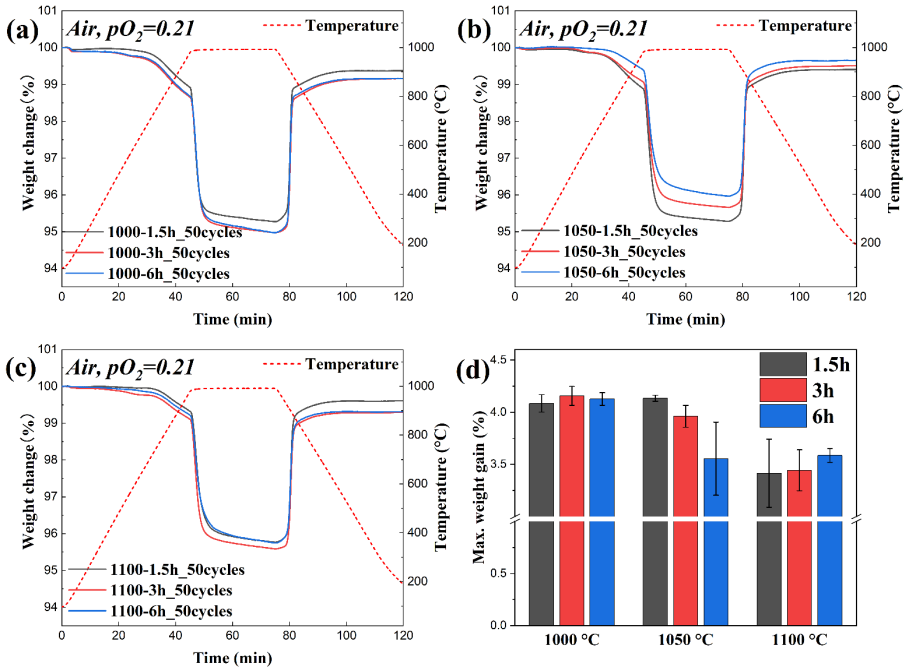

Figure 8-11 Redox behavior under an air atmosphere in 100 – 1000 ℃ for (a) 1000 ℃ porous module after 50 cycles, (b) 1050 ℃ porous module after 50 cycles, (c) 1100 ℃ porous module after 50 cycles; (d): Maximum weight gain for each porous module after 50 cycles.

This phenomenon may be linked to the changes in microscopic morphology of the porous module's surface. For further exploration, SEM observation was performed to investigate the microscopic morphology of each porous module before and after cycling.

SEM images of representative 1100-6h porous modules before and after 50 cycles are presented in Figure 8-12a, 8-12b, 8-12c, and 8-12d. Before the cycling test, the surface

of the as-prepared 1100-6h porous modules appeared dense, with no obvious pore structure (Figure 8-12b). However, after 50 cycles, pores of several-micron-pores in size formed on the sample's surface (Figure 8-12d). This pore structure increases the surface area exposed to oxygen, facilitating the apparent diffusion rate of oxygen on the porous module's surface. This is the primary reason for the performance recovery observed in the TGA test after cycling.

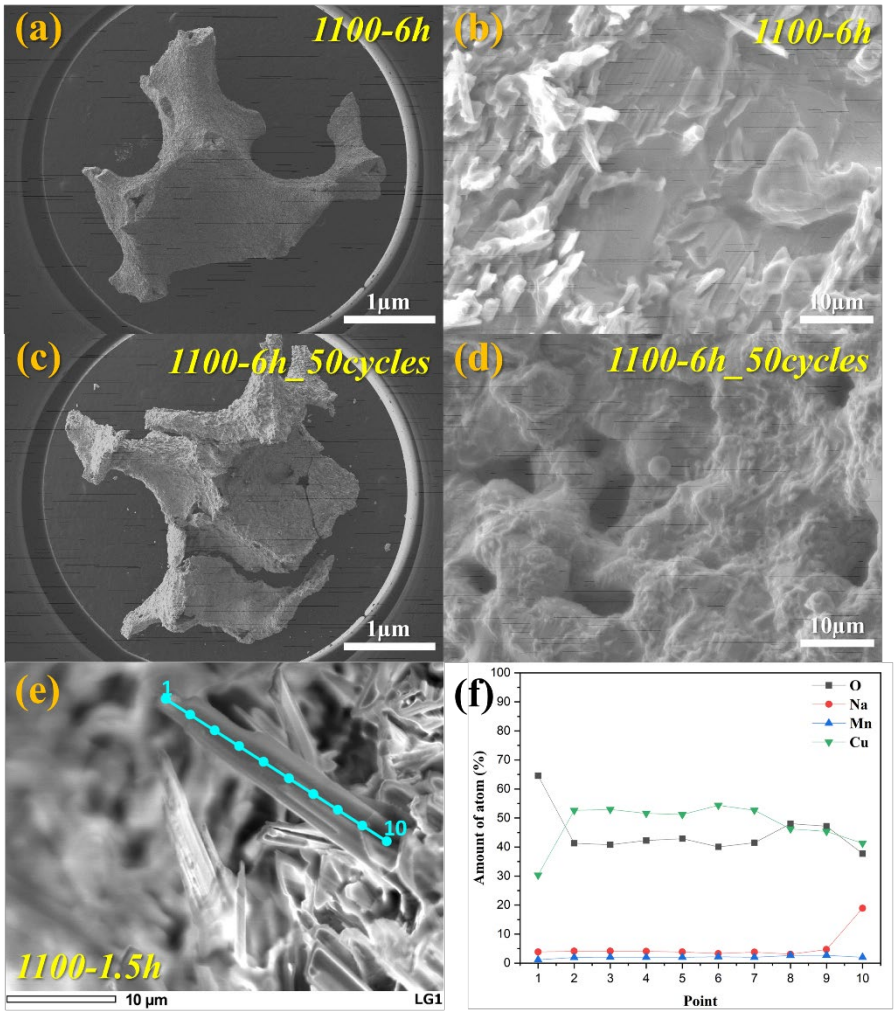

Figure 8-12 (a-b): SEM image of as-prepared 1100-6h porous module's fragment; (c-d): SEM image of 1100-6h porous module's fragment after 50 cycles; (e): Rod-like crystallite within the 1100-1.5h sample; (f): Continuous EDS point-scan analysis for the rod-like crystallite.

The formation of these pores appears to be linked to the reduction process of the porous module. During the high-temperature reduction process, oxygen releases from the samples and expands small pre-existing surface pores, turning them into larger openings. Simultaneously, the sintering of particles at high temperatures and the decreasing of grain boundaries resulted in a shrinkage in the volume fraction of solids, preserving the pore structures. Subsequently, we performed a quantitative analysis of the changes in pore size before and after cycling for each porous module. This was achieved by using SEM images and analyzing them with ImageJ software. The results are listed in Table 8-2. According to the table, the pore size of the porous modules sintered at 1000 ℃ increase from approximately 3μm to 11μm. Interestingly, the porous module sintered at 1050 ℃ and 1100 ℃ developed a pore structure with sizes ranging from approximately 6μm to 13μm after 50 cycles. However, it appears that there is no distinct correlation between the size of the pore structure formed and the sintering conditions. It is also worth noting that the presence of pores can also damage the macroscopic mechanical strength of the porous modules while the formation of pores enhances reactivity.

Table 8-2 Pore size on the surface of porous module before-and-after 50-cycling-test

Sample	Pore size (μm)	
	Before	After
1000-1.5h	3.56 ± 1.83	11.10 ± 5.24
1000-3h	3.37 ± 1.31	11.86 ± 4.61
1000-6h	3.51 ± 1.44	11.22 ± 4.70
1050-1.5h	-	6.06 ± 2.56
1050-3h	-	13.00 ± 5.01
1050-6h	-	8.35 ± 5.01
1100-1.5h	-	9.32 ± 4.47
1100-3h	-	7.44 ± 2.65
1100-6h	-	7.02 ± 3.00

Except for the 1100-3h and 1100-6h porous modules, we observed needle-like

crystallites in nearly all as-prepared porous modules, which significantly differ from the typical $CuMn_2O_4$ morphology. Additionally, more robustly grown rod-like crystallites exist in the 1050-6h and 1100-1.5h porous modules. To identify the composition of a specific rod-like crystallite within the 1100-1.5h porous modules (Figure 8-12e), we performed a continuous EDS point-scan analysis. These results indicate that it is primary constituted by Cu and O element (Figure 8-12f). Based on this, it is reasonable to deduce that the crystallite is composed of CuO, and it has been previously reported in the literature that CuO is readily to form nanowire or nanorod structures during some specific conditions [19–21].

In fact, the presence of CuO nanowires or nanorods is unfavorable for the reaction system in this study. This is because CuO is one of the reactants in the reaction system, as shown in equation (Equation 8-2) below. When CuO agglomerates to form larger crystals, it reduces the contact area with $CuMn_2O_4$ crystals. Consequently, the reaction may deviate from equation (Equation 8-2) and follow another equation (Equation 8-3) instead. In this case, less oxygen is released during the decomposition of 1 mole of $CuMn_2O_4$, directly affecting the heat storage density due to the reduced formation of $CuMnO_2$.

$$CuMn_2O_4 + CuO \Leftrightarrow 2CuMnO_2 + \frac{1}{2}O_2 \qquad (8-2)$$

$$CuMn_2O_4 \Leftrightarrow CuMnO_2 + \frac{1}{3}Mn_3O_4 + \frac{1}{3}O_2 \qquad (8-3)$$

While most of the CuO nanowires on the surface nearly disappeared after cycling, by chance, a significant amount of CuO nanowires was still present in the 1050-6h porous modules. This observation may clarify why, despite the performance (maximum weight loss) has recovered after cycling, the 1050-6h porous modules still exhibit poor

performance compared to the 1050-1.5h and 1050-3h porous modules that sintered at the same temperature. Additionally, the data of 1050-6h module sample (Figure 8-11d) exhibits a large deviation, indicating a more pronounced accumulation of CuO nanowires occurred in this situation.

8.3.6 Optimal preparation conditions and comparison with literature

From the perspective of practical application, we identified the optimal preparation conditions for $CuMn_2O_4$/$CuMnO_2$-based porous heat storage modules as a sintering temperature of 1100 ℃ and a holding time of 6 hours. Although the initial redox of the porous modules prepared under this condition was limited by oxygen diffusion, their redox behavior recovered to a satisfactory level after cycling test which is almost close to that of other porous modules. Notably, these porous modules exhibited good mechanical strength, less distortion, and excellent structural integrity after 50 cycles. Additionally, we have summarized the parameters of currently reported porous heat storage modules in Table 8-3 for comprehensive comparison.

Table 8-3 Comparison between currently reported porous heat storage modules

Module type	Porous foams			
	Material-coated	Material-based		
Material*	Co_3O_4-SiC, Al_2O_3, ZrO_2, Cordierite, SiC, SiSiC, etc.	Co_3O_4	$CaMnO_3$	$CuMn_2O_4$ (*this work*)
Heat storage density of pure material**	Aver. 480 kJ/kg		272 kJ/kg	145 – 236 kJ/kg (94 – 153 kJ/L)
Material loading wt%	13.5 – 33.4%	100%	100%	100%
Best redox performance***	42.2%	~92.0%	~100%	89.5%
Max. durability tested	100 cycles	100 cycles	46 cycles	50 cycles
Mechanical	Same as supports	/	87.5 – 132.4	105.0 kPa

strength			kPa	
PU foam used and sintering conditions	30 PPI (supports); 800 ℃, 4h	30, 45 PPI; 800 ℃, 4h	30 PPI; 1350 ℃, 3h	13 PPI; 1100 ℃, 6h
Experimental results	+ Simple preparation and low cost + Adaptable for a high flow rate of HTF + Good mechanical and chemical stability - Limited heat storage density due to low loading rate	+ Simple preparation and low cost + Adaptable for a high flow rate of HTF + Heat storage density, porosity, and shape can be adjusted by PU foam template - Weak mechanical strength - Difficult to prepare a larger size in monolith		

* Materials are presented in their oxidized forms.

** Only the values of chemical reaction heat measured by DSC are included.

*** By comparing weight change of modules/weight change of powder at first cycle

As highlighted in the introduction, the porous modules possess a crucial feature: the adaptability of large HTF flow rates. This feature is essential for rapid heat storage and release, a characteristic that is also shared with the honeycomb module. However, the porous foam modules do not involve complicated and high-cost preparation. Unlike the material-coated modules based on Al_2O_3 or ZrO_2 porous foam supports, this study utilizes the PU form replica method to prepare porous foam modules directly from $CuMn_2O_4$/$CuMnO_2$, which was named as material-based modules. Theoretically, this method is expected to enhance the heat storage density compared to the former one when the same heat storage material is used.

Table 8-3 shows the similarity between the $CuMn_2O_4$/$CuMnO_2$-based porous modules developed in this study and the literature-reported $CaMnO_3$-based porous modules on reactivity, heat storage densities, and durability. However, the mechanical properties of the former are slightly lower, mainly due to differences in voidage and -porosity since different PU foam template and various sintering temperatures were used. Although the PU foams of 30 PPI were used as templates in most of the prior studies, we chose a cubic

PU foam with a larger 13 PPI pore size to better understand the wall formation process in the PU foam replica method and observe the macro-morphology changes during durability tests. Additionally, the perovskite-type $CaMnO_3$ material requires different sintering temperatures as it does not undergo significant phase transitions. This phenomenon causes its oxygen uptake and release behaviors to be different from those of $CuMn_2O_4$, which typically experiences larger weight change.

In general, the performance of material-based porous modules prepared from the same material is related to two key factors: voidage and porosity. Higher voidage results in lower pressure drops and faster heat storage and release rates but reduces heat storage density. Conversely, smaller voidage increases heat storage density but may cause larger pressure drops. Porosity affects reactivity and mechanical strength; larger porosity enhances reactivity but diminishes mechanical strength, and *vice versa*.

While the material-coated porous modules have superior mechanical strength (primarily dependent on the support's strength), the material-based modules possess higher heat storage densities, which offer a promising modularization concept for fixed-bed thermochemical reactors without frequent equipment transportation needs. However, the PU foam replica method might face issues like deformation or collapse with larger size modules, suggesting the use of multiple smaller-sized modules for stacking will be a wise choice.

8.4 Conclusions

In this chapter, we developed $CuMn_2O_4/CuMnO_2$-based porous heat storage modules that are adaptable to various HTF flow rates and exhibit high reaction activity. Initially, we used the co-precipitation method to produce $CuMn_2O_4/CuMnO_2$ in large quantities. We then performed XRD, TG, and DSC analysis to compare the materials synthesized by both the co-precipitation method and the Pechini method we used in

previous study. The findings revealed that there are no significant differences between the material synthesized by the two different methods, except for the presence of a small amount of Na-Mn oxide impurities in the co-precipitation sample. Subsequently, we employed the co-precipitation material to prepare $CuMn_2O_4$/$CuMnO_2$-based porous modules using the PU foam replica method with a size of 20 × 20 × 20 mm^3 and pore sizes of 13 PPI. The focus of this study is to investigate how various preparation conditions, specifically sintering temperature and holding time, influence the mechanical properties, reactivity, and durability of these porous modules. The results indicate that the modules' compressive strength improves with higher sintering temperature and extended holding time. This improvement is likely due to the densification of particles within the module walls under these conditions. However, we also noticed a deterioration in redox behavior during TG heating and cooling tests as the sintering temperature and holding time increased. A durability test of 50 cycles was then conducted on monolithic module samples using a small muffle furnace. After 50 cycles, the modules maintained their integrity but exhibited variations in volume expansion and color changes. Further investigation on the redox behavior of the after-cycling samples through TG revealed a surprising recovery in reactivity, particularly in porous modules sintered at 1050 °C and 1100 °C. SEM observations of the module samples' fragments, both before and after cycling, showed that a dense surface formed pores of about several-μm after 50 cycles, which likely contributed to the reactivity's recovery. Additionally, the formation of nanowire CuO on the surface of some samples was observed and we believe this formation is unfavorable to the reaction. Although the exact mechanism remains unclear, interestingly, this phenomenon diminished with an increase in the number of cycles.

After evaluating the material characteristics, mechanical properties, reactivity, and durability, we determined that the optimal preparation conditions for $CuMn_2O_4$/$CuMnO_2$-based porous heat storage modules are a sintering temperature of 1100 °C and a holding time of 6 hours. Additionally, our comparison with current research trends in various

porous heat storage modules leads us to conclude that the material-based porous modules are a promising option for designing fixed-bed reactors in redox-type TCES systems. However, it is important to acknowledge the current limitations, particularly the weak mechanical strength of these modules and the challenges in fabricating larger sizes, which should be further investigated in future studies.

Reference

[1] M. Wokon, A. Kohzer, M. Linder, Investigations on thermochemical energy storage based on technical grade manganese-iron oxide in a lab-scale packed bed reactor, Solar Energy 153 (2017) 200–214. https://doi.org/10.1016/j.solener.2017.05.034.

[2] A.J. Schrader, G.L. Schieber, A. Ambrosini, P.G. Loutzenhiser, Experimental demonstration of a 5 kWth granular-flow reactor for solar thermochemical energy storage with aluminum-doped calcium manganite particles, Applied Thermal Engineering 173 (2020) 115257. https://doi.org/10.1016/j.applthermaleng.2020.115257.

[3] M. Hamidi, V.M. Wheeler, X. Gao, J. Pye, K. Catchpole, A.W. Weimer, Reduction of iron–manganese oxide particles in a lab-scale packed-bed reactor for thermochemical energy storage, Chemical Engineering Science 221 (2020) 115700. https://doi.org/10.1016/j.ces.2020.115700.

[4] M. Gigantino, S.S. Brunser, A. Steinfeld, High-temperature thermochemical heat storage via the CuO/Cu2O redox cycle: From material synthesis to packed-bed reactor engineering and cyclic operation, Energy and Fuels 34 (2020) 16772–16782. https://doi.org/10.1021/acs.energyfuels.0c02572.

[5] D. Bielsa, M. Oregui, P.L. Arias, New insights into Mn2O3 based metal oxide granulation technique with enhanced chemical and mechanical stability for thermochemical energy storage in packed bed reactors, Solar Energy 241 (2022) 248–

261. https://doi.org/10.1016/j.solener.2022.06.010.

[6] C. Pagkoura, G. Karagiannakis, A. Zygogianni, S. Lorentzou, M. Kostoglou, A.G. Konstandopoulos, M. Rattenburry, J.W. Woodhead, Cobalt oxide based structured bodies as redox thermochemical heat storage medium for future CSP plants, Solar Energy 108 (2014) 146–163. https://doi.org/10.1016/j.solener.2014.06.034.

[7] A. Singh, S. Tescari, G. Lantin, C. Agrafiotis, M. Roeb, C. Sattler, Solar thermochemical heat storage via the Co3O4/CoO looping cycle: Storage reactor modelling and experimental validation, Solar Energy 144 (2017) 453–465. https://doi.org/10.1016/j.solener.2017.01.052.

[8] S. Tescari, A. Singh, C. Agrafiotis, L. de Oliveira, S. Breuer, B. Schlögl-Knothe, M. Roeb, C. Sattler, Experimental evaluation of a pilot-scale thermochemical storage system for a concentrated solar power plant, Applied Energy 189 (2017) 66–75. https://doi.org/10.1016/j.apenergy.2016.12.032.

[9] M. Ebadi, M. Mehrpooya, A.H. Kani, Sensitivity analysis and optimization of geometric and operational parameters in a thermochemical heat storage redox reactor used for concentrated solar power plants, Journal of Thermal Analysis and Calorimetry 147 (2022) 6415–6435. https://doi.org/10.1007/s10973-021-10980-3.

[10] G. Xiao, Z. Wang, D. Ni, P. Zhu, Kinetics and Structural Optimization of Cobalt-Oxide Honeycomb Structures Based on Thermochemical Heat Storage, Energies 16 (2023). https://doi.org/10.3390/en16073237.

[11] M. Pein, L. Matzel, L. de Oliveira, G. Alkan, A. Francke, P. Mechnich, C. Agrafiotis, M. Roeb, C. Sattler, Reticulated Porous Perovskite Structures for Thermochemical Solar Energy Storage, Advanced Energy Materials 12 (2022) 1–17. https://doi.org/10.1002/aenm.202102882.

[12] C. Agrafiotis, S. Tescari, M. Roeb, M. Schmücker, C. Sattler, Exploitation of thermochemical cycles based on solid oxide redox systems for thermochemical storage of solar heat. Part 3: Cobalt oxide monolithic porous structures as integrated

thermochemical reactors/heat exchangers, Solar Energy 114 (2015) 459–475. https://doi.org/10.1016/j.solener.2014.12.037.

[13] C. Agrafiotis, M. Roeb, M. Schmücker, C. Sattler, Exploitation of thermochemical cycles based on solid oxide redox systems for thermochemical storage of solar heat. Part 2: Redox oxide-coated porous ceramic structures as integrated thermochemical reactors/heat exchangers, Solar Energy 114 (2015) 440–458. https://doi.org/10.1016/j.solener.2014.12.036.

[14] K. Schelm, K. Dammler, U. Betke, M. Scheffler, Tailoring of the Wetting Behavior of Alumina Dispersions on Polymer Foams by Methylcellulose Addition: A Route Toward Mechanically Stable Ceramic Replica Foams, Advanced Engineering Materials 21 (2019) 1–12. https://doi.org/10.1002/adem.201900635.

[15] C.Y. Lee, S. Lee, J.H. Ha, J. Lee, I.H. Song, K.S. Moon, Effect of the processing conditions of reticulated porous alumina on the compressive strength, Journal of the Korean Ceramic Society 58 (2021) 495–506. https://doi.org/10.1007/s43207-021-00128-2.

[16] F. Guo, F. Wu, J. Li, L. Liu, Y. Huang, A facile approach for preparing Al2O3 reticulated porous ceramics with optimized closed-cell struts and excellent mechanical properties, Ceramics International 49 (2023) 22054–22061. https://doi.org/10.1016/j.ceramint.2023.04.031.

[17] F.C.M. Driessens, Phase Equilibria in the System Cu-Mn-O, Zeitschrift Für Anorganische Und Allgemeine Chemie 351 (1967) 48–62. https://doi.org/10.1023/A:1010113711219.

[18] O. GLEMSER, H. SAUER, SECTION 19 - Copper, Silver, Gold, in: G. BRAUER (Ed.), Handbook of Preparative Inorganic Chemistry (Second Edition), Academic Press, 1965: pp. 1003–1066. https://doi.org/10.1016/B978-0-12-395591-3.50005-4.

[19] A.S. Ethiraj, D.J. Kang, Synthesis and characterization of CuO nanowires by a simple wet chemical method, Nanoscale Research Letters 7 (2012) 1–5.

https://doi.org/10.1186/1556-276X-7-70.

[20] G. Fritz-Popovski, F. Sosada-Ludwikowska, A. Köck, J. Keckes, G.A. Maier, Study of CuO Nanowire Growth on Different Copper Surfaces, Scientific Reports 9 (2019) 1–13. https://doi.org/10.1038/s41598-018-37172-8.

[21] M. Košiček, J. Zavašnik, O. Baranov, B. Šetina Batič, U. Cvelbar, Understanding the Growth of Copper Oxide Nanowires and Layers by Thermal Oxidation over a Broad Temperature Range at Atmospheric Pressure, Crystal Growth and Design 22 (2022) 6656–6666. https://doi.org/10.1021/acs.cgd.2c00863.

Chapter 9. $CuMn_2O_4/CuMnO_2$-based honeycomb structure heat storage module

9.1 Introduction

In Chapter 8, we successfully synthesized a large quantity of $CuMn_2O_4/CuMnO_2$ using the co-precipitation method and developed a $CuMn_2O_4/CuMnO_2$-based porous foam heat storage module (20 × 20 × 20 mm^3, 13 PPI) that demonstrated high reaction activity. However, it is important to acknowledge the current limitations of porous heat storage modules, namely their mechanical strength and the challenges associated with fabricating larger sizes.

In addition to the porous foam module, the heat storage module with honeycomb structure also offers an effective solution to the pressure drop issue encountered in the packed bed reactors. This design can adapt to the high flow rates of HTFs, meeting the rapid requirements for heat storage and release. There are two types of honeycomb structure modules: CHS material-coated [1,2] and CHS material-based honeycombs [3]. The former involves coating CHS materials onto the surface of common cordierite of SiC honeycomb ceramic matrices. While this approach is simpler, it limits the overall heat storage density of the module because controlling the thickness of the coating layer is difficult. The latter approach directly synthesizes honeycomb structure from CHS materials, addressing the limitation of low heat storage density. However, this method requires specialized extrusion molding devices and molds.

Recently, Xiao et al. developed a cobalt-oxide-based honeycomb structure model for CHS purposes [3]. The module demonstrated high heat storage density and reactivity. However, it is worth noting that their design incorporated a smaller number of channels (9 channels), which may result in higher pressure losses at high fluid flow rates.

In this chapter, we developed a $CuMn_2O_4/CuMnO_2$-based honeycomb structure module for chemical heat storage applications. The honeycomb module was prepared using the extrusion molding method using the raw sample synthesized via co-precipitation method. Subsequently, we focused on exploring the effects of fluid flow rate and initial reaction temperature on the honeycomb module's heat release performance and

reactivity during the oxidation process.

9.2 Experimental approach

9.2.1 Preparation of honeycomb structure module

The honeycomb structure module (hereinafter referred to as “honeycomb module”) was prepared using extrusion molding method, a widely used technique in ceramic molding technology. Nagamine Manufacturing Co., Ltd. (Japan) provided assistance with the preparation. Due to the proprietary considerations, the detailed preparation process cannot be disclosed; however, a generalized preparation process is illustrated in Figure 9-1. In general, the raw material powder was mixed with water and a binder to achieve plasticity, then fed into an extruder machine. The raw material was extruded through a screw channel and shaped by a mold attached to the outlet of channel.

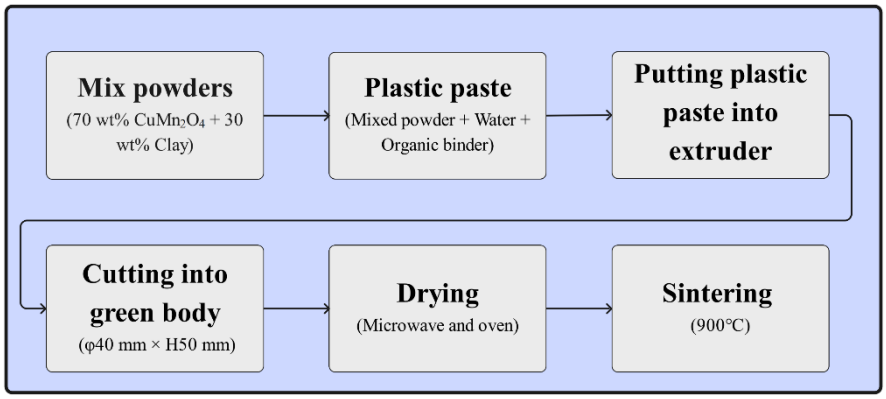

Figure 9-1 Preparation process of honeycomb structure module using extrusion molding method

To enhance the mechanical strength and cycle durability of the honeycomb module, a mixed power of $CuMn_2O_4$/$CuMnO_2$ and Kibushi Clay were used as raw materials, with a weight ratio of 7:3. The specific composition of typical Kibushi Clay is listed in Table 9-1, with its primary components being SiO_2 and Al_2O_3. Subsequently, a small amount of

water and organic binder were added to the mixed powder to improve plasticity and flowability. The resulting plastic paste, which has a texture similar to Plasticine, was fed into a small extruder machine for the extrusion molding process.

Table 9-1 Compositional analysis of typical Kibushi clay (Japan)

Composition	SiO_2	Al_2O_3	Fe_2O_3	CaO	MgO	K_2O	Na_2O	TiO_2	lg.Loss
Weight%	48.60	33.90	1.69	0.16	0.41	0.85	0.09	0.96	12.90

A metal mold with a 40mm diameter and a cell density of 200 cell per square inch (cpsi) was attached to the extruder's outlet. After cutting, the green body of honeycomb module (φ40 mm × H50 mm) was obtained. To ensure the green body retained its shape well before sintering, it was first quickly dried using microwave heating, followed by slow drying in a low-temperature oven. After drying, the apparent volume of green body shrank by approximately 30 %. Finally, the green body was sintered in a muffle furnace with the temperature gradually increasing to 900 °C.

After the sintering process, the resulting honeycomb module is shown in Figure 9-2. Overall, the shape of honeycomb module retained its intended shape, with only a few defective products. The detailed physical parameters of the honeycomb module are provided in Table 9-2.

Table 9-2 Physical parameters of honeycomb structure module

Diameter (mm)	Height (mm)	Weight (g)	Apparent density (g/cm^3)	True density (g/cm^3)	Void fraction (-)	Cell density (cpsi)	Cell wall thickness (mm)
31.76 ± 0.39	48.74 ± 1.35	50.70 ± 1.24	0.76 ± 0.04	3.22 ± 0.11	0.76 ± 0.04	304	1.1

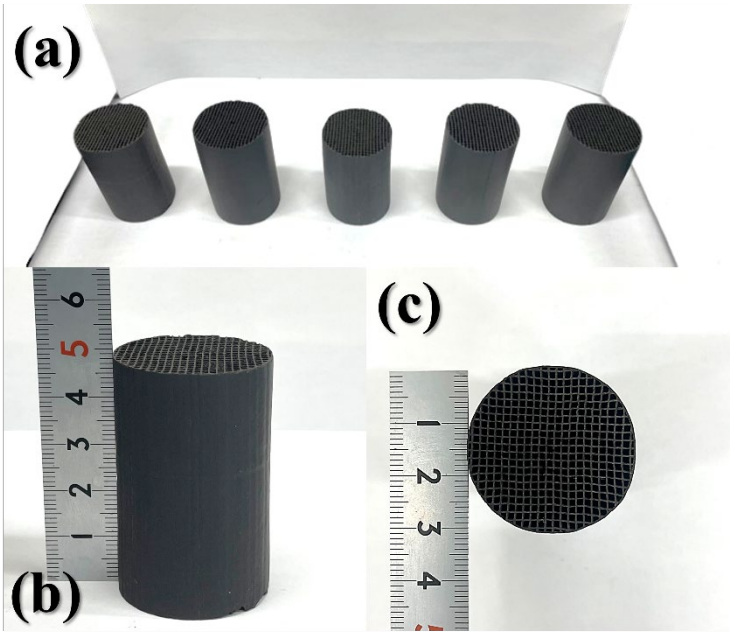

Figure 9-2 (a) Honeycomb structure module resulted from extrusion molding method, (b) Side view, and (c) Top view of honeycomb structure module

The physical parameters reveal that the sintered honeycomb module shrank by approximately 20.60% in the radius direction and 2.52% in the axial direction compared to the green body before drying. For true density measurements, a high-precision gas and vapor adsorption analyzer (BELSORP MAX II, MicrotracBEL Corp.) with helium gas displacement method was used. Compared to the void fraction of the conventional packed bed [4] (0.65–0.40 for spheres; 0.70–0.35 for solid cylinder; 0.70–0.45 for hollow cylinder; 0.80–0.55 for 4-hole cylinder), the honeycomb module prepared in this study exhibits relatively higher void fraction, which is primarily attribute to its thin cell wall thickness. The high void fraction also suggests that the honeycomb module can efficiently handle rapid heat storage and release under condition of high flow rate of heat transfer fluid (e.g., air).

9.2.2 Design of heat release demonstration equipment based on tubular furnace

For the heat release demonstration of the honeycomb module, the equipment was modified from tubular furnace. Its schematic and actual appearance are shown in Figure 9-3a and Figure 9-3b, respectively. The core components of the evaluation setup include two tubular furnaces (ARF-50K, Asahi-rika Co., Ltd.) and a stainless steel (SUS304) reaction tube. The upper tubular furnace maintains the honeycomb module within the desired temperature range, while the lower one preheats the fluid to minimize temperature differences before the fluid reaches the honeycomb module.

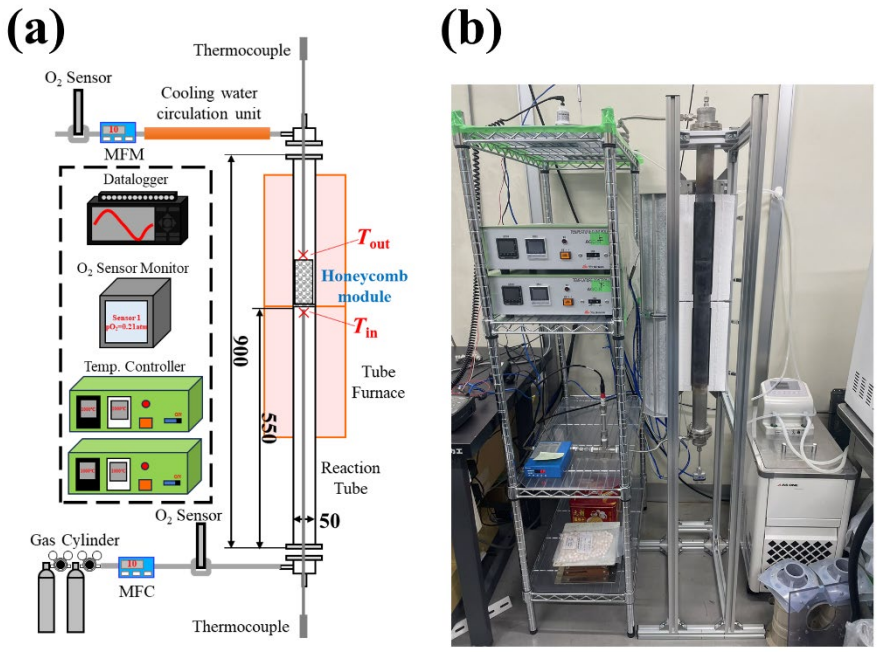

Figure 9-3 (a) Schematic and (b) Photograph of heat release demonstration equipment for honeycomb module

In this study, nitrogen gas (N_2, $pO_2 \approx 0$ atm) and synthetic air gas ($N_2 + O_2$, $pO_2 = 0.21$ atm) were mainly used as the working fluids. Before entering the reaction tube, the gas flow rate was regulated by a mass flow controller (MFC, 8500MC, KOFLOC Corp.) and the oxygen concentration was monitored by an oxygen concentration sensor (JKO-25LJ3-

K, ICHINEN MANUFACURING Co., Ltd.). A cooling water circulation unit was installed at the gas outlet to quickly lower the gas temperature to room temperature. The gas flow rate and oxygen concentration at the outlet were monitored by a mass flow meter (MFM, 8500MC, KOFLOC Corp.) and same type oxygen concentration sensor as the inlet.

The gas temperatures before (T_{in}) and after (T_{out}) passing through the honeycomb module were measured using thermocouples positioned 5 mm from the module. For measuring T_{in}, a K-type thermocouple (φ6.4 mm × L450 mm, INCONEL sheath, Takahashi Thermosensor Co., Ltd.) was used. To precisely evaluate the heat storage and release performance, T_{out} was measured by using a thinner R-type thermocouple (φ3 mm × L450 mm, alumina sheath, Takahashi Thermosensor Co., Ltd.) with a shorter response time.

9.2.3 Experimental conditions and indices

In the pre-experiment of TGA using the fragment of honeycomb module, we found that when the experimental temperature exceeded 900 °C, the honeycomb module exhibited a decline in reactivity due to severe sintering phenomenon, which adversely affected its heat release performance. Additionally, the high-pressure condition during the extrusion process may have contributed to this issue. The addition of clay, intended to improve plasticity and mechanical strength, may also be a contributing factor.

The experimental conditions are shown in Figure 9-4. One single honeycomb module was initially heated to 900 °C under nitrogen gas with a flow rate of 5 L/min for reduction process. Subsequently, it was cooled down to the targeted initial temperature (700 °C, 600 °C, and 500 °C) under nitrogen flow protection at same flow rate. After keeping the temperature isothermally at both T_{in} and T_{out} for an additional 5 minutes, the gas was switched to synthetic air (Q_v = 5 L/min, 2.5 L/min, and 1 L/min) to initiate the oxidation reaction. The oxidation process was conducted at a fixed furnace setting temperature for

60 minutes to ensure the complete conversion of oxidation reaction. It is worth noting that the gas hourly space velocity (GHSV) under these experiment conditions were range from 1553 to 7766 h^{-1}, significantly higher than that of a typical packed bed reactor. For convenience, the experimental conditions are labeled as "x °C-y L/min", such as "600 °C-5 L/min".

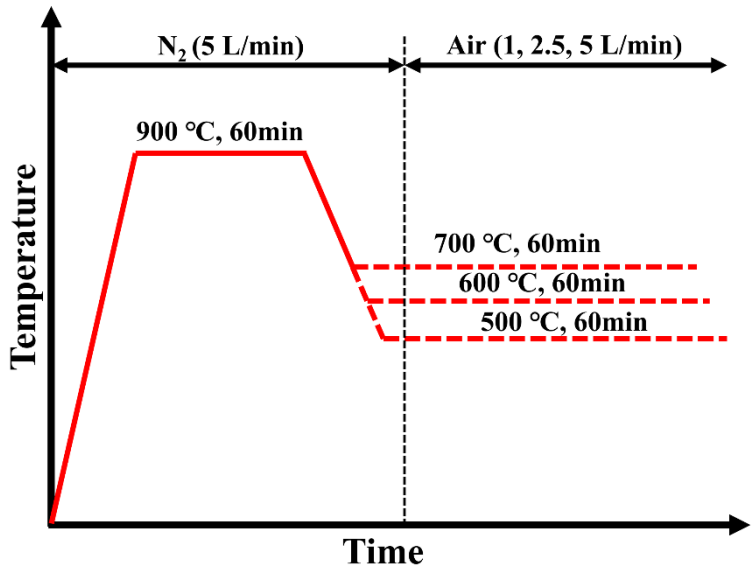

Figure 9-4 Temperature profile and gas flow rate of experimental conditions

For evaluating the heat release performance of the honeycomb module, the following indices were used: maximum outlet temperature change (ΔT_{max}), time to peak (t_{peak}), maximum instantaneous output power (P_{max}), heat recovery amount (Q_{rec}), and heat recovery ratio (η_{rec}). To account for possible minor temperature fluctuations during the experiment, the temperature just before switching the gas to air was taken as the initial temperature (T_{ini}) for calculating the maximum temperature change (ΔT_{max}).

The output power (P) at any given moment can be calculated using Equation 9-1 and the mass flow rate of air ($\dot{m}$) can be calculated using Equation 9-2. The specific heat capacity ($C_{p,hot}$) of air at high temperatures were obtained from the relevant design manuals, and the specific values used in this study are provided in Table 9-3.

$$P = \dot{m} \cdot C_{p,hot} \cdot \left(T_{out,t} - T_{out,ini}\right) \quad (9-1)$$

$$\dot{m} = \frac{P \cdot Q_v \cdot M_{air}}{R \cdot T} = \frac{101.325\ [kPa] \times Q_v \times 29[g/mol]}{8.314\ [J/(mol \cdot K)] \times 293.15\ [K]} \quad (9-2)$$

Table 9-3 Specific heat capacity of air at 25, 500, 600, and 700°C

Temperature (°C)	Specific heat capacity (J/(kg·K))
25	1006
500	1092
600	1115
700	1136

After obtaining the *P*-*t* curve using Equation 9-1, Q_{rec} can be calculated by integrating *P* over the time *t* (Equation 9-3).

$$Q_{rec} = \int_0^t P \cdot dt \quad (9-3)$$

η_{rec} can be obtained by comparing the ratio between Q_{rec} and the estimated heat release amount ($Q_{estimated}$) (Equation 9-4). $Q_{estimated}$ was obtained by multiplying the heat release density and actual weight of the honeycomb module. The heat release density of module was measured by the TG-DSC (TGA/DSC 3+, METTLER TOLEDO International Inc.) at the same temperature program.

$$\eta_{rec} = \frac{Q_{rec}}{Q_{estimated}} \times 100\% = \frac{Q_{rec}}{50.7[g] \times 110.24[J/g]} \times 100\% \quad (9-4)$$

For reactivity evaluation, the oxygen consumption rate (rO_2) was calculated first using

Equation 9-5. $r\mathrm{O_2}$ was calculated by using oxygen concentration (X_{O2}) at the inlet and outlet. In should be noted that because the oxidation reaction consumes oxygen from the air, the gas flow rate decreases accordingly. In contrast to $Q_{v,in}$ at the inlet, $Q_{v,out}$ at the outlet was determined using real-time data from the flow meter rather than a constant value. Subsequently, the following indices were used: peak oxygen consumption rate ($r_{O2,peak}$), time to peak (t_{peak}), oxygen consumption (V_{O2} or n_{O2}), and reaction conversion ratio (α). V_{O2} was calculated by integrating over time with $r\mathrm{O_2}$ (Equation 9-6).

$$r_{o2} = Q_{v,out} \cdot X_{o2,out} - Q_{v,in} \cdot X_{O2,in} \tag{9-5}$$

$$V_{o2} = \int_0^t r_{o2} \cdot dt \tag{9-6}$$

n_{O2} during the oxidation reaction can be calculated using the ideal gas law (Equation 9-7).

$$n_{O2} = \frac{P \cdot V_{o2}}{R \cdot T} = \frac{101.325 \times 10^3\ [Pa] \times V_{o2}}{8.134\ [J/(K \cdot mol)] \times 293.15\ [K]} \tag{9-7}$$

There are two main methods for calculating α: one based on the chemical reaction equation and the other based on the weight changes observed in thermogravimetric analysis. Given the complexity of the $CuMn_2O_4/CuMnO_2$ redox couple's chemical reaction, as identified in the previous chapter, we used the latter one as the estimated oxygen consumption ($n_{O2,estimated}$) for the honeycomb module and calculated α using Equation 9-8. Details on determining $n_{O2,estimated}$ will be provided in the next section.

$$\alpha = \frac{n_{O2}}{n_{O2,estimated}} = \frac{n_{O2}}{0.06734\ [mol]} \tag{9-8}$$

9.3 Results and discussion

9.3.1 Revisiting of $CuMn_2O_4/CuMnO_2$ redox couple

For the heat storage density of the $CuMn_2O_4/CuMnO_2$ redox couple prepared by the co-precipitation method, we reported the value measured using the non-isothermal method (constant heating/cooling rate) in the previous chapter. In this chapter, we supplemented this with the value measured using the isothermal method, where the material was first reduced under an inert atmosphere and then oxidized at a constant temperature by switching gas to the air (Figure 9-5a). These values are presented in Table 9-4.

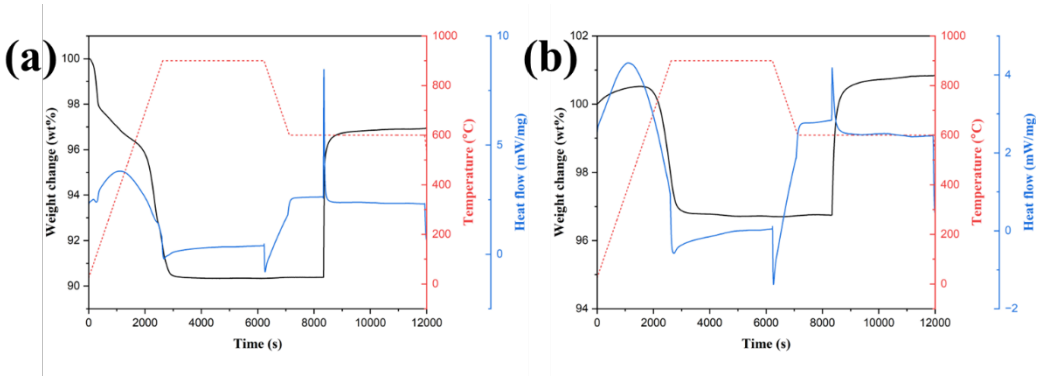

Figure 9-5 TG-DSC results of (a) co-precipitation sample and (b) honeycomb module's powder when reduced at 900 °C in N_2 followed by re-oxidized at 600 °C in air

Table 9-4 Heat storage density (kJ/kg-oxidized state) of $CuMn_2O_4/CuMnO_2$ prepared by the co-precipitation method under different measurement methods

Non-isothermal		Isothermal
Reduction	Oxidation	Oxidation
144.78 ± 36.81	128.81 ± 10.01	234.67 ± 3.37

We also measured the weight gain, and the heat storage density of the powder obtained after crushing the honeycomb module by using the isothermal oxidation method (Figure 9-5b). The results reveal that the honeycomb module's weight gain (4.25 ± 0.13 wt%) was slightly lower than the expected value (4.49 ± 0.08 wt%) based on the percentage of heat storage material within the honeycomb module. Additionally, the honeycomb module's heat storage density (110.24 ± 7.71 kJ/kg) was lower than the value we expected (164.27 ± 2.36 kJ/kg). The addition of clay may have a greater impact on the reactivity and heat storage density of the honeycomb module than initially expected. Although these values are somewhat degraded compared to the pure material, they were used as the basis for calculating $Q_{estimated}$ and $n_{O2,estimated}$ to obtain η_{rec} and α in Equation 9-4 and Equation 9-8.

9.3.2 Representative experimental results

In the pre-experiments, we confirmed using an electric balance that the honeycomb module can reach a fully reduced state after being held in a nitrogen flow at 900 °C for 60 minutes. Therefore, this study focuses solely on the module's heat release performance and reactivity under fixed furnace temperature settings. This approach is similar to the isothermal conditions used in kinetic studies, though there is a slight difference: the heat released by the honeycomb module causes a significant increase in its temperature.

The representative experimental results for 600 °C-5L/min is shown in Figure 9-6, including the change in T_{in} and T_{out}, the change in $X_{O2,in}$ and $X_{O2,out}$, and Q_v. After switching the gas from nitrogen to synthetic air, the T_{out} was increased, reaching a ΔT_{max} of 50.3°C, and then recovered to the initial temperature of T_{out}. In the early stage of the experiment, a decrease in the Q_v at outlet and a delayed rise in $X_{O2,out}$ compared to the $X_{O2,in}$ confirm the progress of the oxidation reaction and demonstrated the heat release from the honeycomb module. Meanwhile, we observed that the $X_{O2,out}$ initially increased, then decreased, and subsequently increased again. This phenomenon is primarily due to

the fact that, after switching the gas to air, a portion of the air passed through the honeycomb module without reacting. As the oxygen concentration around the honeycomb module increased, the reaction rate gradually accelerated because the oxygen diffusion rate within the honeycomb module also increased, leading to the observed decrease in the $X_{O2,out}$ again.

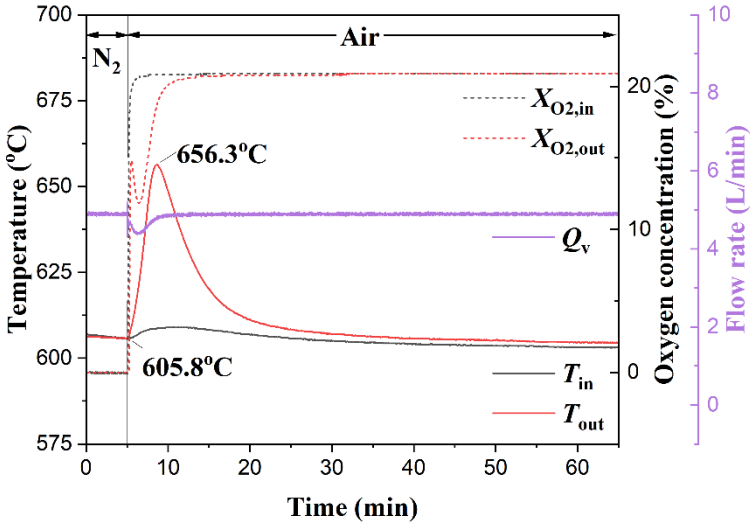

Figure 9-6 Representative experimental results of 600 °C-5L/min with one single honeycomb structure module

It is important to note that the calculation of oxygen consumption using Equation 9-5 and Equation 9-6 depends on the oxygen concentration at both the inlet and outlet. Since the reaction tube was initially filled with nitrogen, it took some time for the air to fully replace the nitrogen after switching to air. This so-called "dead volume" in the reaction tube, resulting from the gas switching, must be subtracted from the oxygen consumption volume calculated using Equation 9-6. Further details regarding this adjustment will be discussed in later sections.

9.3.3 Heat release performance under different experimental conditions

After switching the gas from nitrogen to air under each experimental condition, the ΔT

of outlet resulting from the oxidation reaction are shown in Figure 9-7. The honeycomb module could achieve a ΔT of up to 46.2 ± 4.1 °C at the experimental condition of 600 °C-5L/min. The ΔT_{max} for different isothermal conditions and gas flow rates are summarized in Figure 9-8a. As the Q_v increases, the oxygen concentration around the module rises more rapidly, enhancing the oxygen diffusion rate and accelerating the oxidation reaction rate. Consequently, the ΔT_{max} increases with higher Q_v when the initial reaction temperature conditions are same.

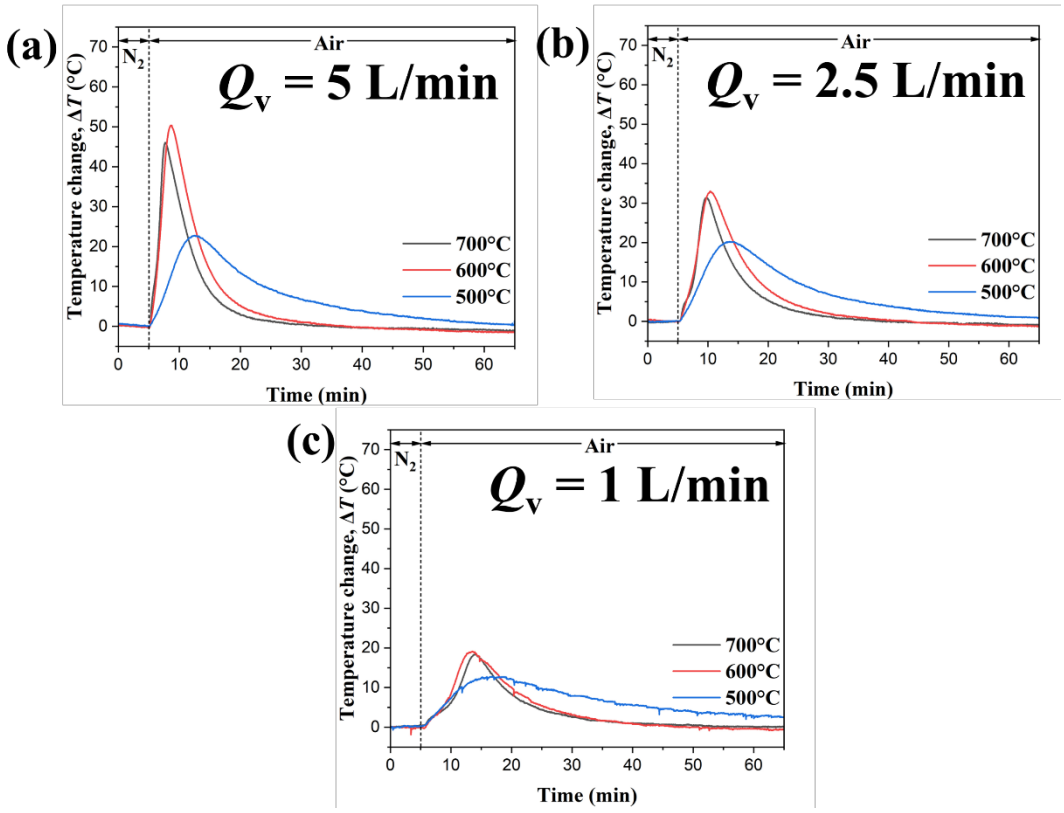

Figure 9-7 Variation of outlet temperature change (ΔT) under different initial reaction temperature at gas flow rate (Q_v) of (a) 5L/min, (b) 2.5 L/min, and (c) 1 L/min

Generally, a higher reaction temperature leads to a faster reaction rate, and a larger ΔT_{max} would be expected. However, we observed that at the same Q_v, ΔT_{max} initially increases but then decreases as the initial reaction temperature rises. Two possible reasons for this phenomenon are: (1) as the reaction temperature increases, heat loss from the

device to the environment also increases, causing more of the heat generated by the oxidation reaction of the honeycomb module to be lost at higher temperatures, which cannot be recovered by the flowing gas in time; (2) as the reaction temperature approaches the equilibrium temperature, the effect of the reduction reaction on the net reaction rate becomes increasingly significant, leading to a lower net reaction rate and a lower observed ΔT_{max}. However, these hypotheses need to be further evaluated by examining oxygen consumption behavior during oxidation reactions.

In addition to the ΔT_{max}, the summarized results of other key thermal performance metrics, such as the t_{peak}, P_{max}, Q_{rec}, and η_{rec} are presented in Figure 9-8b, 9-8c, and 9-8d. As the temperature and the Q_v increase, the temperature change reaches its t_{peak} more quickly, which aligns with the chemical kinetics of the oxidation reaction. By comparing Figure 9-8a and 9-8c, it is clear that the trends are identical because the temperature change is used in the calculation of the P in Equation 9-1. The honeycomb module could achieve a P_{max} of up to 4.97 ± 0.49 W (97.99 ± 9.59 W/kg) at the experimental condition of 600 °C-5L/min.

Similarly, the η_{rec} shown in Figure 9-8d follows the same trend as the Q_{rec}. Overall, both of them tend to decrease as the gas flow rate decreases. At the Q_v of 2.5 L/min and 1 L/min, the Q_{rec} show a decreasing trend as the reaction temperature increases. This may be attributed to the faster reaction rate at higher temperatures, which makes it difficult for the gas to effectively recover the heat generated from the module at a low Q_v, as mentioned earlier.

The situation becomes more complex when the gas flow rate is increased to 5 L/min. At 500 °C, the primary limitation of the oxidation reaction is no longer the oxygen concentration but the reaction temperature. As indicated in Figure 9-8a, both 500 °C-5L/min and 500 °C-2.5L/min exhibit nearly the same $\Delta T_{max.}$ On one hand, the lower reaction temperature slows down the reaction rate; on other hand, the higher gas flow rate accelerates both the reaction and heat exchange rates, creating a competitive relationship.

This competition may lead to significant variations in the results, especially when small differences in the initial experimental conditions occur, such as the sudden switching of gases.

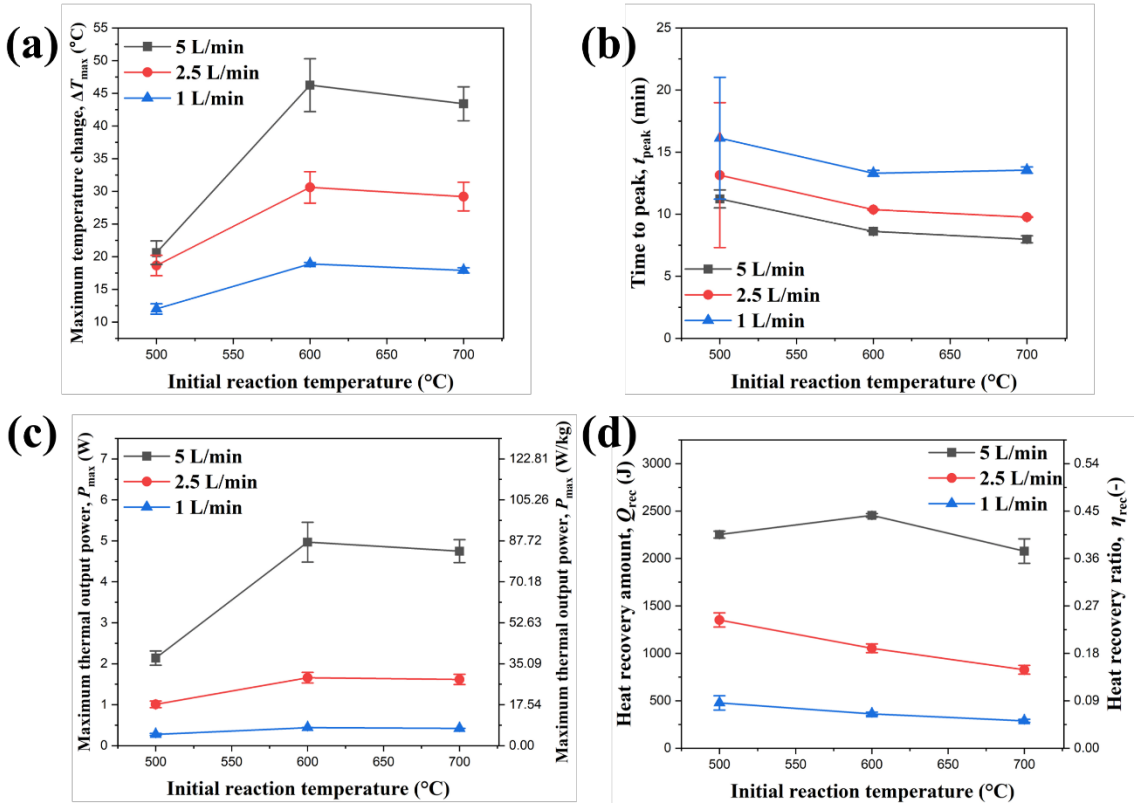

Figure 9-8 Variation of (a) Maximum temperature change (ΔT_{max}) (b) Time to peak (t_{peak}), (c) Maximum thermal output power (P_{max}), (d) Heat recovery amount (Q_{rec}) and Heat recovery ratio (η_{rec}) under different experimental conditions

In addition, an increase in the T_{in} during the oxidation reaction was observed, which could not be explained by convective heat transfer since this phenomenon occurred before the gas exchanged heat with the honeycomb module. The temperature changes at T_{in} for each experimental condition are presented in Figure 9-9. Since the baseline was not stable, we were unable to perform quantitative analysis. However, from a qualitative perspective, the rate of temperature increase at T_{in} accelerates with higher initial reaction temperatures.

Additionally, the width of the temperature peak tends to increase as the Q_v decreases. Overall, this phenomenon can be attributed to the effects of thermal radiation. Initially, the honeycomb module and the K-type thermocouple are at T_{in} the same temperature. However, as the oxidation reaction proceeds, the temperature of module rises, allowing the thermocouple to catch the thermal radiation from the honeycomb module, causing the thermocouple's temperature to increase. Subsequently, the thermocouple exchanges heat with the cooler gas, and the temperature falls.

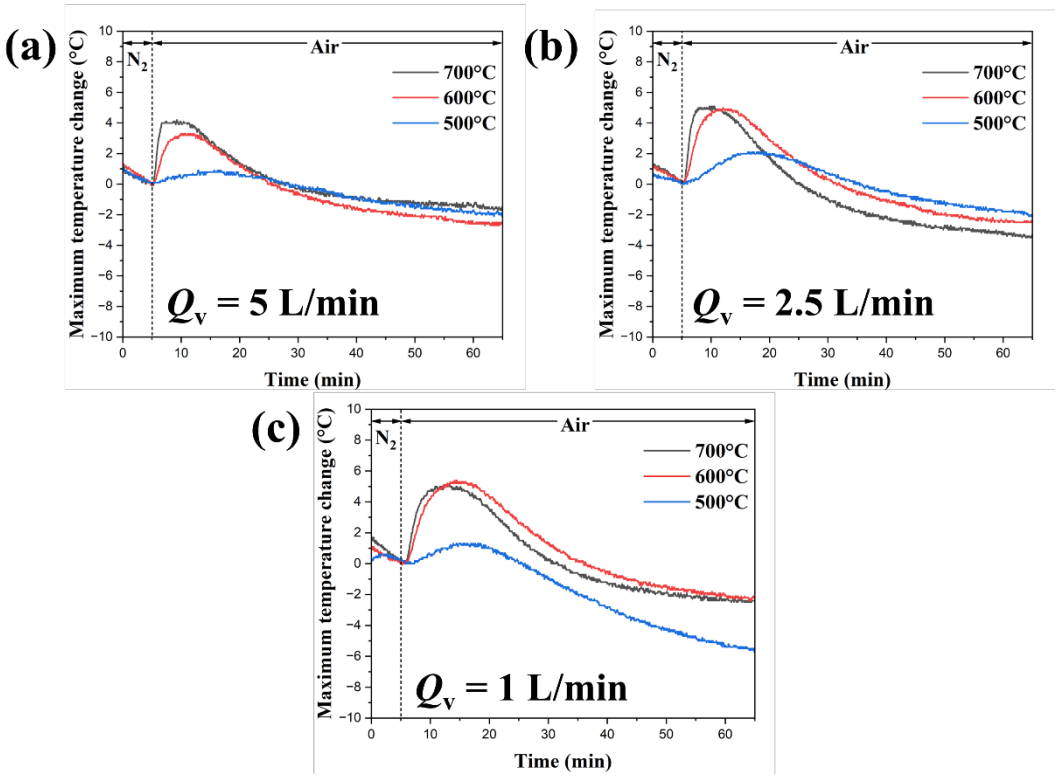

Figure 9-9 Variation of inlet temperature change under different initial reaction temperature at gas flow rate (Q_v) of (a) 5L/min, (b) 2.5 L/min, and (c) 1 L/min

This combination of convective heat transfer and thermal radiation is complex and beyond the scope of this study, so it will not be further explored. However, it is important to note that exothermic reactions at high temperatures may result in significant thermal radiation losses, which can severely impact the heat recover efficiency at the outlet.

9.3.4 Reactivity under different experimental conditions

The original oxygen consumption rates at different gas flow rates under different reaction temperatures are shown in Figure 9-10. From the figure, it is evident that the oxygen consumption rate exhibits two distinct peaks, a sharp initial peak followed by a relatively flat one, occurring immediately after the gas was switched. The second peak is attributed to the oxidation reaction, while the first one is believed to be related to the gas switching. Initially, the reaction tube is filled with nitrogen, and after the gas switching, the oxygen takes some time to refill the tube, which explains the sharp peak observed in the original oxygen consumption rate. This behavior is similar to the concept of "dead volume".

It is important to note that these two peaks overlap to some extent in most experiments, making it difficult to accurately evaluate the reactivity of the honeycomb module. To address this, we analyzed the oxygen dead volume phenomenon during gas switching for each experimental condition. Since the honeycomb module might undergo a minor redox reaction at 600°C and 700°C, we conducted experiments without the honeycomb module in the reaction tube, as shown in Figure 9-11a and 9-11b. As the gas flow rate increases, the oxygen dead volume decreases. Similarly, a higher initial reaction temperature leads to a reduction in oxygen dead volume. This phenomenon is likely related to the expansion of gases at higher temperatures, resulting in a faster actual flow rate in the reaction tube. To ensure that the presence or absence of the modules does not significantly affect the oxygen dead volume, we conducted an experiment with one honeycomb module at 500°C, as shown in Figure 9-11c. As the results demonstrate, the presence or absence of the honeycomb module has no notable impact on oxygen dead volume. Therefore, these data were used to adjust the oxygen consumption rate by subtracting the dead volume effect.

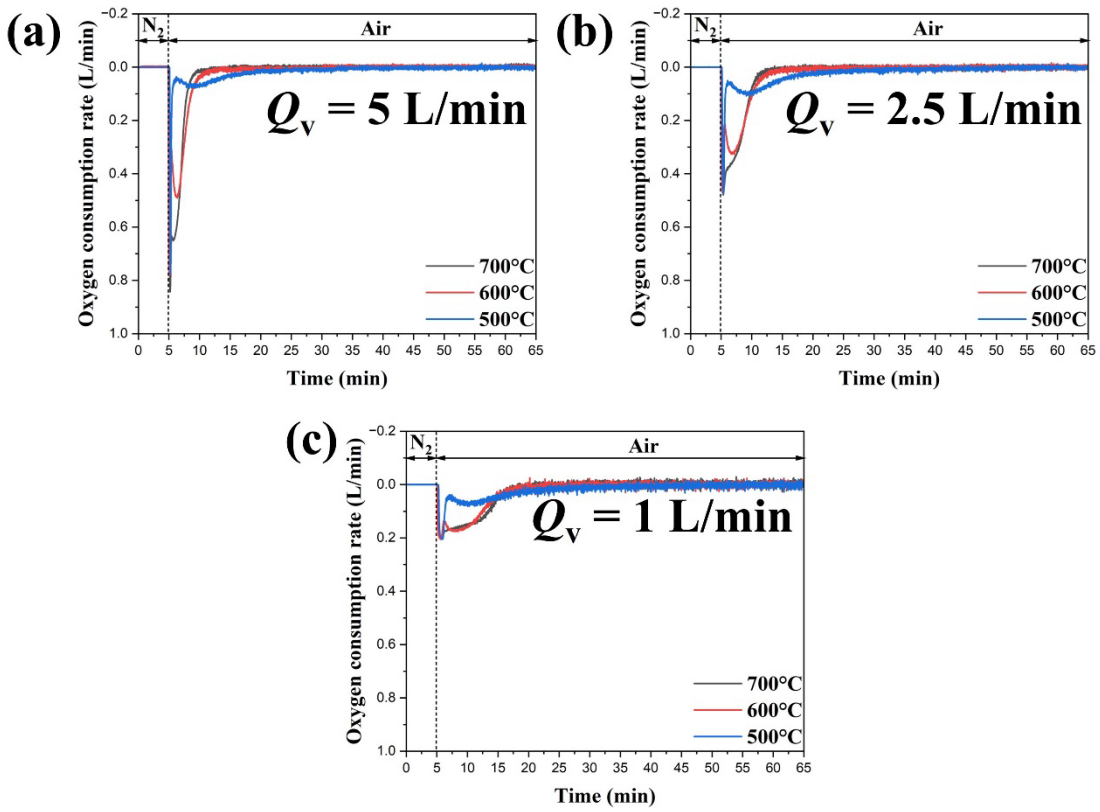

Figure 9-10 Variation of original oxygen consumption rate under different initial reaction temperature at flow rate of (a) 5L/min, (b) 2.5 L/min, and (c) 1 L/min

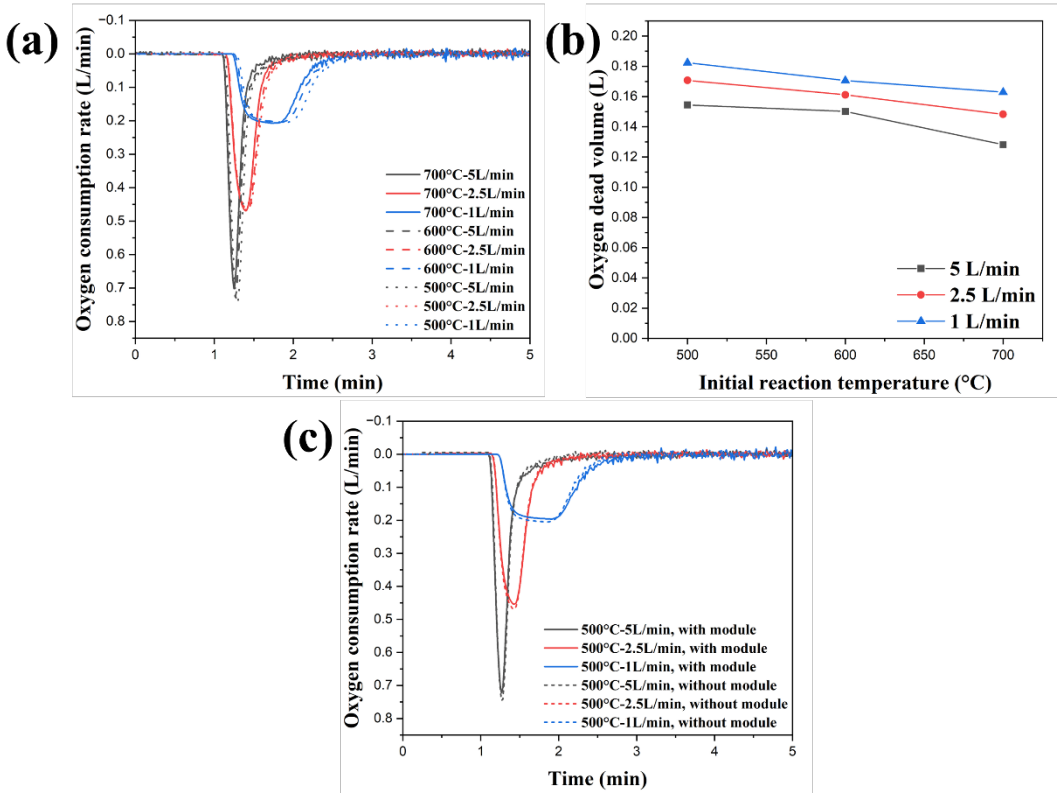

Figure 9-11 (a) Oxygen consumption rate and (b) Oxygen dead volume under different initial reaction temperature and gas flow rate; (c) Oxygen consumption rate with and without module at 500℃

The adjusted oxygen consumption rate is shown in Figure 9-12, where the honeycomb module reaches a $r_{O2,peak}$ of 0.621 ± 0.022 L/min (0.509 ± 0.018 mol/(kg·min)) at 700 °C-5 L/min. Moreover, the data fluctuations in the oxygen consumption rate increased slightly after switching the gas from nitrogen to air, especially under the Q_v of 2.5 L/min and 1 L/min. These fluctuations are primarily due to the mass flow meter and the outlet, caused by the uneven flow of the heated and expanded gas, which is then cooled again.

After summarizing the $r_{O2,peak}$ in Figure 9-13, we observe that the $r_{O2,peak}$ increases both the initial reaction temperature and the Q_v, which aligns with the conventional reaction kinetics. The trend of the t_{peak} (Figure 9-13b) shows an inverse relationship to the $r_{O2,peak}$,

which is also consistent with the chemical kinetic principle that higher temperatures lead to faster reaction rates. As shown in Figure 9-13c, the V_{O2} increases with reaction temperature across all gas flow rate conditions. This is mainly because the reaction rate accelerates as the temperature rises. At lower temperatures, the reaction may eventually stop at a quasi-equilibrium state, resulting in a lower total oxygen consumption.

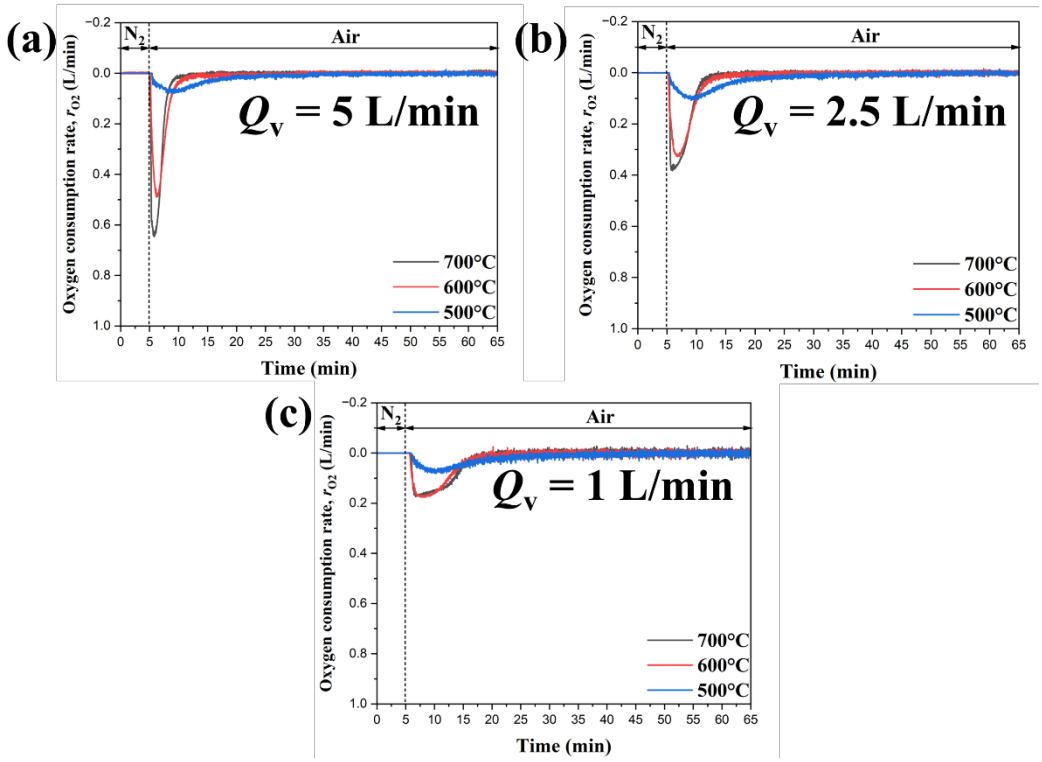

Figure 9-12 Variation of oxygen consumption rate (r_{O2}) under different initial reaction temperature at flow rate of (a) 5L/min, (b) 2.5 L/min, and (c) 1 L/min

At the same reaction temperature, the V_{O2} shows a clear trend for the Q_v are 2.5 L/min and 1 L/min. However, the behavior becomes more complicated at 5 L/min. Initially, the V_{O2} at 5 L/min appears lower than that at 2.5 L/min and 1 L/min, but then it falls between them. This phenomenon may be explained by the fact that, at higher gas flow rates, although the reaction rate increases, the change in oxygen concentration detected by the oxygen sensor decreases. Given that the resolution of the oxygen concentration sensor

used in this experiment is 0.1%, the margin of error increases at higher flow rates, leading to an underestimation of the V_{O2} at 5 L/min.

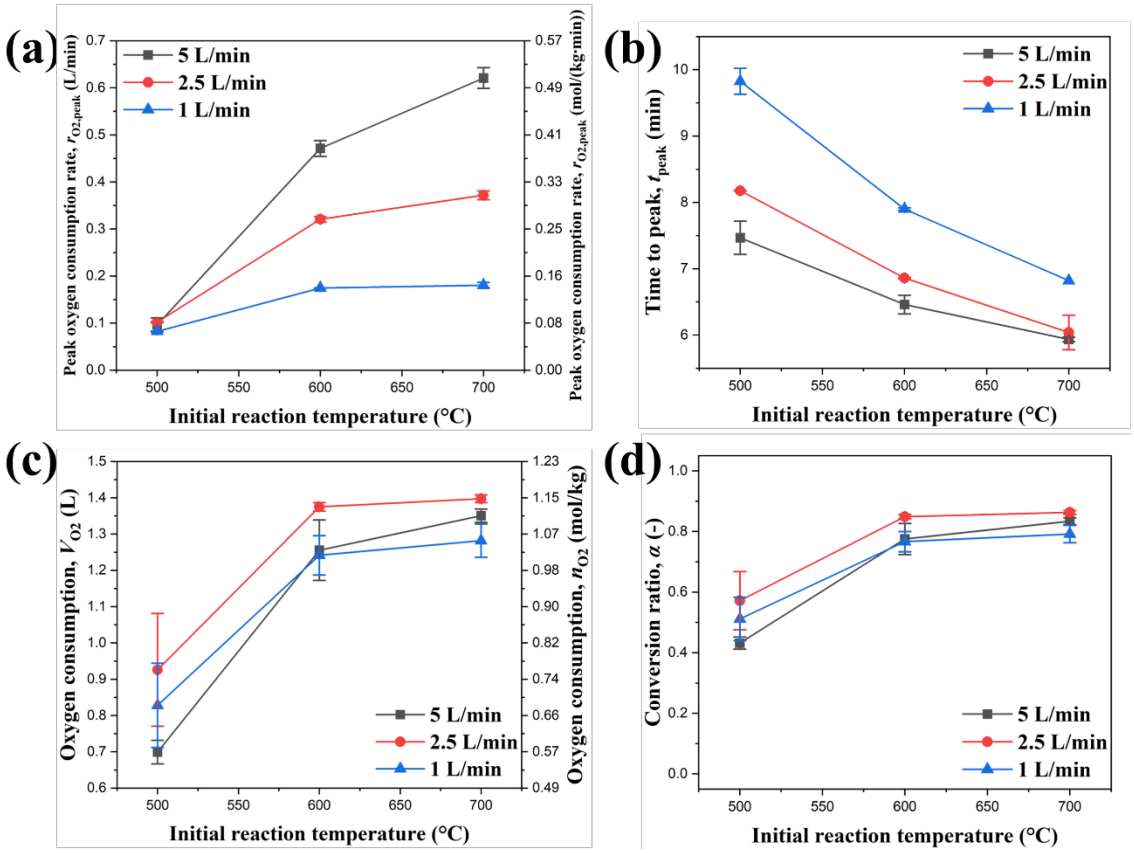

Figure 9-13 Variation of (a) Peak oxygen consumption rate ($r_{O2,peak}$) (b) Time to peak (t_{peak}), (c) Oxygen consumption (V_{O2}, n_{O2}), and (d) Conversion ratio (α) under different experimental conditions

The α, calculated from the V_{O2}, is presented in Figure 9-13d. At 700 °C-2.5 L/min, the α of honeycomb module reached a maximum value of 0.863 ± 0.007. Further weighing of the fully reduced and fully oxidized honeycomb modules using an electronic balance confirmed that the weight changes were consistent with the TGA results, suggesting that the α calculated from the oxygen sensor was somewhat underestimated generally. However, these results still accurately reflect the overall trends at different reaction

temperatures and gas flow rates. Specifically, the honeycomb module exhibits good oxidation reactivity at 600°C and above, while the reaction proceeds slowly and tends to stop at a quasi-equilibrium state at 500°C. Additionally, while the gas flow rate has a significant effect on the instantaneous oxygen consumption rate at the same reaction temperature, it has a minor effect on the total oxygen consumption and the overall reaction conversion ratio.

In addition, as discussed in the previous section, two possible reasons could be used to explain the lower magnitude of temperature change (ΔT), smaller heat output power (P_{max}) and reduced heat recovery ratio (η_{rec}) observed at an initial reaction temperature of 700 °C compared to 600 °C (Figure 9-8). Further analysis of Figure 9-13d reveals that, at the same gas flow rate, the differences of oxidation conversion ratio (α) at initial reaction temperature of 700 °C and 600 °C are relatively small. This suggests that the decrease in the net reaction rate due to the temperature being close to the equilibrium temperature, has a lesser impact. Instead, the reduction in heat performance at 700 °C can primarily be attributed to the higher heat loss associated with higher initial reaction temperatures.

9.4 Conclusions

In this chapter, we used $CuMn_2O_4/CuMnO_2$ as raw materials to prepare honeycomb structure heat storage module (φ 32mm × H 49 mm, 304 cpsi) containing 70 wt% $CuMn_2O_4/CuMnO_2$ via extrusion molding for chemical heat storage applications. A demonstration equipment setup was designed based on tube furnaces, was used to evaluate the heat release performance and reactivity of the module. The honeycomb module was first placed in the reaction tube and heated to 900 °C under an N_2 flow to fully reduce (charge) into its reduced state. It was cooled to the target initial reaction temperature under the protection of N_2 flow. Once the temperature stabilized, the N_2 gas was switched to air to trigger the oxidation reaction. Initial reaction temperatures of

700 °C , 600 °C , and 500 °C were investigated, alongside air flow rates of 5 L/min, 2.5 L/min, and 1 L/min.

From the representative experimental results, a noticeable temperature change was observed when the gas was switched from N_2 to air. Additionally, a significant delay in the change of oxygen concentration at the outlet compared to the inlet, along with a decrease in flow rate, was observed. These phenomena demonstrated that the oxidation reaction could occur under these experimental conditions, effectively releasing the stored heat.

By analyzing the heat release performance of the honeycomb module, it was observed that a maximum outlet temperature change of 46.2 ± 4.1 °C and a thermal output of 4.97 ± 0.49 W (97.99 ± 9.59 W/kg) were achieved at an initial reaction temperature of 600 °C and a flow rate of 5L/min. Generally, increasing the initial reaction temperature typically accelerates the reaction rate, leading to higher temperature changes and larger thermal output power. However, the experimental results at 700 °C exhibited a smaller temperature change compared to those at 600 °C. By further analyzing the module' reaction conversion ratio, it is speculated that this phenomenon is primarily due to larger overall heat loss in the system at the higher initial reaction temperature.

For reactivity analysis, we observed that a delay in the change of oxygen concentration at the outlet compared to the inlet occurred after switching the gas from N_2 to air. This phenomenon cannot be attributed to the oxidation reaction but related to the initial presence of N_2 in the reaction tube. After deducing the inherent error of the demonstration setup, the honeycomb module exhibited a maximum peak oxygen consumption rate of 0.621 ± 0.022 L/min (0.509 ± 0.018 mol/(kg·min)) at 700 °C with an air flow rate of 5 L/min. Further analysis of oxygen consumption revealed that the module can achieve a maximum conversion ratio of 0.863 ± 0.007, demonstrating excellent chemical reaction activity.

In general, $CuMn_2O_4$/$CuMnO_2$-based honeycomb structure heat storage module

prepared via extrusion molding exhibits rapid heat storage and release capacity with excellent chemical reactivity under high gas flow rates. However, it is worth noting that clay additives are used to enhance mechanical strength and may negatively affect module's reactivity when heated at temperatures exceeding 900 °C. Some components of the clay may react with Cu-Mn oxides, potentially reducing the heat storage density of the modules. Future studies should focus on modifying clay composition to mitigate these issues.

Reference

[1] C. Agrafiotis, M. Roeb, M. Schmücker, C. Sattler, Exploitation of thermochemical cycles based on solid oxide redox systems for thermochemical storage of solar heat. Part 2: Redox oxide-coated porous ceramic structures as integrated thermochemical reactors/heat exchangers, Solar Energy 114 (2015) 440–458. https://doi.org/10.1016/j.solener.2014.12.036.

[2] A. Singh, S. Tescari, G. Lantin, C. Agrafiotis, M. Roeb, C. Sattler, Solar thermochemical heat storage via the Co3O4/CoO looping cycle: Storage reactor modelling and experimental validation, Solar Energy 144 (2017) 453–465. https://doi.org/10.1016/j.solener.2017.01.052.

[3] G. Xiao, Z. Wang, D. Ni, P. Zhu, Kinetics and Structural Optimization of Cobalt-Oxide Honeycomb Structures Based on Thermochemical Heat Storage, Energies 16 (2023). https://doi.org/10.3390/en16073237.

[4] F. Benyahia, K.E. O'Neill, Enhanced Voidage Correlations for Packed Beds of Various Particle Shapes and Sizes, Particulate Science and Technology 23 (2005) 169–177. https://doi.org/10.1080/02726350590922242.

Chapter 10. Data circulation in chemistry fields – from a multi-scale perspective

10.1 Introduction

Since 2020, I have actively participated in various activities as a trainee in the Graduate Program for Real-world Data Circulation Leaders (hereinafter referred to as "'the program") established by Nagoya University [1]. This program was established in 2014 as a 5-year program spanning from master's to doctoral courses. It focuses on understanding and designing various data circulation in the real world and further optimizing and improving the secondary iteration of process of data circulation.

In this chapter, I will discuss the specific applications of data circulation in my field of study, chemistry, along with its methodology and social value.

10.1.1 Definition of data circulation

In modern society, the importance of various data sciences is becoming more and more prominent, and how to efficiently collect, analyze, and apply data in the complex real-world has become the core to promote the technological development of various fields and the overall progress of society in the future. In response to this need, this program proposes an innovative data circulation model (Figure 10-1) [2], i.e., the cycle of "Data Acquisition, Analysis, and Implementation".

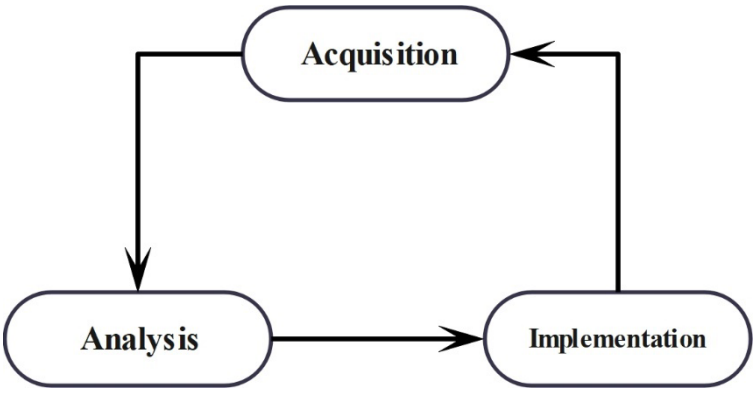

Figure 10-1 Data circulation of acquisition, analysis, and implementation

This circulation emphasizes the use of methodologies related to convenience, speed,

health, and prosperity in basic sciences such as engineering, intelligence, medicine, and economics to achieve the full integration of real-world data resources in various fields. This is coupled with a scientifically rigorous approach to analyzing and ultimately applying the results to real-world problem solving, with specific definitions of the various nodes as shown below:

- ***Data Acquisition:*** This involves employing efficient and accurate methods to collect multi-dimensional data from various real-world sources. These may include laboratory experimental results, monitoring data from industrial production processes, statistical data from socio-economic activities, and publicly available information on finance and livelihoods from governmental departments. The key focus of data acquisition is ensuring that the collected data are: (I) Complete—reflecting the entirety of the objective facts, (II) Accurate—providing an exact description of the objective facts, and (III) Current—capable of supporting predictions about future trends.
- ***Data Analysis***: Utilizing the acquired data, methods such as statistical analysis, mathematical modeling, and machine learning are applied to process the data, aiming to extract valuable insights and patterns. Special attention is given to converting non-numerical data—such as images, waveforms, sound waves, and textual information—into numerical formats that can be directly analyzed by computers. The core objective of this stage is to transform complex data into interpretable formats, providing a scientific insight for solving real-world problems.
- ***Data Implementation***: This stage involves applying the models or conclusions derived from data analysis to real-world scenarios to validate their accuracy and feasibility. Examples include optimizing industrial production processes, assisting doctors in making more precise diagnoses, or devising effective strategies for

socio-economic systems. Importantly, the models and data developed during the initial cycle must be updated periodically, as real-world phenomena often evolve over time. For example, aging equipment in industrial production can lead to new challenges, or economic cycles can cause shifts in socio-economic trends. Therefore, data implementation is not the conclusion or end but rather the starting point of a new data cycle, ensuring continuous adaptation and improvement.

This circulation model emphasizes a time-oriented approach rather than pure theoretical concepts. It links scientific research theories to societal needs. It focuses on exploring practical applications of research outcomes generated at universities and other institutions.

10.2 Application of the data circulation in chemistry – a multi-scale perspective

Research in chemistry-related subjects, such as material science, chemical engineering, and chemical process control, often involves a series of multiscale problems. These problems can be categorized into hierarchical scales, spatial scales, and temporal scales. Given that the core objective of this study is to explore the integrated research of redox-type chemical heat storage systems in medium-high temperature ranges, this chapter primarily focuses on hierarchical scales in chemistry-related research.

Hierarchical scales are typically subdivided into four levels: micro-scales, meso-scales, device-scales, and system scales. The following subsections explore the application of data circulation at each of these scales:

- ***Micro-scales:*** Application of data circulation in the design of inorganic materials and organic compounds
- ***Meso- and device-scales:*** application of data circulation in chemical experiments,

process optimization, device design

- ***System-scales:*** Application of data circulation in chemical process control, management, and soft sensors.

These discussions provide a systematic perspective on solving multiscale problems in chemistry-related subjects and further promote integration and advancement of data science methods in these research fields.

10.2.1 Application of data circulation in design of inorganic materials and design of organic compounds

With the rapid advancement of computer hardware technology, we now have the capability to design high-performance materials using data circulation and machine learning methods. This integration of computational chemistry and data science in materials design is commonly known as Materials Informatics (MI), addressing the fundamental question: "What to make?".

In Chapter 7, we investigated how different doping elements affect the reaction temperature of $CuMn_2O_4/CuMnO_2$. This study is part of the Global Challenge II (GC2) project I worked on at Hokkaido University. The traditional way of developing new materials involves the circulation of synthesizing, testing, and analyzing. It would take years and substantial costs if we want to explore the doping effect of all elements in the periodic table for $CuMn_2O_4/CuMnO_2$. To address this problem, we introduced a new approach related to data circulation (Figure 10-2). This method helps us design materials more efficiently by following 3 main steps:

1) ***Create dataset***: Use Density Functional Theory (DFT) to calculate the structure of some key materials to get accurate initial data. And then create a larger dataset by applying data enhancement techniques, which will be used to train the machine learning model.

2) ***Model training and prediction***: Train the machine learning model to predict the performance of material structures that haven't been calculated with DFT yet.

3) ***Validation and optimization***: Check the accuracy of the model's predictions with more DFT calculations and experiments. Use these results to improve the model and refine the material design process.

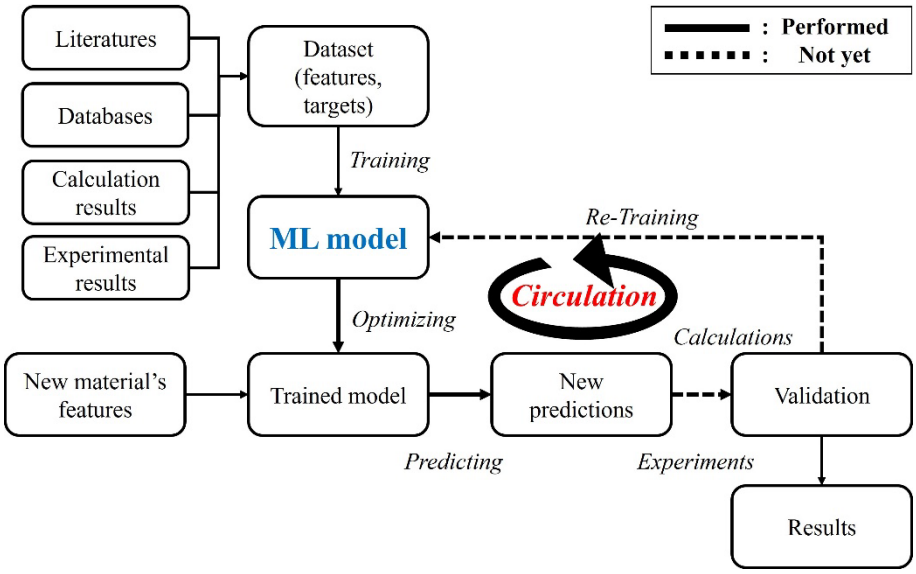

Figure 10-2 Machine learning assisted dopant optimization based on data circulation

This data-driven approach significantly increases the efficiency of material screening while also reducing both experimental and computational costs.

Similar research methodologies have been demonstrated by other researchers. For instance, Iwasaki et al. proposed a highly autonomous materials development cycle for designing new magnetic alloys with high magnetization [3]. Instead of relying on large-scale datasets, their approach models the human decision-making process to autonomously explore materials. Specifically, they achieved this by starting with an initial material structure and integrating virtual material synthesis, virtual testing, and machine learning (Figure 10-3). This iterative process allowed them to predict the next material structure to investigate. Almost at the same time, Shimizu et al. expanded on this concept

by incorporating robotic systems capable of synthesizing materials, automatically testing their properties, and leveraging machine learning to predict subsequent research directions (Figure 10-4) [4].

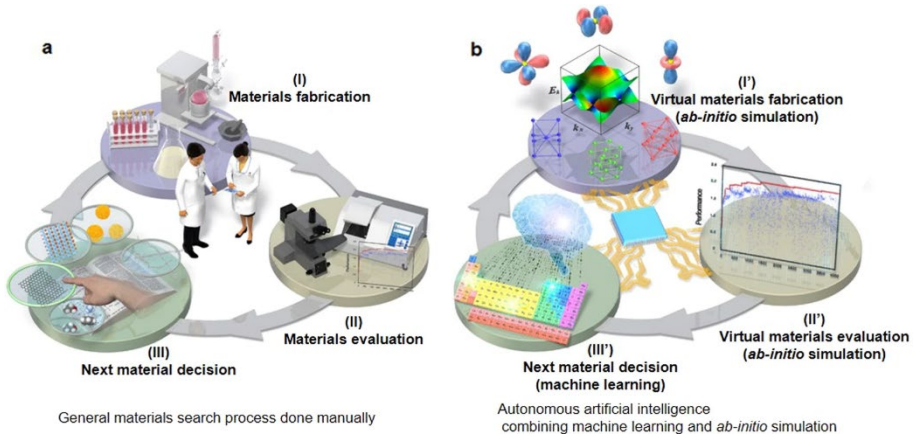

Figure 10-3 Concept of autonomous materials search system (a) Conventional materials search process; (b) Autonomous materials search system

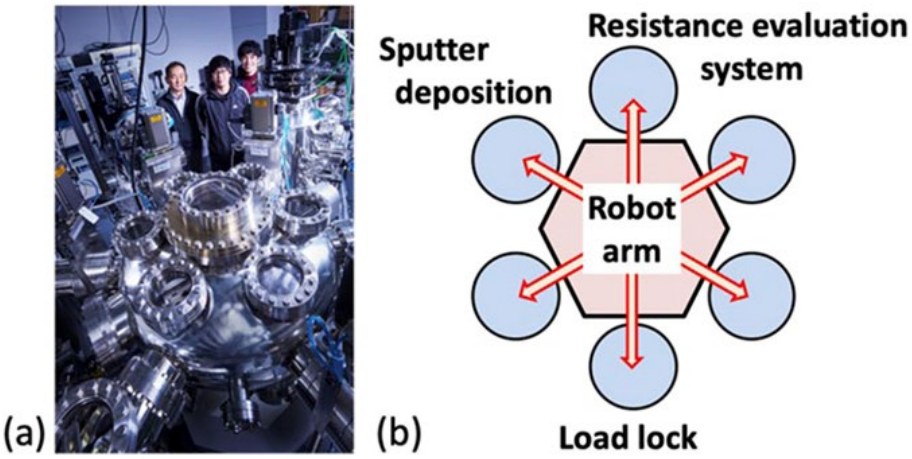

Figure 10-4 (a) Photograph and (b) Schematic diagram of the robotic system

By incorporating data circulation approach, failure data from experiments can be utilized to reverse-engineer potential success pathways. For instance, Raccuglia et al. demonstrated this approach by using experimental failure data to train a machine learning model that predicted synthesis routes for Metal-Organic Frameworks (MOFs) [5]. Their

model achieved a remarkable 89% success prediction rate, significantly outperforming traditional manual strategies. Notably, while MOFs can be synthesized via hydrothermal methods, the underlying mechanisms of their formation remain incompletely understood, emphasizing the continued importance of exploratory experiments by researchers.

Data circulation holds significant promise not only for the design of inorganic materials but also for the development of molecules such as pharmaceuticals. For instance, in the case of organic compounds used in pharmaceuticals, a key step is quantifying chemical structures and extracting characteristic parameters (commonly referred to as descriptors). By correlating these descriptors with the compound's physical properties, biological activity, and toxicity, regression models can be constructed using machine learning techniques. During the design of new compounds, their properties can be predicted by extracting the relevant descriptors and inputting them into the model, with the predictions subsequently validated through experiments.

In conclusion, data circulation offers extensive potential applications in the design of both inorganic materials and organic compounds. It not only facilitates efficient exploration of unexplored areas but also has the capacity to yield counterintuitive or unconventional findings, potentially leading to breakthroughs in the development of next-generation materials.

10.2.2 Application of data circulation in design of chemical experiments, processes and equipment

In the previous section, we discussed the application of data circulation in the design of materials and compounds. However, designing high-performance material is only part of the challenge. Such materials will not generate economic benefits for society unless they can be synthesized at scale in a practical and cost-effective way. Moreover, the desired properties of a material or product are not determined solely by the raw material itself but are also influenced by the synthesis processes. This problem is particularly evident in fields such as polymer materials, catalyst preparation, and medical product

synthesis.

For instance, in the design of polymer materials, physical properties such as strength, hardness, density, glass transition temperature, refractive index, and electrical conductivity are influenced by factors like monomer types, composition ratios, reaction temperatures. To meet specific requirements, it is essential to design experiments carefully to identify optimal production conditions. Ideally, this process should minimize the number of experiments and reduce development time, while balancing the costs of experimentation, production, and the overall development cycle.

Therefore, Kaneko proposed an optimization method for experimental conditions based on data circulation (Figure 10-5) [6]. In the initial stages, employing Design of Experiments (DOE) is an effective strategy for identifying potential experimental or production conditions. DOE facilitates the analysis of relationships between variables, such as condition X and characteristic y, enabling the construction of regression or classification models to predict y. Once a reliable model is established, new experimental conditions X' can be input to predict their corresponding characteristics y', effectively conducting a "virtual experiment." This approach significantly reduces the need for actual experiments, saving both time and resources.

Additionally, examining the model's predictions allows for the identification of potential conditions that meet the desired target characteristics. For instance, when aiming to develop a material with a specific characteristic y, Inverse Modeling can be employed to determine candidate conditions X that are likely to achieve the target y. This approach enables a more targeted and efficient exploration of experimental conditions.

However, inverse analysis of models is not always effective, primarily because it may not fully account for the applicability domain of the model or the reliability of its predictions. To address this, Bayesian optimization can be introduced when selecting the next experimental condition. Bayesian optimization represents predicted values as probability distributions, allowing the calculation of the likelihood that a candidate

condition will achieve the target characteristic. This enables the selection of the optimal next condition based on probability. Specifically, the process begins with the random generation of an initial set of conditions. Then, the candidate condition with the highest probability of success is selected for the next experiment. Alternatively, genetic algorithms can be combined with Bayesian optimization to refine the candidate conditions and identify options with higher probabilities or expected values. If experimental validation confirms that the target characteristics are achieved, the design process is complete. Otherwise, the new experimental data are added to the database, and the optimization cycle is repeated.

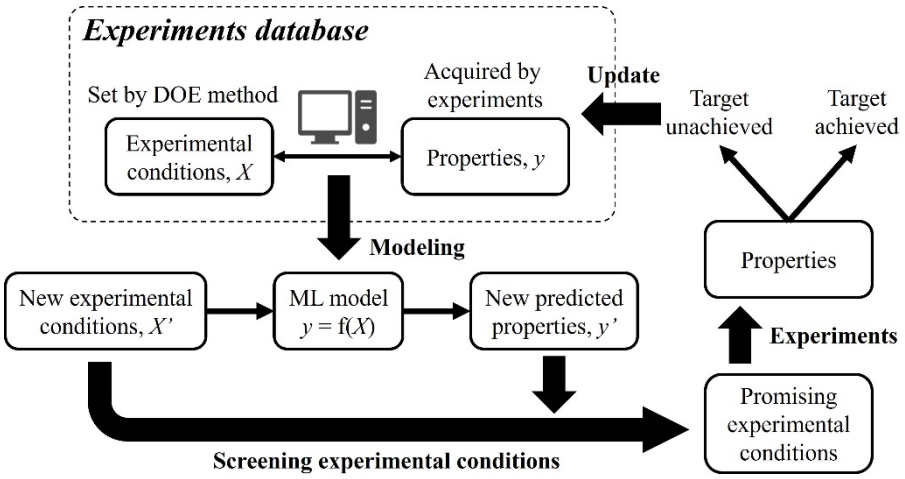

Figure 10-5 An optimization method for experimental conditions based on data circulation

Recently, Ono et al. employed an approach that integrates an automated flow system with machine learning to optimize the synthesis conditions of metal nanoparticles [7]. The experimental setup included a pump, a micro-mixer, a micro-reactor, and a UV-Vis on-line spectroscopic testing instrument, with the system automated via LabVIEW. By combining a classification algorithm with machine learning, the study successfully identified a set of optimal conditions for synthesizing nanoparticles with high

concentration and small particle size. Notably, unlike the iterative strategy of progressively determining the next experiment direction using Bayesian optimization, Ono et al. adopted a more exhaustive approach. They systematically explored all possible experimental conditions within a defined parameter range and selected the optimal solution. While this method ensures the discovery of a globally optimal solution, it may be less efficient for large condition spaces due to the increased computational and experimental demands.

In the actual production of materials and products, it is also important to consider the design of the processes and equipment. Parameters such as the shape and size of the reactor directly affect the materials or product's performance and their production efficiency. However, due to the time and cost constraints, it is impractical to optimize designs through repeated experiments involving physical equipment. Conventional methods usually design processes and equipment based on empirical assumption, followed by fine-tuning during the actual operation, which makes it difficult to achieve global optimization.

To solve this problem, we can use computer simulations to create virtual production processes and equipment. This allows us to study how production conditions affect the outcome without building the equipment. However, as processes and equipment become more complex, the models need to be more accurate, which takes more time to simulate. This makes it important to reduce the number of simulations as much as possible.

The optimization process for processes and equipment design is similar to that for materials and product design. In this case, "experimental or production conditions" are replaced with "equipment parameters," and "experiments" are replaced with "simulations." By building data circulation models and using optimization methods like Bayesian optimization or genetic algorithms, the best equipment parameters can be identified with fewer simulations, making the design process more efficient.

Whether designing materials, products, or processes and equipment, data circulation

methods have great potential. With careful experimental design, model predictions, inverse analysis, and optimization techniques, we can significantly reduce development costs and time while creating practical solutions for large-scale production.

10.2.3 Data circulation in chemical process control, process management and soft sensors

In industrial facilities such as chemical plants, controlling process variables (e.g., temperature, pressure, flow rate, concentration) is a central task of production activities. For example, when adjusting product yields or switching product types, parameters such as raw material inputs and temperatures in the reactor need to be dynamically adjusted to reach the target yield as quickly as possible.

However, the production process is not only influenced by internal parameter settings but also by the external environment (e.g., temperature, humidity, atmospheric pressure). Such external factors affecting production are known as disturbance. The plant must ensure product quality and production stability under disturbance conditions. At the same time, to avoid safety accidents, it must be ensured that process variables such as temperature, pressure, and flow rate remain within normal limits.

For variables that are easy to measure, such as temperature and pressure, abnormalities can be detected promptly through real-time monitoring. However, variables such as concentration, density, viscosity, or particle size in a fluid are often difficult to measure in real time. Measuring these variables can be time-consuming (often conducted in batches), resulting in the problem being out of the normal range when it is detected. This delay increases the complexity of anomaly detection and process control.

To solve this problem, soft sensor technology has been proposed [6]. Soft sensors enable real-time prediction of difficult-to-measure variables by establishing regression or classification models between easy-to-measure variables (e.g., temperature, pressure) and difficult-to-measure variables (e.g., concentration, density). Using the easy-to-measure variable x monitored in real time, the value of the difficult-to-measure variable y can be

inferred, which enables early detection of abnormal conditions, even if the difficult-to-measure variable has not yet been directly measured (Figure 10-6).

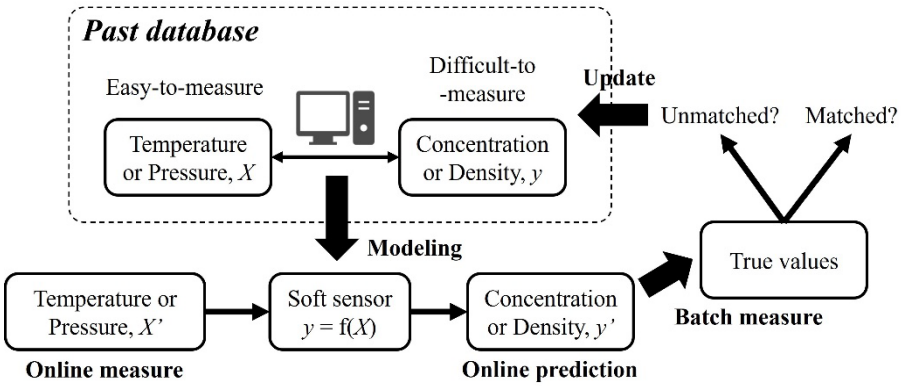

Figure 10-6 A soft sensor concept based on data circulation

During my research internship at Morimatsu T&S Co., Ltd., I explored the application of soft sensors in the recycling of lithium-ion batteries using the citric acid hydrothermal leaching method (Figure 10-7). The process is a continuous reaction in which black powder from lithium-ion batteries passes sequentially through a pre-heater, heater, settling separator, cooler, filter, and finally a collector. During the process, most of the black powder is leached out by citric acid and dissolved into the fluid in the heater and settling separator, while a small amount of black powder remains in the fluid as particles. Real-time monitoring of the particle size in the fluid at the outlet is essential for process optimization.

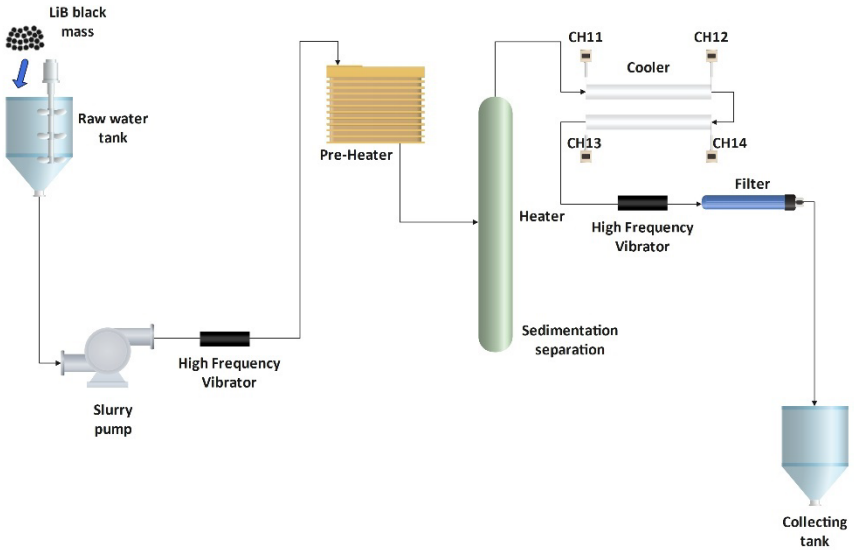

Figure 10-7 Soft sensors in the recycling of lithium-ion batteries

For this purpose, we proposed installing high-frequency vibrators at the inlet and outlet of the fluid to infer particle size by analyzing the attenuation characteristics of the vibration waveform. This idea is based on ultrasonic measurements of fluid flow rate outside the tube. However, the experimental results were not satisfactory, and we encountered the following challenges:

1) Difficulty in capturing the effect of particles on physical properties such as fluid viscosity, specific heat capacity, and refractive index using a high-frequency vibrator.
2) Vibrational noise from fluid flow contaminated the waveform, significantly complicating data resolution.

Nevertheless, we believe that by incorporating additional sensor types (e.g., temperature sensors, transmittance sensors) to supplement the data, we can potentially realize real-time particle size monitoring through soft sensors.

Although soft sensors have promising applications, their most significant challenge is

model degradation. Over time, the predictive performance of soft sensors may decline, resulting in substantial discrepancies between the inferred and actual values. Reasons for model degradation include:

- Changes in feedstock chemistry
- Catalyst deactivation
- Line fouling accumulation
- Variations in environmental factors (e.g., temperature, humidity, atmospheric pressure)
- Physical sensor aging

To maintain the long-term prediction performance of soft sensors, training datasets need periodic updates. However, manually updating the training dataset is time-consuming and labor-intensive, making the development of adaptive soft sensors essential. Three models are commonly used for implementing adaptive soft sensors:

1) Moving Window (MW) model: Dynamically updates model parameters using data from the most recent period.
2) Just-In-Time (JIT) model: Selects similar data for modeling based on current conditions.
3) Time Difference (TD) model: Uses the changing trend of time series data to update the model.

Different models are applicable to various scenarios, and the optimal method should be selected according to specific requirements.

The role of soft sensors in chemical process management extends beyond real-time monitoring to include anomaly detection and diagnosis. In multivariable systems, such as

multistage distillation columns, process variables typically exhibit correlations. For instance, in a system with two distillation column temperatures (T1 and T2), the relationship between these temperatures might deviate from the conventional pattern, even when individual measurements remain within normal ranges. Through principal component analysis (PCA) or classification modeling, anomalies can be identified in scatter plots to further investigate their root causes.

Data circulation soft sensors can effectively address real-time monitoring challenges by integrating correlation models of easy-to-measure and difficult-to-measure variables. However, their practical application still confronts challenges such as model degradation. By combining adaptive technology and data loops, soft sensors are poised to enhance the efficiency and intelligence of chemical process management, offering more reliable solutions for industrial production.

10.3 Conclusions

The concept of data circulation offers numerous possibilities for innovation and development across various societal domains, including resource utilization, technological advancement, public management, and addressing complex challenges.

In this chapter, we explore the applications of data circulation in chemistry-related fields from a multi-scale perspective, ranging from micro to macro. In materials design, materials informatics-based data circulation can be used to develop new inorganic materials and organic compounds with desirable properties. Chemical experiments, process, and equipment design can leverage data circulation to efficiently identify promising synthetic processes and optimize design methodologies. In chemical process control, process management, and soft sensor applications, data circulation provides effective real-time prediction methods for difficult-to-detect variables and reliable anomaly detection.

From a society value perspective, data circulation not only enhances research and production efficiency in traditional engineering subjects and industrial fields, but also significantly reduces the waste of human, financial, and material resources caused by trial and error. Additionally, the concept of data circulation facilitates efficient collaboration and rapid integration across fundamental science, artificial intelligence (AI), engineering technology, and government policymaking, providing critical support for interdisciplinary development. An often overlooked yet crucial aspect of data circulation is their role in driving innovation and technological progress. By using statistical analysis and AI, data circulation can yield insights that defy human-being's intuition, however, these insights that often hold the key to solving complex problems. Such counterintuitive findings may lead to groundbreaking discoveries in new materials, novel mechanisms, or even fundamental laws of physics, thereby expanding the frontiers of scientific research and technological applications.

Despite the significant potential of data circulation in chemistry-related fields, the current diffusion and adoption of AI in traditional industries remains limited and slow. This situation stems from several challenges inherent to traditional industries, including:

- Difficult data acquisition
- Complex production processes
- Stringent safety and reliability requirements
- Long economic and return on investment cycles
- Scarcity of professionals with interdisciplinary backgrounds

Future progress requires a comprehensive approach such as developing reliable AI algorithms based on data-driven and mechanistic modeling methods, strengthening government policy support and industry collaboration, validating AI's application value through small-scale demonstration.

By systematically addressing these challenges, more practitioners can recognize AI's potential in traditional industries, paving the way for future technological advancements.

Referenc

[1] Graduate Program for Real-world Data Circulation Leaders, Nagoya University, (n.d.). https://www.rwdc.is.nagoya-u.ac.jp/.

[2] K. Takeda, I. Ide, V. Muhandiki, Frontiers of digital transformation, Springer, Singapore, c2021.

[3] Y. Iwasaki, R. Sawada, E. Saitoh, M. Ishida, Machine learning autonomous identification of magnetic alloys beyond the Slater-Pauling limit, Commun Mater 2 (2021) 31. https://doi.org/10.1038/s43246-021-00135-0.

[4] R. Shimizu, S. Kobayashi, Y. Watanabe, Y. Ando, T. Hitosugi, Autonomous materials synthesis by machine learning and robotics, APL Materials 8 (2020) 111110. https://doi.org/10.1063/5.0020370.

[5] P. Raccuglia, K.C. Elbert, P.D.F. Adler, C. Falk, M.B. Wenny, A. Mollo, M. Zeller, S.A. Friedler, J. Schrier, A.J. Norquist, Machine-learning-assisted materials discovery using failed experiments, Nature 533 (2016) 73–76. https://doi.org/10.1038/nature17439.

[6] 金子弘昌, 化学のための Python によるデータ解析・機械学習入門, オーム社, 東京, 2023.

[7] T. Ono, Y. Takebayashi, T. Kashiwagi, K. Sue, Data-Driven Optimization of Au Nanoparticle Synthesis with Automated Flow Microreaction System, Journal of Chemical Engineering of Japan 56 (2023) 2211125. https://doi.org/10.1080/00219592.2023.2211125.

Chapter 11. Conclusions and outlook

11.1 Conclusions

This study focuses on developing an oxidized-reduced chemical heat storage system for medium- to high-temperature applications (500–1000°C). The research spans the development of novel heat storage materials, analysis and modeling of reaction kinetics, design and validation of heat storage modules, and optimization of operating conditions to improve performance. The key findings of each chapter are summarized below:

Chapter 2 explores Sr-based perovskite/brownmillerite materials for chemical heat storage. Among them, $SrFeO_{3-\delta}$ demonstrated excellent reactivity in the 500–1000°C range and good re-oxidation below 500°C. However, its maximum heat storage density was only 81.7 ± 3.4 kJ/kg-$ABO_{3-\delta}$ (473.5 ± 20.0 kJ/L-$ABO_{3-\delta}$), which is relatively low compared to conventional materials, limiting its practical application.

Chapter 3 focuses on Cu-based spinel/delafossite materials. The equilibrium temperature of the $CuMn_2O_4/CuMnO_2$ reaction was around 969°C, with a moderate heat storage density of 258.32 ± 15.31 kJ/kg-$CuMnO_2$ (1402.68 ± 83.13 kJ/L-$CuMnO_2$). This material exhibited good reactivity, durability, and the ability to release heat below 500°C during re-oxidation, likely due to its low activation energy.

Chapter 4 investigates the effects of Cr doping on $CuMn_2O_4/CuMnO_2$. Doping with 0.3 Cr increased heat storage density to 305.61 ± 16.45 kJ/kg (1.68 ± 0.09 MJ/L), while 0.1 Cr doping reduced the reoxidation temperature of $CuMnO_2$ to 305°C. These effects may be related to the increased instability in the crystal structure caused by Cr, lowering the activation energy.

Chapters 5 and 6 analyze the reaction kinetics of both undoped and Cr-doped $CuMn_2O_4/CuMnO_2$. For undoped materials, reduction kinetics were studied using non-isothermal methods, while oxidation kinetics used non-isothermal and isothermal methods. For Cr-doped materials, the oxidation reaction model was refined by incorporating an oxygen pressure term, accurately reflecting behavior under varying conditions and aiding numerical simulations.

Chapter 7 combines machine learning and DFT to systematically study the doping effects of almost all periodic table elements on $CuMn_2O_4/CuMnO_2$. Results indicate that small amounts of transition metals (e.g., Co, V) at the A-site effectively reduce reaction temperatures, while elements with larger ionic radii (e.g., Na, Ca) at the B-site may have similar effects.

Chapters 8 and 9 introduce two heat storage module designs: porous foam and honeycomb structures. The foam module, made via sacrificial sponge templating and sintered at 1100°C for 6 hours, suffered deformation due to poor mechanical strength, limiting scalability. The honeycomb module, made via extrusion molding, had better strength and achieved a temperature increase of 46.2 ± 4.1°C and a transient power output of 4.97 ± 0.49 W (97.99 ± 9.59 W/kg) under an initial reaction temperature of 600°C and 5 L/min airflow. It showed a maximum oxidation conversion ratio of 0.863 ± 0.007, confirming its reactivity and heat storage performance.

Chapter 10 highlights the role of data circulation in material design, experimental planning, process control, and soft sensors. Examples demonstrate how data-driven approaches can optimize research in chemistry-related fields, summarizing this work's contribution to the Graduate Program for Real-world Data Circulation Leaders.

11.2 Limitations of the current study and directions for future research

This study explores the potential application of $CuMn_2O_4/CuMnO_2$ in medium- to high-temperature oxidized-reduced chemical heat storage technology. While the material and its system demonstrate significant research and application value, several challenges remain. Below are the identified limitations and future research directions.

a) Limitations in Chemical Heat Storage Material Development

Currently, no perfect redox-type chemical heat storage material has been identified for the 500–1000°C temperature range. $SrFeO_{3-\delta}$ offer a suitable operating range but suffers

from low heat storage density, limiting their practical application. The reaction equilibrium temperature of $CuMn_2O_4/CuMnO_2$ is close to 1000°C, and while Cr doping has reduced this temperature, the effect is limited. Potential dopants identified through machine learning and DFT calculations have yet to be experimentally validated.

Future research should focus on identifying an optimal third component to lower the reaction temperature effectively without significantly compromising heat storage density or reactivity.

b) Limitations in Reaction Kinetics Studies

The reaction kinetics model developed in this study is complex, prioritizing accuracy but making it less suitable for direct engineering applications. Additionally, these kinetics studies are based on TGA experiments using powder materials, which differ from the behavior of modules like honeycomb structures due to oxygen diffusion resistance.

Future research should include kinetic studies on materials in practical morphologies (e.g., granules or honeycomb structures) to bridge the gap between laboratory findings and real-world applications.

c) Limitations in Heat Storage Module Design

The honeycomb-structured module's mechanical strength is enhanced by adding clay, which may undergo sintering and react with $CuMn_2O_4/CuMnO_2$ at high temperatures, reducing the module's heat storage density and reactivity. Additionally, the current module design has not been optimized in terms of size, number of cells, size of cells, or wall thickness.

Future work should involve numerical simulations to optimize the module’s geometry and material composition. Exploring new molding techniques or additives is also essential to improve mechanical strength without compromising reactivity.

d) Limitations in Application Scenarios

Medium- to high-temperature chemical heat storage systems are primarily applied in CSP (concentrated solar power) systems. However, the relatively small quantity of high

temperatures industrial waste heat, such as in the steel industry, limit broader application scenarios. Recent interest in Carnot batteries, particularly in Europe, offers new opportunities [1,2]. A Carnot battery system comprises three main components:

- **P2T (Power-to-Thermal):** Converts renewable energy (solar, wind, etc.) into high-temperature thermal energy.
- **TES (Thermal Energy Storage):** Stores energy as sensible, latent, or chemical heat.
- **T2P (Thermal-to-Power):** Releases stored thermal energy to generate electricity.

The efficiency of Carnot batteries is governed by Carnot's law, which states that higher temperature differences improve system efficiency. This gives oxidized-reduced chemical heat storage technology an advantage in such systems. However, rock-based sensible heat storage systems, a competing solution, are cost-effective. Future research must focus on improving the overall cost-effectiveness of thermochemical systems to enhance their competitiveness.

Comprehensive and integrated research on medium-high temperature redox-type chemical heat storage systems not only provides a deep understanding of their core mechanism but also offers theoretical guidance for optimizing the design of heat storage materials, modules, reactors, and systems. These findings establish a robust technical foundation for achieving Carbon Neutrality, particularly in the areas of renewable energy utilization and industrial waste heat recovery.

References

[1] O. Dumont, G.F. Frate, A. Pillai, S. Lecompte, M. De paepe, V. Lemort, Carnot battery technology: A state-of-the-art review, Journal of Energy Storage 32 (2020). https://doi.org/10.1016/j.est.2020.101756.

[2] T. Liang, A. Vecchi, K. Knobloch, A. Sciacovelli, K. Engelbrecht, Y. Li, Y. Ding, Key components for Carnot Battery: Technology review, technical barriers and selection criteria, Renewable and Sustainable Energy Reviews 163 (2022) 112478. https://doi.org/10.1016/j.rser.2022.112478.

Achievements

List of Publications (first author):

1. **Chen, X.**, Kubota, M., Yamashita, S. & Kita, H. Investigation of Sr-based Perovskites for Redox-type Thermochemical Energy Storage Media at Medium-high Temperature. *Journal of Energy Storage*, 38, 102501 (2021).
2. **Chen, X.**, Kubota, M., Yamashita, S. & Kita, H. Exploring Cu-Based Spinel/delafossite Couples for Thermochemical Energy Storage at Medium-high Temperature. *ACS Applied Energy Materials*, 4(7), 7242-7249 (2021).
3. **Chen, X.**, Kubota, M., Kobayashi, N., Yamashita, S. & Kita, H. Effect of Cr Addition on Cu−Mn Spinel/Delafossite Redox Couples for Medium-High Temperature Thermochemical Energy Storage. *ACS Applied Energy Materials*, 5(5), 5811-5821 (2022)
4. **Chen, X.**, Kubota, M., Kobayashi, N., Yamashita, S. & Kita, H. An In-depth Oxidation Kinetic Study of $CuCr_xMn_{1-x}O_2$ (x = 0, 0.1, 0.3) for Thermochemical Energy Storage at Medium-high Temperature. *Solar Energy Materials and Solar Cells*, 260, 112495 (2023)
5. **Chen, X.**, Kubota, M., Kobayashi, N., Lin S., Deng L. Li J., Yamashita, S. & Kita, H. Development of Redox-type Thermochemical Energy Storage Module: A Support-Free Porous Foam Made of $CuMn_2O_4/CuMnO_2$ Redox Couple. *Chemical Engineering Journal*, 485, 149540 (2024)

List of Publications (co-author):

1. Zhang, W., **Chen, X.**, Yamashita, S., Kubota, M. & Kita, H. B4C–SiC Ceramics with Interfacial Nano-relief Morphologies and Low Underwater Friction and Wear. *ACS Applied Nano Materials*, 4, 3159-3166. (2021).
2. Zhang, W., **Chen, X.**, Yamashita, S., Kubota, M. & Kita, H. Effect of Water Temperature on Tribological Performance of B4C-SiC Ceramics under Water Lubrication. *Tribology Letters*, 69, 1–13 (2021).
3. Zhang, W., **Chen, X.**, Yamashita, S., Kubota, M. & Kita, H. Frictional

characteristics of carbide Ceramics in Water. *Journal of Tribology*, 144(1), 011702 (2021).

4. Zhang, W., **Chen, X.**, Yamashita, S., Kubota, M. & Kita, H. Tribological behaviour of B4C-SiC composite ceramics under water lubrication: influence of counterpart. *Materials Science Technology*, 37(9), 863-876 (2021).
5. Liao, S., Zhou, X., **Chen, X.**, Li, Z., Yamashita, S., Kubota, M., Kita, H. Development of Macro-Encapsulated Phase-Change Material Using Composite of NaCl-Al_2O_3 with Characteristics of Self-Standing. *Processes*, 12(6), 1123. (2024)
6. Liao, S., Zhou, X., **Chen, X.**, Bao, F., Zhang, H., Yamashita, S., Kita, H. Development of rice husk composite ceramic sphere with enhanced radiation heat transfer for rapid heat storage and release at high temperature. *Ceramics International*, 50(20), Part A, 38051-38062 (2024)

Other Publications

1. 窪田 光宏, **陳 暁宇**, 高温熱の高密度貯蔵・利用を目指した酸化還元反応型化学蓄熱システムの開発. クリーンテクノロジー, 34(11), 57-61（2024）

International Conferences

1. **Chen, X.**, Kubota, M., Yamashita, S., Kita, H., The 2nd Asian Conference on Thermal Sciences (2nd ACTS), 30522, Fukuoka, Japan, Oct 2021.
2. **Chen, X.**, Kubota, M., Kobayashi, N., Yamashita, S., Kita, H., The Sixth International Symposium on Innovative Materials and Processes in Energy Systems (IMPRES 2022), ID 158, Barcelona, Spain, Oct 2022.
3. **Chen, X.**, Kubota, M., Kobayashi, N., Yamashita, S., Kita, H., Materials Today Conference 2023, O5A.9, Singapore, Aug 2023.
4. **Chen, X.**, Kubota, M., Kobayashi, N., Lin S., Deng L. Li J., Yamashita, S. & Kita, H., The Asian Conference on Thermal Sciences (3rd ACTS), O-0207, Shanghai, China, Jun 2024.

Acknowledgment

Looking back on my five years of study in Japan, I am overwhelmed with a myriad of emotions. I had often imagined the moment that I would complete my doctoral thesis and compose a heartfelt acknowledgement. Now that the time has come, I find myself at a loss for words to fully express the depth of my gratitude and reflections. The journey has been both challenging and rewarding, leaving me with countless memories and invaluable lessons that are difficult to capture on paper.

But anyway, I feel incredibly fortunate. The experience has not only broadened my horizons but has also given me the determination and confidence to move forward in life. Pursuing and completing a doctoral degree is one of the few life choices I can confidently describe as the “RIGHT” one. Throughout this process, I have been fortunate to receive invaluable support and encouragement from many individuals.

First and foremost, I would like to express my heartfelt gratitude to my advisor, Professor KITA Hideki, who also served as the main examiner of the Doctoral Thesis Committee. Over five years ago, when I was still an undergraduate student at a relatively obscure university, I was fortunate to receive his recognition and support, which provided me with the opportunity to pursue my master’s degree at Nagoya University. His invaluable guidance in shaping the general direction of my research encouraged me to think beyond conventional boundaries and adopt a broader perspective on academic challenges.

I would also like to extend my sincere thanks to the esteemed members of my Doctoral Thesis Committee: Associate Professor KOBAYASHI Noriyuki, Professor NAGANO Hosei, Associate Professor MACHIDA Hiroshi, and Professor HASEGAWA Yasuhisa. Their insightful and constructive feedback greatly enhanced the quality of my doctoral thesis. I am deeply grateful for their time and effort in reviewing my work and offering

their expertise.

My special appreciation goes to Assistant Professor KUBOTA Mitsuhiro, who provided guidance on every aspect of my research, from the fine details to the overarching framework of my thesis. He has been not only a mentor on my academic journey but also a supportive friend in my personal life. His encouragement helped me strike a balance between my research and life in Japan, making this experience both fulfilling and enriching.

Additionally, I am deeply thankful to Assistant Professor YAMASHITA Seiji, and Laboratory Technician SHIBATA Mika of Kita Laboratory. Their assistance in conducting experiments allowed me to concentrate on the core aspects of my research work.

During my academic journey, I have been fortunate to receive tremendous support from my seniors in the Kita Laboratory, particularly Dr. ZHANG Wei and Dr. ZHOU Xin. As exemplary roles, they selflessly shared their experiences and offered invaluable encouragement, helping me avoid unnecessary detours in both research and my personal growth.

In addition to my academic research, I was fortunate to participate in the Graduate Program for Real-world Data Circulation (RWDC). Through this interdisciplinary program, I gained proficiency in cutting-edge technologies related to data science and artificial intelligence and cultivated the idea of integrating data science techniques into traditional engineering research. This experience may open a new avenue for my future research endeavors.

Beyond academia, I owe my deepest gratitude to my family for their unwavering support. They have always been my strongest pillar of strength, standing by me through every step of my journey. No matter where I am in the world, their unconditional love and care have been a constant source of motivation and comfort, giving me the courage to keep moving forward.

Finally, I would like to express gratitude to my younger self—the one who, five years

ago, made bold and resolute decisions at countless crossroads in life. Today, I can proudly claim that I have lived up to the motto of my *alma mater*, becoming a "勇気ある知識人 (a courageous intellectual)". The road ahead will undoubtedly bring new challenges and uncertainties, but this journey has taught me the true meaning of perseverance and the profound value of devotion.